ENHANCED FULLY NONLINEAR BOUSSINESQ-TYPE EQUATIONS IN CONSERVED VARIABLE FORM AND LINEAR ANALYTICAL PROPERTIES WITH COMPACT FINITE DIFFERENCE SCHEMES

A DISSERTATION SUBMITTED TO THE GRADUATE DIVISION OF THE UNIVERSITY OF HAWAIʻI AT MĀNOA IN PARTIAL FULFILLMENT OF THE REQUIREMENTS FOR THE DEGREE OF

DOCTOR OF PHILOSOPHY

IN

OCEAN AND RESOURCES ENGINEERING

AUGUST 2023

By

Troy W. Heitmann

Dissertation Committee:

Kwok Fai Cheung, Chairperson

Zhenhua Huang
Marcelo H. Kobayashi
Eva-Marie Nosal
Justin E. Stopa

Keywords: Boussinesq, water waves, fully nonlinear, dispersion, compact finite difference, coastal processes

Dedicated to my mother, whose unwavering support fueled my journey; to my father, whose work ethic became my compass; and to my sister, my pillar of reliability.

"I can because of you."

ACKNOWLEDGMENTS

I would like to express my sincere appreciation to the individuals and organizations that have played a crucial role in inspiring and supporting this work over the years.

First and foremost, I am profoundly grateful to Professor Cheung, my advisor and mentor, for his resolute support and guidance throughout my research endeavors. From the very beginning, he has been a constant presence, providing invaluable assistance even during the most challenging times. I deeply appreciate his faith in my abilities and for allowing me the freedom to forge my own path forward. I have grown academically far beyond personal expectation and now find myself seeking leadership in a field that I'm passionate about. I can only hope that one day I will be able to give back in ways Professor Cheung has given to me. He truly is an exceptional advisor.

The collective words of encouragement from friends and colleagues have become the rhythmic pulse that propels me in my daily life, instilling the much-needed strength and motivation to persevere. I would like to individually acknowledge Justin Stopa, Volker Roeber, and Yefei Bai, for taking me under their wing early on, exposing me to practical wave modeling applications and laying the foundations of my research. Their mentorship has been instrumental in shaping the path I find myself on today.

Special thanks to Eva-Marie Nosal, Zhenhua Huang, Yoshiki Yamazaki, Krishnakumar (Kumar) Rajagopalan, and the greater ORE ohana. Being far from home, it has been comforting to know that I can always count on my hanai family in times of need. I am indebted to all for their guidance and support throughout this journey and I am truly grateful for their presence in my life.

I also want to acknowledge Marcelo Kobayashi and his rousing endorsement to push boundaries. Throughout this endeavor, he has been a tremendous source of inspiration, providing invaluable insights that have ignited fresh ideas and opened new avenues for future research. His guidance and mentorship have significantly contributed to my personal growth and development as a researcher.

Lastly, I extend my heartfelt gratitude to those who have provided financial support: Professor Cheung with the Department of Ocean and Resources Engineering, Professor Fletcher with the Department of Earth Sciences, The Link Foundation, and Dr. Cross with the Hawaii Natural Energy Institute. Without the availability of these funding opportunities, completing my PhD would not have been possible.

ABSTRACT

In coastal engineering applications, Boussinesq-type models are limited by orders of approximation originating in both the governing equations and numerical schemes employed. Dispersive model solutions reflect a composition of approximations dependent upon finite sampling intervals. This study aims to improve understanding of both theoretical and numerical facets, with the end goal of strengthening community awareness in model applicability.

A modern approach to parameterize wave breaking in Boussinesq-type equations is to leverage the hyperbolic structure of the leading order nonlinear shallow water equations and approximate overturning processes using shock capturing methods designed to conserve both mass and momentum. In this approach, it is well known that the governing partial differential equations (PDEs) must be expressed in conserved variable form to attain proper shock speeds. A new independent formulation covering a family of fully nonlinear, weakly dispersive Boussinesq-type equations is derived in conserved variable form by depth integrating Euler's equations of motion under an irrotational flow assumption. A projected Taylor series expansion of the vertical velocity about an arbitrary material surface is utilized in the depth integration of the irrotational flow condition to give an expression for the horizontal velocity. Through a change of variables, the dependency of the horizontal velocity is expressed with reference to an arbitrary point of evaluation. A new weighted average of horizontal velocity expansions at the material surfaces defines the model velocity at a datum invariant reference attached to the flow depth. In comparison to existing theories, the approach introduces an additional term which enhances nonlinear dispersion. Imposing constraints on the orders of approximation, leading order theories are recovered, thus showing theoretical advancement.

Transforming the governing PDEs into discrete approximations facilitates numerical simulation of nonlinear processes over a complex bathymetry, in which the approximations result in a system of modified PDEs (MPDEs) possessing unique solutions specific to the numerical methods employed. In practical application, practitioners are burdened with an unnecessary level of uncertainty during the selection of discretization parameters, despite their fundamental roles in the governing MPDEs. Beyond numerical experiments, there has been little effort to explicitly communicate numerical implications in Boussinesq-type models. For the Boussinesq-type equations derived herein, dispersion emerges through Taylor series expansions along the vertical axis, in which the methods of approximation mirror those used in finite difference methods. Therefore, a complementary finite difference framework is adopted in which the time integration is performed using linear multistep schemes. Difference operators, including those with compact support, are expressed in symbolic form for the purpose of generalization. Difference operators are expressed in symbolic form to promote generalization while seamlessly enabling the novel application of compact finite difference schemes.

Applying Fourier-Laplace transforms, the symbolic operators are mapped into spectral space, where waveform resolution is evaluated as a function of time, Δt, and space, Δx, sampling intervals. The approach facilitates a complex propagation factor analysis of amplitude and phase modulations, both of which may be present in physical theory. To better accommodate operator interactions occurring in systems of equations, definitions of operator support and coefficients are adjourned to maintain complex degrees of freedom during the full system analysis. As a result, the solution to the MPDEs becomes an objective, as opposed to an outcome, when defining schemes.

Developments on Boussinesq-type equations have largely focused on dispersion enhancements to the governing PDEs, in which family members having the same formal order of accuracy exhibit very different dispersive behaviors. The same level of research has not been carried out with regard to the respective MPDEs, where different schemes lead to unique dispersive solutions. The linearized MPDEs are cast into spectral space using Fourier-Laplace transforms. Substituting in the symbolic operators, the newly derived numerical dispersion relation for Boussinesq-type equations matches that of the PDEs provided the discrete operators are replaced by their continuous counterparts. The dispersion relation of the MPDEs is dependent upon not only on the wave number, k, and still water depth, h, but also Δt and Δx sampling intervals. The function domain of the celerity, or phase speed, is thus multidimensional, collapsing only to k and h in the limit of vanishing sampling intervals for stable consistent schemes. Several leading order Boussinesq-type equations are analyzed, in which the error associated with the MPDEs quantifies the bounds for application. Theories which exhibit increases in phase speed with relative depth are best suited to finite difference methods. This is due to a counter balancing decrease in phase speed imposed by finite difference methods. The transparency of error associated with the MPDEs gives further insights on the selection of sampling intervals and permits optimal mesh design for a given application.

TABLE OF CONTENTS

LIST OF TABLES

LIST OF FIGURES

CHAPTER 1
INTRODUCTION

Oceanic and coastal free-surface wave fields under the restoring force of gravity are said to be some of the most complex dynamic systems found in physical science (Feynman 1970, pp. V1-51-4). Atypically, the associated time and space scales are tangible to the laymen. We can see with our naked-eye the emergent complexities and record observations with remarkable precision. Whether or not the heralding complexity is a bias product of our senses, history has shown that water serves as a comprehensive medium in the study of wave dynamics. Modeling free-surface waves in a phase-resolving manner requires flow constituents be well resolved in both time and space. For time-dependent problems spanning many wavelengths, the application requirement rules out ideal implementation of nonlinear three-dimensional inviscid Euler equations for an incompressible fluid. Free-surface waves propagate perpendicular to the gravitational field, in which depth integrating the governing partial differential equations (PDEs) reduces the dimensionality, leading to significant computational cost savings. The quasi-3D approach suitably models free-surface wave processes, provided the velocity and pressure profiles are resolved.

Identifying characteristic scales of the physical problem, the Euler equations can be expressed in dimensionless form to quantify the scale contribution of individual terms. Focusing on long wave applications, where the characteristic wavelength, L_c, largely exceeds the characteristic still water depth, h_c, dimensional analysis of the governing equations reveals that the horizontal scales dominate over the vertical ones. At the leading order, the depth dependency of the pressure in the vertical momentum is governed by the displacement below the free-surface. Therefore, the horizontal pressure gradient is governed by the free-surface displacement alone, implying that the vertical distribution of the horizontal velocity must be uniform. Depth integration of the PDEs results in the conserved variable form of the hyperbolic nonlinear shallow water equations (NSWEs), which are applicable to many geophysical fluid flow problems (Saint-Venant 1871). Despite the allure of the NSWEs, the lack of dispersion is a fundamental shortcoming. In nature, the free-surface wave spectrum is dominated by wind generated waves which propagate in a dispersive manner.

Storm generated free-surface waves lead to broadband frequency spectra having high energy density. These characteristics impose significant design challenges to assure the functionality and survival of coastal structures. Operations analysis and risk mitigation begin with an understanding of how incident waves transform and propagate through coastal waters. In Airy wave theory (Airy 1845),

wave propagation is governed by the frequency dispersion relation

$$\omega^2 = k^2 g h \frac{\tanh kh}{kh} \tag{1.1}$$

in which h is the still water depth, g is the gravitational constant, $\omega = 2\pi/T$ is the angular frequency, and $k = 2\pi/L$ is the wave number, where T and L are the wave period and wavelength. For a given still water depth, relation (1.1) states that the phase speed, or celerity, $c = \omega/k$, is a function of the wave number. The group speed, $c_g = d\omega/dk$, which defines the speed of energy propagation, is also a function of the wave number and it is this property which asserts the dispersive nature of free-surface water waves under Airy wave theory (Whitham 1974). In coastal applications, attention is directed towards the asymptotic behavior of the PDEs as the relative depth, kh, vanishes. Applying a Taylor series expansion to the rational expression in (1.1) gives

$$\frac{\tanh kh}{kh} = 1 - \frac{(kh)^2}{3} + \frac{2(kh)^4}{15} - \frac{17(kh)^6}{315} + \frac{62(kh)^8}{2835} + O((kh)^{10}) \tag{1.2}$$

whereas $kh \to 0$, the expansion becomes unity, and (1.1) reduces to a dispersion relation governing linear shallow water waves. In addition, the group speed is no longer a function of the wave number, which means the waves are nondispersive. The same conclusions are attained in the small amplitude limit of the NSWEs, thus forming a junction between the two theories. Beyond the leading order term in (1.2), the wave number dependency is retained. Consequently, adding a dispersive perturbation of $O((kh)^2)$ to the NSWEs invokes a paradigm shift in long wave theory. For waves propagating over a constant still water depth, the leading order effects of frequency dispersion can be readily appended to the NSWEs with little effort (Whitham 1974). A linear correction term composed of a third derivative with unknown coefficient, is added to the momentum equation. Linearizing the NSWEs and solving for the dispersion relation, the unknown coefficient is chosen such that the resultant coefficient matches the coefficient in expansion (1.2) associated with the third derivative. As a result, the relative depth range of application is extended beyond the nondispersive shallow water limit to include weakly dispersive waves. The heuristic implies that as long as the order of frequency dispersion terms retained in the formulation is sufficient, nonlinear dispersive free-surface water waves can be described under the umbrella of long wave theory.

Hydrodynamic research on nonlinear dispersive evolution of free-surface water waves dates back to at least the mid 19^{th} century (Craik 2004; Craik 2005). Specifically, the pioneering equations of Boussinesq (1871) and Boussinesq (1872) have stood the test of time, only to be further substantiated in the mid 20^{th} century. Studying the dimensionless parameter, $U = a_c L_c^2/h_c^3$, in which a_c is the characteristic amplitude, Ursell (1953) showed that the Boussinesq (1872) equations were essential in deciphering the long wave paradox presented earlier by Stokes (1891). The fundamental parameter U exhibits a salient attribute, coupling measures of nonlinearity, $\epsilon = a_c/h_c$, and disper-

sion, $\mu^2 = h_c^2/L_c^2$, as $U = \epsilon/\mu^2$, which is effectively a relative measure between the two physical processes. Dimensional analysis unveiled that long wave theories assume either $U >> 1$ or $U << 1$; however the regime solutions are unique, hence the paradox. Classical Boussinesq equations are governed by the assumption $U = 0(1)$ and retain terms covering both limiting assumptions, thus unifying previous theories. Furthermore, the analysis highlights that the assumption $\epsilon\mu << 1$ alone is insufficient to justify implementation of linear wave theory in finite depth. The condition $U << 1$ is also a requirement, which additionally states that the dispersion must be much larger than the nonlinearity. Although Ursell (1953) studied a specific set of equations ascribed to Boussinesq (1872), the reciprocity between nonlinearity and dispersion transcends beyond water wave theories and is in general, theoretically significant in the study of nonlinear PDEs. Accordingly, variants of Boussinesq equations have been collectively referred to as Boussinesq-type equations, where measures of both nonlinearity and dispersion apply.

1.1 Boussinesq-Type Equations

Boussinesq-type equations represent a local approximation to the fully-nonlinear, fully-dispersive water wave problem in terms of the surface elevation and horizontal velocity. In the long wave asymptotic limit $kh \to 0$, dispersive perturbations are introduced through series expansions of the velocity profile for theoretical extension to include wind-generated wave applications. The ambiguous definition of the model velocity, as well as the ability to alter high order corrections through leading order substitutions, lead to families of equations characterized by a formal order of accuracy whose members possess unique mathematical structures (Long 1964; Benjamin et al. 1972; Peregrine 1974; J. L. Bona and Smith 1976). Employing these manipulations, dispersion can manifest through either model variable in both the continuity and momentum equations. In general, this implies the dispersion relation is defined by rational, as opposed to polynomial, functions. To elaborate, consider an $O(\mu^4)$ Taylor polynomial approximation. With regard to Padé rational approximations, the $O(\mu^4)$ Taylor approximation formally represents a family consisting of Padé [4/0], Padé [2/2], and Padé [0/4] approximations, in which the numerator and denominator reflect the manifestation of dispersion through the variables in the temporal and spatial derivatives respectively. Figure 1.1 depicts a qualitative (ϵ, μ^2) parameter space, in which the diagonal, $\epsilon = \mu^2$, represents a balance between nonlinearity and dispersion. Classical Boussinesq equations emerge from the "weak" assumption $\epsilon = \mu^2 << 1$, which limits nonlinearity and dispersion in application.

In the late 1960s, the long standing Boussinesq equations, governing the nonlinear dispersive evolution of long waves over constant depth, were reformulated for applications over variable depth (Mei and Le Mehaute 1966; Peregrine 1967). These early variants of Boussinesq-type equations marked a significant breakthrough in practical application. Although the equations of Mei and

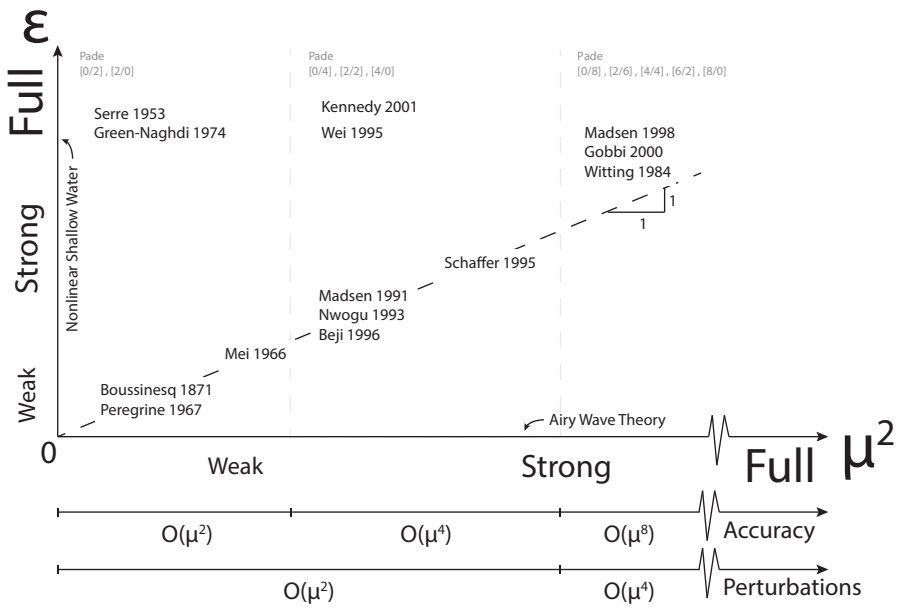

Figure 1.1: Domain sketch of dispersion, $\mu^2 = (kh)^2$, versus nonlinearity, $\epsilon = a/h$, showing qualitative orders of accuracy. Select models discussed in this study are grouped for reference, where the Padé regions assert the accuracy of approximation. The perturbations retained in the PDEs are also highlighted to indicate the order of computational complexity.

Le Mehaute (1966) and Peregrine (1967) share the same formal order of accuracy, $O(\mu^2)$, their dispersive correction terms reflect the model horizontal velocity being defined at the seabed and as the depth-average velocity, respectively. Furthermore, their frequency dispersion relations correspond to [2/2] and [0/2] rational functions, albeit the former does not achieve the accuracy of a Padé [2/2] approximation, hence remaining $O(\mu^2)$ accurate. In Peregrine (1967) and O. Madsen and Mei (1969), the newly derived Boussinesq-type equations were discretized with finite difference methods to study solitary wave transformations over a realistic sloping beach. Although the domains were academic in nature, the practicality of the studies would inspire the coastal engineering community to adopt Boussinesq-type models as a tool for the assessment of coastal processes. In an early example, building on nearly two decades of computational developments focused on NSWEs, M. B. Abbott et al. (1978) extended the model of M. B. Abbott et al. (1973) to include a set of Boussinesq-type equations expressed in terms of depth integrated variables, which appear similar to those of Peregrine (1967), but are actually quite different (e.g., Jensen 1983). Having already shown great success in early applications, a surge of interest to extend the relative depth range of Boussinesq-type equations through theoretically developments followed.

Witting (1984) introduces a model horizontal velocity variable with unknown coefficients into Taylor series expansions of a free-surface velocity expression and the depth average horizontal velocity in a system of PDEs, in which a recursive solution method was formulated to extend the relative depth

range of the frequency dispersion relation. Of primary interest, the method leads to the use of Padé rational, as opposed to Taylor polynomial, expansions to evaluate the coefficients in the dispersion relation. In comparison, Padé rational expansions improve stability properties and expand the region of convergence. Witting (1984) presents several approximations, with Padé [4/4] being the highest. Boussinesq was apparently aware of stability concerns in his original works, having chosen to work with a system of PDEs which result in a Padé [0/2] approximation of the dispersion relation (Whitham 1974), albeit the Padé approximation method did not come into existence until nearly 20 years later (Pade 1892).

The study by Witting (1984) would prove to be pivotal in guiding the development of Boussinesq-type equations, with immediate interest drawn to implementation of Padé rational functions in the dispersion relation. Instead of following the approach of Witting (1984) verbatim, P. A. Madsen et al. (1991) substituted truncated series expansions about a model horizontal velocity, with unknown coefficients, directly into a variant of the leading order long wave equations to close the system. Analyzing the frequency dispersion relation of the system PDEs, a single degree of freedom was identified using Padé rational approximations, unifying the weakly dispersive leading order Boussinesq-type equations under a single family. The choice of the coefficient could recover the Padé [0/2], Padé [2/0], and Padé [2/2] formulations in earlier approaches. The additional degree of freedom however means that the coefficients could be made to match a Padé [2/2] approximation, thus, achieve $O(\mu^4)$ accuracy unlike Mei and Le Mehaute (1966). Accordingly, the analysis added clarity to the significance of the study by Witting (1984). To further demonstrate the flexibility within the Padé [2/2] family, leading order substitutions are utilized to enhance the Boussinesq-type equations of M. B. Abbott et al. (1984). It is further shown that the degree of freedom can be utilized in an optimization procedure, however the formal $0(\mu^4)$ accuracy is sacrificed in doing so. Relaxing the mild-slope assumption in the added correction terms, the new Boussinesq-type equations were further extended for applications over variable depth in which shoaling characteristics could be enhanced as well (P. A. Madsen and Sorensen 1992).

The utilization of a model velocity at an arbitrary reference depth was revisited by Nwogu (1993) in a formal derivation of a new set of Boussinesq-type equations for applications over variable depth. Depth integrating the continuity and Euler equations, it was discovered that the free coefficient is defined by a quadratic equation. Normalizing the vertical coordinate by the still water depth showed that one of the roots is physically interpreted as a percentage of the still water depth. Hence, the degree of freedom controls where the model velocity is defined within the water column. Analyzing the frequency dispersion shows that the set of PDEs belongs to the same Padé [2/2] family presented in P. A. Madsen et al. (1991); however the dispersive flux term manifests through the continuity equation, as opposed to the momentum equation. Nevertheless, the study advanced the community understanding on the pivotal role of the model velocity at an arbitrary depth. Like

P. A. Madsen et al. (1991), the degree of freedom was later chosen to be optimized, thus sacrificing the formal $0(\mu^4)$ accuracy.

Combining the use of a model velocity at an arbitrary reference depth within the water column and leading order substitutions, Schaffer and P. A. Madsen (1995b) introduced new linear dispersion operators to derive a Boussinesq-type model for applications over variable depth. Unlike previous formulations, the additional degrees of freedom facilitate a Padé [4/4] frequency dispersion relation. Of most significance, the equations only retain third derivatives (i.e. $O(\mu^2)$ terms) in the derivation, thus limiting the computational complexity. It is important to emphasize that the extra degrees of freedom are necessary to achieve Padé [4/4] accuracy, even if the expansions are carried out to a higher order giving a [4/4] rational function (e.g., Dingemans 1997). A low order example of this is given by the governing equations of Mei and Le Mehaute (1966), which exhibit a [2/2] rational function but are formally $O(\mu^2)$ accurate.

An additional unique set of Boussinesq-type equations for variable depth applications is presented by Beji and Nadaoka (1996), in which the enhancement techniques utilized in P. A. Madsen and Sorensen (1992) are questioned with regard to consistency. It was argued that the leading approximations should be substituted into, as opposed to added to, the momentum equations for the conservation of energy. In the approach, a degree of freedom is introduced to distribute enhancement opportunities amongst system variables. A series of informative follow up discussions is found in Schaffer and P. A. Madsen (1998) and Beji and Nadaoka (1998), in which the latest discussion by Schaffer and P. A. Madsen (1999) shows that the equations of Beji and Nadaoka (1996), as well as many others, serve as special cases of the general approach (e.g., Schaffer and P. A. Madsen 1995b; Schaffer and P. A. Madsen 1995a). By treating the linear enhancement operators independently, their addition is understood to be an interpolation between variables. Consistency is maintained up to the order of approximation while offering additional flexibility.

Solitary waves are one of the most fundamental solutions in Boussinesq-type equations, which result from a perfect balance between nonlinearity and dispersion (Zabusky and Kruskal 1965). When a physical problem is modelled with too much nonlinearity (or lack of dispersion), a cascade of energy towards the wave front can lead to premature bore formation, whereas if there is too much dispersion (or lack of nonlinearity), the energy is distributed over successive trailing waves (e.g., Peregrine 1966). Having grasped a methodology to enhance frequency dispersion in support of deep water applications, attention turned towards enhancing nonlinear properties to support modeling of physical wave forms beyond the weakly nonlinear assumption. As waves propagate into decreasing relative depths, shoaling causes the wave amplitude to grow, in which nonlinear processes begin to take effect. At the wave front, there is a simultaneous increase in wave number leading to an increase in dispersion (Whitham 1974), which necessitates further increase in nonlinearity to support the amplification processes. It is in these nonlinear regions where the classical Boussinesq assumption,

$O(\mu^2) = O(\epsilon) << 1$, begins to breakdown in providing an accurate physical model due to dispersive bias (e.g., McCowan 1981). Nonlinear constraints can be lifted by relaxing the weakly nonlinear assumption to give so-called fully nonlinear theories (e.g., Serre 1953; Su and Gardner 1969; Green et al. 1974). As a result, μ is the only parameter assumed small in the derivation of fully nonlinear Boussinesq-type equations. Building on prior theories with enhanced frequency dispersion, P. Liu (1994) and Wei et al. (1995) derived a set of fully nonlinear, weakly dispersive equations, whose numerical solutions showed improved accuracy in comparison with physical experiments targeting nonlinear dispersive processes. P. A. Madsen and Schaffer (1998) further showed how frequency dispersion enhancement techniques can be applied to fully nonlinear formulations to achieve Padé [4/4] accuracy in equations capable of modeling nearly all coastal processes of practical interest, including wave-current interactions (e.g., Yoon and P. L.-F. Liu 1989; Q. Chen et al. 1998; Q. Chen 2003). Applying the frequency dispersion enhancement techniques from Schaffer and P. A. Madsen (1995b) to the fully nonlinear equations of Wei et al. (1995), P. A. Madsen and Schaffer (1998) showed that there is a simultaneous improvement in the nonlinear properties while retaining the desired complexity associated with $O(\mu^2)$ expansions. Gobbi et al. (2000) took an alternative approach, by retaining $O(\mu^4)$ terms and extending the approach of Nwogu (1993) by adding a second model velocity reference to give an additional degree of freedom that is needed to achieve Padé [4/4] accuracy (e.g., Dingemans 1997). Kennedy et al. (2001) further assumed the reference depth be non-stationary, which lead to nonlinear enhancement. If the time dependent reference is bound to a fixed fraction of the total water depth, then the reference becomes datum invariant, which is an appealing characteristic to have in surf zone applications, where changes in the mean water level can be significant (e.g., Longuet-Higgins and Stewart 1964). Furthermore, with the reference being attached to the flow depth, it reduces complications at the shoreline boundary in runup applications.

The review given here on Boussinesq-type equations is by no means exhaustive. In the opening remarks of Brocchini (2013), a survey is presented depicting upwards of 1200 published papers on Boussinesq-type equations between 1970-2010, where the ones outlined above are most relevant to this work. A logical progression to further enhance both linear and nonlinear properties followed the push for applications to relative depths orders of magnitude larger than the classical deep water limit (e.g., Agnon et al. 1999; P. A. Madsen et al. 2002; P. A. Madsen et al. 2003; P. A. Madsen et al. 2006). Variants of the state-of-the-art can be found in a series of studies (e.g., Chazel et al. 2009; Chazel et al. 2011; Z. Liu and Fang 2015; Z. Liu and Fang 2016; Z. B. Liu et al. 2018), which build on the multi-layer approach of P. Lynett and P. Liu (2004) and is attractive from a numerical practical standpoint due to the low complexity. Regardless of the approach, Boussinesq-type equations are no longer limited to near-field wave transformation studies and have evolved to include far-field propagation of broadband spectral waves.

The inclusion of wave breaking approximations further extends applications through the surf-zone, leading to an all encompassing framework to study coastal processes. At the offshore boundary, the incident wave spectrum is often multi-modal having both direction and frequency distributions ranging from low-frequency infra-gravity to high-frequency wind-generated waves. Applying the time-dependent forcing offshore, incident waves slowly adapt to the physical environment through the governing system of PDEs before undergoing highly nonlinear transformations in the coastal region with complex intra-propagation of energy. This is the ideal computational modeling philosophy; however it is important to acknowledge that waves must now propagate over greater distances, leading to extended residence times within the computational domain. This places more stress on the design and implementation of numerical methods, but most importantly, communication of model limitations. With the recent influx of general purpose computing on graphics processing units and affordable high performance computing centers, domains in excess of tens of millions of nodes are increasingly possible. Although enticing, error accumulation is increasingly inevitable, which can lead to false interpretations of model results. Understanding how to identify and mitigate these errors is therefore of significant interest to assert application constraints.

1.2 Numerical Dispersion

In the derivation of Boussinesq-type equations presented herein, the leading order dispersion terms manifest through Taylor series expansions of the velocity profile at a reference location along the vertical axis. The expansions give local approximations in which the parity of the derivatives correspond to amplitude (even) and phase (odd) constituents. For free-surface water waves, the physical process of dispersion is governed by a hyperbolic tangent function whose Taylor series expansion in the long wave limit is purely odd (phase). Collectively, the approximations in the theoretical formulation motivate implementation of finite difference methods, in which the method of undetermined coefficients is used to derive optimal schemes. The discretization relies heavily on Taylor series expansions whose terms readily combine with those physical in the theoretical formulation. Discretization of the governing PDEs results in a system of modified PDEs (MPDEs) whose finite difference solution is a function of time and space sampling intervals $(\Delta t, \Delta x)$. Vichnevetsky and De Schutter (1975) highlight two viewpoints in which sampling errors can be evaluated. The first considers "accuracy in the small" with a focus on analytic properties of the approximation, such as consistency in the case of vanishing sampling intervals. This viewpoint is of little interest to practitioners and often reserved for model developers. Of primary interest is "accuracy in the large", which quantifies the effects of sampling resolution. For finite difference methods, the applicable upper bound of the sampling intervals is defined by the stability limit beyond which errors become more pronounced. Practitioners balance accuracy with compute time due to limited resources, which translates to a compromise in selection of sampling intervals Δt and Δx.

Attaining a convergent solution indicative of the PDEs may be impractical. This realization is accentuated when acknowledging the broadband temporal and spatial scales native to free-surface wave fields. If stability alone is used as a proxy to measure model performance, the results are highly susceptible to dispersion (phase) or dissipation (amplitude) errors resulting from insufficient sampling resolution. The effects of discretization errors have received much more attention in non-dispersive models and the related technical literature provides a foundation for investigation of Boussinesq-type models.

1.2.1 Nonlinear Shallow Water Models

Scientists and engineers embraced the new age of digital computers in the mid 20^{th} century with practical applications focusing on oceanic tides, storm surge, and open channel flows governed by the NSWEs. By the late 1960's, numerous numerical studies on hydrodynamic and hydraulic processes began to appear (e.g., Hansen 1949; Hansen 1956; Isaacson et al. 1958; Preissmann 1961; Hansen 1962; M. B. Abbott and Ionescu 1967). The rapid growth in literature was in part due to the availability of preexisting numerical schemes that could be readily implemented (e.g., Richtmyer and Morton 1967), as well as the fact that the NSWEs belong to a more general class of hyperbolic equations, which permits interdisciplinary research (e.g., Platzman 1958; N. Phillips 1959; Arakawa 1966). While the fundamental Fourier analysis of John von Neumann (Richtmyer and Morton 1967) had been classically used to define stability characteristics, a pivotal study by Leendertse (1967) extended the analysis to include the phase argument. Collectively, the sampling error is quantified over the resolvable spectrum in terms of a complex propagation factor, whose modulus and argument respectively define the amplitude (dissipation) and phase (dispersion) factors. The viability of the complex propagation factor analysis is further showcased in a comparative study by Sobey (1970), with application to the explicit schemes of Reid and Bodine (1968) and Heaps (1969) and the implicit schemes of Leendertse (1967) and Abbott [unpublished at the time but found in M. B. Abbott (1979)]. The significance of the study by Leendertse (1967) was later emphasized in a paper by M. B. Abbott (1976) addressing members of the International Association for Hydro-Environment Engineering and Research (IAHR) over concerns that false interpretations of physical processes could occur due to computational errors. While Leendertse (1967) is not explicitly cited, the utility of the analysis is trivial. Numerical approximations can be expressed as a function of points per wavelength (or period), which is easily understood by any practitioner (e.g., M. B. Abbott and Rodenhuis 1972; M. B. Abbott et al. 1978; M. Abbott et al. 1981). The analysis can be used to guide mesh construction as well as a supplement in the interpretation of results.

Finite difference schemes are often characterized by the leading order truncation error of approximation. In practical applications concerned with "accuracy in the large", the truncation error is admissible due to the fact that the coefficients in the series expansion are governed by finite

sampling intervals. When temporal and spatial schemes are derived independently, the respective derivative expressions associated with truncation errors are generally unique. However, like Boussinesq-type equations, leading order approximations can be used in substitution to unify the expressions. Collecting like terms, the coefficients of the truncation errors in the MPDEs become functions of both time and space sampling intervals (e.g., Richtmyer and Morton 1967; Warming and Hyett 1974). For central scheme approximations of the first derivative, the leading order truncation error is second order, which means the coefficients of the third derivative are proportional to the square of the sampling intervals. In the discretization of the shallow water equations, a unified expression of the leading order error will represent a third derivative whose coefficient is proportional to a linear combination of the squared time and space sampling intervals. The dependency of the error on the third derivative mirrors that associated with the leading order frequency dispersion found in Boussinesq-type equations, thus giving an example of how MPDEs in general posses unique solutions whose intrinsic properties differ from the governing PDEs. As a means to mitigate errors, the leading order truncation errors can be utilized to define so-called correction terms, which are added to the difference equation, pushing the resultant approximation to higher order (e.g., M. B. Abbott et al. 1978; McCowan 1978; M. B. Abbott 1979; M. Abbott et al. 1981). The dispersion associated with the added correction term is quantified by M. Abbott et al. (1981) as a ratio between the coefficients of a discretized Boussinesq term over those of the correction term. The ratio is shown to be a function of the shallow water Courant (Courant et al. 1967), $C_r = \sqrt{gh}\Delta t/\Delta x$, and Abbott[1] (M. B. Abbott and Minns 1998), $A_b = h/\Delta x$, numbers, both of which are expressions of the sampling intervals. Altering the performance of the MPDEs through the addition of correction terms falls under the general concept of numerical filtering, where the objectives of the filter application can vary to meet specific design goals. It is emphasized that the MPDEs converge to the PDEs with the addition of the numerical filters. Therefore, the MPDEs maintain "accuracy in the small", but exhibit improvements with "accuracy in the large" that are of practical significance.

In the tsunami wave modelling community, the debate as to whether or not dispersion needs to be included in the governing PDEs is not so much about the inclusion of the physics, but rather the numerical costs of including the physics. Clearly the addition of dispersion auspiciously extends validity of long wave theory; however, the modification mathematically alters the hyperbolic structure of the NSWEs and the additional nonhydrostatic pressure terms greatly increases computational demand. An ultimate goal being discussed in the tsunami wave modelling community is to report event based predictions following generation, which requires, at minimum, near real-time simulation (e.g., Titov et al. 2016). Therefore, any computation overhead is of primary concern. The origin of the debate is clear when acknowledging the relative lack of computational resources in early years of

[1]The inverse is referred to as the "leptic ratio" by Scotti and Mitran (2008), which is fitting due to the geometric nature of the ratio.

development (e.g., Shuto and Fujima 2009). Emphasis on nondissipative computationally efficient schemes led to leading order finite difference methods employing staggered leap-frog central difference schemes. As pointed out earlier (e.g. Warming and Hyett 1974), Imamura and Goto (1988) found that the derivatives in the expression of the leading order truncation error of the MPDEs matches those in the dispersion terms of Boussinesq-type equations. By equating the corresponding coefficients, which is analogous to a ratio of unity (M. Abbott et al. 1981), the sampling intervals could be chosen such that the error mimics physical frequency dispersion for transoceanic propagation. The implications would be significant due to the simple fact that frequency dispersion is included at no additional computational cost and because of this, the methodology would become an active area research (e.g., Shuto 1991; Imamura 1997). The concept is similar to that presented earlier by M. Abbott et al. (1981), where the differences lie in the objectives. In M. Abbott et al. (1981), the objective is to introduce correction terms in the difference scheme as numerical filters, which take on the form of the original leading order truncation error, thereby canceling the leading order error in the MPDEs. In contrast, the leading order truncation errors are retained by Imamura and Goto (1988) and the coefficients are selected such that the error associated with the MPDEs mimics physical frequency dispersion found in Boussinesq-type equations.

The methodology presented by Imamura and Goto (1988) was extended by Cho (1995) and Cho and Yoon (1998) for two-dimensional applications by reducing the effects of mesh anisotropy on the leading order frequency dispersion through the application of numerical filters. For practical applications over varying depth, Yoon (2002) introduced a local virtual mesh, which bypassed the need of a variable mesh to maintain the necessary sampling requirements to mimic physical dispersion. Burwell et al. (2007) provides a comprehensive analysis on a finite difference tsunami model developed by Titov and Synolakis (1995). Since the time integration is performed using a forward difference approximation, there are damping as well as dispersion errors involved. While the model differs in many ways from those previously mentioned, the analysis serves as an extension by evaluating the spectral performance of the MPDEs. According to Vichnevetsky and De Schutter (1975), the spectral viewpoint embodies "accuracy in the large", in which approximation errors are evaluated over the full Nyquist interval (Shannon 1949). The study shows the model performance beyond the leading order and makes uses of the dimensionless wave number, $k\Delta x$, to show broadband capabilities for a given mesh. Like prior studies (e.g., Imamura and Goto 1988), Burwell et al. (2007) further shows that the mesh design can be configured in application to mimic the effects of physical dispersion with the objective in choosing the sampling intervals being defined in the context of broadband characteristics. Extensions to weakly nonlinear systems of PDEs over variable depth were given by Wang and P. L.-F. Liu (2011) and the virtual mesh approach of Yoon (2002) was enhanced to relax constraints on the choice of spatial sampling intervals.

The allure of mimicking physical dispersion through the application of numerical filters is clear;

however, implementation in practical application can be difficult. Yoon et al. (2007) presented yet another approach in which no virtual mesh is required. The combined linear free-surface equation is split into an alternative system of PDEs (e.g. Lynch and Gray 1979; Gray 1980; Vichnevetsky and Bowles 1982). Like M. Abbott et al. (1981), correction terms are introduced to the difference scheme, where the difference in approach is that the degrees of freedom remain in the coefficients of the correction terms. The spatial scheme is expanded to a weighted 9-node configuration, in which one degree of freedom is determined to eliminate anisotropy errors in the leading order frequency dispersion. The remaining degree of freedom is then determined to improve the leading order frequency dispersion. The approach is shown to relax constraints on the choice of spatial sampling intervals and generalizes the conditionals presented by Imamura and Goto (1988) and Cho and Yoon (1998). A very similar concept is presented by Cho et al. (2007) in which the coefficient constraint generally matches that presented by Yoon et al. (2007), but differs by a constant scale factor. In either case, the removal of the local virtual mesh greatly simplifies implementation. Recently, Ha and Cho (2015) extended the formulation of Cho et al. (2007) by explicitly accounting for varying depth, which results in an additional numerical filter. For the purpose of verification, the model is compared with a recent version of the Boussinesq-type model FUNWAVE (Shi et al. 2012) and does show qualitative improvements, but dispersion errors are apparent at higher frequencies. Nevertheless, the computational model is at least an order of magnitude faster than latest version of FUNWAVE, which highlights the primary goal of retaining an adequate level of dispersion without the added computational cost of a Boussinesq-type model. To digress somewhat, it is worth pointing out that while comparisons with Boussinesq-type results are instructive, it is unclear if bias exists in the comparison of computational times. In the latest version of FUNWAVE, for example, the scheme is designed specifically to handle wave breaking and highly nonlinear waves in coastal systems. These features come with added computational cost. Applying the scheme to small amplitude transoceanic tsunamis likely leads to redundant computations with little contribution to the overall solution; thus presumably, the computational work related to dispersion should be isolated for better comparison.

1.2.2 Boussinesq-type Models

The research lines of development outlined above clearly focus on leveraging numerical filters dependent upon finite sampling intervals to mimic physical dispersion. Like leading order shallow water models, Boussinesq-type models also suffer from numerical dispersion. McCowan (1981) shows the necessity of including correction terms introduced by M. Abbott et al. (1981) when modeling weakly dispersive Boussinesq-type equations. Left uncorrected, dispersion due to the leading order truncation errors can dominate the physical dispersion. As mentioned prior, M. Abbott et al. (1981) quantifies the relative source of dispersion through the ratio of the respective coefficients,

in which reducing the mesh size, the contribution of numerical dispersion is suppressed. The lack of accounting for this interaction is, at least in part, why some authors claim the need for a very small mesh when modeling Boussinesq-type equations (e.g., Baba et al. 2017). Once the correction terms are introduced, the mesh size limitations can be relaxed (e.g., McCowan 1981). An alternative approach is presented by Wei and Kirby (1995), in which all nondispersive terms are approximated using fourth order accurate schemes, whereas the dispersion terms are approximated using second order accurate schemes. As a result, derivatives in the leading order truncation errors no longer mimic physical dispersion terms associated with a third derivative found in weakly dispersive Boussinesq-type equations. This approach does forfeit flexibility, but it too relaxes mesh size constraints.

The influence of numerical dispersion discussed above, with regard to the tsunami wave modeling community, largely focused on "accuracy in the small" using Taylor series analysis and evaluating the leading order truncation errors. Numerical dispersion, or dissipation, can be fully appreciated in Fourier spectral space, where the viewpoint of "accuracy in the small" is accounted for in the convergence behavior. However, as mentioned prior, the spectral domain covers the full Nyquist interval (Shannon 1949), giving a viewpoint of "accuracy in the large" beyond the leading order. Of the NSWE models reviewed within the tsunami modelling community, Burwell et al. (2007) was the only one to leverage this perspective. In spectral space, the resolvable bandwidth of a scheme is defined to be the domain over which the dimensionless wave number, $k\Delta x$, or angular frequency, $\omega\Delta t$, is well approximated within a defined tolerance for error. In a conventional monotonic sense, increasing the order of the truncation error is analogous to increasing the resolvable bandwidth. Therefore, the resolvable bandwidth quantifies a proportional relationship between the wave number, or angular frequency, and the respective sampling interval, which directly quantifies the propagation characteristics of a scheme.

Boussinesq-type models are more computationally demanding than NSWE models due to the incurred cost of high derivatives in theoretical formulation. For classic central difference approximations to odd derivatives, the resolvable bandwidth decreases with increasing derivative. This necessitates a reduction in mesh size and underlines the fundamental constraints on computational efficiency. In an early study by Kreiss and Oliger (1972), approximate solutions to linear first order hyperbolic equations were evaluated using classic second, fourth, and sixth order central difference schemes. The relative performance of each scheme was quantified based on an established tolerance for error and number of wave periods to simulate. It was determined that the increase in computational complexity is proportional to the order of accuracy; however, the resolvable bandwidth increases at a lesser rate. It was concluded that the fourth order scheme is an optimal compromise between wave number resolution and computational effort. Although the study focused on first order equations, the trend is likely similar, if not worse, with high order equations. If further

wave number resolution is required, high order schemes theoretically apply; however, the practical advantage in employing classic schemes beyond sixth order is futile. This implies that the fourth order approach by Wei and Kirby (1995) is near optimal with regard to classic schemes and in order to reduce computational costs in Boussinesq-type models, alternative approaches must be explored.

Intrinsic properties of Boussinesq-type equations cover a broadband range of temporal and spatial scales, which advocates implementation of spectral schemes to improve the resolvable bandwidth. However, taking into consideration the diversity and irregularity of boundary conditions in the study of coastal processes, spectral schemes pose significant challenges. Compact finite difference schemes offer a compromise, in which the global dependence on function values is retained, while relaxing constraints on mesh geometry and boundary conditions (Lele 1992). The fundamental difference between classic and compact finite difference methods is that the derivatives are treated as unknowns in the latter. Essentially, the former uses Lagrange interpolation, whereas the latter uses Hermitian interpolation, which is a relative generalization. Considering the introduction of so-called spectral-like schemes dates back to the 1930s (Kobayashi 1999), implementation in the practical application of Boussinesq-type models is relatively new. To digress, the KortewegDe Vries (KDV) equation (Korteweg and de Vries 1895), and Camassa-Holm (CH) equation (Camassa and Holm 1993), although dispersive long wave equations, do not fall under the class of Boussinesq-type equations referenced herein. Strictly speaking, the KDV and CH equations assume waves travel in one direction only. There are also variants of Boussinesq-type equations which make the same assumption (e.g., Dingemans 1997). In coastal environments, riddled with reflective boundaries, the unidirectional equations are impractical. Nevertheless, the theories are ideal for validating numerical methods applied to weakly nonlinear, weakly dispersive waves due to the fact that exact solutions exist. Therefore, a rich history on the equations, and their numerical approximations, can be found throughout the literature, including those which implement compact methods (e.g., Iskandar and Jain 1980; Mohsen et al. 1993; El-Zoheiry 2002; J. Li and Visbal 2006; Chiu et al. 2009; Lu 2016; Wongsaijai et al. 2020). It should be emphasized that the previous list of references is by no means exhaustive and surely important works have been left out. This direction of research is more theoretical, with focus on integrable equations and solitary wave interactions over flat bottoms, therefore is outside the scope of this work. The Boussinesq-type equations focused on herein allow for wave reflection over a variable bathymetry, making them ideal for coastal applications.

The first implementation of compact schemes in the study of Boussinesq-type equations referenced herein appears to be presented by Cienfuegos et al. (2006) using finite volume methods. The governing equations solved are those of Serre (1953) with application of dispersion enhancement techniques discussed by P. A. Madsen and Schaffer (1998). The equations are cast into a weakly-conservative form by introducing an auxiliary variable and discretized using a staggered finite

volume method with cell face reconstruction methods (Kobayashi 1999; J. M. Pereira et al. 2000; J. Pereira et al. 2001; Lacor et al. 2004). Derivatives are computed using fourth order compact schemes presented by Lele (1992) and the time integration is carried out using a classic fourth order Runge-Kutta scheme. A thorough Fourier analysis on the scheme is carried out employing the concept of a complex propagation factor, which directly leads to the derivation of a numerical dispersion relation. To compare with the mixed order approach of Wei and Kirby (1995), dispersion terms are also evaluated using a second order scheme. A relative phase comparison with the physical dispersion is given, in which asymptotic behaviors are explored through Taylor series expansions about $k\Delta x = 0$. As a general conclusion, the fourth order scheme is recommended due to its superior resolvable bandwidth. Although in agreement with their conclusion, their justification for the mixed approach needs further clarification. The goal of the mixed order approach is to ensure that the truncation error does not interfere with the physical dispersion. Take for example a second order central scheme approximation to the third derivative. In the leading order truncation error, the derivative operator is a fifth derivative. The same is true for a fourth order central scheme approximation of first derivatives. If both derivatives were approximated to the same order, then the truncation error of the third derivative approximation would contain a seventh derivative. This likely explains the differences in convergence behavior observed by Cienfuegos et al. (2006). Nevertheless, third derivatives are absent in the truncation errors, thus either approach ensure that the truncation error does not interfere with the physical dispersion. The fundamental advantage of fourth over second order schemes, as pointed out by Cienfuegos et al. (2006), is the former has a higher resolvable bandwidth.

In the Fourier analysis carried out by Cienfuegos et al. (2006), the numerical dispersion relation is the fundamental tool used to assess the phase resolving capabilities of the scheme. Of the studies reviewed herein, Witting (1984) is the only other one who derives a numerical dispersion relation for a Boussinesq-type model. Since the focus of the study was largely theoretical, a second order finite difference scheme proved sufficient to verify the newly introduced physical dispersion terms. Taking into consideration the vast number of publications identified by Brocchini (2013), this poses a serious gap in the advancement of Boussinesq-type models used in practical application. In general, as the order of dispersion increases, the order of the derivatives increases, however the bandwidth resolution decreases and this relationship is not linear. Therefore, theories which exceed the conventional deep water limit by orders of magnitude would presumably have a very small resolvable bandwidth in application. Furthermore, for broadband waves, the sampling intervals would need to be so small that the model becomes impractical. As pointed out by Lele (1992), these are the same issues encountered in computational fluid dynamics studies on turbulence. One way to combat the restrictions is to limit the order of derivatives in theory, but this is pushing away from the quasi-3D strength of Boussinesq-type models. The other way to combat restrictions is by implementing more advanced numerical methods. However, this advancement further divides

the knowledge gap between model developers and model practitioners. To ensure the success of a model in practice, the schemes must be accompanied by a thorough analysis on the resolvable bandwidth of the physical processes governed by the PDEs. This begins at the Fourier level using the complex propagation factor, in which the results are best conveyed through the "accuracy in the large" where the domain of dependence is a function of the sampling intervals. If the simplicity of communication between model developers and practitioners is lost, so is trust in application. History has already proven in the early years of acceptance that this trust is conditional. Once lost, the models become purely academic, leaving one to ask, what is the point?

1.3 Scientific Questions

The literature review has fostered a number of theoretical and numerical questions regarding Boussinesq-type equations and their application that provide the impetus for this dissertation. Three specific questions on the theoretical aspects are addressed by carrying out an independent derivation of a fully nonlinear, weakly dispersive Boussinesq-type system of equations. As for the numerical aspects, two general questions are addressed through the implementation of high order compact finite difference methods and corresponding Fourier analysis. Each of these questions is detailed below in context.

Boussinesq-type equations are often derived under the assumption of irrotational flow, which naturally leads to a theoretical framework based on potential flow. Mathematically, the velocity potential offers the advantage of being a scalar function, thus limiting complexities. This approach has been favored most throughout history; however, it is possible to carry out the derivation in the context of the vector velocity (e.g., O. M. Phillips 1966; Peregrine 1967; Nwogu 1993; Dingemans 1997). All other things equal, both approaches should lead to the same formal solution; however, due to different paths travelled, the resultant sets of equations can appear quite different. By design, the fully nonlinear, weakly dispersive equations derived by Wei et al. (1995) reduce to the weakly nonlinear, weakly dispersive equations of Nwogu (1993), in which the former employs potential flow theory. Extending the formal derivation of Nwogu (1993) to fully nonlinear, the resultant should be formally equivalent to Wei et al. (1995), and yet it is unclear how the equations will differ in presentation. If they are different, then their difference approximations would presumably be different, which can alter the numerical properties (e.g., Gray 1980). This study aims to build on the previous works of Nwogu (1993) by carrying out an independent derivation of a fully nonlinear, weakly dispersive Boussinesq-type system of equations. The intent is to not only add further clarity on the derivation presented by Nwogu (1993), but to also assert the theoretical equivalence with the fully nonlinear, weakly dispersive theory given by Wei et al. (1995). Overall, it seems reasonable to assume that alternative perspectives will lead to a better understanding of the problem and

potentially unveil opportunities for new developments. Furthermore, if the irrotational assumption is to be relaxed in the future, a vector approach is inevitable, thus the derivation could offer insights to the more general case.

Wave breaking is often parameterized to support transformations over the surf zone, resulting in an all encompassing coastal wave model. One such approach that has gained recent interest is implementation of shock capturing methods to approximate overturning processes (e.g., Tonelli and Petti 2009; Roeber et al. 2010; Roeber and Cheung 2012; Tissier et al. 2012; Shi et al. 2018). The implementation, however, requires that the PDEs be expressed in conserved variable form to attain proper shock speeds (e.g., Whitham 1974; M. B. Abbott 1979; LeVeque 1992; Toro 2009). Building on the previous works of Nwogu (1993), this is formally achieved by depth integrating the continuity and Euler equations of motion, following Leibniz integration rule. The use of conserved variables is fully compatible with the derivation of the fully nonlinear, weakly dispersive Boussinesq-type equations in terms of vector velocity. The resulting set of equations can then be compared with the state-of-the-art equations found in Shi et al. (2012), which govern the open sourced model, "FUNWAVE-TVD", currently supported by the US Army Corps of Engineers. Although the conserved variable form is clear at the leading order, the ability to manipulate the dispersion terms introduces further questions on the appropriate conserved variable form at higher order. Implementation of shock capturing methods will not be explicitly addressed in this study, however, it is clear that a conserved variable form is needed to permit the application of shock capturing methods.

Early developments on Boussinesq-type equations focused on improving frequency dispersion characteristics; however, nonlinear characteristics did not show comparable improvements. Although a completely new approach to approximate the vector velocity profile has become the focus of modern research (e.g., Agnon et al. 1999; P. A. Madsen et al. 2002; P. A. Madsen et al. 2003; P. A. Madsen et al. 2006; Chazel et al. 2009; Chazel et al. 2011; Z. Liu and Fang 2015; Z. Liu and Fang 2016; Z. B. Liu et al. 2018), it is not immediately clear why prior derivations saw marginal improvements, despite moving to a fully nonlinear assumption. However, it does appear that simply relaxing the nonlinear assumption is not enough (Wei et al. 1995). One way to further extend the nonlinear characteristics is to make the arbitrary reference, introduced by Nwogu (1993), a function of time and link its motion to the free surface (Kennedy et al. 2001). Of particular interest is to keep the arbitrary reference at a fixed fraction of the flow depth. Kennedy et al. (2001) highlights that this approach leads to a datum invariant reference, in which the mean level is permitted to change significantly over time. In coastal applications, such circumstances are often encountered during tidal variations, surf beat, and other low frequency long-wave phenomenon (e.g. infragravity waves). Kennedy et al. (2001) also states the approach is highly stable and converges most rapidly in comparison to other nonlinear enhancements, which suggests this is a promising approach. Kennedy

et al. (2001) introduced the enhancement to the preexisting formulation of Wei et al. (1995) without considering broader influences on series expansions of the velocity profile. Therefore, it is unclear if the approach of Kennedy et al. (2001) is fully extended to the nonlinear dispersion properties. With this in mind, the arbitrary reference is assumed to be a function of both time and space throughout the derivation of the fully-nonlinear, weakly dispersive Boussinesq-type equations presented herein.

Selection of numerical schemes is as important as the governing equations in providing accurate solutions for practical application. Implementation of compact spectral-like methods has been proposed by Cienfuegos et al. (2006) as a means to improve the overall resolvable bandwidth of Boussinesq-type models. As a result, restrictions on sampling intervals are reduced, making for a more practical approach with high order PDEs. Although Cienfuegos et al. (2006) employs finite volume methods, the compact methodology also applies to finite difference methods. Furthermore, Cienfuegos et al. (2006) implements a classic fourth order Runge-Kutta time integration scheme, which belongs to a family of single-step methods. In this study, an interdisciplinary approach is taken by adopting the methodology outlined by C. Tam and Webb (1993), which utilizes a consistent finite difference framework for both time and space with the implementation of linear multistep time integration schemes. The methodology is presented in the field of Computational Aeroacoustics, in which the flow of a compressible fluid is governed by the nondispersive Euler equations of motion. Although the governing PDEs are quite different from Boussinesq-type equations, the underlying computational challenges are similar due to broadband wave field applications. Collectively, the linear multistep and high order compact finite difference approach appears to fill a knowledge gap between the approach of Wei and Kirby (1995), which employs linear multistep and classic finite difference schemes, and Cienfuegos et al. (2006), which employs singe step and compact finite volume schemes. Furthermore, since classic finite difference schemes are a subset of compact schemes, the combined methodology facilitates an explicit analysis of common finite difference schemes found throughout the literature review. Given that the approach taken herein encompasses families of schemes, applied to families of weakly dispersive Boussinesq-type equations, it is expected that many questions will be answered along the way.

The fundamental strength of the methodology presented by C. Tam and Webb (1993) is that once the difference operators are mapped into spectral space through application of Fourier-Laplace transforms, the resultant numerical dispersion relation mirrors the physical dispersion relation. As highlighted by Leendertse (1967) with the introduction of the complex propagation factor, the numerical dispersion relation is key to understanding the phase resolving accuracy of a broadband wave field. Supporting evidence is found in the study by L. Li and Cheung (2019) on numerical dispersion emerging from a dispersive, non-hydrostatic model (Yamazaki et al. 2009), which is based on a class of equations fundamentally different from Boussinesq-type equations (e.g., Bai

et al. 2018). Since the operators are functions of the sampling intervals, the bounds of application for the MPDEs can be directly linked to sampling intervals defined by practitioners. The errors, being analyzed in spectral space, depict "accuracy in the large" beyond the leading order effects of numerical dispersion, which is more practical than using Taylor series methods alone. Aside from helping to answer questions regarding the effects sampling intervals, the "accuracy in the large" can answer questions like how do the correction methods of M. Abbott et al. (1981) compare with those of Wei et al. (1995), despite their ability to achieve the same goals at the leading order. Also, given the diversity of Boussinesq-type equations, and knowing their MPDEs are unique, the "accuracy in the large" can help determine which theories are better suited to a particular discretization scheme and configuration. The concept of resolvable bandwidth is central in Computational Aeroacoustics, in which model developers are willing to sacrifice the formal order of accuracy in favor of schemes that provide a greater resolvable bandwidth (e.g. Lele 1992; C. Tam and Webb 1993). This is analogous to the concept of numerical filters discussed prior, in which different optimization objectives are employed. Given that the error analysis can be carried out over the relative water depth, this poses an opportunity to optimize schemes with the objective of improving the numerical celerity, in much the same way researchers leverage degrees of freedom in the PDEs to achieve a higher bandwidth given a tolerance for error (e.g., Nwogu 1993). Although focus is directed towards frequency dispersion, there is reason to believe that the general idea applies to all aspects of Boussinesq-type equations (shoaling, refraction, etc.), in which the end goal is comprehensive and the question is rhetorical: can we better communicate implementation constraints beyond that of numerical stability?

CHAPTER 2
MATHEMATICAL FORMULATION

For numerical models used in coastal engineering practice, the derivation of free-surface wave theories often takes a perturbation approach, stemming from the asymptotic long-wave limit $kh \to 0$, where the wavelength is much greater than the water depth. At the leading order, the NSWEs accurately model tides, storm surge, and other nondispersive flows of primary interest. In this flow regime, the pressure is assumed hydrostatic, which leads to a uniform depth profile of the horizontal velocity. As a result, the governing equations become two dimensional (2D), which significantly reduces the computation requirements in practical application. The goal in developing Boussinesq-type models is to retain the 2D efficiency while extending the range of application to cover dispersive flows in a quasi-3D model. This is achieved by imposing an approximation of the vertical flow structure to include nonhydrostatic effects. This chapter covers an independent derivation of a system of Boussinesq-type equations in conserved variable form, in which the continuity and inviscid Euler equations of motion are depth integrated without approximation to the nonlinearity. This serves an extension to the formal approach presented by Nwogu (1993), with additional insights in connection to more recent fully nonlinear, weakly dispersive theories. Unique to the formulation herein, a new weighted polynomial approximation is introduced, which includes an expansion about the free surface.

2.1 Free-Surface Flow

The inviscid Euler equations, together with the continuity equation, are presented in dimensional form first. An incompressible fluid and irrotational flow are assumed facilitating the use of potential flow theory; however, the derivation will follow a vector velocity approach. Introducing characteristic scales, the governing equations are rewritten in dimensionless form, in which measures of nonlinearity, ϵ, and dispersion, μ^2, emerge. Lastly, the kinematic and dynamic boundary conditions are presented in dimensionless form.

2.1.1 Dimensional Form

The problem sketch shown in Figure 2.1 depicts a free-surface water wave at an instantaneous time t', propagating over an irregular seabed. A spatial Cartesian coordinate (x', y', z') system is employed with the z'-coordinate oriented in the positive vertical direction and still water line serving

as the reference. The flow field is bound by two scalar functions defining the free-surface, $\eta'(t', x', y')$, and seabed, $h'(t', x', y')$, displacements from the reference along the vertical coordinate axis. The difference in displacement along the vertical axis defines the flow depth, $H'(t', x', y') = \eta' + h'$, which is a conserved variable, independent of the frame of reference.

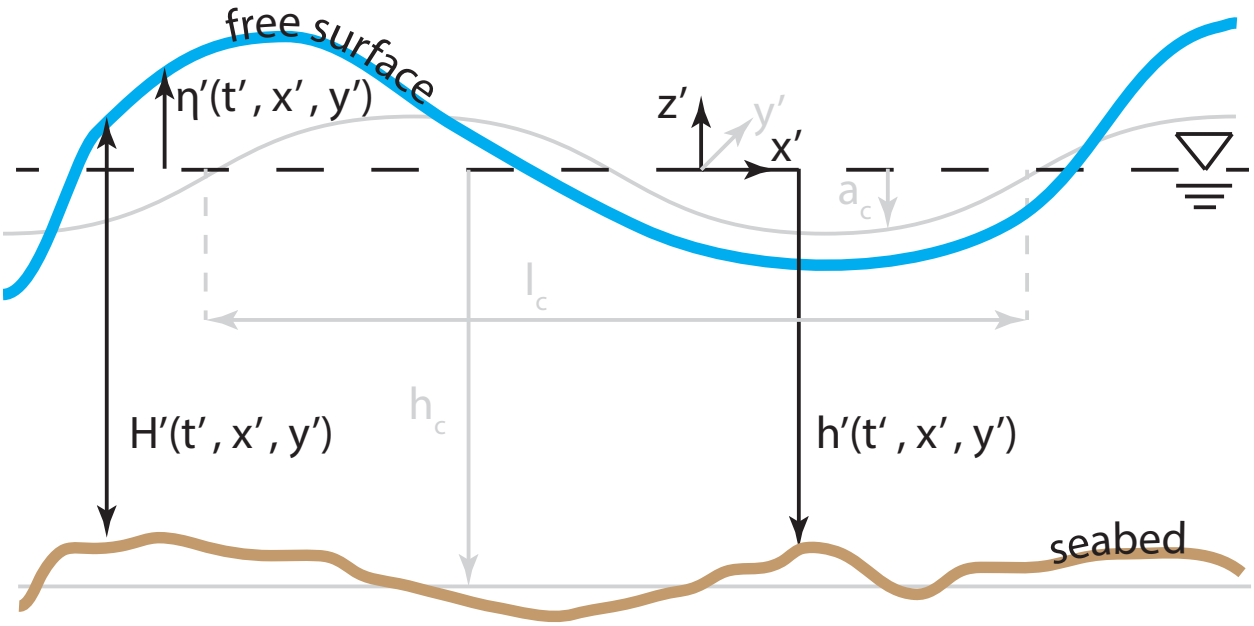

Figure 2.1: Instantaneous definition sketch depicting a vertical slice along the x-z plane of the domain showing the characteristic scales (gray) and function definitions.

Assuming an incompressible, inviscid fluid, the governing equations are the continuity equation and the Euler equations of motion. In dimensional form, the continuity equation is

$$u'_{x'} + v'_{y'} + w'_{z'} = 0 \tag{2.1}$$

where $\{u', v', w'\}$ are the components of the vector velocity function. The coordinate subscript notation denotes application of partial derivative operators (e.g., $u'_{x'} \equiv \frac{\partial u'}{\partial x'}$) along the respective axis and will be used throughout interchangeably when convenient. The dimensional Euler equations of motion are

$$u'_{t'} + u'u'_{x'} + v'u'_{y'} + w'u'_{z'} = -\frac{1}{\rho}p'_{x'} \tag{2.2}$$

$$v'_{t'} + u'v'_{x'} + v'v'_{y'} + w'v'_{z'} = -\frac{1}{\rho}p'_{y'} \tag{2.3}$$

$$w'_{t'} + u'w'_{x'} + v'w'_{y'} + w'w'_{z'} = -\frac{1}{\rho}p'_{z'} - g \tag{2.4}$$

in which p' is the pressure, ρ is the density, and g is the constant gravitational acceleration acting

along the vertical axis. The flow is further assumed to be irrotational, which mathematically states that the curl of the vector velocity is zero. In terms of components, the condition is given by

$$w'_{y'} - v'_{z'} = 0, \quad u'_{z'} - w'_{x'} = 0, \quad v'_{x'} - u'_{y'} = 0 \tag{2.5}$$

which are associated with the $\hat{i}, \hat{j}$, and $\hat{k}$ unit vectors respectively.

2.1.2 Long Wave Scaling

The governing equations are considered exact under the given assumptions; however, the contribution of each term to the overall solution generally depends on the physical application. Introducing scaling arguments representing physical characteristics of the geometry and flow field, individual contributions can be quantified through dimensionless parameters. This facilitates the exclusion of terms exceeding governing assumptions, which are motivated by application interests.

The horizontal and vertical spatial coordinates shown in Figure 2.1 are geometrically scaled by the characteristic wavelength, l_c, and still water depth, h_c, respectively. The temporal coordinate is scaled by the characteristic wave period in the linear long wave limit of Airy wave theory (Airy 1845). Collectively, the dimensionless coordinates are given by

$$x = \frac{x'}{l_c}, \quad y = \frac{y'}{l_c}, \quad z = \frac{z'}{h_c}, \quad t = \frac{\sqrt{gh_c}}{l_c}t' \tag{2.6}$$

The scalar surface displacement functions shown in Figure 2.1 are expressed in dimensionless form as

$$\eta(t,x,y) = \frac{\eta'(t',x',y')}{a_c}, \quad h(t,x,y) = \frac{h'(t',x',y')}{h_c} \tag{2.7}$$

in which a_c is the characteristic free-surface amplitude. The resulting dimensionless flow depth is $H(t,x,y) = \epsilon\eta + h$, where the scale factor $\epsilon = a_c/h_c$ defines a measure of nonlinearity. Following Wu (2001), the remaining scalar pressure and vector velocity terms are scaled by corresponding magnitudes at the still water level in the linear long wave limit of Airy wave theory (Airy 1845). The resulting dimensionless pressure function is

$$p(t,x,y,z) = \frac{p'(t',x',y',z')}{\rho g a_c} \tag{2.8}$$

and the vector velocity components are

$$
\begin{aligned}
u(t,x,y,z) &= \frac{h_c}{a_c\sqrt{gh_c}}u'(t',x',y',z') \\
v(t,x,y,z) &= \frac{h_c}{a_c\sqrt{gh_c}}v'(t',x',y',z') \\
w(t,x,y,z) &= \frac{1}{\mu}\frac{h_c}{a_c\sqrt{gh_c}}w'(t',x',y',z')
\end{aligned}
\tag{2.9}
$$

where the scale factor $\mu = h_c/l_c$ defines the relative depth.

Applying the scale arguments above, the governing continuity (2.1) and Euler (2.2-2.4) equations are expressed in dimensionless form as

$$u_x + v_y + w_z = 0 \tag{2.10}$$

$$u_t + \epsilon u u_x + \epsilon v u_y + \epsilon w u_z + p_x = 0 \tag{2.11}$$

$$v_t + \epsilon u v_x + \epsilon v v_y + \epsilon w v_z + p_y = 0 \tag{2.12}$$

$$w_t + \epsilon u w_x + \epsilon v w_y + \epsilon w w_z + \frac{1}{\mu^2}p_z + \frac{1}{\epsilon\mu^2} = 0 \tag{2.13}$$

and the dimensionless irrotational condition (2.5) becomes

$$\mu^2 w_y - v_z = 0, \quad u_z - \mu^2 w_x = 0, \quad v_x - u_y = 0 \tag{2.14}$$

in which the square relative depth, μ^2, serves as a measure of linear frequency dispersion. In comparison with their dimensional form, the dimensionless governing equations now include measures ϵ and μ^2 to quantify nonlinear and dispersive contributions of each term. In Nwogu 1993, the vertical velocity is scaled by μ^2, which results in the dimensionless equations being presented in a different form, where the vorticity components are weighted equally. The connection between the dimensionless equations are given by $w_{Nwogu} = \mu^2 w$ for comparison.

2.1.3 Boundary Conditions

Having defined the dimensionless set of governing PDEs and irrotational constraints, boundary conditions for the surface scalar functions are addressed. Focusing on wave propagation, in which the horizontal axis is unbound, lateral boundary conditions will not be discussed. The dimensionless generalized kinematic condition (A.3) is applied to the dimensionless free-surface and seabed to

give

$$w|_{\epsilon\eta} = \eta_t + \epsilon u|_{\epsilon\eta}\eta_x + \epsilon v|_{\epsilon\eta}\eta_y \tag{2.15}$$

$$w|_{-h} = -\frac{1}{\epsilon}h_t - u|_{-h}h_x - v|_{-h}h_y \tag{2.16}$$

in which the notation, e.g., $w|_{\epsilon\eta} \equiv w(t, x, y, z = \epsilon\eta)$, denotes the vertical point of function evaluation. The dimensionless dynamic boundary condition at the free-surface is simply

$$p|_{\epsilon\eta} = 0 \tag{2.17}$$

in which the scaling has no effect. To this point, the governing equations and boundary conditions are all presented in dimensionless form, using scaling arguments in the linear long wave limit of Airy wave theory (Airy 1845).

2.2 Velocity Profile

In this study, the domain is reduced in dimension by assuming uniform flow along the y-axis to focus on theoretical concepts associated with nonlinearity and dispersion. The objective is to express the resulting 2D-vector velocity components as a function of a model horizontal velocity, thereby closing a quasi-2D system with two equations and two unknowns. The connection between the velocity components is given by the irrotational condition (2.14) and like all Boussinesq-type equations, the physical assumption $O(\mu^2) << 1$ is imposed to facilitate formulation of the depth dependent velocity using continuous function approximations in terms of series expansions, where, in general, an increasing number of terms retained in the series reflects an increasing order of dispersion. This section focuses on the derivation of the depth dependent velocity to be substituted into the governing PDEs. To ensure the velocity function obeys the kinematic boundary conditions, surface projections are introduced within the series expansions. The derivation follows that of Nwogu (1993), in which the model velocity is defined at an arbitrary reference within the water column.

2.2.1 Taylor Series

In Nwogu (1993), the vertical velocity is obtained by depth integrating the continuity equation (2.10) from the seabed to an arbitrary level in the water column. While this is theoretically exact, the horizontal velocity function remains to be defined. Nwogu (1993) develops a mathematical model by constructing a local Taylor series expansion of the horizontal velocity function about the seabed. Although the resultant $O(\mu^2)$ Taylor polynomial is correct, the algorithm is convoluted. Herein a direct approach is presented, offering additional insights.

The irrotational condition (2.14) links the vector velocity components, in which a polynomial approximation of the horizontal velocity function results in a bound polynomial approximation of the vertical velocity function. Therefore, truncating a local Taylor series expansion of the vertical velocity function to begin with serves the same purpose. A series expansion of the vertical velocity function about an arbitrary point, $z = z_0$, in the water column is given by

$$w(t,x,z) = w|_{z_0} + \frac{\Delta z_0}{1!}\frac{\partial w}{\partial z}|_{z_0} + \frac{(\Delta z_0)^2}{2!}\frac{\partial^2 w}{\partial z^2}|_{z_0} + \frac{(\Delta z_0)^3}{3!}\frac{\partial^3 w}{\partial z^3}|_{z_0} + \dots \tag{2.18}$$

in which $\Delta z_0 = z - z_0$ is the vertical displacement between z, the point of evaluation, and z_0, the point of expansion. Applying the continuity equation (2.10) and irrotational condition (2.14) transforms the series (2.18) into an $O(\mu^{2n})$ expansion, in which the even (left) and odd (right) derivatives within the series are shown below as

$$\begin{array}{l|l}
\frac{\partial^0 w}{\partial z^0}|_{z_0} = \mu^0 \frac{\partial^0 w}{\partial x^0}|_{z_0} & \frac{\partial w}{\partial z}|_{z_0} = -\mu^0 \frac{\partial u}{\partial x}|_{z_0} \\
\frac{\partial^2 w}{\partial z^2}|_{z_0} = -\mu^2 \frac{\partial^2 w}{\partial x^2}|_{z_0} & \frac{\partial^3 w}{\partial z^3}|_{z_0} = \mu^2 \frac{\partial^3 u}{\partial x^3}|_{z_0} \\
\frac{\partial^4 w}{\partial z^4}|_{z_0} = \mu^4 \frac{\partial^4 w}{\partial x^4}|_{z_0} & \frac{\partial^5 w}{\partial z^5}|_{z_0} = -\mu^4 \frac{\partial^5 u}{\partial x^5}|_{z_0} \\
\frac{\partial^6 w}{\partial z^6}|_{z_0} = -\mu^6 \frac{\partial^6 w}{\partial x^6}|_{z_0} & \frac{\partial^7 w}{\partial z^7}|_{z_0} = \mu^6 \frac{\partial^7 u}{\partial x^7}|_{z_0} \\
\vdots & \vdots \\
\frac{\partial^{2n} w}{\partial z^{2n}}|_{z_0} = (-1)^n \mu^{2n} \frac{\partial^{2n} w}{\partial x^{2n}}|_{z_0} & \frac{\partial^{2n+1} w}{\partial z^{2n+1}}|_{z_0} = (-1)^{n+1} \mu^{2n} \frac{\partial^{2n+1} u}{\partial x^{2n+1}}|_{z_0}
\end{array} \tag{2.19}$$

in which $n \in \mathbb{N}$, zero inclusive. The result shows that all partial derivatives in the series are now taken along the x-coordinate, despite the series expansion being applied along the z-coordinate. Multiply both sides by μ, a general form of the Taylor series expansion is given by

$$\mu w(t,x,z) = \sum_{n=0}^{\infty} (-1)^n \mu^{2n} \frac{\Delta z_0^{2n}}{(2n)!}\frac{\partial^{2n} \mu w}{\partial x^{2n}}|_{z_0} - (-1)^n \mu^{2n+1} \frac{\Delta z_0^{2n+1}}{(2n+1)!}\frac{\partial^{2n+1} u}{\partial x^{2n+1}}|_{z_0} \tag{2.20}$$

The same procedure can be carried out for the series expansion of the horizontal velocity (Appendix C) to give

$$u(t,x,z) = \sum_{n=0}^{\infty} (-1)^n \mu^{2n} \frac{\Delta z_0^{2n}}{(2n)!}\frac{\partial^{2n} u}{\partial x^{2n}}|_{z_0} + (-1)^n \mu^{2n+1} \frac{\Delta z_0^{2n+1}}{(2n+1)!}\frac{\partial^{2n+1} \mu w}{\partial x^{2n+1}}|_{z_0} \tag{2.21}$$

Introducing an operator $Q^m = \mu^m \Delta z_0^m \frac{\partial^m}{\partial x^m}$, where m is a dummy variable, the generalized Taylor series expansions (2.20 and 2.21) can be expressed in compact trigonometric form by applying cosine (G.16) and sine (G.17) series expansion identities. Combining the expressions in matrix

form gives

$$\begin{bmatrix} u(t,x,z) \\ \mu w(t,x,z) \end{bmatrix} = \left(\begin{bmatrix} \cos(Q) & \sin(Q) \\ -\sin(Q) & \cos(Q) \end{bmatrix} \begin{bmatrix} u \\ \mu w \end{bmatrix} \right) |_{z_0} \tag{2.22}$$

where it is important to note that that operator Q does not commute (e.g., $Q^{2n+1} \neq Q^{2n}Q$) when z_0 is spatially dependent. It is highlighted that order of μ associated with the trigonometric operators differ, with the sine operator being one order higher. The orthogonal square matrix on the right hand side of (2.22) represents clockwise rotational transformation in Euclidean space. The determinant gives an expression for a unit circle with $Q = \mu \Delta z_0 \frac{\partial}{\partial x}$ being the dimensionless phase argument of the trigonometric function.

In the case when the point of expansion for the series is a stationary seabed, $z_0 = -h(x)$, and the function is evaluated at the still water level, $z = 0$, then $\Delta z_0 = h(x)$ and the phase argument reduces to $Q = \mu h \frac{\partial}{\partial x}$ which, in dimensional form, agrees with Agnon et al. (1999) for the quasi-2D case. To go one step further, Agnon et al. (1999)[1] also introduces the notation $L_c(f) \equiv \cos(h\frac{\partial f}{\partial x})$ and $L_s(f) \equiv \sin(h\frac{\partial f}{\partial x})$, in which (2.22) shows

$$u(t,x,z) = L_c(u)|_{-h} + L_s(\mu w)|_{-h} \tag{2.23}$$

$$\mu w(t,x,z) = L_c(\mu w)|_{-h} - L_s(u)|_{-h} \tag{2.24}$$

Switching the point of evaluation and the point of expansion, in which $\Delta z_0 = -h(x)$, switches the rotation transform to counterclockwise due to the parity of the trigonometric functions.

2.2.2 Surface Projection

Infinite series expansions (2.20 and 2.21) are exact; however, if the point of expansion lies on a surface function (e.g., $z_0 = -h(t,x)$), the temporal and spatial dependency is unaccounted for by the operators. This can be corrected through the use of projections (e.g., Wu 2001), which involves application of the chain rule when taking derivatives. This section is dedicated to the mathematical details in an general setting.

Given an arbitrary scalar function $f(t,x,z)$ and surface $z = s(t,x)$, the notation $f|_s \equiv f(t,x,z = s(t,x))$ indicates the function evaluation on the surface. A vector valued sigma function $\sigma : \mathbb{R}^3 \to \mathbb{R}^3$ is introduced, which maps the (t,x,z) coordinate domain to a surface $\sigma(t,x,z) = (t,x,s(t,x))$

[1] Agnon et al. (1999) made a sign error in the expression for $w(t,x,z)$, however this is corrected in later studies (e.g., P. A. Madsen et al. 2002)

coordinate. The scalar function in sigma-coordinates is thus given by

$$f|_s \equiv f(t,x,s(t,x)) = f(\sigma(t,x,z)) = (f \circ \sigma)(t,x,z) \tag{2.25}$$

where the latter notation, $(f \circ \sigma)$, denotes the function composition. Introducing the operator $\mathbf{D} = (\partial_t, \partial_x, \partial_z)$, the derivative $\mathbf{D}f|_\sigma = (\mathbf{D}f)|_\sigma \mathbf{D}\sigma$ would be given by the chain rule

$$\mathbf{D}f|_\sigma = \begin{bmatrix} \frac{\partial f}{\partial t}|_\sigma & \frac{\partial f}{\partial x}|_\sigma & \frac{\partial f}{\partial z}|_\sigma \end{bmatrix} \begin{bmatrix} \frac{\partial t}{\partial t} & \frac{\partial t}{\partial x} & \frac{\partial t}{\partial z} \\ \frac{\partial x}{\partial t} & \frac{\partial x}{\partial x} & \frac{\partial x}{\partial z} \\ \frac{\partial \sigma}{\partial t} & \frac{\partial \sigma}{\partial x} & \frac{\partial \sigma}{\partial z} \end{bmatrix} = \begin{bmatrix} \frac{\partial f}{\partial t}|_\sigma & \frac{\partial f}{\partial x}|_\sigma & \frac{\partial f}{\partial z}|_\sigma \end{bmatrix} \begin{bmatrix} 1 & 0 & 0 \\ 0 & 1 & 0 \\ \frac{\partial \sigma}{\partial t} & \frac{\partial \sigma}{\partial x} & 0 \end{bmatrix} \tag{2.26}$$

Observing the notation equivalence, $|_s \equiv |_\sigma$, matrix multiplication gives the partial derivatives for each component as

$$\frac{\partial f|_s}{\partial t} = \frac{\partial f}{\partial t}|_s + \frac{\partial f}{\partial z}|_s \frac{\partial s}{\partial t} \tag{2.27}$$

$$\frac{\partial f|_s}{\partial x} = \frac{\partial f}{\partial x}|_s + \frac{\partial f}{\partial z}|_s \frac{\partial s}{\partial x} \tag{2.28}$$

$$\frac{\partial f|_s}{\partial z} = 0 \tag{2.29}$$

The matrix in (2.26) is a projection matrix, which can be proved by showing idempotency, where its square returns the original matrix. The projection serves as a linear transformation mapping the partial derivatives in the original coordinate system to a new sigma coordinate system.

2.2.3 Taylor Polynomials

Series expansions of the vector velocity along the z-coordinate (2.18 and C.1) have been modified such that all derivatives in the series are with respect to the x-coordinate. Replacing the arbitrary scalar function, f, in (2.28) with the respective vector velocity component, derivatives in (2.20 and 2.21) can be projected such that the operators apply to functions evaluated at the point of expansion. Although the infinite series expansions are exact, they are often truncated to achieve the desired order of dispersion in practical application. In this study, focus is directed on model equations defined by $O(\mu^2)$ Taylor polynomial approximations, thus retaining the leading order effects of dispersion.

There are multiple paths to follow when deriving the polynomial approximations of the velocity components to be substituted into the governing equations. To begin, the point of expansion in (2.20

and 2.21) is defined to be an arbitrary surface, $z_0 = s(t, x)$, which is a function of time and space. To each series expansion, (2.28) is recursively applied while employing the irrotational condition and continuity equation until all derivative operators: (a) act on velocity functions evaluated at the point of expansion, and (b) are taken with respect to the x-coordinate. The series are then truncated at the desired order. Although this method is direct, Nwogu (1993) presents an alternative approach with valuable insight. Once the vertical velocity approximation is known, the irrotational condition can be utilized to derive the horizontal velocity approximation. Employing either method will lead to the same approximate solution. Therefore, to complement the approach of Nwogu (1993), the vertical velocity approximation is first derived using the projection method, then the horizontal velocity approximation is derived by depth integrating the irrotational condition.

In Nwogu (1993), the Taylor polynomial expression for the horizontal velocity is derived by depth integrating the irrotational condition (2.14) from the seabed to an arbitrary z-level in the water column. Generalizing the seabed surface, $s(t, x)$, the integration gives

$$u(t, x, z) - u|_s = \mu^2 \int_s^z \frac{\partial w}{\partial x} dz \tag{2.30}$$

which is exact. As an approximation, a Taylor polynomial of the vertical velocity is derived by truncating series expansion (2.20) at $O(\mu^2)$, due to the leading μ^2 term in (2.30), to give a linear approximation of the vertical velocity

$$w(t, x, z) = w|_s - \Delta z_s \frac{\partial u}{\partial x}|_s \tag{2.31}$$

in which $\Delta z_s = z - s(t, x)$ is the vertical displacement between z, the point of evaluation, and $s(t, x)$, the surface point of expansion. Applying a projection (2.28) to the derivative term in (2.31) and invoking the general kinematic condition (A.3) gives the truncated linear Taylor polynomial approximation

$$w(t, x, z) = \frac{1}{\epsilon}\frac{\partial s}{\partial t} + \frac{\partial su|_s}{\partial x} - z\frac{\partial u|_s}{\partial x} + O(\mu^2) \tag{2.32}$$

which can be substituted into (2.30) to give the Taylor polynomial approximation for the horizontal velocity

$$u(t, x, z) = u|_s + \frac{\mu^2}{\epsilon}\Delta z_s \frac{\partial^2 s}{\partial t \partial x} + \mu^2 \Delta z_s \frac{\partial^2 su|_s}{\partial x^2} - \mu^2 \left(\frac{z^2 - s^2}{2}\right) \frac{\partial^2 u|_s}{\partial x^2} + O(\mu^4) \tag{2.33}$$

Approximations (2.32 and 2.33) are valid for any surface point of expansion. Substitution of a stationary seabed surface, $s = -h(x)$, gives the set of approximations found in Nwogu (1993), with the only difference being due to the scaling (2.9) of the problem. The left image shown in figure 2.2 qualitatively depicts the accuracy decay of a local Taylor polynomial with increasing distance

from the seabed surface. The accuracy is improved with increasing number of terms in the series expansion (2.18) or decreasing the relative depth, in which the approximation approaches a uniform distribution indicative of NSWEs.

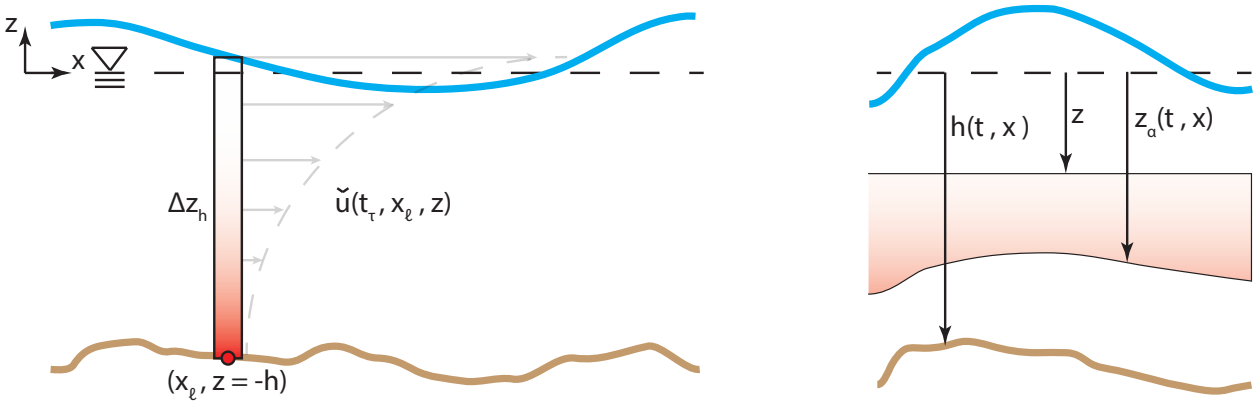

Figure 2.2: Stationary profile view of: (left) local Taylor series expansion about the seabed with gradient representing a qualitative decay in accuracy, and (right) integral definition of corresponding function approximation after making a change in reference.

Having derived the equivalent equations found in Nwogu (1993), while employing the projection methods of Wu (2001), reveals that the algorithm presented by Nwogu (1993) is in effect applying derivative operators to the vector velocity evaluated on the seabed surface. In Nwogu (1993), the Leibniz integration rule was applied to the governing equations a priori the velocity function expansions. Therefore substitution of a Taylor polynomial, without having made the projection, leads to a loss of information at the boundaries. To correct this, the Leibniz integration rule must be inverted in the algorithm of Nwogu (1993) to obtain proper expressions in the series expansion. The importance of having the derivative operators applied to the velocity functions defined on the seabed was not explicitly shown, nor discussed, despite the fundamental importance. Nevertheless, the approach given herein offers clarity and it is further emphasized that (2.33) can be derived directly from the series (2.21) by applying (2.28) without having to depth integrate the irrotational condition as shown above.

2.2.4 Nonlinear Enhancement

The principle contribution of Nwogu (1993) is a formal derivation of the vector velocity function in terms of an arbitrary reference, $z_\alpha(x)$, over an irregular seabed. The arbitrary reference location within the water column serves as a degree of freedom for optimizing the mathematical model, in which the linear frequency dispersion of Airy wave theory (Airy 1845) often serves as a baseline for quantitative assessment. It is important to note that this approach does not formally change the

approximating series expansion, but instead introduces a change of reference giving an alternative measure of the velocity profile. With the derivation not being explicitly presented in Nwogu (1993), insights can be found in Y. Chen and P. L.-F. Liu (1995) using potential flow theory. Evaluating the horizontal velocity function (2.33) at $z = z_\alpha(x)$ shows that $u|_s = u|_{z_\alpha} + O(\mu^2)$, which implies that substitutions can be made in the $O(\mu^2)$ terms without altering the order of approximation. Subtracting the resultant expression for $u|_{z_\alpha}$ from (2.33) gives a general function approximation in terms of a horizontal velocity defined at an arbitrary reference

$$u(t,x,z) = u|_{z_\alpha} + \frac{\mu^2}{\epsilon}\Delta z_\alpha \frac{\partial^2 s}{\partial t \partial x} + \mu^2 \Delta z_\alpha \frac{\partial^2 s u|_{z_\alpha}}{\partial x^2} - \mu^2 \left(\frac{z^2 - z_\alpha^2}{2}\right) \frac{\partial^2 u|_{z_\alpha}}{\partial x^2} + O(\mu^4) \tag{2.34}$$

in which $\Delta z_\alpha = z - z_\alpha(x)$ is the vertical displacement between z, the point of evaluation and $z_\alpha(t,x)$, the arbitrary reference. This procedure is identical to

$$\int_s^z f(t,x,z)dz - \int_s^{z_\alpha} f(t,x,z)dz = \int_{z_\alpha}^z f(t,x,z)dz \tag{2.35}$$

in which $f(t,x,z)$ is an arbitrary function. Equation (2.35) shows that the degree of freedom associated with the arbitrary reference is independent of the definition of the point of expansion. Furthermore, the arbitrary reference in (2.34) can be defined as a function of time and space, $z_\alpha(t,x)$, without loss, which enhances the nonlinearity of the approximation (Kennedy et al. 2001).

The schematic on the right of figure 2.2 highlights a qualitatively range of the polynomial approximation, Δz_α, when the point of expansion is defined to be $s = -h(x)$, as in Nwogu (1993). Although the point of evaluation, z, is explicitly defined by integrals in the governing equations, it is instructive to understand the integral behaviour at this junction. If the point of evaluation, z, does not equal the point of expansion, $-h(x)$, then the interval of the polynomial approximation adjacent to the point of expansion is excluded, leaving a less accurate upper interval to contribute. Visually, this is reminiscent of an annulus. Only when the point of evaluation equals the point of expansion does the region form a disk. Furthermore, if the point of evaluation, z, is above or below the arbitrary reference, z_α, then there is a sign change in the $O(\mu^2)$ terms. Thus, when integrated over the flow depth for example, there is a net contribution weighted by the location of z_α in the water column. This is the action of the degree of freedom. In other words, the location of z_α controls the relative contribution of the $O(\mu^2)$ terms, irrespective of the limits of integration. If the arbitrary reference is defined to be the point of expansion, then the degree of freedom is lost, in which any integral is purely dependent on the profile defined by the polynomial approximation at the point of expansion. It is important to emphasize that z_α simply changes the reference and does not control the underlying polynomial. If the flow depth becomes too large, then no matter where you place the reference, there will be a net contribution of the $O(\mu^2)$ terms which are erroneous. Nevertheless, keeping the arbitrary reference away from the point of expansion permits some level

of control over the $O(\mu^2)$ terms.

The set of depth dependent velocity functions presented by Nwogu (1993) and Kennedy et al. (2001) are solely dependent upon a series expansion about a stationary seabed. Therefore, the notation $\breve{u}(t,x,z)$ is introduced, as in figure 2.2, to indicate the surface point of expansion associated with the polynomial approximation. In this study, an expansion about the free-surface is introduced, $s=\epsilon\eta(t,x)$, where the left image of figure 2.3 depicts the accuracy decay of a local Taylor polynomial with increasing distance from the free-surface. The right image of figure 2.3 is analogous to that shown in figure 2.2, in which the analysis above applies, with only difference being a change in the point of expansion.

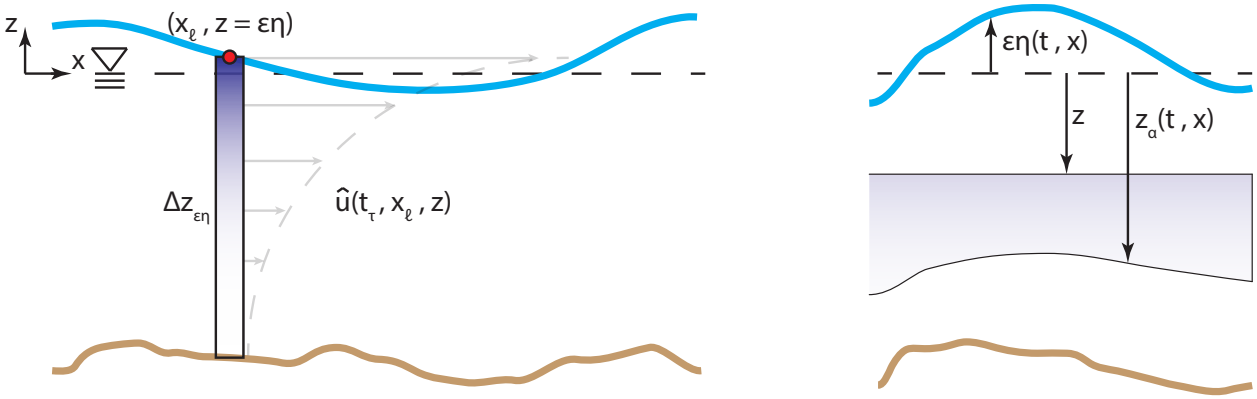

Figure 2.3: Stationary profile view of: (left) local Taylor series expansion about the free-surface with gradient representing a qualitative decay in accuracy, and (right) integral definition of corresponding function approximation after making a change in reference.

The Taylor polynomials, being local, are only accurate near the points of expansion. Combining approximations $\breve{u}(t,x,z)$ and $\hat{u}(t,x,z)$ in a weighted sum allows for the local influence of each approximation to contribute, giving an overall improved profile approximation

$$u(t,x,z)=(1-\gamma)\breve{u}+\gamma\hat{u}=\breve{u}+\gamma(\hat{u}-\breve{u}) \tag{2.36}$$

in which $0\leq\gamma\leq 1$ is a new degree of freedom weighting of the surface points of expansion. As stated prior, this degree of freedom is independent of that associated with the reference. For the case $\gamma=0$, equation (2.36) reduces to that found in Nwogu (1993) for $z_\alpha(x)$, and Kennedy et al. (2001) for $z_\alpha(t,x)$, thus the weighted polynomial serves as an additional nonlinear extension by including an expansion about the free-surface. Figure 2.4 depicts a qualitative merger of figures 2.2 and 2.3 to reflect the new weighted polynomial approximation. An explicit expression for the right hand side of (2.36) is determined by adding points of expansion $s=-h$, for $\breve{u}$, to $s=\gamma(\epsilon\eta+h)=\gamma H$, for

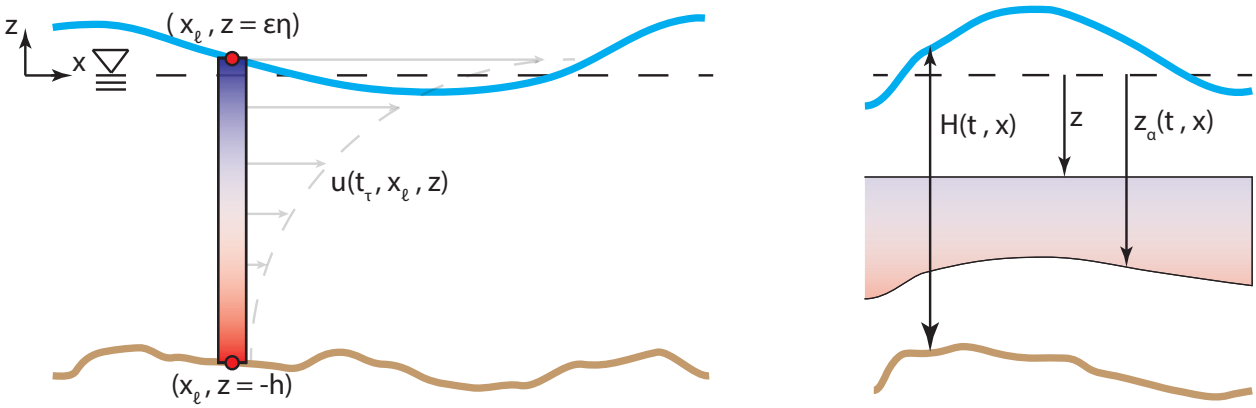

Figure 2.4: Stationary profile view of: (left) combined local Taylor series expansion about the seabed and free-surface with gradient representing a qualitative decay in accuracy, and (right) integral definition of corresponding function approximation after making a change in reference.

$\hat{u}-\check{u}$, to give $s=-h+\gamma H$ as the new point of expansion to be substituted into (2.34) giving

$$\begin{aligned} u(t,x,z) =& u|_{z_\alpha} - \left(\frac{\mu^2}{\epsilon}\Delta z_\alpha \frac{\partial^2 h}{\partial t \partial x} + \mu^2 \Delta z_\alpha \frac{\partial^2 h u|_{z_\alpha}}{\partial x^2}\right) - \mu^2 \left(\frac{z^2 - z_\alpha^2}{2}\right) \frac{\partial^2 u|_{z_\alpha}}{\partial x^2} \\ &+ \gamma \left(\frac{\mu^2}{\epsilon}\Delta z_\alpha \frac{\partial^2 H}{\partial t \partial x} + \mu^2 \Delta z_\alpha \frac{\partial^2 H u|_{z_\alpha}}{\partial x^2}\right) + O(\mu^4) \end{aligned} \tag{2.37}$$

The new surface point of expansion, $s=-h+\gamma H$, is identical in structure to the datum invariant reference, $z_\alpha(t,x) = -h+\beta H$, introduced by Kennedy et al. (2001), where β is defined to be a fraction of the flow depth for a physically meaningful reference. Assuming the general form $z_\alpha(t,x)=\zeta h+\beta\epsilon\eta$ implies $\beta=\zeta+1$, in which $-1\leq\zeta\leq 0$ is a free parameter. In the linear case, $z_\alpha(x)=\zeta h$ corresponds to a fraction of the still water depth (Nwogu 1993). Thus, in general, two degrees of freedom are employed to define the approximation.

In the case where the point of expansion is set equal to the datum invariant reference, then the substitution $s(t,x)=z_\alpha(t,x)$ could be made into (2.34) giving

$$u(t,x,z) = u|_{z_\alpha} + \frac{\mu^2}{\epsilon}\Delta z_\alpha \frac{\partial^2 z_\alpha}{\partial t \partial x} + \mu^2 \Delta z_\alpha \frac{\partial^2 z_\alpha u|_{z_\alpha}}{\partial x^2} - \mu^2 \left(\frac{z^2 - z_\alpha^2}{2}\right) \frac{\partial^2 u|_{z_\alpha}}{\partial x^2} + O(\mu^4) \tag{2.38}$$

in which $\gamma=\beta=\zeta+1$ not only preserves the degree of freedom defining the time varying reference (Kennedy et al. 2001), but it simultaneously weighs the local polynomial approximations about seabed and free-surface. Considering the datum invariant reference mirrors the material surfaces, it too can be treated as a material surface, which validates the kinematics in (2.38), despite the virtual nature of the reference. In contrast to earlier, if $\gamma=0$ (i.e., $\zeta=-1$), the equations of Nwogu (1993) and Kennedy et al. (2001), defined as a function of an arbitrary reference, are not

recovered. Instead the equations reduce to a set defined early on in Nwogu (1993), when both the reference and point of expansion are defined at the seabed (i.e., $s = -h(x)$ in 2.34). To the best of the author's knowledge, (2.38) has never been presented in the literature. Furthermore, substituting $s(t,x) = z_\alpha(t,x)$ into the general vertical velocity approximation (2.32) gives

$$w(t,x,z) = -\left(\frac{1}{\epsilon}\frac{\partial h}{\partial t} + \frac{\partial h u|_{z_\alpha}}{\partial x} + z\frac{\partial u|_{z_\alpha}}{\partial x}\right) + \gamma\left(\frac{1}{\epsilon}\frac{\partial H}{\partial t} + \frac{\partial H u|_{z_\alpha}}{\partial x}\right) + O(\mu^2) \tag{2.39}$$

$$= \frac{1}{\epsilon}\frac{\partial z_\alpha}{\partial t} + \frac{\partial z_\alpha u|_{z_\alpha}}{\partial x} - z\frac{\partial u|_{z_\alpha}}{\partial x} + O(\mu^2) \tag{2.40}$$

Following the assumptions and methods herein, it does not seem possible to arrive at (2.39) without asserting $s(t,x) = z_\alpha(t,x)$, because the expression for $u|_s$ in (2.32) would contain terms involving velocity expressions at the material surfaces, thus the approximations would be functions of multiple unknowns instead of a single model velocity. Furthermore, since the vertical velocity is truncated at $O(\mu^2)$, leading order expressions could not be simply substituted in without violating the order of approximation. This is not the case in Nwogu (1993) because the scaling arguments used therein results in the vertical velocity being $O(\mu^2)$, which is different from the scaling arguments used herein as pointed out earlier.

Polynomial approximations (2.37 and 2.39) are functions of the model velocity $u|_{z_\alpha}$, and free-surface elevation, $\epsilon\eta$, in which a single degree of freedom, $\gamma = \beta = \zeta + 1$, defines a datum invariant reference level within the water column and the weighting of the Taylor polynomials at the material surfaces. Kennedy et al. (2001) advises $\gamma = \beta = \sqrt{1/5}$ to achieve a Padé [2/2] approximation of the linear dispersion relation. The enhancement in (2.37) and (2.39) is realized in the nonlinear terms, which differ from those in Kennedy et al. (2001) due to the weighted polynomial approximation. In the next section, polynomial approximations (2.37) and (2.39) will be substituted into the governing equations to complete the derivation of the mathematical formulation.

2.3 Governing Equations in Conserved Variable Form

The dimensions of the domain are reduced by substituting the velocity profiles into the continuity and Euler equations, then integrating them over the flow depth. Implementation of the Leibniz integration rule (B) pulls differentials out of the integral, which results in the equations being expressed in conserved form. Since the polynomial approximations for the velocity profile are expressed in terms of a single model velocity, with the only other unknown being the free-surface elevation, the resulting system of equations is closed with two equations and two unknowns. This section begins with a formulation of the depth averaged momentum, followed by a brief digression to verify the derivation in connection with that derived by Wei et al. (1995) using potential flow

theory. The governing equations are then depth integrated to arrive at a new system of equations, which is then compared with the quasi-2D state-of-the-art FUNWAVE equations of Shi et al. (2012) to place the nonlinear enhancement in context.

2.3.1 Depth Average

In the derivation of modern Boussinesq-type equations, a theoretical benchmark is the fully nonlinear, weakly dispersive theory of Wei et al. (1995). Under the assumption of weak nonlinearity, the theory reduces to Nwogu (1993), which for selected dispersive coefficients, can be further reduced to Peregrine (1967). Therefore, the theory of Wei et al. (1995) represents a family of Boussinesq-type equations built upon a well established foundation. Kennedy et al. (2001) later enhanced the nonlinear properties of Wei et al. (1995) by incorporating a time varying reference, thus giving the most advanced theory along these lines of development. The assumption of irrotational flow permits the introduction of a scalar velocity potential function in place of the vector velocity function and serves as an alternative approach to derive Boussinesq-type equations. This is the approach taken by Wei et al. (1995), which results in a set of governing equations whose presentation is quite different from those derived herein employing the vector velocity. Since the assumptions are consistent, the governing equations of Wei et al. (1995) should serve as a subset of those derived herein, which includes additional nonlinear terms, thereby progress is shown in the development.

The continuity equation presented in Wei et al. (1995) is derived by depth integrating (2.10) over the flow depth, which will be addressed in the next section. Jumping ahead, it turns out to be identical to the one presented herein under the same assumptions. Therefore, focus here is directed on the quasi-2D equations of motion. Begin by integration the vertical momentum equation (2.13) from an arbitrary level, z, in the water column to the free-surface to get an expression for the level pressure

$$p(t,x,z) = \mu^2 \int_z^{\epsilon\eta} \frac{\partial w}{\partial t} dz + \epsilon\mu^2 \int_z^{\epsilon\eta} u \frac{\partial w}{\partial x} dz + \epsilon\mu^2 \int_z^{\epsilon\eta} w \frac{\partial w}{\partial z} dz + \frac{\epsilon\eta - z}{\epsilon} \tag{2.41}$$

Taking the partial derivative along the x-coordinate, p_x, and substituting the expression into the horizontal momentum equation (2.11) gives

$$\frac{\partial u}{\partial t} + \epsilon u \frac{\partial u}{\partial x} + \epsilon w \frac{\partial u}{\partial z} + \mu^2 \frac{\partial}{\partial x} \left(\int_z^{\epsilon\eta} \left(\frac{\partial w}{\partial t} + \epsilon u \frac{\partial w}{\partial x} + \epsilon w \frac{\partial w}{\partial z} \right) dz \right) + \frac{\partial \eta}{\partial x} = 0 \tag{2.42}$$

A general equation for the horizontal velocity approximation (2.37) is $u(t,x,z) = u|_{z_\alpha} + \mu^2 u_\mu$, in which u_μ corresponds to the $O(\mu^2)$ terms. Since the series is truncated at $O(\mu^4)$, terms of μ^4 in (2.42) are dropped upon substitution. Furthermore, we emphasize that $u|_{z_\alpha}$ is not a function of the z-coordinate, thus can be pulled out from under the integral. Applying the irrotational condition

(2.14) to the third term and the Leibniz integration rule (B) to the fourth term to exchange the operators gives

$$\frac{\partial u|_{z_\alpha}}{\partial t} + \epsilon u|_{z_\alpha}\frac{\partial u|_{z_\alpha}}{\partial x} + \frac{\partial \eta}{\partial x} = -\mu^2 V_1 - \epsilon\mu^2 V_2 + O(\mu^4) \tag{2.43}$$

in which

$$V_1 = \frac{\partial}{\partial t}\left(u_\mu + \int_z^{\epsilon\eta}\frac{\partial w}{\partial x}dz\right) + \frac{\partial}{\partial t}\left(\frac{\partial \epsilon\eta}{\partial x}w|_{\epsilon\eta}\right) - \frac{\partial}{\partial x}\left(\frac{\partial \epsilon\eta}{\partial t}w|_{\epsilon\eta}\right) \tag{2.44}$$

$$V_2 = \frac{\partial}{\partial x}\left(u|_{z_\alpha}\left(u_\mu + \int_z^{\epsilon\eta}\frac{\partial w}{\partial x}dz\right)\right) + \frac{\partial}{\partial x}\int_z^{\epsilon\eta} w\frac{\partial w}{\partial z}dz + w\frac{\partial w}{\partial x} \tag{2.45}$$

It remains to shown that V_1 and V_2 match the expressions given by Wei et al. (1995). The key is to recognize that the general expression for u_μ is given by $\int_{z_\alpha}^{z} w_x dz$, which readily sums with the integral sharing a common integrand to change the limits of integration

$$V_1 = \frac{\partial}{\partial t}\int_{z_\alpha}^{\epsilon\eta}\frac{\partial w}{\partial x}dz + \frac{\partial \epsilon\eta}{\partial x}\frac{\partial w|_{\epsilon\eta}}{\partial t} - \frac{\partial \epsilon\eta}{\partial t}\frac{\partial w|_{\epsilon\eta}}{\partial x} \tag{2.46}$$

$$V_2 = \frac{\partial}{\partial x}\left(u|_{z_\alpha}\int_{z_\alpha}^{\epsilon\eta}\frac{\partial w}{\partial x}dz\right) + \frac{\partial}{\partial x}\int_z^{\epsilon\eta} w\frac{\partial w}{\partial z}dz + w\frac{\partial w}{\partial x} \tag{2.47}$$

The expression for V_2 is addressed first, whose operator form is already in agreement with Wei et al. (1995). The integrand of the trailing integral in (2.47) is expressed in conserved form and the integration is carried out to cancel the last term

$$V_2 = \frac{\partial}{\partial x}\left(u|_{z_\alpha}\int_{z_\alpha}^{\epsilon\eta}\frac{\partial w}{\partial x}dz\right) + \frac{1}{2}\frac{\partial}{\partial x}\left(w|_{\epsilon\eta}^2\right) \tag{2.48}$$

Substituting the expression for the vertical velocity (2.39), assuming an expansion about the seabed ($\gamma = 0$) only, and carrying out the integration gives

$$V_2 = \frac{\partial}{\partial x}\left((z_\alpha - \epsilon\eta)\,u|_{z_\alpha}\frac{\partial^2 hu|_{z_\alpha}}{\partial x^2} + \frac{z_\alpha^2 - (\epsilon\eta)^2}{2}u|_{z_\alpha}\frac{\partial^2 u|_{z_\alpha}}{\partial x^2}\right) + \frac{1}{2}\frac{\partial}{\partial x}\left(\left(\frac{\partial hu|_{z_\alpha}}{\partial x} + \epsilon\eta\frac{\partial u|_{z_\alpha}}{\partial x}\right)^2\right) \tag{2.49}$$

The expression for V_2 in this form matches that given by Wei et al. (1995).

The expression for V_1 is a bit more involved, in which the Leibniz integration rule (B) is needed to exchange the time and space differential operators in (2.46) such that the time derivative is applied directly to the horizontal velocity in the leading integral expression. As a result, the trailing boundary expressions also change

$$V_1 = \frac{\partial}{\partial x}\int_{z_\alpha}^{\epsilon\eta}\frac{\partial w}{\partial t}dz + \frac{\partial z_\alpha}{\partial x}\frac{\partial w|_{z_\alpha}}{\partial t} - \frac{\partial z_\alpha}{\partial t}\frac{\partial w|_{z_\alpha}}{\partial x} \tag{2.50}$$

Carrying out the integration, it is found that the second term cancels due to the product rule, leaving

$$V_1 = z_\alpha \frac{\partial^3 hu|_{z_\alpha}}{\partial t \partial x^2} + \frac{z_\alpha^2}{2}\frac{\partial^3 u|_{z_\alpha}}{\partial t \partial x^2} - \frac{\partial}{\partial x}\left(\epsilon\eta \frac{\partial^2 hu|_{z_\alpha}}{\partial t \partial x} + \frac{(\epsilon\eta)^2}{2}\frac{\partial^2 u|_{z_\alpha}}{\partial t \partial x}\right) - \frac{\partial z_\alpha}{\partial t}\frac{\partial w|_{z_\alpha}}{\partial x} \tag{2.51}$$

In Wei et al. (1995), the reference is defined as a function of space alone, $z_\alpha(x)$, hence the last term drops out and the resulting expression for V_1 matches that given by Wei et al. (1995). If the reference is defined as a function of time and space, the trailing term in (2.51) is retained, in which the equation matches that given by Kennedy et al. (2001) upon substitution of the vertical velocity expression and application of the product rule.

Having proved that V_1 (2.44) and V_2 (2.45) are mathematically equivalent to those found in Wei et al. (1995), which follows the velocity potential approach, the derivation of the depth averaged momentum equation is verified following the vector velocity approach of Nwogu (1993). Therefore, by extension, the quasi-2D equations of Kennedy et al. (2001), Nwogu (1993), and Peregrine (1967), are all subsets of the theory presented herein. The depth averaged momentum equation is expressed in terms of the flow velocity, which is a primitive variable. For implementation of conservation principles, momentum is the preferred variable representation.

2.3.2 Depth Integration

A depth integrated system of equations is derived in this section through application of the Leibniz integration rule (B) to pull differential operators out of the depth averaged momentum equation. Although not explicitly addressed in this study, the introduction of conserved variables foster implementation of shock capturing methods as a means to approximate wave breaking, which has been addressed in previous studies (e.g., Tonelli and Petti 2009; Roeber et al. 2010; Roeber and Cheung 2012; Tissier et al. 2012; Shi et al. 2012). Therefore, the resulting system of equations serves to update the theoretical foundation in existing model equations found in practical application.

To facilitate clarity throughout the derivation, a few preliminary remarks are made. The depth average of an arbitrary depth dependent function, $f(t,x,z)$, is given by

$$\overline{f}(t,x) = \frac{1}{H}\int_{-h}^{\epsilon\eta} f(t,x,z)dz \tag{2.52}$$

which holds regardless of the definition of the depth dependent function. In the previous section, the variable u_μ was introduced to represent the $O(\mu^2)$ terms in (2.37) for clarity. Substituting

$u(t,x,z) = u|_{z_\alpha} + \mu^2 u_\mu + O(\mu^4)$ into (2.52) gives the following

$$\overline{u}(t,x) = \frac{1}{H}\int_{-h}^{\epsilon\eta} \left(u|_{z_\alpha} + \mu^2 u_\mu\right) dz + O(\mu^4) = u|_{z_\alpha} + \mu^2 \overline{u_\mu} + O(\mu^4) \tag{2.53}$$

in which

$$\begin{aligned}\overline{u_\mu} = \frac{1}{H}\int_{-h}^{\epsilon\eta} u_\mu dz = \left(z_\alpha + \frac{h}{2} - \frac{\epsilon\eta}{2}\right)\left(\frac{1}{\epsilon}\frac{\partial^2(h-\gamma H)}{\partial t \partial x} + \frac{\partial^2 (h-\gamma H)u|_{z_\alpha}}{\partial x^2}\right) + \\ \left(\frac{z_\alpha^2}{2} - \frac{h^2}{6} + \frac{\epsilon\eta h}{6} - \frac{(\epsilon\eta)^2}{6}\right)\frac{\partial^2 u|_{z_\alpha}}{\partial x^2}\end{aligned} \tag{2.54}$$

The volume flux (per unit breadth) is thus given by $H\overline{u} = Hu|_{z_\alpha} + \mu^2 H\overline{u_\mu} + O(\mu^4)$, which is conserved up to the order of approximation. The depth average of the vertical velocity (2.39) is given by

$$\overline{w}(t,x) = \frac{1}{H}\int_{-h}^{\epsilon\eta} w dz = \frac{1}{\epsilon}\frac{\partial(-h+\gamma H)}{\partial t} + \frac{\partial(-h+\gamma H)u|_{z_\alpha}}{\partial x} - \frac{\epsilon\eta - h}{2}\frac{\partial u|_{z_\alpha}}{\partial x} + O(\mu^2) \tag{2.55}$$

The depth averaged approximations (2.53) and (2.55) facilitate clarity when presenting the final set of governing equations.

Integrating the continuity equation (2.10) over the flow depth, then applying the kinematic boundary conditions (2.15, 2.16), gives

$$\frac{\partial H}{\partial t} + \epsilon\frac{\partial}{\partial x}\int_{-h}^{\epsilon\eta} u dz = 0 \tag{2.56}$$

which is identical to the continuity equation often presented in the literature (e.g., Nwogu 1993; Wei et al. 1995; Kennedy et al. 2001). Substituting the depth average horizontal velocity into (2.56) gives the homogeneous volume conservation law, $H_t + \epsilon(H\overline{u})_x = 0$, which again, is valid independent of the model horizontal velocity. In the NSWEs, the horizontal velocity is uniform over depth, in which the depth average horizontal velocity is often the model velocity employed (e.g., Whitham 1974; M. B. Abbott 1979; LeVeque 1992; Toro 2009). The freedom to define the model velocity in Boussinesq-type equations leads to many variants of equations found in the literature. In variants where the depth averaged velocity is employed (e.g., Peregrine 1967), equation (2.56) is exact; however, the equation of motion will still be an approximation. For the model velocity employed herein, $H\overline{u} = Hu|_{z_\alpha} + \mu^2 H\overline{u_\mu} + O(\mu^4)$ is substituted into the volume conservation law to give

$$\frac{\partial H}{\partial t} + \epsilon\frac{\partial Hu|_{z_\alpha}}{\partial x} + \epsilon\mu^2\frac{\partial H\overline{u_\mu}}{\partial x} = \psi_\eta + O(\mu^4) \tag{2.57}$$

where ψ_η is a place holder representing arbitrary volume source terms, which technically makes

(2.57) a volume balance law. The second term, $\epsilon(Hu|_{z_\alpha})_x$, in (2.57) is of the same form as $\epsilon(H\overline{u})_x$ found in the NSWEs, since $u|_{z_\alpha}$ is independent of the z-coordinate. In the absents of source and $O(\mu^4)$ terms, the volume conservation law (2.57) states that the flux is governed by a change in the hydrostatic flux, $Hu|_{z_\alpha}$, plus a change in the nonhydrostatic flux, $H\overline{u_\mu}$, due to the dispersive nature of the waves.

The leading term in (2.56 and 2.57) contains a time derivative of the seabed, which has not been explicitly addressed to this point. Linearizing the flux in (2.56), the leading order continuity equation, in the absents of source terms, is given by

$$\frac{\partial \eta}{\partial t} + \frac{1}{\epsilon}\frac{\partial h}{\partial t} + \frac{\partial hu|_{z_\alpha}}{\partial x} = 0 \tag{2.58}$$

which recovers the classical leading order equation for a stationary seabed. The inclusion of a dynamic seabed in Boussinesq-type equations is addressed by P. Lynett and P. L.-F. Liu (2002) in a study on landslide generated tsunamis. In fact, for $\gamma = 0$, the $O(\mu^2)$ terms given by equation (2.54) are identical to those found in P. Lynett and P. L.-F. Liu (2002). Assuming that the seabed displacement can be defined as $h'(t,x) = h'_s(x) + h'_d(t,x)$, where h'_s is the static still water depth and h'_d is the dynamic deformation[2], a new characteristic amplitude a_h is introduced to scale the deformation. The dimensionless still water depth (2.7) is modified as $h(t,x) = h_s(x) + \delta h_d(t,x)$, in which $\delta = a_h/h_c$ is a measure of nonlinearity due to the deformation. The definition of the flow depth does not change; however, expansion $H(t,x) = \epsilon\eta(t,x) + h_s(x) + \delta h_d(t,x)$ shows the decomposition. Furthermore, it has been assumed to this point that the time scales of the seabed deformation are the same as those of the free-surface waves, which is not necessarily the case for all physical processes. Introducing $t_w = L_c\sqrt{gh_c}$ for the wave time scales defined in (2.6) and t_h for the dynamic seabed time scales, leads to a new parameter $\xi = t_w/t_h$ out in front of the time derivative of the dynamic seabed component (e.g., P. Lynett and P. L.-F. Liu 2002). Furthermore, to account for the difference in time scales, the independent time variable needs to change to $\tau = \xi t$ in the seabed deformation (e.g., Lannes 2013). In this study, only creeping deformations, $\xi = 1$, are consider, as in P. Lynett and P. L.-F. Liu (2002), thus, $\tau = t$ and no changes are needed in the independent variables. Following these modifications, only the time derivatives involving the seabed deformation need to be addressed, in which the linearized continuity equation (2.58) becomes

$$\frac{\partial \eta}{\partial t} + \frac{\partial h_s u|_{z_\alpha}}{\partial x} = -\frac{\delta}{\epsilon}\frac{\partial h_d}{\partial t} \tag{2.59}$$

The leading parameter, δ/ϵ, is assumed $O(1)$ to maintain the conservation of mass (P. Lynett and P. L.-F. Liu 2002).

[2]The sign convention implies that a "positive deformation" leads to a "increase in depth".

Having clarified the time derivative of the seabed and leading order approximation, the $O(\mu^2)$ expression given in (2.54) needs to be updated. Substituting the datum invariant reference, $z_\alpha = -h + \beta H$, into each each of the coefficients gives

$$-h + \beta H + \frac{h}{2} - \frac{\epsilon\eta}{2} = H\left(\beta - \frac{1}{2}\right) \tag{2.60}$$

$$\frac{(-h+\beta H)^2}{2} - \frac{h^2}{6} + \frac{\epsilon\eta h}{6} - \frac{(\epsilon\eta)^2}{6} = -hH\left(\beta - \frac{1}{2}\right) + H^2\frac{1}{2}\left(\beta^2 - \frac{1}{3}\right) \tag{2.61}$$

in which the latter coefficient expansion shows that the leading term can be combined with the former coefficient expansion. Terms associated with each coefficient in (2.54) are now addressed. Making use of the leading order continuity equation (2.58), the first set of terms expands as

$$\frac{1}{\epsilon}\frac{\partial^2(h-\gamma H)}{\partial t\partial x} + \frac{\partial^2(h-\gamma H)u|_{z_\alpha}}{\partial x^2} = \frac{\delta}{\epsilon}\frac{\partial^2 h_d}{\partial t\partial x} + \frac{\partial^2 hu}{\partial x^2} - \gamma\frac{\partial^2}{\partial x^2}\left(\delta h_d u|_{z_\alpha} + \epsilon\eta u|_{z_\alpha}\right) \tag{2.62}$$

Applying the product rule to the second term, $(hu)_{xx}$, on the right hand side of (2.62) will produce a hu_{xx} term that will cancel with the hu_{xx} term generated by the first coefficient on the right hand side of (2.61). The updated $O(\mu^2)$ expression of (2.54) is thus given by

$$\begin{aligned}\overline{u_\mu} = \frac{1}{H}\int_{-h}^{\epsilon\eta} u_\mu dz = {} & H\left(\beta - \frac{1}{2}\right)\left(\frac{\partial h}{\partial x}\frac{\partial u|_{z_\alpha}}{\partial x} + \frac{\partial}{\partial x}\left(u|_{z_\alpha}\frac{\partial h}{\partial x}\right)\right) + H^2\frac{1}{2}\left(\beta^2 - \frac{1}{3}\right)\frac{\partial^2 u|_{z_\alpha}}{\partial x^2} \\ & + H\left(\beta - \frac{1}{2}\right)\frac{\delta}{\epsilon}\frac{\partial^2 h_d}{\partial t\partial x} \\ & - \gamma H\left(\beta - \frac{1}{2}\right)\frac{\partial^2}{\partial x^2}\left(\delta h_d u|_{z_\alpha} + \epsilon\eta u|_{z_\alpha}\right)\end{aligned} \tag{2.63}$$

Given a static seabed, $h_d = 0$, and $\gamma = 0$, the expression matches that give by Kennedy et al. (2001) for a datum invariant reference. It was already state earlier that for $\gamma = 0$ the expression given by (2.54) is identical to the one given by P. Lynett and P. L.-F. Liu (2002) that has now been amended to include a dynamic seabed deformation following their methodology. The fully nonlinear expression, including the dynamic seabed deformation terms, was not explicitly given by P. Lynett and P. L.-F. Liu (2002), nor is a datum invariant reference imposed. However, they do give the weakly nonlinear equations, which appear to show consistency. The last line in (2.63) is due to the weighted polynomial expansion and is completely new. Operating on the free-surface and dynamic seabed deformation, it serves as a nonlinear enhancement to the equations of Kennedy et al. (2001) and P. Lynett and P. L.-F. Liu (2002), which takes into account the spatial curvature of the seabed and free-surface. The expression for the vertical velocity (2.39), and its depth average

(2.55), are also updated to give

$$w(t,x,z) = -\left(\frac{\delta}{\epsilon}\frac{\partial h_d}{\partial t} + \frac{\partial hu|_{z_\alpha}}{\partial x} + z\frac{\partial u|_{z_\alpha}}{\partial x}\right) + \gamma\frac{\partial}{\partial x}\left(\delta h_d u|_{z_\alpha} + \epsilon\eta u|_{z_\alpha}\right) + O(\mu^2) \tag{2.64}$$

$$\overline{w} = \frac{1}{H}\int_{-h}^{\epsilon\eta} w dz = -\left(\frac{\delta}{\epsilon}\frac{\partial h_d}{\partial t} + \frac{\partial hu|_{z_\alpha}}{\partial x}\right) - \frac{\epsilon\eta - h}{2}\frac{\partial u|_{z_\alpha}}{\partial x} + \gamma\frac{\partial}{\partial x}\left(\delta h_d u|_{z_\alpha} + \epsilon\eta u|_{z_\alpha}\right) + O(\mu^2) \tag{2.65}$$

It is emphasized that approximations (2.63) and (2.65) are specific cases of (2.54) and (2.55) respectively, where the former accounts for slowly varying dynamic seabed deformations.

The horizontal momentum equation (2.11) contains products of velocity components and their derivatives. Applying the product rule and continuity equation (2.10) facilitates the Leibniz integration rule (B) for integration over the flow depth. Applying the kinematic (2.15, 2.16) and dynamic (2.17) boundary conditions gives

$$\frac{\partial}{\partial t}\int_{-h}^{\epsilon\eta} u dz + \epsilon\frac{\partial}{\partial x}\int_{-h}^{\epsilon\eta}(uu)dz + \frac{\partial}{\partial x}\int_{-h}^{\epsilon\eta} p dz - \frac{\partial h}{\partial x}p|_{-h} = 0 \tag{2.66}$$

in which the scalar pressure function, $p(t,x,z)$, is defined by depth integrating the vertical momentum equation (2.13) to an arbitrary level in the water column. The free-surface is chosen as the upper limit, knowing that the dynamic boundary condition (2.17) simplifies the expression, leaving only a depth dependent pressure term. Like the horizontal momentum equation, the vertical momentum equation contains products of velocity components and their derivatives. Applying the product rule and continuity equation (2.10) facilitates the Leibniz integration rule (B) for integration over a portion of the flow depth. Applying the kinematic (2.15) and dynamic (2.17) free-surface boundary conditions, then solving for the pressure function results in

$$p(t,x,z) = \mu^2\frac{\partial}{\partial t}\int_{z}^{\epsilon\eta} w dz + \epsilon\mu^2\frac{\partial}{\partial x}\int_{z}^{\epsilon\eta}(uw)dz + \eta - \frac{z}{\epsilon} - \epsilon\mu^2 w^2 \tag{2.67}$$

which is technically correct, but it is important to recognize that the lower integration limit, z, represents a level in the water column, not a surface. Substituting $z = \epsilon\eta$ makes this abundantly clear, giving $p|_{\epsilon\eta} = -\epsilon\mu^2 w|^2_{\epsilon\eta}$, which does not agree with the dynamic boundary condition (2.15) stating $p|_{\epsilon\eta} = 0$ on the free-surface. Substituting a surface function, dependent upon time and space, into z changes the behavior of the integration. This is exactly what the Leibniz integration rule accounts for, thus there is an implicit $(\mu^2/\epsilon)z_t w|_z + \epsilon\mu^2 z_x(uw)|_z$ set of terms trailing (2.67), which drop out because the z-coordinate is not dependent on time or space. Thus, when the material surface $z = \epsilon\eta$ is substituted in, the implicit boundary terms apply and the kinematic boundary condition (2.15) cancels the $-\epsilon\mu^2 w|^2_{\epsilon\eta}$ term, giving the correct solution for the pressure, $p|_{\epsilon\eta} = 0$, on the free-surface. By the same argument, the pressure at the seabed, $p|_{-h}$, in the depth integrated horizontal momentum equation (2.66) is obtained by evaluating equation (2.67) at the seabed,

$z = -h$, and applying the kinematic seabed boundary condition (2.16) to give

$$p|_{-h} = \mu^2 \frac{\partial}{\partial t} \int_{-h}^{\epsilon\eta} w dz + \epsilon\mu^2 \frac{\partial}{\partial x} \int_{-h}^{\epsilon\eta} (uw) dz + \frac{H}{\epsilon} \tag{2.68}$$

In general, the trailing stress term, $-\epsilon\mu^2 w^2|_z$, drops out when evaluated at a material surface. The difference in pressure, $-\epsilon\mu^2 w^2|_z$, is merely a result of the vertical flux being measured through a horizontal plane in the coordinate reference system. In other words, if the flux is measured while traveling with a material surface, the additional stress is absent.

The pressure function (2.67) is substituted into the depth integrated horizontal momentum equation (2.66) to give the governing equations of motion

$$\frac{\partial}{\partial t} \int_{-h}^{\epsilon\eta} u dz + \epsilon \frac{\partial}{\partial x} \int_{-h}^{\epsilon\eta} \left(u^2 - \mu^2 w^2\right) dz + \frac{\partial}{\partial x} \left(\frac{H^2}{2\epsilon}\right) + \epsilon\mu^2 \frac{\partial}{\partial x} \int_{-h}^{\epsilon\eta} Q dz = \epsilon\mu^2 \frac{\partial h}{\partial x} Q|_{-h} + \frac{\partial h}{\partial x} \frac{H}{\epsilon} \tag{2.69}$$

in which

$$Q = \frac{1}{\epsilon} \frac{\partial}{\partial t} \int_{z}^{\epsilon\eta} w dz + \frac{\partial}{\partial x} \int_{z}^{\epsilon\eta} (uw) dz \tag{2.70}$$

Presented in this form, the exact equations of motion highly reflect those discussed in Longuet-Higgins and Stewart (1960) and Longuet-Higgins and Stewart (1964). If an analogy is made, $u^2 - \mu^2 w^2$ relates to a balance between horizontal and vertical Reynolds stress. In the shallow water limit ($\mu \to 0$), the $\mu^2 w^2$ term vanishes, the particle orbits become horizontal, and the integrand $u^2 - \mu^2 w^2$ reduces to twice the kinetic energy density, or the total energy density of the waves (Longuet-Higgins and Stewart 1964). Increasing the relative depth, the particle orbits become more circular and the stress eventually becomes isotropic. The point here is that by depth integrating the fully nonlinear Euler equations of motion in the derivation, a direct correspondence with the well established theory presented by Longuet-Higgins and Stewart (1960) and Longuet-Higgins and Stewart (1964) becomes more apparent.

Introducing the horizontal velocity approximation $u = u|_{z_\alpha} + \mu^2 u_\mu$ and isolating the dispersive terms gives

$$\begin{aligned} \frac{\partial H u|_{z_\alpha}}{\partial t} + \epsilon \frac{\partial H u|_{z_\alpha}^2}{\partial x} + \frac{\partial}{\partial x} \left(\frac{H^2}{2\epsilon}\right) - \frac{\partial h}{\partial x} \frac{H}{\epsilon} = \\ - \mu^2 \frac{\partial}{\partial t} \int_{-h}^{\epsilon\eta} u_\mu dz - \epsilon\mu^2 \frac{\partial}{\partial x} \int_{-h}^{\epsilon\eta} \left(2u|_{z_\alpha} u_\mu - w^2\right) dz - \epsilon\mu^2 \frac{\partial}{\partial x} \int_{-h}^{\epsilon\eta} Q \\ + \epsilon\mu^2 \frac{\partial h}{\partial x} Q|_{-h} + \psi_u + O(\mu^4) \end{aligned} \tag{2.71}$$

in which

$$Q = \frac{1}{\epsilon}\frac{\partial}{\partial t}\int_z^{\epsilon\eta} w dz + \frac{\partial}{\partial x}\int_z^{\epsilon\eta} (u|_{z_\alpha} w) dz \tag{2.72}$$

As was done with the continuity equation, a place holder, ψ_u, is introduced representing arbitrary momentum source terms. The expression on the left hand side of (2.71) matches, pending a change of reference, the conserved variable form of the NSWEs (see, e.g., George 2006). The form of the depth integrated momentum equation (2.71) will be utilized in the next section for verification purposes.

2.3.3 FUNWAVE Comparison

The Boussinesq-type model "FUNWAVE" is an open source state-of-the-art model implemented world-wide in practical application and endorsed by US Army Corps of Engineers. At present, the governing equations of "FUNWAVE" are based on those of Shi et al. (2012), which provide an alternative presentation of the fully nonlinear weakly dispersive equations of Kennedy et al. (2001) in conserved variable form. Although not explicitly addressed in this study, the conserved variable form fosters implementation of shock capturing methods as a means to approximate wave breaking, which has been addressed in previous studies (e.g., Tonelli and Petti 2009; Roeber et al. 2010; Roeber and Cheung 2012; Tissier et al. 2012; Shi et al. 2018). Theoretical consistency implies the quasi-2D equations of Shi et al. (2012) should formally match the governing equations derived herein when $\gamma = 0$ and the seabed is static, despite the difference in presentation.

The conserved variable form of the NSWEs has been utilized extensively in throughout the literature (e.g., Whitham 1974; M. B. Abbott 1979; LeVeque 1992; Toro 2009). The practical motivation is the ability to represent hydraulic jumps as viscous flow discontinuities, over which both volume and momentum are conserved. When applied in Boussinesq-type equations, the dispersion is locally removed and the flow discontinuity is resolved through the leading order conserved variable form of the NSWEs. This approach to serves as an alternative to the eddy viscosity and surface roller methods commonly used to approximate wave breaking (e.g., Zelt 1991; Kennedy et al. 2000; P. J. Lynett et al. 2002; Svendsen 1984; Schaffer et al. 1993; P. Madsen et al. 1997). Working with the governing equations of Nwogu (1993), Roeber et al. (2010) cast the governing equations into conserved form by making use of the product rule, which serves as an alternative method of derivation in comparison to the depth integration methods presented in the previous section. The strength of the former approach is that equations employing the depth averaged momentum are readily cast into conserved variable form with little effort, however the connection with the depth integrated approach is not readily apparent. To elaborate by example, the quasi-2D equations from George (2006) are expressed in dimensionless form under the current scaling arguments and still

water reference

$$\frac{\partial H}{\partial t}+\epsilon\frac{\partial Hu}{\partial x}=0 \tag{2.73}$$

$$\frac{\partial Hu}{\partial t}+\epsilon\frac{\partial Hu^2}{\partial x}+\frac{\partial}{\partial x}\left(\frac{H^2}{2\epsilon}\right)-\frac{\partial h}{\partial x}\frac{H}{\epsilon}=0 \tag{2.74}$$

in which $u=\overline{u}$ is the model velocity employed in the NSWEs. Applying the product rule to the first two terms in the momentum equation (2.74) gives the expansion

$$\frac{\partial Hu}{\partial t}+\epsilon\frac{\partial Hu^2}{\partial x}+\frac{\partial}{\partial x}\left(\frac{H^2}{2\epsilon}\right)-\frac{\partial h}{\partial x}\frac{H}{\epsilon}=u\left(\frac{\partial H}{\partial t}+\epsilon\frac{\partial Hu}{\partial x}\right)+H\left(\frac{\partial u}{\partial t}+\epsilon u\frac{\partial u}{\partial x}+\frac{\partial \eta}{\partial x}\right) \tag{2.75}$$

Comparing the terms in parenthesis on the right hand side to any primitive Boussinesq-type equation, it is observed that the corresponding continuity and momentum dispersion terms can be substituted in without loss.

The model velocity employed by Wei et al. (1995) is $u=u|_{z_\alpha}+\mu^2 u_\mu$, in which, $u=u|_{z_\alpha}$, is substituted into the left hand side of (2.73) and (2.75) for the leading order velocity. Substituting the $O(\mu^2)$ terms from the depth average momentum equation (2.43) and depth integrated continuity equation (2.57) into the right hand side gives

$$\frac{\partial H}{\partial t}+\epsilon\frac{\partial Hu|_{z_\alpha}}{\partial x}=-\epsilon\mu^2\frac{\partial H\overline{u_\mu}}{\partial x}+O(\mu^4) \tag{2.76}$$

$$\frac{\partial Hu|_{z_\alpha}}{\partial t}+\epsilon\frac{\partial Hu|_{z_\alpha}^2}{\partial x}+\frac{\partial}{\partial x}\left(\frac{H^2}{2\epsilon}\right)-\frac{\partial h}{\partial x}\frac{H}{\epsilon}=u|_{z_\alpha}\left(\frac{\partial H}{\partial t}+\epsilon\frac{\partial Hu|_{z_\alpha}}{\partial x}\right)-H\left(\mu^2V_1+\epsilon\mu^2V_2\right)+O(\mu^4) \tag{2.77}$$

in which (2.76) and the left hand side of (2.77) match those of the new conserved model derived herein. Formally, (2.76) and (2.77) should give the quasi-2D governing equations of Shi et al. (2012). Since terms $V1$ and $V2$, defined in (2.44) and (2.45) respectively, have already been verified, the goal here is to verify the momentum equation (2.71) derived following the depth integrated approach in the previous section, which is clearly expressed in an alternative form.

The terms $V1$ and $V2$ on the right hand side of (2.77) are independent of the z-coordinate, thus can be expressed as an integral over the flow depth

$$-\mu^2HV_1=-\mu^2\int_{-h}^{\epsilon\eta}\left(\frac{\partial}{\partial t}\left(u_\mu+\int_z^{\epsilon\eta}\frac{\partial w}{\partial x}dz\right)+\frac{\partial}{\partial t}\left(\frac{\partial \epsilon\eta}{\partial x}w|_{\epsilon\eta}\right)-\frac{\partial}{\partial x}\left(\frac{\partial \epsilon\eta}{\partial t}w|_{\epsilon\eta}\right)\right)dz \tag{2.78}$$

$$-\epsilon\mu^2HV_2=-\epsilon\mu^2\int_{-h}^{\epsilon\eta}\left(\frac{\partial}{\partial x}\left(u|_{z_\alpha}\left(u_\mu+\int_z^{\epsilon\eta}\frac{\partial w}{\partial x}dz\right)\right)+\frac{\partial}{\partial x}\int_z^{\epsilon\eta}w\frac{\partial w}{\partial z}dz+w\frac{\partial w}{\partial x}\right)dz \tag{2.79}$$

Derivatives in the second term of (2.78) are interchanged through the application of the Leibniz

integration rule (B), which also removes the trailing boundary terms to give

$$-\mu^2 HV_1 = -\mu^2 \int_{-h}^{\epsilon\eta} \left(\frac{\partial u_\mu}{\partial t} dz + \frac{\partial}{\partial x} \int_z^{\epsilon\eta} \frac{\partial w}{\partial t} dz \right) dz \tag{2.80}$$

The full expression for $-H(\mu^2 V_1 + \epsilon\mu^2 V_2)$ is thus given by

$$-\epsilon\mu^2 \int_{-h}^{\epsilon\eta} \left(\frac{1}{\epsilon} \frac{\partial u_\mu}{\partial t} + \frac{\partial u|_{z_\alpha} u_\mu}{\partial x} + w \frac{\partial w}{\partial x} + \frac{\partial}{\partial x} \int_z^{\epsilon\eta} \left(\frac{1}{\epsilon} \frac{\partial w}{\partial t} + u|_{z_\alpha} \frac{\partial w}{\partial x} + w \frac{\partial w}{\partial z} \right) dz \right) dz \tag{2.81}$$

The expression is split up for evaluation, focusing first on the interior integral over an arbitrary depth. Applying the Leibniz integration rule (B) to pull out the spatial derivative gives

$$-\epsilon\mu^2 \frac{\partial}{\partial x} \int_{-h}^{\epsilon\eta} F + \epsilon\mu^2 \frac{\partial h}{\partial x} F|_{-h} + \epsilon\mu^2 \frac{\partial \epsilon\eta}{\partial x} F|_{\epsilon\eta} \tag{2.82}$$

in which

$$F = \int_z^{\epsilon\eta} \left(\frac{1}{\epsilon} \frac{\partial w}{\partial t} + u|_{z_\alpha} \frac{\partial w}{\partial x} + w \frac{\partial w}{\partial z} \right) dz \tag{2.83}$$

Clearly, the last term in (2.82) is equal to zero. The product rule is applied to the last two terms, in which the continuity equation is then applied to the latter term. Since (2.82) is already $O(\mu^2)$, terms of $O(\mu^2)$ are dropped, which leads to a cancellation in the former term. Further application of the Leibniz integration rule (B) and kinematic free-surface boundary condition (2.15) reduces (2.82) to

$$-\epsilon\mu^2 \frac{\partial}{\partial x} \int_{-h}^{\epsilon\eta} Q dz + \epsilon\mu^2 \frac{\partial}{\partial x} \int_{-h}^{\epsilon\eta} w^2 dz + \epsilon\mu^2 \frac{\partial h}{\partial x} Q|_{-h} \tag{2.84}$$

in which

$$Q = \frac{1}{\epsilon} \frac{\partial}{\partial t} \int_z^{\epsilon\eta} w dz + \frac{\partial}{\partial x} \int_z^{\epsilon\eta} (u|_{z_\alpha} w) dz \tag{2.85}$$

The expression for Q is identical to definition (2.72) given prior.

The remaining terms in (2.81) are now addressed. To the third term, the irrotational condition is applied and expanded using the product rule. Substituting the expansion $u = u|_{z_\alpha} + \mu^2 u_\mu$ reveals that only the $\mu^2 u_\mu$ terms are retained. Carrying out the integration, applying the continuity equation, and truncating $O(\mu^4)$ terms gives

$$-\epsilon\mu^2 \int_{-h}^{\epsilon\eta} u_\mu \frac{\partial u|_{z_\alpha}}{\partial x} - \epsilon\mu^2 (u_\mu w)|_{\epsilon\eta} + \epsilon\mu^2 (u_\mu w)|_{-h} \tag{2.86}$$

Upon applying the Leibniz integration rule (B) to the first two terms in (2.81), it is found that the trailing boundary terms in (2.86) cancel due to the kinematic surface boundary conditions. The overall last term to address is the leading expression on the right hand side of (2.77), which is the continuity dispersion terms on the right hand side of (2.76) by definition. Applying the product rule results in a cancellation of the first term in (2.86), leaving a single advection term. Collecting the remaining terms and adding them to (2.84) gives

$$-\mu^2\frac{\partial}{\partial t}\int_{-h}^{\epsilon\eta} u_\mu dz - \epsilon\mu^2\frac{\partial}{\partial x}\int_{-h}^{\epsilon\eta}\left(2u|_{z_\alpha}u_\mu - w^2\right)dz - \epsilon\mu^2\frac{\partial}{\partial x}\int_{-h}^{\epsilon\eta} Q dz + \epsilon\mu^2\frac{\partial h}{\partial x}Q|_{-h} \tag{2.87}$$

which is identical to expression on the right hand side of (2.71), thus verifying the conserved set of equations. It is therefore deduced that for $\gamma = 0$ and a static seabed, the new conserved model derived herein should be formally equivalent to the governing equations employed by Shi et al. (2012).

In the derivation by Shi et al. (2012), the model velocity used in (2.73) and (2.74) is $u = \overline{u} = u|_{z_\alpha} + \mu^2\overline{u_\mu}$, which is perfectly valid. Following the expansion, this implies that the right hand side of (2.76), as well as the leading set of terms on right hand side of (2.77), would be $O(\mu^4)$, which are then absorbed into the truncation error. Therefore, only the trailing set of terms on the right hand side of (2.77) is of concern for the model velocity used by Shi et al. (2012). Again, it is emphasized that the left hand side would be in terms of $\overline{u}$, not $u|_{z_\alpha}$, as shown in (2.76) and (2.77) above. Upon reviewing equation (17) for the quasi-2D case in Shi et al. (2012), the only discrepancy found appears to be the presence of an $O(\mu^4)$ term in the nonlinear advection, which should be dropped to be consistent with the order of approximation. The $O(\mu^4)$ terms are correctly removed on the right hand side, but not the left. It is worth pointing out, that even if the $O(\mu^4)$ terms associated with the nonlinear advection on the right hand side were retained, as a means to correct those on the left, the equation would still be $O(\mu 4)$ because of the fact that the leading set of terms on right hand side of (2.77) cancel due to the continuity equation. This is a result of the product rule used in expansion (2.75) and highlights the importance of confirming the order of approximation on both sides of the equation. After personal communication with the authors, it has been confirmed that the $O(\mu^4)$ terms associated with the nonlinear advection should have been dropped in Shi et al. (2012) to match those in (2.71), which are $O(\mu^2)$. Therefore, the equations of Shi et al. (2012), upon correction, do agree with those derived herein.

Having verified the governing equations in conserved form, assuming $\gamma = 0$ and a static seabed, with the quasi-2D governing equations of Shi et al. (2012), it can be concluded, by extension, that the governing equations derived herein recover those of Shi et al. (2012), Kennedy et al. (2001), Wei et al. (1995), and Nwogu (1993) under the appropriate assumptions. Relaxing the assumption of a static seabed to include slowly varying seabed deformations further extends the datum invariant

fully nonlinear, weakly dispersive equations in terms of conserved variables. The most fundamental contribution is achieved when $\gamma \neq 0$, which leads to additional nonlinear terms from an expansion about the the free-surface. Herein, focus is directed on the particular case $\gamma = \beta$, in which the weight is governed by the datum invariant reference. To close out this chapter, the governing equations derived herein are gathered and presented collectively. Applying some minor simplifications, the continuity and equations of motion are restated as

$$\frac{\partial H}{\partial t} + \epsilon \frac{\partial H\overline{u}}{\partial x} = \psi_\eta + O(\mu^4) \tag{2.88}$$

$$\frac{\partial H\overline{u}}{\partial t} + \epsilon \frac{\partial}{\partial x}\left(H\overline{u_*^2} + \frac{H^2}{2\epsilon^2} + S\right) = \frac{\partial h}{\partial x}\left(\frac{H}{\epsilon} + \mu^2 Q|_{-h}\right) + \psi_u + O(\mu^4) \tag{2.89}$$

in which

$$H = \epsilon\eta + h_s + \delta h_d \tag{2.90}$$

$$\overline{u} = u|_{z_\alpha} + \mu^2 \overline{u_\mu} \tag{2.91}$$

$$\overline{u_*^2} = u|_{z_\alpha}^2 + 2\mu^2 u|_{z_\alpha}\overline{u_\mu} \tag{2.92}$$

$$S = \mu^2 H\left(\overline{Q} - \overline{w^2}\right) \tag{2.93}$$

$$Q|_{-h} = \frac{\partial H\overline{w}}{\partial t} + \epsilon \frac{\partial H u|_{z_\alpha}\overline{w}}{\partial x} \tag{2.94}$$

$$Q = \frac{1}{\epsilon}\frac{\partial}{\partial t}\int_z^{\epsilon\eta} w dz + \frac{\partial}{\partial x}\int_z^{\epsilon\eta} (u|_{z_\alpha} w) dz \tag{2.95}$$

$$\begin{aligned}\overline{u_\mu} =& H\left(\beta - \frac{1}{2}\right)\left(\frac{\partial h}{\partial x}\frac{\partial u|_{z_\alpha}}{\partial x} + \frac{\partial}{\partial x}\left(u|_{z_\alpha}\frac{\partial h}{\partial x}\right)\right) + H^2\frac{1}{2}\left(\beta^2 - \frac{1}{3}\right)\frac{\partial^2 u|_{z_\alpha}}{\partial x^2} \\ &+ H\left(\beta - \frac{1}{2}\right)\frac{\delta}{\epsilon}\frac{\partial^2 h_d}{\partial t \partial x} - \gamma H\left(\beta - \frac{1}{2}\right)\frac{\partial^2}{\partial x^2}\left(\delta h_d u|_{z_\alpha} + \epsilon\eta u|_{z_\alpha}\right)\end{aligned} \tag{2.96}$$

$$\overline{w} = -\left(\frac{\delta}{\epsilon}\frac{\partial h_d}{\partial t} + \frac{\partial h u|_{z_\alpha}}{\partial x}\right) - \frac{\epsilon\eta - h}{2}\frac{\partial u|_{z_\alpha}}{\partial x} + \gamma\frac{\partial}{\partial x}\left(\delta h_d u|_{z_\alpha} + \epsilon\eta u|_{z_\alpha}\right) \tag{2.97}$$

For a flat bottom, equations (2.88) and (2.89) mirror those found in Whitham (1974), where S would be the radiation stress (Longuet-Higgins and Stewart 1960), which is proportional to the energy density and scaled by a function of the group and phase speeds. Although the energy density, group speed, and phase speed are not immediately apparent in the definition of S above, the form of (2.89) is very appealing in that it implies, by analogy, a conservation of momentum over a flat bottom. A vivid account of the radiation stress is imperceptible in the Boussinesq-type formulations reviewed herein. The ability to explicitly quantify the radiation stress in a phase resolving manner would be of value in applications focused on the study of high order coastal processes like wave setup and surf beat. Over a static seabed, with $\gamma = 0$, equations (2.88) and (2.89) have been verified on multiple levels with those from Wei et al. (1995), which clearly proves that the vector velocity and scalar

potential approaches give the same formal set of equations, albeit presented in different form. As a fundamental contribution, the additional nonlinear terms in the velocity profile, capturing the material surface curvature, extending the Padé [2/2] family of equations. The $O(\mu^2)$ continuity (2.88) and equation of motion (2.89) are presented as functions of two unknowns, $\epsilon\eta$ and $u|_{z_\alpha}$, with forced slowing varying seabed deformations through h_d, thus close the fully nonlinear, weakly dispersive, governing system of equations. In the next chapter, linear properties are examined to facilitate analysis of the corresponding numerical implementation. For clarity in presentation, $O(\mu^4)$ terms are dropped, with it being understood that the equations are in fact approximations. Furthermore, having established the model velocity, $u|_{z_\alpha}$, the notation $u \equiv u|_{z_\alpha}$ will be utilized hereafter to represent the model velocity, where it is important to acknowledge that the model velocity is not a function of depth.

CHAPTER 3
THEORETICAL DISPERSION

The fully nonlinear, weakly dispersive, Boussinesq-type equations derived in the previous chapter include a single parameter, β, which (1) locates the datum invariant reference within the water column and (2) due to the assumption $\gamma = \beta$ in the nonlinear enhancement, serves as a weight factor coupling the series expansions at the seabed and free-surface. The degree of freedom establishes a family of equations, which encapsulates other theories found in the literature (e.g., Peregrine 1967; Nwogu 1993; Wei et al. 1995; Kennedy et al. 2001). In this chapter, the single parameter family is extended to a three parameter family by invoking linear leading order substitutions. As a result, $O(\mu^2)$ effects are distributed among the dependent variables, thereby further enhancing the system of equations with two additional degrees of freedom. The resulting set of equations is shown to be unique among those found in the literature due the relaxation of the static seabed assumption. The three parameter family in Section 3.1 marks the conclusion of theoretical developments performed herein and a transition to studying the role of numerical dispersion begins.

Central to this study is the development of tools which quantify numerical limitations and convey those to the community in a clear concise manner in order to minimize false interpretations in practical application. The remaining sections of this chapter establish a theoretical foundation on frequency dispersion, which serves as a leading order linear performance metric. Being a linear property, the governing equations are linearized and cast into spectral space using Fourier-Laplace transforms, in which the fundamental nature of frequency dispersion is shown. Analytic solutions of the three parameter family are then derived to facilitate subsequent validation of the numerical analysis. Above all, the analysis serves as the basis of future chapters focusing on numerical dispersion, where the discretization introduces modified spectral variables which take on the role of their continuous counterparts.

3.1 Three Parameter Family

One of the well known properties of Boussinesq-type equations is that leading order linear substitutions can be made into $O(\mu^2)$ terms without altering the formal order of approximation (e.g., Long 1964; Benjamin et al. 1972; Peregrine 1974; J. L. Bona and Smith 1976). For clarity, the enhancement is performed on the linearized ($\epsilon \to 0, \delta \to 0$) set of governing equations, which can easily be recovered by adding the nonlinear $O(\epsilon, \epsilon\mu^2)$ terms to the enhanced equations. In the current set of equations, the $O(\mu^2)$ effects are only associated with the model horizontal velocity

variable. Using leading order linear substitutions, the $O(\mu^2)$ effects are distributed to include potential effects which manifest through the free-surface variable. This leads to a three-parameter family of equations that can be optimized for selected properties, such as frequency dispersion. The three-parameter family of equations is compared with others found in the literature, which assume either a static seabed (Schaffer and P. A. Madsen 1995b) or lack the processes of linear shoaling (M. Chen 2003). The comparison not only emphasizes uniqueness of the equations derived herein, it also helps bridge the gap between pursuits in the study of Boussinesq-type equations carried out by coastal engineers and mathematicians.

3.1.1 Linearization

The continuity (2.88) and momentum (2.89) equations are linearized to give

$$\frac{\partial \eta}{\partial t} + \frac{\partial h_s u}{\partial x} + \mu^2 \frac{\partial \mathcal{L}\left(H\overline{u_\mu}\right)}{\partial x} = -\frac{\delta}{\epsilon}\frac{\partial h_d}{\partial t} + \psi_\eta \tag{3.1}$$

$$h_s \frac{\partial u}{\partial t} + h_s \frac{\partial \eta}{\partial x} + \mu^2 \frac{\partial \mathcal{L}\left(H\overline{u_\mu}\right)}{\partial t} + \mu^2 \frac{\partial}{\partial x}\int_{-h_s}^{0}\left(\frac{\partial}{\partial t}\int_z^0 \mathcal{L}\left(w\right)dz\right)dz = \mu^2 \frac{\partial h_s}{\partial x}\frac{\partial \mathcal{L}\left(H\overline{w}\right)}{\partial t} + \psi_u \tag{3.2}$$

where the operator $\mathcal{L}\left(\right)$, which casts function arguments into linear form, has been introduced for clarity. The linear expansions are given by

$$\mathcal{L}\left(H\overline{u_\mu}\right) = \int_{-h_s}^{0}\mathcal{L}\left(u_\mu\right)dz = \int_{-h_s}^{0}\left(\int_{z_\alpha}^{z}\frac{\partial \mathcal{L}\left(w\right)}{\partial x}dz\right)dz = h_s^2\left(\beta - \frac{1}{2}\right)\left(\mathcal{A} + \frac{\delta}{\epsilon}\mathcal{C}\right) + h_s^3\frac{1}{2}\left(\beta^2 - \frac{1}{3}\right)\mathcal{B} \tag{3.3}$$

$$\mathcal{L}\left(H\overline{w}\right) = \int_{-h_s}^{0}\mathcal{L}\left(w\right)dz = -h_s\left(\frac{\delta}{\epsilon}\frac{\partial h_d}{\partial t} + \frac{\partial h_s u}{\partial x}\right) + \frac{h_s^2}{2}\frac{\partial u}{\partial x} \tag{3.4}$$

in which

$$\mathcal{A} = \frac{\partial h_s}{\partial x}\frac{\partial u}{\partial x} + \frac{\partial}{\partial x}\left(u\frac{\partial h_s}{\partial x}\right) \tag{3.5}$$

$$\mathcal{B} = \frac{\partial^2 u}{\partial x^2} \tag{3.6}$$

$$\mathcal{C} = \frac{\partial^2 h_d}{\partial t \partial x} \tag{3.7}$$

Substituting (3.3) into the linearized continuity equation (3.1) gives the trivial expansion

$$\begin{aligned}\frac{\partial \eta}{\partial t} + \frac{\partial h_s u}{\partial x} + \mu^2 \frac{\partial}{\partial x}\left(h_s^2\left(\beta - \frac{1}{2}\right)\mathcal{A} + h_s^3\frac{1}{2}\left(\beta^2 - \frac{1}{3}\right)\mathcal{B}\right) = \\ -\frac{\delta}{\epsilon}\frac{\partial h_d}{\partial t} + \mu^2\frac{\delta}{\epsilon}\frac{\partial}{\partial x}\left(h_s^2\left(\beta - \frac{1}{2}\right)\mathcal{C}\right) + \psi_\eta\end{aligned} \tag{3.8}$$

in which the processes of linear frequency dispersion and shoaling are coupled in the flux terms. The processes can be decoupled and isolated by applying the product rule; however, the conserved form is abandoned.

In the linearized momentum equation (3.2), the double integral can be resolved by employing various methods. The most direct method involves application of the Leibniz integration rule (B) in order to push the spatial derivative operator inside the outer most integral. Substituting the integral form of $\mathcal{L}\left(H\overline{w}\right)$ defined by (3.4), it is clear that the seabed source term on the right hand side drops out. In the remaining term, the limits of integration are not functions of time; therefore, the temporal derivative operator is pulled out in front of the outer integral. Likewise, the inner integral is not a function of space; therefore, the spatial derivative operator can be pushed inside the inner integral. Substituting the integral form of $\mathcal{L}\left(H\overline{u_\mu}\right)$ from (3.3) gives

$$h_s\frac{\partial u}{\partial t}+h_s\frac{\partial \eta}{\partial x}+\mu^2\frac{\partial}{\partial t}\int_{-h_s}^{0}\left(\int_{z_\alpha}^{z}\frac{\partial\mathcal{L}\left(w\right)}{\partial x}dz+\int_{z}^{0}\frac{\partial\mathcal{L}\left(w\right)}{\partial x}dz\right)dz=\psi_u \tag{3.9}$$

in which the two integrals are combined and the integration is carried out to give

$$h_s\frac{\partial u}{\partial t}+h_s\frac{\partial \eta}{\partial x}+\mu^2\frac{\partial}{\partial t}\left(h_s^2\left(\beta-1\right)\mathcal{A}+h_s^3\frac{1}{2}\left(\beta^2-1\right)\mathcal{B}\right)=-\mu^2\frac{\delta}{\epsilon}\frac{\partial}{\partial t}\left(h_s^2\left(\beta-1\right)\mathcal{C}\right)+\psi_u \tag{3.10}$$

An alternative method, which arrives at the same solution above, is to carry out the integration in (3.2) explicitly. The double integral gives

$$\mu^2\frac{\partial}{\partial x}\int_{-h_s}^{0}\left(\frac{\partial}{\partial t}\int_{z}^{0}\mathcal{L}\left(w\right)dz\right)dz=-\mu^2\frac{\partial}{\partial x}\left(h_s^2g(t,x)\right) \tag{3.11}$$

in which

$$g(t,x)=\frac{1}{2}\left(\frac{\delta}{\epsilon}\frac{\partial^2 h_d}{\partial t^2}+\frac{\partial^2 h_s u}{\partial t\partial x}\right)-\frac{h_s}{6}\frac{\partial^2 u}{\partial t\partial x} \tag{3.12}$$

Applying the product rule to decouple the flux terms on the right hand side of (3.11) to isolate the gradient of the seabed gives

$$\frac{\partial}{\partial x}\left(h_s^2g(t,x)\right)=2h_s\frac{\partial h_s}{\partial x}g(t,x)+h_s^2\frac{\partial g}{\partial x} \tag{3.13}$$

Distributing the difference operator over $g(t,x)$ and applying the product rule to the last term,

again, to isolate the gradient of the seabed, gives the double integral as

$$\begin{aligned}\mu^2\frac{\partial}{\partial x}\int_{-h_s}^{0}\left(\frac{\partial}{\partial t}\int_{z}^{0}\mathcal{L}\left(w\right)dz\right)dz = &-\mu^2\frac{\partial h_s}{\partial x}\frac{\partial}{\partial t}\left(h_s\left(\frac{\delta}{\epsilon}\frac{\partial h_d}{\partial t}+\frac{\partial h_s u}{\partial x}\right)-\frac{h_s^2}{2}\frac{\partial u}{\partial x}\right)\\ &-\mu^2\frac{\partial}{\partial t}\left(h_s^2\frac{1}{2}\left(\mathcal{A}+\frac{\delta}{\epsilon}\mathcal{C}\right)+h_s^3\frac{1}{3}\mathcal{B}\right)\end{aligned} \tag{3.14}$$

On the right hand side, the first set of terms cancels with $\mu^2\mathcal{L}\left(H\overline{w}\right)_t$ and the last set of terms combines with $\mu^2\mathcal{L}\left(H\overline{u_\mu}\right)_t$ to give the expression in (3.10) found above. While more tedious, the method gives a detailed breakdown of the linear $O(\mu^2)$ momentum flux term into its constituents. Having already decoupled the momentum flux, isolating terms associated with dispersion and shoaling is trivial, in which $-\mu^2 h_s^3(1/3)\mathcal{B}_t$ is purely dispersive, while the rest involve derivatives of the seabed.

3.1.2 Linear Enhancement

At the leading order ($\mu^2 \to 0$), the linearized continuity (3.1) and momentum (3.2) equations reduce to

$$\frac{\partial \eta}{\partial t}+\frac{\partial h_s u}{\partial x} = -\frac{\delta}{\epsilon}\frac{\partial h_d}{\partial t} \tag{3.15}$$

$$\frac{\partial u}{\partial t}+\frac{\partial \eta}{\partial x} = 0 \tag{3.16}$$

which can be utilized to distribute the $O(\mu^2)$ effects among the dependent variables in both the continuity and momentum equations (e.g., P. A. Madsen et al. 1991; P. A. Madsen and Sorensen 1992; Beji and Nadaoka 1996; Schaffer and P. A. Madsen 1995b; Bona et al. 2002).

Applying the operator ∂_x to the leading order linear continuity equation (3.15) and the operator ∂_{xx} to the leading order linear momentum equation (3.16) gives

$$h_s\mathcal{B} = -\left(\mathcal{A}+\frac{\delta}{\epsilon}\mathcal{C}+\frac{\partial^2\eta}{\partial t\partial x}\right) \tag{3.17}$$

$$\frac{\partial \mathcal{B}}{\partial t} = -\frac{\partial^3\eta}{\partial x^3} \tag{3.18}$$

in which the substitution $(h_s u)_{xx} = \mathcal{A}+h_s\mathcal{B}$ was made in the continuity equation. Applying the expansion $f = (1-\Lambda)f+\Lambda f$ to $f \in \{hs\mathcal{B}, \mathcal{B}_t\}$ then substituting (3.17) and (3.18) into the respective

trailing term, Λf ,the following equations are introduced without loss

$$h_s\mathcal{B} = (1-\Lambda_1)h_s\mathcal{B} - \Lambda_1\left(\mathcal{A} + \frac{\delta}{\epsilon}\mathcal{C} + \frac{\partial^2\eta}{\partial t\partial x}\right) \tag{3.19}$$

$$\frac{\partial\mathcal{B}}{\partial t} = (1-\Lambda_2)\frac{\partial\mathcal{B}}{\partial t} - \Lambda_2\frac{\partial^3\eta}{\partial x^3} \tag{3.20}$$

in which $\Lambda_n \in \mathbb{R}$ for $n \in \{1,2\}$ are free parameters. The equations above are substituted into (3.8) and (3.10) to give

$$\begin{aligned}\frac{\partial\eta}{\partial t} + \frac{\partial h_s u}{\partial x} - \mu^2\frac{\partial}{\partial x}\left(\sigma_1 h_s^2\frac{\partial^2\eta}{\partial t\partial x}\right) + \mu^2\frac{\partial}{\partial x}\left(\nu_1 h_s^2\mathcal{A} - \sigma_2 h_s^3\mathcal{B}\right) = \\ -\frac{\delta}{\epsilon}\left(\frac{\partial h_d}{\partial t} + \mu^2\frac{\partial}{\partial x}\left(\nu_1 h_s^2\mathcal{C}\right)\right) + \psi_\eta\end{aligned} \tag{3.21}$$

$$\frac{\partial u}{\partial t} + \frac{\partial\eta}{\partial x} + \mu^2\frac{\partial}{\partial t}\left(h_s\nu_2\mathcal{A} - \sigma_3 h_s^2\mathcal{B}\right) - \mu^2\sigma_4 h_s^2\frac{\partial^3\eta}{\partial x^3} = -\mu^2\frac{\delta}{\epsilon}\frac{\partial}{\partial t}\left(h_s\nu_2\mathcal{C}\right) + \psi_u \tag{3.22}$$

in which

$$\sigma_1 = \frac{1}{2}\left(\beta^2 - \frac{1}{3}\right)\Lambda_1 \tag{3.23}$$

$$\sigma_2 = -\left(\frac{1}{2}\left(\beta^2 - \frac{1}{3}\right)(1-\Lambda_1)\right) = -\left(\frac{1}{2}\left(\beta^2 - \frac{1}{3}\right) - \sigma_1\right) \tag{3.24}$$

$$\sigma_3 = -\left(\frac{1}{2}\left(\beta^2 - 1\right)(1-\Lambda_2)\right) = -\left(\frac{1}{2}\left(\beta^2 - 1\right) - \sigma_4\right) \tag{3.25}$$

$$\sigma_4 = \frac{1}{2}\left(\beta^2 - 1\right)\Lambda_2 \tag{3.26}$$

$$\nu_1 = \left(\beta - \frac{1}{2}\right) - \frac{1}{2}\left(\beta^2 - \frac{1}{3}\right)\Lambda_1 = \left(\beta - \frac{1}{2}\right) - \sigma_1 \tag{3.27}$$

$$\nu_2 = \beta - 1 \tag{3.28}$$

The $O(\mu^2)$ linearized continuity (3.21) and momentum (3.22) equations represent a three-parameter $\{\beta, \Lambda_1, \Lambda_2\}$ family of equations which support linear dispersion, shoaling, and seabed deformations.

Variants of the three-parameter family have been studied in the literature, which warrants digression. In the first case, a static seabed, $\partial_t h_d = 0$, is assumed, in which $h_s \equiv h$ simplifies notation. Substituting $\sigma_1 = \boldsymbol{\beta}_1 - \boldsymbol{\beta}_2$ into (3.21), $\sigma_4 = \boldsymbol{\gamma}_1 - \boldsymbol{\gamma}_2$ into (3.22), and applying the linear expansion

of the reference $\beta = z_\alpha/h + 1$ gives

$$\frac{\partial \eta}{\partial t} + \frac{\partial hu}{\partial x} + \mu^2 \frac{\partial}{\partial x}\left(\left(\frac{z_\alpha^2}{2} - \frac{h^2}{6}\right) h \frac{\partial^2 u}{\partial x^2} + \left(z_\alpha + \frac{h}{2} - \boldsymbol{\beta}_1 h\right) h \frac{\partial^2 hu}{\partial x^2}\right) + \mu^2 \frac{\partial}{\partial x}\left(\boldsymbol{\beta}_2 \frac{\partial}{\partial x}\left(h^2 \frac{\partial hu}{\partial x}\right) - \boldsymbol{\beta}_1 h^2 \frac{\partial^2 \eta}{\partial t \partial x} + \boldsymbol{\beta}_2 \frac{\partial}{\partial x}\left(h^2 \frac{\partial \eta}{\partial t}\right)\right) = 0 \tag{3.29}$$

$$\frac{\partial u}{\partial t} + \frac{\partial \eta}{\partial x} + \mu^2 \left(\left(\frac{z_\alpha^2}{2} - \boldsymbol{\gamma}_1 h^2\right) \frac{\partial^3 u}{\partial t \partial x^2} + (z_\alpha + \boldsymbol{\gamma}_2 h) \frac{\partial^3 hu}{\partial t \partial x^2}\right) - \mu^2 \left(\boldsymbol{\gamma}_1 h^2 \frac{\partial^3 \eta}{\partial x^3} - \boldsymbol{\gamma}_2 h \frac{\partial^2}{\partial x^2}\left(h \frac{\partial \eta}{\partial x}\right)\right) = 0 \tag{3.30}$$

These are the linear quasi-2D equations derived by Schaffer and P. A. Madsen (1995b) in which $\{\boldsymbol{\beta}, \boldsymbol{\gamma}\} \equiv \{\sigma_1, \sigma_4\}$ gives an equivalence in notation. Depending on the approach to deriving (3.29), the following expression emerges

$$\mu^2 \frac{\partial}{\partial x}\left(\boldsymbol{\beta}_2 2h \frac{\partial h}{\partial x}\left(\frac{\partial \eta}{\partial t} + \frac{\partial hu}{\partial x}\right)\right) \tag{3.31}$$

which upon substitution of the leading order continuity equation, is equivalent to zero. This emphasizes an important feature of the enhancement technique, regardless of approach. In Schaffer and P. A. Madsen (1995b), $O(\mu^2)$ operators are introduced and applied to the $O(\mu^2)$ governing equations. Due to truncation at $O(\mu^4)$, the operators only act on the leading order terms. Therefore, when added to the $O(\mu^2)$ governing equations, it is no different than adding zero, in which the same can be said herein with the introduction of Λ_n as free parameters. In either approach, the objective is to redistribute the $O(\mu^2)$ effects in a conserved manner. To use an analogy; the shape of the curve can change as long as the area under it remains unity. A thorough discussion can be found in the series of work by Schaffer and P. A. Madsen (1998), Beji and Nadaoka (1998), and Schaffer and P. A. Madsen (1999), in which the latter acknowledges the flexibility in defining the distributions.

Another line of pursuit led by mathematicians can be found in the literature (e.g., J. L. Bona and M. Chen 1998; Bona et al. 2002; M. Chen 2003). Herein, the seabed is defined by an expression of the form $h'(t,x) = h'_s(x) + h'_d(t,x)$; however, it is also possible to define the seabed as $h'(t,x) = \overline{h'} + h'_d(t,x)$, where $\overline{h'}$ is the mean seabed level, and assume $\overline{h'} = h_c$ without loss (M. Chen 2003). In dimensionless form, the seabed is $h(t,x) = 1 + \delta h_d(t,x)$, which implies $h_s(x) = 1$ herein. This change in perspective has a dramatic impact on the linear equations. Substituting $h_s(x) = 1$ and $\Lambda_1 = (1 - \Lambda_1)$ into the linearized continuity (3.21) and momentum (3.22) equations, followed by a

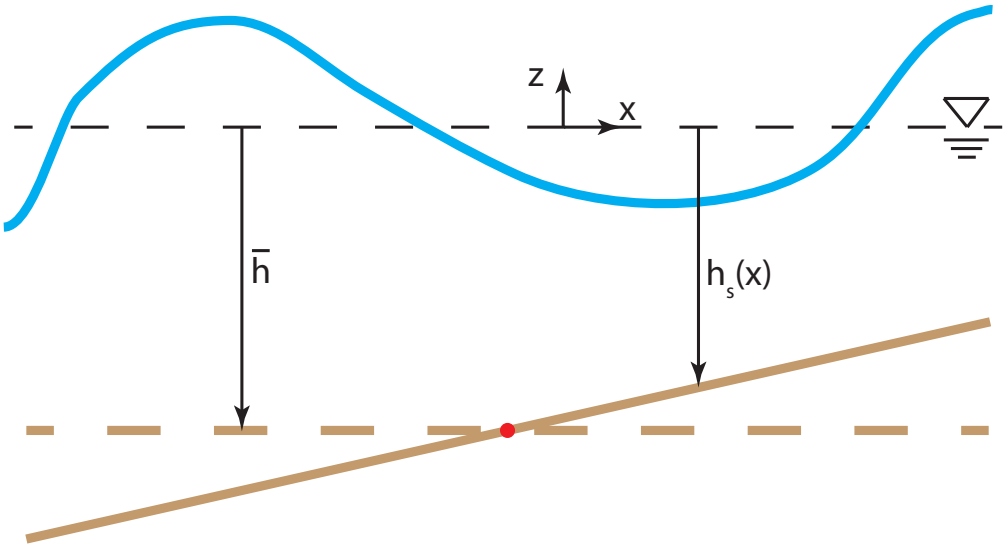

Figure 3.1: Instantaneous sketch depicting a free-surface wave propagating over a static, spatially varying, seabed with the brown dashed line denoting the mean level.

change in notation $\{\sigma_1, -\sigma_2, -\sigma_4, \sigma_3\,\beta, \Lambda_1, \Lambda_2\} \equiv \{a, b, c, d, \theta, \lambda, \mu\}$, gives

$$\frac{\partial \eta}{\partial t} + \frac{\partial u}{\partial x} + \mu^2 a \frac{\partial^3 u}{\partial x^3} - \mu^2 b \frac{\partial^3 \eta}{\partial t \partial x^2} = -\frac{\delta}{\epsilon}\frac{\partial h_d}{\partial t} + \mu^2 \frac{\delta}{\epsilon}\frac{1}{2}\left(\left(\theta^2 - \frac{1}{3}\right)(1-\lambda) - 2\theta + 1\right)\frac{\partial^3 h_d}{\partial t \partial x^2} \tag{3.32}$$

$$\frac{\partial u}{\partial t} + \frac{\partial \eta}{\partial x} + \mu^2 c \frac{\partial^3 \eta}{\partial x^3} - \mu^2 d \frac{\partial^3 u}{\partial t \partial x^2} = \mu^2 \frac{\delta}{\epsilon}(1-\theta)\frac{\partial^3 h_d}{\partial t^2 \partial x} \tag{3.33}$$

which are the linearized equations of M. Chen (2003) for Boussinesq-type equations over an uneven seabed. The most striking observation is that shoaling is not accounted for in linear equations of M. Chen (2003) due to the definition of the seabed. Upon linearization, the definition reduces to a mean level (normalized to unity), which is equivalent to assuming a flat seabed, hence why the coefficients associated with the dispersion and forcing terms are consistent with those herein. Figure 3.1 assumes a static, but spatially varying seabed, in which incident linear waves are known to shoal over the slope (e.g., Dean and Dalrymple 1991). In application of (3.32) and (3.33), clearly derivatives of the seabed drop out due to the static assumption, leaving the same linear equations used over a flat seabed (e.g., Bona et al. 2002). Therefore, a hydrodynamic shoaling response of the waves traveling over the slope in Figure 3.1 would be lacking in the linear formulation of M. Chen (2003). Shoaling would only be accounted for in the linear equations of M. Chen (2003) if the mean seabed level exhibits spatial dependency (i.e. a local mean); however, spatial dependency of the mean is not included in the formulation. Nevertheless, Figure 3.1 shows that a change in slope can occur independent of the mean, which would lead to a change in the shoaling response. Taking into consideration that shoaling processes are not explicitly discussed in M. Chen (2003), it is evident that the equations therein are catered to processes other than shoaling, thus highlighting that the

equations derived herein are in fact unique.

3.2 Frequency Dispersion

In a phase resolving model, the ability to accurately predict the wave phase is paramount. At the leading order, frequency dispersion processes are isolated for independent evaluation by assuming a static ($\partial_t h_d = 0$) and flat ($\partial_x h = 0$) seabed in the linear formulation. Under the given assumptions, the notation for the seabed is simplified to $h \equiv h_s$ for the sake of clarity moving forward. Fourier-Laplace transforms are invoked, mapping the system of PDEs into spectral space to form an algebraic system of equations whose dependent variables are defined by the transform of partial differential operators. An eigenanalysis is performed on the algebraic system to derive linear solutions to the transformed free-surface and model horizontal velocity. Solution poles of the integrand are defined by the linear frequency dispersion relation, which over the ω-plane are attributed to forward and backward propagating modes. Focusing on the forward propagating mode, various members of the three-parameter are evaluated in terms of wave celerity, which forms the foundation to study numerical dispersion in later chapters.

3.2.1 Ideal Seabed

The assumptions of a static, flat, seabed assert $A = C = 0$ and linear equations (3.21) and (3.22) reduce to

$$\frac{\partial}{\partial t}\left(\eta - \mu^2\sigma_1 h^2 \frac{\partial^2 \eta}{\partial x^2}\right) + h\frac{\partial}{\partial x}\left(u - \mu^2\sigma_2 h^2 \frac{\partial^2 u}{\partial x^2}\right) = \psi_\eta \tag{3.34}$$

$$\frac{\partial}{\partial t}\left(u - \mu^2\sigma_3 h^2 \frac{\partial^2 u}{\partial x^2}\right) + \frac{\partial}{\partial x}\left(\eta - \mu^2\sigma_4 h^2 \frac{\partial^2 \eta}{\partial x^2}\right) = \psi_u \tag{3.35}$$

where combinations of the dispersion coefficients, σ_n, lead to variants of the system of PDEs. For $\sigma_n = 0$, the system reduces to the primitive linear shallow water equations, which serve as the leading order nondispersive long wave approximation. The constraint equation $\sigma_1 - \sigma_2 + \sigma_3 - \sigma_4 = 1/3$ establishes the three parameter family of linear Boussinesq-type equations under consideration, whose members possess different physical and mathematically properties (e.g., Bona et al. 2002). Despite the differences, the family members are formally equivalent. This is shown by eliminating either the free-surface elevation or horizontal velocity in the system of PDEs to give the following homogeneous equation in absence of source terms

$$\left(\frac{\partial^2}{\partial t^2} - h\frac{\partial^2}{\partial x^2} - \mu^2\frac{1}{3}h^3\frac{\partial^4}{\partial x^4}\right) f(t,x) = 0 \tag{3.36}$$

where $\partial_t^2 - c^2\partial_x^2$ is the long wave d'Alembert operator with $c = \sqrt{h}$ being the wave speed for the dimensionless form of the equations and $f(t,x)$ is the respective dependent variable following the reduction. Equation (3.36) represents a linear high order extension of the classical wave equation, which is indicative of linearized Boussinesq-type equations.

3.2.2 Fourier-Laplace

The linearization permits application of Fourier-Laplace Derivative Theorems (D.3) and (D.7) to the continuity (3.34) and momentum (3.35) equations which map the PDEs into the spectral domain to form an algebraic system of equations

$$-i\omega\widetilde{\eta} - \frac{\widetilde{\eta_o}}{2\pi} - i\sigma_1\omega(kh)^2\widetilde{\eta} - \frac{\widetilde{\eta_o}\sigma_1(kh)^2}{2\pi} + ikh\widetilde{u} + i\sigma_2 kh(kh)^2\widetilde{u} = \widetilde{\psi_\eta} \tag{3.37}$$

$$-i\omega\widetilde{u} - \frac{\widetilde{u_o}}{2\pi} - i\sigma_3\omega(kh)^2\widetilde{u} - \frac{\widetilde{u_o}\sigma_3(kh)^2}{2\pi} + ik\widetilde{\eta} + i\sigma_4 k(kh)^2\widetilde{\eta} = \widetilde{\psi_u} \tag{3.38}$$

in which ω and k respectively denote the angular frequency and wave number. Collecting terms involving the initial conditions, η_o and u_o, on the right hand side with the source terms, the equations are

$$\omega\widetilde{\eta} + \sigma_1\omega(kh)^2\widetilde{\eta} - kh\widetilde{u} - \sigma_2 kh(kh)^2\widetilde{u} = \frac{i\widetilde{\eta_o}(1+\sigma_1(kh)^2)}{2\pi} + i\widetilde{\psi_\eta} \tag{3.39}$$

$$\omega\widetilde{u} + \sigma_3\omega(kh)^2\widetilde{u} - k\widetilde{\eta} - \sigma_4 k(kh)^2\widetilde{\eta} = \frac{i\widetilde{u_o}(1+\sigma_3(kh)^2)}{2\pi} + i\widetilde{\psi_u} \tag{3.40}$$

or in $\mathbf{A}\widetilde{\mathbf{U}} = \widetilde{\mathbf{G}}$ matrix notation as

$$\begin{bmatrix} \omega(1+\sigma_1(kh)^2) & -kh(1+\sigma_2(kh)^2) \\ -k(1+\sigma_4(kh)^2) & \omega(1+\sigma_3(kh)^2) \end{bmatrix} \begin{bmatrix} \widetilde{\eta} \\ \widetilde{u} \end{bmatrix} = \begin{bmatrix} \widetilde{G_1} \\ \widetilde{G_2} \end{bmatrix} \tag{3.41}$$

in which $\widetilde{\mathbf{G}}$ contains the transform of the respective initial conditions and source terms

$$\widetilde{G_1} = \frac{i}{2\pi}\left(\widetilde{\eta_o}(1+\sigma_1(kh)^2) + 2\pi\widetilde{\psi_\eta}\right) \tag{3.42}$$

$$\widetilde{G_2} = \frac{i}{2\pi}\left(\widetilde{u_o}(1+\sigma_3(kh)^2) + 2\pi\widetilde{\psi_u}\right) \tag{3.43}$$

The leading square matrix, $\mathbf{A}$, in equation (3.41) defines a linear transformation whose characteristic behavior defines the system dynamics. To identify the characteristic behavior, an eigenanalysis is

carried out

$$(\mathbf{A}-\lambda\mathbf{I})\,\mathbf{X}=\begin{bmatrix}\omega(1+\sigma_1(kh)^2)-\lambda & -kh(1+\sigma_2(kh)^2)\\ -k(1+\sigma_4(kh)^2) & \omega(1+\sigma_3(kh)^2)-\lambda\end{bmatrix}\mathbf{X}=0 \tag{3.44}$$

where $\mathbf{I}$ is the identity matrix, λ represents a scalar eigenvalue, and $\mathbf{X}$ a right eigenvector. For a nonzero eigenvector, the quadratic polynomial $p(\lambda)=det(\mathbf{A}-\lambda\mathbf{I})$ is set equal to zero giving the characteristic equation

$$\begin{aligned}\lambda^2-\omega(2+(\sigma_1+\sigma_3)(kh)^2)\lambda+\omega^2(1+\sigma_1(kh)^2)(1+\sigma_3(kh)^2)\\ -hk^2(1+\sigma_2(kh)^2)(1+\sigma_4(kh)^2)=0\end{aligned} \tag{3.45}$$

The two roots of the characteristic polynomial over λ define the eigenvalues as

$$\lambda_{1,2}=\omega\left(1+\frac{(\sigma_1+\sigma_3)(kh)^2}{2}\right)\mp\frac{\Psi}{2} \tag{3.46}$$

in which

$$\Psi=\sqrt{(\sigma_1-\sigma_3)^2\omega^2(kh)^4+4hk^2(1+\sigma_2(kh)^2)(1+\sigma_4(kh)^2)}$$

The product $(\lambda_1\lambda_2)$ and sum $(\lambda_1+\lambda_2)$ of the eigenvalues equal the determinant and trace of $\mathbf{A}$ respectively as a check. For each eigenvalue, λ_n , an associated eigenvector, $\mathbf{X}_n$, is determined. Substituting λ_1 into (3.44) and solving for $\mathbf{X}_1$ gives the first eigenvector

$$\mathbf{X}_1=\varphi\begin{bmatrix}\frac{\Psi-(\sigma_1-\sigma_3)(kh)^2\omega}{2k(1+\sigma_4(kh)^2)}\\ 1\end{bmatrix} \tag{3.47}$$

in which φ is an arbitrary real scalar factor giving a 1-parameter family of solutions emerging from row reduction. The second eigenvector is obtained following the same procedure to give

$$\mathbf{X}_2=\varphi\begin{bmatrix}-\frac{\Psi+(\sigma_1-\sigma_3)(kh)^2\omega}{2k(1+\sigma_4(kh)^2)}\\ 1\end{bmatrix} \tag{3.48}$$

The eigenvectors are collectively expressed as $\varphi\mathbf{X}=\varphi\,[\mathbf{X}_1,\mathbf{X}_2]$, where the full matrix indicates that the linear dispersive water wave system experiences fluctuations in all modes. The solution to equation (3.41) is expressed as a linear combination of the eigenvectors as

$$\begin{bmatrix}\widetilde{\eta}\\ \widetilde{u}\end{bmatrix}=\varphi\left(\frac{C_1}{\lambda_1}\mathbf{X}_1+\frac{C_2}{\lambda_2}\mathbf{X}_2\right) \tag{3.49}$$

in which the components of the coefficient, $\mathbf{C} = \mathbf{X}^{-1}\widetilde{\mathbf{G}}$, are calculated as

$$\begin{bmatrix} C_1 \\ C_2 \end{bmatrix} = \begin{bmatrix} \frac{k(1+\sigma_4(kh)^2)}{\Psi} & \frac{1}{2} + \frac{(\sigma_1-\sigma_3)(kh)^2\omega}{2\Psi} \\ -\frac{k(1+\sigma_4(kh)^2)}{\Psi} & \frac{1}{2} - \frac{(\sigma_1-\sigma_3)(kh)^2\omega}{2\Psi} \end{bmatrix} \begin{bmatrix} \widetilde{G_1} \\ \widetilde{G_2} \end{bmatrix} \tag{3.50}$$

Substituting the expressions for the eigenvalues (3.46), eigenvectors (3.47) and (3.48), and coefficients (3.50) into equation (3.49), the final transformed free-surface elevation and velocity are given as

$$\widetilde{\eta} = \varphi \frac{\omega(1+\sigma_3(kh)^2)\widetilde{G_1} + kh(1+\sigma_2(kh)^2)\widetilde{G_2}}{\omega^2(1+\sigma_1(kh)^2)(1+\sigma_3(kh)^2) - k^2h(1+\sigma_2(kh)^2)(1+\sigma_4(kh)^2)} \tag{3.51}$$

$$\widetilde{u} = \varphi \frac{k(1+\sigma_4(kh)^2)\widetilde{G_1} + \omega(1+\sigma_1(kh)^2)\widetilde{G_2}}{\omega^2(1+\sigma_1(kh)^2)(1+\sigma_3(kh)^2) - k^2h(1+\sigma_2(kh)^2)(1+\sigma_4(kh)^2)} \tag{3.52}$$

The focus of this study is on the unimpeded propagation of dispersive waves from an initial state, therefore the source terms in (3.42) and (3.43) will be set equal to zero. Implementing inverse Fourier-Laplace transforms gives integral solutions to the homogeneous linear system of equations in terms of the free-surface elevation and velocity as

$$\eta = \frac{i\varphi}{2\pi} \int_\Gamma \int_{-\infty}^{\infty} \frac{(1+\sigma_3(kh)^2)\left(\omega(1+\sigma_1(kh)^2)\widetilde{\eta_o} + kh(1+\sigma_2(kh)^2)\widetilde{u_o}\right)}{\omega^2(1+\sigma_1(kh)^2)(1+\sigma_3(kh)^2) - k^2h(1+\sigma_2(kh)^2)(1+\sigma_4(kh)^2)} e^{i(kx-\omega t)} dk d\omega \tag{3.53}$$

$$u = \frac{i\varphi}{2\pi} \int_\Gamma \int_{-\infty}^{\infty} \frac{(1+\sigma_1(kh)^2)\left(k(1+\sigma_4(kh)^2)\widetilde{\eta_o} + \omega(1+\sigma_3(kh)^2)\widetilde{u_o}\right)}{\omega^2(1+\sigma_1(kh)^2)(1+\sigma_3(kh)^2) - k^2h(1+\sigma_2(kh)^2)(1+\sigma_4(kh)^2)} e^{i(kx-\omega t)} dk d\omega \tag{3.54}$$

in which Γ is the contour of integration over the ω-plane.

3.2.3 Dispersion Relation

The rational integrands in (3.53) and (3.54) share a common denominator, which fundamentally contributes to the integral solutions. According to C. K. W. Tam (1995), the denominator expression defines the dispersion function

$$f_D(\omega, k) = \omega^2(1+\sigma_1(kh)^2)(1+\sigma_3(kh)^2) - k^2h(1+\sigma_2(kh)^2)(1+\sigma_4(kh)^2) \tag{3.55}$$

which can be derived independent of the eigenanalysis by evaluating the determinant, $det(\mathbf{A})$, in (3.41) above; however, the goal of the previous section was to derive analytic solutions to the

transformed variables, thus warranting the detailed analysis. Setting the dispersion function (3.55) equal to zero, or equivalently $det(\mathbf{A}) = 0$, and solving for the angular frequency gives the dispersion relation

$$\omega^2(k) = hk^2 \frac{(1+\sigma_2(kh)^2)(1+\sigma_4(kh)^2)}{(1+\sigma_1(kh)^2)(1+\sigma_3(kh)^2)} \tag{3.56}$$

which identifies a relation between ω and k that must be satisfied such that the kernel of $\mathbf{A}$ contains nontrivial solutions to $\mathbf{A}\widetilde{\mathbf{U}} = 0$. As a denominator of the rational integrands, the roots of the dispersion function are associated with singularities of the inverse transforms. On the complex ω-plane, the roots of the dispersion function give rise to two simple poles

$$\omega_1(k) = k\sqrt{h}\sqrt{\frac{(1+\sigma_2(kh)^2)(1+\sigma_4(kh)^2)}{(1+\sigma_1(kh)^2)(1+\sigma_3(kh)^2)}} \tag{3.57}$$

$$\omega_2(k) = -k\sqrt{h}\sqrt{\frac{(1+\sigma_2(kh)^2)(1+\sigma_4(kh)^2)}{(1+\sigma_1(kh)^2)(1+\sigma_3(kh)^2)}} \tag{3.58}$$

which are associated with a forward and backward propagating wave mode. The relation between the poles, $\omega_1(k) = -\omega_2(k) = \omega_2(-k)$, shows that the parity is odd, with the forward propagation mode being the negative of the backward. The odd parity derives from the poles of the shallow water dispersion relation ($\sigma_n = 0$) being linearly dependent on the wave number, whereas the degree of the additional dispersion terms is strictly even with respect to the wave number.

The coefficients σ_2 and σ_4 can be expanded in order to make connections with other studies in the literature. Substituting $\beta = \zeta + 1$ into (3.24) and (3.25) gives

$$\sigma_2 = -\left(\frac{1}{2}\zeta^2 + \zeta + \frac{1}{3} - \sigma_1\right) = -\left(\alpha + \frac{1}{3} - \sigma_1\right) \tag{3.59}$$

$$\sigma_3 = -\left(\frac{1}{2}\zeta^2 + \zeta - \sigma_4\right) = -\left(\alpha - \sigma_4\right) \tag{3.60}$$

where α is the classic coefficient associated with the arbitrary linear reference (e.g., Nwogu 1993). Stating the dispersion relation (3.56) in terms of the alternative coefficient expressions gives

$$\omega^2(k) = hk^2 \frac{\left(1-\left(\alpha+\frac{1}{3}-\sigma_1\right)(kh)^2\right)(1+\sigma_4(kh)^2)}{(1+\sigma_1(kh)^2)\left(1-(\alpha-\sigma_4)(kh)^2\right)} \tag{3.61}$$

which is equivalent to the frequency dispersion relation given by Schaffer and P. A. Madsen (1995b) for $\sigma_1 \equiv \boldsymbol{\beta}$ and $\sigma_4 \equiv \boldsymbol{\gamma}$, which is just a change in notation.

The set of coefficients, σ_n, not only govern the dispersion relation (3.56), they also identify members of the three-parameter family. In section 3.1.2, the coefficients, σ_n, are shown to be functions of

Theory	$-\sigma_1$ (η_{txx})	$-\sigma_2$ (u_{xxx})	$-\sigma_3$ (u_{txx})	$-\sigma_4$ (η_{xxx})	α	β^2	ζ	Λ_1	Λ_2
Boussinesq	0	0	0	1/3	-1/3	1/3	-0.4226	Λ_1	1
Peregrine	0	0	-1/3	0	-1/3	1/3	-0.4226	Λ_1	0
Kaup	0	1/3	0	0	0	1	0	0	Λ_2
Set A	-1/3	0	0	0	0	1	0	1	Λ_2
Mei	0	-1/6	-1/2	0	-1/2	0	-1	0	0
Madsen	0	0	-7/18	-1/18	-1/3	1/3	-0.4226	Λ_1	-1/6
Nwogu	0	-0.0562	-0.3896	0	-0.3896	0.2209	-0.5300	0	0
Witting	0	-1/15	-2/5	0	-2/5	1/5	-0.5528	0	0
Schaffer	-0.4053	-0.1006	-0.0392	-0.0105	-0.0286	0.9427	-0.0291	1.3301	-0.3672
BBM	-1/6	0	-1/6	0	-1/6	2/3	-0.1835	1	0
KDV KDV	0	1/6	0	1/6	-1/6	2/3	-0.1835	0	1
KDV BBM	0	1/6	-1/6	0	-1/6	2/3	-0.1835	0	0
BBM KDV	-1/6	0	0	1/6	-1/6	2/3	-0.1835	1	1

Table 3.1: Select members of the $O(\mu^2)$ three-parameter family. Coefficients shown are rounded to five significant digits; however, plots and simulations are generated with double precision.

$\{\beta, \Lambda_1, \Lambda_2\}$, which implies a unique three-parameter set for each member. Table 3.1 lists several members of the $O(\mu^2)$ three-parameter family discussed herein, as well as a few additional members found in the literature introduced by mathematicians (e.g., Bona et al. 2002). Two addition columns for α and ζ are shown for completeness, with the latter indicating the location of the linear reference depth, hence $-1 \leq \zeta \leq 0$ for physical meaningful solutions. In some instances, Λ_n remains arbitrary due to the value of β and either σ_1 or σ_4 being equal to zero. Take for instance the coefficient set attributed to Peregrine (1967). Substituting $\beta^2 = 1/3$ into (3.23), it is clear that $\sigma_1 = 0$ independent of Λ_1, thus remains arbitrary as indicated in the table. The set denoted "Set A" has been added to the table to complete the apparent pattern and show that by making $\Lambda_1 = 1$, coefficients σ_1 and σ_2 in the continuity, along with the sign, swap due to the Λ_1 and $(1 - \Lambda_1)$ expressions in the respective coefficients. The same can be said for Λ_2 and the coefficients in the momentum. The coefficients attributed to P. A. Madsen et al. (1991) and Nwogu (1993) result from sacrificing the formal order of accuracy to improve bandwidth resolution. Therefore, the coefficients are listed as decimal approximations. In the set given by P. A. Madsen et al. (1991), the fact that Λ_2 is nonzero further shows that the different methods of linear enhancement discussed in section 3.1.2 are in fact formally equivalent. The coefficient set by Witting (1984) gives the Padé [2/2] approximation, which for a rational approximation gives the best formal order of accuracy. The coefficient set by Schaffer and P. A. Madsen (1995b) is obtained by matching the coefficients to the Padé [4/4] approximation. For the three-parameter family, several solutions exist, in which the ones shown correspond to those recommended by Schaffer and P. A. Madsen (1995b), where again, the coefficients are listed as decimal approximations which should be carried out to higher precision during implementation. The remaining four coefficient sets are found in Bona et al. (2002) and

included herein to analyze their practical limitations.

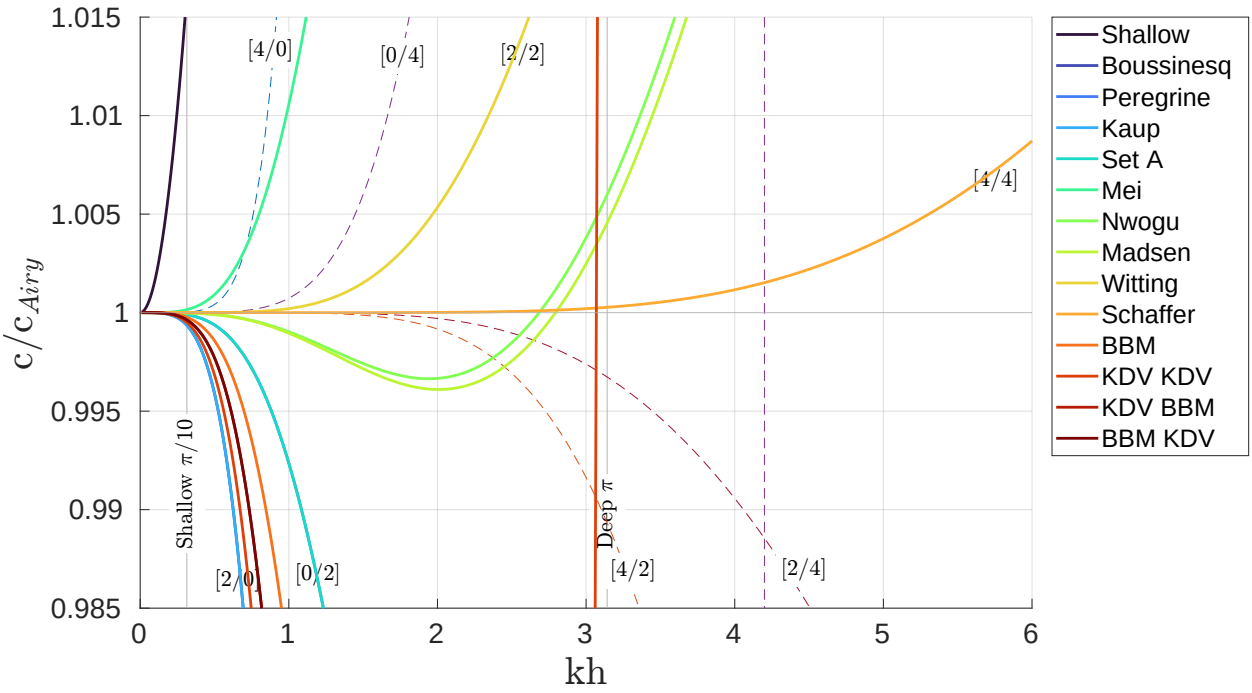

Figure 3.2: Normalized wave celerity for select members of the three-parameter family. Padé approximations are shown for reference as dotted lines (Witting 1984). The following approximations are indistinguishable at scale: Boussinesq-Kaup-Padé [2/0], Peregrine-Set A-Padé [0/2], KDV BBM - BBM KDV, Schaffer-Padé [4/4].

In practical application, the objective is to choose the set of coefficients such that the physical characteristics of the problem are well resolved. Dividing the forward propagating mode (3.57) by the wave number results in the wave celerity, $c = \omega/k$, which defines a linear performance metric measuring the phase speed of propagation. In Figure 3.2, the relative celerity associated with each member of the three-parameter family tabulated in Table 3.1, in addition to the leading order ($\mu^2 \to 0$) shallow water approximation, is shown as a function of the relative depth. Clearly, the nondispersive shallow water approximation is limited to very shallow water regions, with the addition of dispersion significantly improving the theoretical limitations. Overall, the approximations can be categorized into two groups: those which exhibit a phase lag and those which exhibit a phase lead with increasing relative depth. Padé approximations, introduced by Witting (1984), are shown as a reference. For $kh \in \mathbb{R}$, the Padé [0/4] approximation exhibits a singularity beyond deep water, which appears as a vertical line. At the scale shown, a portion of the "KDV KDV" approximation also appears as a vertical line near the deep water limit, but in fact continues to grow exponentially over the range of relative depths considered. The optimized approximations of P. A. Madsen et al. (1991) and Nwogu (1993) clearly show a sacrifice in the formal order of accuracy as compared to the

Padé [2/2] of Witting (1984); however, the integral phase error is smaller over a greater bandwidth by design. As a result, there is a phase lag up to $kh \approx 2.75$, followed by a phase lead. To the left and right of the max lag, occurring near $kh \approx 2$, waves possessing different wave numbers will appear to travel at the same speed. According to linear wave theory, this is physically incorrect, as the phase speed should monotonically decrease with increasing relative depth. These properties are dependent upon the optimization procedure, hence what is depicted merely reflects a specific set of coefficients. P. A. Madsen et al. (1991), for example, depicts results from several sets of coefficients, in which only one set is shown here for discussion purposes. Clearly the approximation given by Schaffer and P. A. Madsen (1995b) is superior, matching the Padé [4/4] approximation which is within 1% error at twice the conventional deep water limit. Unlike the approximations of P. A. Madsen et al. (1991) and Nwogu (1993), the errors increase monotonically with the relative depth. Beyond the graphical limits shown in Figure 3.2, a few theories exhibit a complex celerity. The approximations of Boussinesq and Kaup (1975), being equivalent in terms of frequency dispersion, become complex near $kh \approx 1.74$, while the approximations of "KDV BBM" and "BBM KDV", also being equivalent in terms of frequency dispersion, become complex near $kh \approx 2.45$, which can lead to either wave amplification or decay. The stability behaviour should be further investigated prior to implementation. In fact, Boussinesq himself favored the use of leading order substitutions to obtain a Padé [0/2] approximation, which gives improved stability characteristics (Whitham 1974).

3.3 Analytic Solutions

Having derived a solution to the dependent variables in terms of Fourier-Laplace integrals, inverse transforms are applied in order to map the solutions back into the time-space domain. Beginning with the integral over the angular frequency domain, the solutions are expressed as a linear superposition of the wave modes which govern the frequency dispersion relation. Initial conditions are given for both standing and progressive waves in order to derive general solutions for the three parameter linear $O(\mu^2)$ approximations. These solutions will serve as the basis of comparison in later chapters on the validation of the numerical analysis.

3.3.1 Inverse Laplace

Integrals (3.53) and (3.54) can be evaluated to give analytic solutions for the free-surface elevation and model velocity. Isolating the numerator and denominator of the rational expression (3.53)

gives

$$P(\omega,k) = (1+\sigma_3(kh)^2)\left(\omega(1+\sigma_1(kh)^2)\widetilde{\eta_o} + kh(1+\sigma_2(kh)^2)\widetilde{u_o}\right)e^{i(kx-\omega t)} \tag{3.62}$$

$$Q(\omega,k) = \omega^2(1+\sigma_1(kh)^2)(1+\sigma_3(kh)^2) - k^2h(1+\sigma_2(kh)^2)(1+\sigma_4(kh)^2) \tag{3.63}$$

in which $P(\omega,k)$ and $Q(\omega,k)$ are assumed entire. The integral over the ω-plane is evaluated using the Residue Theory for simple poles, which are determined by

$$R_n = \frac{P}{\frac{\partial Q}{\partial \omega}}\bigg|_{\omega=\omega_n} = \frac{(1+\sigma_3(kh)^2)\left(\omega(1+\sigma_1(kh)^2)\widetilde{\eta_o} + kh(1+\sigma_2(kh)^2)\widetilde{u_o}\right)}{2\omega(1+\sigma_1(kh)^2)(1+\sigma_3(kh)^2)}e^{i(kx-\omega t)}\bigg|_{\omega=\omega_n} \tag{3.64}$$

Assuming a counterclockwise winding contour, the integral solution over the ω-plane, $2\pi i\Sigma R_n$, is substituted into (3.53) to update the solution for the free-surface elevation as

$$\eta = \sum_{n=1}^{2}\int_{-\infty}^{\infty}\frac{\omega_n(1+\sigma_1(kh)^2)\widetilde{\eta_o} + kh(1+\sigma_2(kh)^2)\widetilde{u_o}}{2\omega_n(1+\sigma_1(kh)^2)}e^{i(kx-\omega_n t)}dk \tag{3.65}$$

in which the free parameter, $\varphi = -1$, preserves a positive solution. Invoking the odd parity of the poles in the second integral expression and dropping the subscript notation for the angular frequency, $\omega \equiv \omega_1$, gives

$$\begin{aligned}\eta = &\int_{-\infty}^{\infty}\frac{1}{2}\left(\widetilde{\eta_o} + \frac{\widetilde{u_o}kh(1+\sigma_2(kh)^2)}{\omega(1+\sigma_1(kh)^2)}\right)e^{i(kx-\omega t)}dk \quad + \\ &\int_{-\infty}^{\infty}\frac{1}{2}\left(\widetilde{\eta_o} - \frac{\widetilde{u_o}kh(1+\sigma_2(kh)^2)}{\omega(1+\sigma_1(kh)^2)}\right)e^{i(kx+\omega t)}dk\end{aligned} \tag{3.66}$$

The superposition of the intrinsic modes can also be presented in terms of trigonometric functions. Combining the integrals and applying identities (G.1) and (G.2), an equivalent solution to the free-surface elevation is

$$\eta = \int_{-\infty}^{\infty}\left(\widetilde{\eta_o}\cos(\omega t) - \frac{i\widetilde{u_o}kh(1+\sigma_2(kh)^2)}{\omega(1+\sigma_1(kh)^2)}\sin(\omega t)\right)e^{ikx}dk \tag{3.67}$$

The trigonometric form of the solution will later be utilized when solving the integral over the k-plane for both standing and progressive waves.

The multi-modal solution presented in (3.66) is utilized to verify the derivation by comparison to the general Fourier integral solution for two propagating wave modes Appendix E. The arbitrary

functions in the Fourier integrals (E.2) are clearly defined

$$\widetilde{f_1}(k) = \frac{1}{2}\left(\widetilde{\eta_o} + \frac{\widetilde{u_o}kh(1+\sigma_2(kh)^2)}{\omega(1+\sigma_1(kh)^2)}\right) = \frac{1}{2}\left(\widetilde{\eta_o} + \frac{i\left(-i\widetilde{u_o}kh(1+\sigma_2(kh)^2)\right)}{\omega(1+\sigma_1(kh)^2)}\right) \tag{3.68}$$

$$\widetilde{f_2}(k) = \frac{1}{2}\left(\widetilde{\eta_o} - \frac{\widetilde{u_o}kh(1+\sigma_2(kh)^2)}{\omega(1+\sigma_1(kh)^2)}\right) = \frac{1}{2}\left(\widetilde{\eta_o} - \frac{i\left(-i\widetilde{u_o}kh(1+\sigma_2(kh)^2)\right)}{\omega(1+\sigma_1(kh)^2)}\right) \tag{3.69}$$

The Fourier transform of the two initial conditions can be extracted from the function definitions above by comparison with the general function definitions (E.7) and (E.8) giving

$$\widetilde{\phi_1}(k) = \widetilde{\eta_o} \tag{3.70}$$

$$\widetilde{\phi_2}(k) = -i\widetilde{u_o}kh\left(\frac{1+\sigma_2(kh)^2}{1+\sigma_1(kh)^2}\right) \tag{3.71}$$

As a check for consistency, consider $\phi_1(x) = \phi(0,x)$ and $\phi_2(x) = \phi_t(0,x)$ as a set of generalized initial conditions. Substituting the dependent variable, $\phi = \eta$, in the first condition and applying the Fourier transform to both sides, it is clear that (3.70) is correct. Similarly, the second condition gives $\widetilde{\phi_2} = \widetilde{\partial_t \eta_o} = -i\omega\widetilde{\eta_o}$, which after solving (3.37) and (3.38) in the absents of source terms, shows that (3.71) is also correct.

The ω-integral of the model velocity (3.54) is evaluated following the same procedure as outlined above to give

$$\begin{aligned} u = &\int_{-\infty}^{\infty} \frac{1}{2}\left(\widetilde{u_o} + \frac{\widetilde{\eta_o}k(1+\sigma_4(kh)^2)}{\omega(1+\sigma_3(kh)^2)}\right) e^{i(kx-\omega t)}dk \quad + \\ &\int_{-\infty}^{\infty} \frac{1}{2}\left(\widetilde{u_o} - \frac{\widetilde{\eta_o}k(1+\sigma_4(kh)^2)}{\omega(1+\sigma_3(kh)^2)}\right) e^{i(kx+\omega t)}dk \end{aligned} \tag{3.72}$$

or in trigonometric form as

$$u = \int_{-\infty}^{\infty} \left(\widetilde{u_o}\cos(\omega t) - \frac{i\widetilde{\eta_o}k(1+\sigma_4(kh)^2)}{\omega(1+\sigma_3(kh)^2)}\sin(\omega t)\right) e^{ikx}dk \tag{3.73}$$

The derivation is validated as before, in which (3.72) clearly defines the arbitrary functions in the Fourier integrals of the two propagation modes. The Fourier transform of the initial conditions are

then inferred from the function definitions as

$$\widetilde{\phi_1}(k) = \widetilde{u_o} \tag{3.74}$$

$$\widetilde{\phi_2}(k) = \frac{-i\widetilde{\eta_o}k(1+\sigma_4(kh)^2)}{(1+\sigma_3(kh)^2)} \tag{3.75}$$

For the generalized initial conditions, $\phi_1(x) = \phi(0,x)$ and $\phi_2(x) = \phi_t(0,x)$, it is trivial to see that (3.74) is correct upon substitution of the dependent variable. The second condition gives $\widetilde{\phi_2} = \partial_t \widetilde{u_o} = -i\omega\widetilde{u_o}$, which after solving (3.37) and (3.38) in the absents of source terms, shows that (3.75) is also correct.

Given initial conditions of the free-surface elevation, η_o, and model velocity, u_o, integrals (3.67) and (3.73) can be solved analytically. For wave problems of interest that follow, the initial conditions for the free-surface elevation are $\eta_o(0,x) = A\cos(k_o x)$, in which A is the wave amplitude and k_o is the initial wave number. Applying Fourier transform (F.1) gives

$$\widetilde{\eta_o}(k) = \frac{A}{2}\left(\delta(k-k_o) + \delta(k+k_o)\right) \tag{3.76}$$

in which $\delta()$ is the delta function. The remaining initial condition for the model velocity is problem dependent.

3.3.2 Standing Waves

The initial condition of the model velocity for standing waves is $u_o(0,x) = 0$. Substituting the transform of the initial conditions for the free-surface (3.76) and model velocity, $\widetilde{u_o}(k) = 0$, into the integral solutions (3.67) and (3.73) gives

$$\eta = \int_{-\infty}^{\infty} \frac{A_s}{2}\left(\delta(k-k_o) + \delta(k+k_o)\right)\cos(\omega t)e^{ikx}dk \tag{3.77}$$

$$u = \int_{-\infty}^{\infty} -\frac{A_s}{2}\left(\delta(k-k_o) + \delta(k+k_o)\right)\frac{k(1+\sigma_4(kh)^2)}{\omega(1+\sigma_2(kh)^2)}i\sin(\omega t)e^{ikx}dk \tag{3.78}$$

in which A_s is the standing wave amplitude. Focusing on the free-surface elevation (3.77), let $f(k) = \frac{A_s}{2}\cos(\omega t)e^{ikx}$ in the application of (F.3) to show that the free-surface elevation is

$$\eta = \frac{A_s}{2}\cos(\omega t)e^{ik_o x} + \frac{A_s}{2}\cos(\omega t)e^{-ik_o x} \tag{3.79}$$

Collecting like terms and applying the trigonometric definition (G.1) gives the standing wave free-surface solution as

$$\eta = A_s \cos(\omega t)\cos(k_o x) \tag{3.80}$$

For the integral solution of the model velocity, let $f(k) = -\frac{A_s}{2}\frac{k(1+\sigma_4(kh)^2)}{\omega(1+\sigma_3(kh)^2)} i \sin(\omega t) e^{ikx}$ in the application of equation (F.3) to show

$$u = -\frac{A_s}{2}\frac{k_o(1+\sigma_4(k_o h)^2)}{\omega(1+\sigma_3(k_o h)^2)} i \sin(\omega t) e^{ik_o x} + \frac{A_s}{2}\frac{k_o(1+\sigma_4(k_o h)^2)}{\omega(1+\sigma_3(k_o h)^2)} i \sin(\omega t) e^{-ik_o x} \tag{3.81}$$

Collecting like terms and applying the trigonometric definition (G.2) gives

$$u = A_s \frac{k_o(1+\sigma_4(k_o h)^2)}{\omega(1+\sigma_3(k_o h)^2)} \sin(\omega t)\sin(k_o x) \tag{3.82}$$

Without loss, the expression for the model velocity solution (3.82) can be reformulated using the dispersion relation (3.56) to give the full solution for the standing wave problem alternatively as

$$\eta = A_s \cos(\omega t)\cos(k_o x) \tag{3.83}$$

$$u = \frac{A_s}{h}\frac{\omega(1+\sigma_1(k_o h)^2)}{k_o(1+\sigma_2(k_o h)^2)} \sin(\omega t)\sin(k_o x) \tag{3.84}$$

For $\sigma_n \to 0$, these solutions agree with those presented in the literature for standing wave solutions to the linear nondispersive shallow water equations (see, e.g., Dean and Dalrymple 1991). Importantly, solutions (3.82) and (3.84) show that only part of the linear dispersion relation (3.56) in the family of BTEs is responsible for the deviation from the nondispersive solution. In (3.82), only terms associated with the continuity are found, whereas in (3.84), only terms associated with the momentum are found. In other words, simply substituting the linear dispersion relation (3.56) into the solution for the linear nondispersive shallow water equations will lead to errors in phase through the velocity expression.

3.3.3 Progressive Wave

The initial condition of the model velocity for progressive waves is $u_o(0,x) = \eta_o T_r$, in which T_r is a linear transform between the model velocity and free-surface given by the linear continuity equation. Substituting the Fourier transform, $\widetilde{u_o}(k) = \widetilde{\eta_o}\widetilde{T_r}$ into the integral solutions (3.67) and

(3.73), while utilizing the dispersion relation, gives

$$\eta = \int_{-\infty}^{\infty} \widetilde{\eta_o} e^{i(kx-\omega t)} dk \tag{3.85}$$

$$u = \int_{-\infty}^{\infty} \widetilde{\eta_o} \widetilde{T_r} e^{i(kx-\omega t)} dk \tag{3.86}$$

in which

$$\widetilde{T_r} = \frac{\omega(1+\sigma_1(k_o h)^2)}{k_o h(1+\sigma_2(k_o h)^2)} \tag{3.87}$$

Substituting the transform of the initial condition for the free-surface elevation (3.76) into the equations above gives

$$\eta = \int_{-\infty}^{\infty} \frac{A_p}{2} \left(\delta(k-k_o) + \delta(k+k_o)\right) e^{i(kx-\omega t)} dk \tag{3.88}$$

$$u = \int_{-\infty}^{\infty} \frac{A_p}{2} \widetilde{T_r} \left(\delta(k-k_o) + \delta(k+k_o)\right) e^{i(kx-\omega t)} dk \tag{3.89}$$

in which A_p is the progressive wave amplitude. For the integral solution of the free-surface (3.88), let $f(k) = \frac{A_p}{2} e^{i(kx-\omega t)}$ in the application of equation (F.3) to show that the free-surface elevation is

$$\eta = \frac{A_p}{2} \left(e^{i(k_o x-\omega t)} + e^{i(-k_o x+\omega t)}\right) \tag{3.90}$$

Applying the trigonometric definition (G.1) gives

$$\eta = A_p \cos(k_o x - \omega t) \tag{3.91}$$

For the integral solution of the model velocity (3.89), let $f(k) = \frac{A_p}{2} \widetilde{T_r} e^{i(kx-\omega t)}$ in the application of equation (F.3) to show that the velocity is

$$u = \frac{A_p}{2} \widetilde{T_r} (e^{i(k_o x-\omega t)} + e^{i(-k_o x+\omega t)}) \tag{3.92}$$

Applying the trigonometric definition (G.1) and substituting in the expression for the linear transform (3.87) gives

$$u = \frac{A_p}{h} \frac{\omega(1+\sigma_1(k_o h)^2)}{k_o(1+\sigma_2(k_o h)^2)} \cos(k_o x - \omega t) \tag{3.93}$$

This again shows that only part of the linear dispersion relation (3.56) in the family of Boussinesq-

type equations is responsible for the deviation from the nondispersive solution.

The relationship between progressive and standing waves is well known and serves as a check to confirm the analysis. Combining two progressive waves traveling in opposite directions, where the second wave utilizes the ω_2-mode, the resulting wave form is that of standing wave. Beginning with the free-surface elevation, two waves of the form (3.85) are superimposed to give

$$\eta = \int_{-\infty}^{\infty} \widetilde{\eta_{o1}} e^{i(kx-\omega_1 t)} dk + \int_{-\infty}^{\infty} \widetilde{\eta_{o2}} e^{i(kx-\omega_2 t)} dk \tag{3.94}$$

Substituting the relation $\omega_1(k) = -\omega_2(k)$, dropping the subscript notation, and acknowledging that the free-surface elevations are equal, the trigonometric definition (G.1) is applied to simplify equation (3.94) to

$$\eta = \int_{-\infty}^{\infty} 2\widetilde{\eta_o} e^{-i\omega t} \cos(kx) dk \tag{3.95}$$

Substituting the transform of the initial condition for the free-surface elevation (3.76) and letting $f(k) = A_p e^{-i\omega t} \cos(kx)$ in the application of equation (F.3), the free-surface is

$$\eta = A_p e^{-i\omega t} \cos(k_o x) + A_p e^{i\omega t} \cos(k_o x) \tag{3.96}$$

Applying the trigonometric definition (G.1), the free-surface solution is

$$\eta = 2A_p \cos(k_o x) \cos(\omega t) \tag{3.97}$$

In comparison with the free-surface elevation for standing waves (3.83), it is clear that the solutions are identical with $A_s = 2A_p$, confirming the free-surface elevation analysis.

Following the same procedure, two model velocities of the form (3.86) are superimposed

$$u = \int_{-\infty}^{\infty} \widetilde{u_{o1}} e^{i(kx-\omega_1 t)} dk + \int_{-\infty}^{\infty} \widetilde{u_{o2}} e^{i(kx-\omega_2 t)} dk \tag{3.98}$$

Substituting the relation $\omega_1(k) = -\omega_2(k)$, dropping the subscript notation, and acknowledging that the the model velocities are equal in amplitude, but opposite in direction, the trigonometric definition (G.2) is applied to simplify equation (3.98) to

$$u = \int_{-\infty}^{\infty} i2\widetilde{u_o} e^{-i\omega t} \sin(kx) dk \tag{3.99}$$

The Fourier transform of the initial condition of the velocity, $\widetilde{u_o} = \widetilde{\eta_o}\widetilde{T_r}$, followed by that of the free-surface (3.76), is substituted in. Letting $f(k) = iA_p\widetilde{T_r} e^{-i\omega t} \sin(kx)$ in the application of equation

(F.3), the model velocity is

$$u = iA_p\widetilde{T}_r e^{-i\omega t}\sin(k_o x) - iA_p\widetilde{T}_r e^{i\omega t}\sin(k_o x) \tag{3.100}$$

Applying the trigonometric definition (G.2) and substituting in the expression for the linear transform (3.87), the model velocity is

$$u = \frac{2A_p}{h}\frac{\omega(1+\sigma_1(k_o h)^2)}{k_o(1+\sigma_2(k_o h)^2)}\sin(\omega t)\sin(k_o x) \tag{3.101}$$

In comparison with the velocity for standing waves (3.101), it is clear that the solutions are identical with $A_s = 2A_p$, confirming the velocity analysis.

CHAPTER 4
FINITE DIFFERENCE METHOD

In the previous chapter, a linear enhancement method was applied to the governing equations to derive a new three-parameter family of Boussinesq-type equations which allow for dynamic seabed deformations. As shown in Figure 3.2, select members of the family are evaluated in terms of relative celerity, which serves as a leading order property of the phase resolving dynamics. Although the theoretical curves facilitate practical application, by aiding in the selection of coefficients which leads to an appropriate theory, the curves only tell half of the story. In practical application, practitioners rely on numerical methods when solving the nonlinear system of PDEs, in which the discretization leads to a system of modified PDEs (MPDEs). The remaining focus of this study is on the implementation of finite difference methods with emphasis on how the relatively celerity shown in Figure 3.2 is modified through the discretization. The modified curves result from so-called numerical dispersion, which is a function of the discrete sampling intervals, designated by practitioners in practical application.

In this chapter, families of finite difference approximations are derived for implementation in the subsequent chapter. Since the derivative operators being approximated are with respect to the independent variables, the function notation, $f(t, x)$, is employed as a generalization of the dependent variables. The first section focuses on the discretization, in which linear difference operators of finite order are derived. The operators are then applied over time and space to formulate families of schemes. Through the application of Fourier-Laplace transforms, the schemes are then mapped into spectral space to evaluate their resolvable bandwidth. In the spectral domain, the absolute effects of numerical dispersion and dissipation associated with the operator become evident. In closing, degrees of freedom are introduced to show how the schemes can be modified to meet various objectives. This interdisciplinary chapter is heavily influenced by the works of Lele (1992) and C. Tam and Webb (1993), whose principle applications were directed towards computational fluid dynamics and aeroacoustics respectively. Although the governing equations employed in these fields are uniquely different from Boussinesq-type equations, the success of the methods applied therein has been inspirational. Therefore, this chapter is largely instructional, with new insights being offered in the context of application to Boussinesq-type equations.

4.1 Discretization

The development of a numerical model begins by discretizing the domain of the continuum. Consequently, differential operators need to be converted into difference operators. The operators used in finite difference methods serve as approximations characterized by a leading order truncation error, which directly reflects the asymptotic accuracy as a function of the sampling intervals. Assuming a smooth continuum, the operators are built from local Taylor series expansions in the neighborhood of the dependent variable to which the operator is applied. The extent of the neighborhood is often referred to as the stencil, in which both classic and compact stencils are considered herein.

4.1.1 Domain

The system of PDEs yields a mathematical model governing physical processes evolving over time, $t \in \mathbb{R}$, and space, $x \in \mathbb{R}$, in which the ordered pair (t, x) denotes coordinates of the $\mathbb{R}^2$ domain. A discrete mesh of observation points embedded in the domain is defined by the ordered pair (t_τ, x_ℓ) with coordinates

$$\begin{aligned} \{t_\tau \mid \tau \in \mathbb{Z}\} &\equiv \ldots, t_{-2}, t_{-1}, t_0, t_1, t_2, \ldots \\ \{x_\ell \mid \ell \in \mathbb{Z}\} &\equiv \ldots, x_{-2}, x_{-1}, x_0, x_1, t_2, \ldots \end{aligned} \tag{4.1}$$

in which $\Delta t_\tau = t_{\tau+1} - t_\tau$ and $\Delta x_\ell = x_{\ell+1} - x_\ell$ denote the difference between adjacent coordinates. Herein, observation points are uniformly distributed, which implies $\Delta t_\tau \equiv \Delta t$ and $\Delta x_\ell \equiv \Delta x$ for all τ and ℓ, thus forming a regular mesh. Figure 4.1 depicts the relation between the two domains, in which the notation $f_\ell^\tau \equiv f(t_\tau, x_\ell)$ is used to represent a function definition on the mesh. The

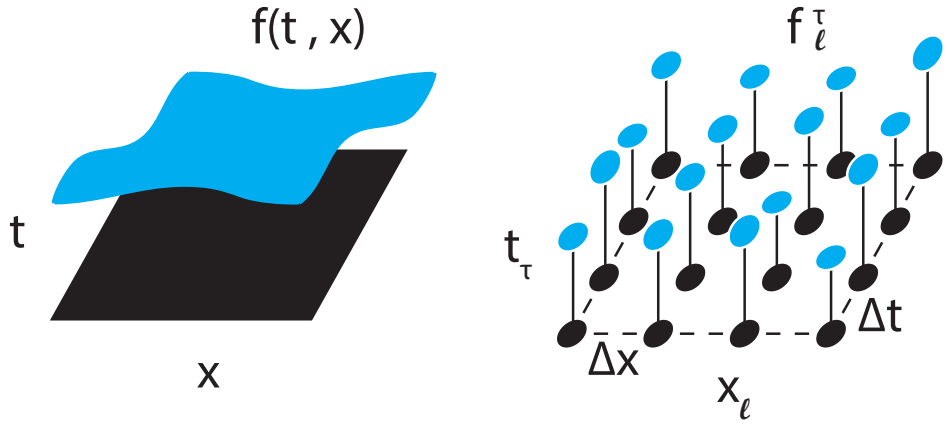

Figure 4.1: Discretization of the continuum domain, (t, x), into discrete observation points, (t_τ, x_ℓ), to form a regular time space mesh.

continuum is assumed smooth, which allows for the mesh to be oriented in an arbitrary manner. Therefore, it is equally valid to consider, for example, $f(t + \Delta t, x_\ell)$ in place of $f(t_\tau + \Delta t, x_\ell)$ since $t_\tau \in t$ and $\Delta t \in \mathbb{R}$ is an arbitrary shift (e.g., C. Tam and Webb 1993). The same can be said for the spatial coordinate. These generalizations permit application of continuous operators in subsequent sections.

4.1.2 Shift Operator

In the calculus of finite differences (e.g. Jordan 1979), the shift, or displacement, operator $\mathbf{E}$ maps functions to a neighboring position, in which $\mathbf{E}_t$ and $\mathbf{E}_x$ denote a shift in time and space respectively. Focusing on the temporal dimension, a mathematical definition is established by applying a Taylor series expansion to the smooth function, f, at the shifted location

$$f(t + \Delta t, x) = f(t, x) + \frac{\Delta t}{1!}\frac{\partial f(t, x)}{\partial t} + \frac{(\Delta t)^2}{2!}\frac{\partial^2 f(t, x)}{\partial t^2} + \frac{(\Delta t)^3}{3!}\frac{\partial^3 f(t, x)}{\partial t^3} + \dots \tag{4.2}$$

An operator substitution, $\mathbf{Q} \equiv \Delta t \frac{\partial}{\partial t}$, is introduced in (4.2), where $\{\mathbf{Q}^n \equiv (\Delta t)^n \frac{\partial^n}{\partial t^n} \mid n \in \mathbb{Z}\}$ is understood. Factoring out the operators acting on $f(t, x)$ gives

$$f(t + \Delta t, x) = \left(1 + \frac{\mathbf{Q}}{1!} + \frac{\mathbf{Q}^2}{2!} + \frac{\mathbf{Q}^3}{3!} + \dots\right) f(t, x) \tag{4.3}$$

The operator series in parenthesis matches the Taylor series of $e^{\mathbf{Q}}$ by definition. An operator substitution $\mathbf{E}_t \equiv e^{\mathbf{Q}}$ simplifies (4.3) to

$$f(t + \Delta t, x) = \mathbf{E}_t f(t, x) \tag{4.4}$$

The definition of the shift operator is extended to the more general case, $\{m\Delta t | m \in \mathbb{Z}\}$, representing multiples of the displacement and expressed with regard to the regular mesh as

$$f_\ell^{\tau+m} = \mathbf{E}_t^m f_\ell^\tau \tag{4.5}$$

in which $\mathbf{E}^0 \equiv e^0 = 1$ gives the operator identity. Beyond the trivial case, $m = 0$, the identity is also recovered as $m\Delta t \frac{\partial}{\partial t} \to 0$ due to a vanishing sampling interval. The shift operator is not limited to operations on the dependent variable. Replacing f with its derivative in the Taylor series expansion (4.2), it is trivial to show that the shift operator applies to the n^{th} derivative as well. The spatial shift operator, $\mathbf{E}_x$, is derived following the same logic and shares the same properties (e.g., Vichnevetsky and Bowles 1982).

4.1.3 Difference Approximation

Finite difference approximations rely on information from a subset of mesh points referred to as the stencil. Focusing on the temporal dimension, a classic difference equation for n^{th} derivative is given by

$$\left(\frac{\partial^n f}{\partial t^n}\right)_\ell^\tau = \frac{1}{\Delta t^n}\sum_m b_m^n f_\ell^{\tau+m} + \varepsilon \tag{4.6}$$

where $b_m \in \mathbb{R}$ is a set of unknown constant coefficients, $m \in \mathbb{Z}$ is the stencil index, and ε is the error of approximation. It is noted that coefficient superscripts, for example, b^n, are not to interpreted as powers. Instead, they serve as a label to affiliate the coefficient with the corresponding derivative. The stencil index $m = 0$ will always be associated with the point of evaluation, whereas positive and negative indices will be associated with neighbors to the right/forward and left/backward respectively. Figure 4.2 depicts an application of (4.6) for $n = 1$ and $m = \{-1, 0, 1\}$, which gives a central 3-point first difference stencil. Conceptually, the stencil structure holds for all n and m, but as will be shown, is constrained by the number of unknowns and number of equations governing the approximation objectives.

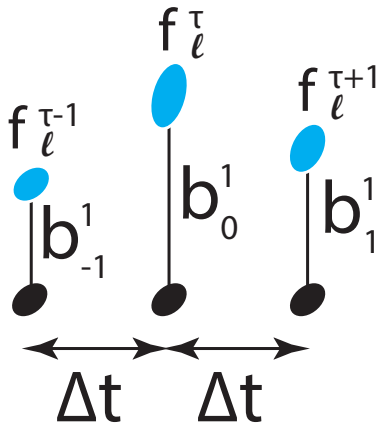

Figure 4.2: Sample 3-point first difference stencil, with corresponding coefficients

The information governing the stencil approximation in (4.6) is limited to the dependent variable alone. Following Lele (1992), the information can be extended to include the derivative of the dependent variable

$$\sum_r a_r^n \left(\frac{\partial^n f}{\partial t^n}\right)_\ell^{\tau+r} = \frac{1}{\Delta t^n}\sum_m b_m^n f_\ell^{\tau+m} + \varepsilon \tag{4.7}$$

in which $a_r \in \mathbb{R}$ is a set of unknown constant coefficients and $r \in \mathbb{Z}$ is a stencil index. Approxima-

tions of the form (4.7) are known as compact approximations. Following Vichnevetsky and Bowles (1982), the dependent variable and its derivative can be factored out with the application of the temporal shift operator, $\mathbf{E}_t$, to give

$$\mathbf{A}_n \left(\frac{\partial^n f}{\partial t^n} \right)_\ell^\tau = \frac{1}{\Delta t^n} \mathbf{B}_n f_\ell^\tau + \varepsilon \tag{4.8}$$

in which

$$\mathbf{A}_n = \sum_r a_r^n \mathbf{E}_t^r \tag{4.9}$$

$$\mathbf{B}_n = \sum_m b_m^n \mathbf{E}_t^m \tag{4.10}$$

are new operators given by polynomials in $\mathbf{E}_t$ whose coefficients are unknown. Introducing a new set of operators, $\mathbf{C}$ and $\mathbf{D}$, to delineate space from time, compact spatial difference approximations are given by

$$\mathbf{C}_n \left(\frac{\partial^n f}{\partial x^n} \right)_\ell^\tau = \frac{1}{\Delta x^n} \mathbf{D}_n f_\ell^\tau + \varepsilon \tag{4.11}$$

in which

$$\mathbf{C}_n = \sum_r c_r^n \mathbf{E}_x^r \tag{4.12}$$

$$\mathbf{D}_n = \sum_m d_m^n \mathbf{E}_x^m \tag{4.13}$$

Compact difference approximations (4.8) and (4.11) are employed in the subsequent chapter during implementation. The remainder of this chapter focuses on the development and analysis of compact difference approximations using schemes commonly found in the literature as a basis for discussion. As a subset of the compact configuration, classic schemes are included for comparison purposes.

Herein, the coefficients are derived using the so-called method of undetermined coefficients (e.g., LeVeque 2007), in which coefficients of the shift operator series $(1 + \mathbf{Q}^1 + \mathbf{Q}^2 + \ldots)$ on the left hand side are set equal to those on the right hand side with the corresponding differential operator. An example application for the first spatial derivative, $n = 1$, is presented below for stencils of observation points consisting of three neighboring derivatives of the dependent variable and five

neighboring dependent variables

$$\begin{bmatrix} 0 & 0 & 0 \\ 1 & 1 & 1 \\ r_1 & r_2 & r_3 \\ \frac{r_1^2}{2} & \frac{r_2^2}{2} & \frac{r_3^2}{2} \\ \frac{r_1^3}{3!} & \frac{r_2^3}{3!} & \frac{r_3^3}{3!} \\ \vdots & \vdots & \vdots \end{bmatrix} \begin{bmatrix} c_{r_1} \\ c_{r_2} \\ c_{r_3} \end{bmatrix} = \begin{bmatrix} 1 & 1 & 1 & 1 & 1 \\ m_1 & m_2 & m_3 & m_4 & m_5 \\ \frac{m_1^2}{2} & \frac{m_2^2}{2} & \frac{m_3^2}{2} & \frac{m_4^2}{2} & \frac{m_5^2}{2} \\ \frac{m_1^3}{3!} & \frac{m_2^3}{3!} & \frac{m_3^3}{3!} & \frac{m_4^3}{3!} & \frac{m_5^3}{3!} \\ \frac{m_1^4}{4!} & \frac{m_2^4}{4!} & \frac{m_3^4}{4!} & \frac{m_4^4}{4!} & \frac{m_5^4}{4!} \\ \vdots & \vdots & \vdots & \vdots & \vdots \end{bmatrix} \begin{bmatrix} d_{m_1} \\ d_{m_2} \\ d_{m_3} \\ d_{m_4} \\ d_{m_5} \end{bmatrix} \tag{4.14}$$

in which $\{r_j, m_j | j \in \mathbb{N}\}$ correspond to indices of an arbitrary stencil configuration. Each row represents an equation corresponding to the differential operator $(1, \partial_x, \partial_{xx}, \partial_{xxx}, \ldots)$, whereas each column represents a neighboring observation point in the regular mesh. Given eight unknown coefficients, eight equations can be prescribed to produce a linear system of equations. In this particular example, it will be assumed that $\{r_1, r_2, r_3\} = \{-1, 0, 1\}$ and $\{m_1, m_2, m_3, m_4, m_5\} = \{-2, -1, 0, 1, 2\}$, such that each stencil is centered. The coefficients c_r are constrained to be symmetric, whereas the coefficients d_m are constrained to be skew-symmetric, which provides four of eight equations. An additional constraint, $c_0 = 1$, asserts that the coefficient of the first derivative operator, ∂_x, on the left hand side is unity. These constraints directly reflect the stencil configuration, leaving the need for three equations. Substituting the index values and constraints into (4.14) gives

$$\begin{bmatrix} 0 & 0 & 0 \\ 1 & 1 & 1 \\ -1 & 0 & 1 \\ \frac{1}{2} & 0 & \frac{1}{2} \\ -\frac{1}{3!} & 0 & \frac{1}{3!} \\ \vdots & \vdots & \vdots \end{bmatrix} \begin{bmatrix} c_{-1} \\ 1 \\ c_{-1} \end{bmatrix} = \begin{bmatrix} 1 & 1 & 1 & 1 & 1 \\ -2 & -1 & 0 & 1 & 2 \\ 2 & \frac{1}{2} & 0 & \frac{1}{2} & 2 \\ -\frac{8}{3!} & -\frac{1}{3!} & 0 & \frac{1}{3!} & \frac{8}{3!} \\ \frac{16}{4!} & \frac{1}{4!} & 0 & \frac{1}{4!} & \frac{16}{4!} \\ \vdots & \vdots & \vdots & \vdots & \vdots \end{bmatrix} \begin{bmatrix} d_{-2} \\ d_{-1} \\ 0 \\ -d_{-1} \\ -d_{-2} \end{bmatrix} \tag{4.15}$$

Truncating the series after three nontrivial equations are obtained, the unique solution is given by $\{c_{-1}, d_{-2}, d_{-1}\} = \{1/3, -1/36, -7/9\}$, which represents coefficient values for the left half of the configuration. The local truncation error is given by the next nontrivial equation in the series. In the particular case above, this occurs at the seventh derivative, which after dividing by Δx in (4.11)

gives $\varepsilon = O(\Delta x^6)$ to characterize the error of approximation. Also, since the equation for the local truncation error is a function of the coefficients, an explicit expression can be obtained. The parity of the derivative in the local truncation error is odd, thus the leading order error is dispersive. Furthermore, since the coefficients for all even derivatives are equal to zero, the approximation is nondissipative. The latter result is from the symmetrical constraints imposed on the stencil configuration.

The method of undetermined coefficients is able to generate both temporal and spatial finite difference schemes with compact support. However, if the stencils become too large, the method can suffer from numerical instabilities (e.g., LeVeque 2007), in which case the methods of Fornberg (1998) are recommended. Nevertheless, stencil sizes under consideration herein are relatively small, thus the method of undetermined coefficients will suffice.

4.2 Fourier-Laplace

The frequency dispersion relation (3.56) is derived in spectral space upon application of Fourier-Laplace Derivative Theorems to the differential operators in the linearized PDEs. In this section, the same methods are applied to the compact difference operators, which effectively maps the MPDEs into spectral space for analysis in the subsequent chapter.

Applying the Laplace Derivative theorem (D.7) to the compact difference approximation (4.8) gives

$$\widetilde{\mathbf{A}}_n \, (-i\omega)^n \, \widetilde{f}_\ell^\tau = \frac{1}{\Delta t^n} \widetilde{\mathbf{B}}_n \widetilde{f}_\ell^\tau + \varepsilon \tag{4.16}$$

in which

$$\widetilde{\mathbf{A}}_n = \sum_r a_r^n \widetilde{\mathbf{E}_t^r} \tag{4.17}$$

$$\widetilde{\mathbf{B}}_n = \sum_m b_m^n \widetilde{\mathbf{E}_t^m} \tag{4.18}$$

The transform of the shift operator, for example, $\widetilde{\mathbf{E}_t^r}$, is given by $e^{-i\omega(r\Delta t)}$, which is consistent with the Laplace Shift Theorem (D.8) for an arbitrary displacement. Solving for the continuous angular frequency in the algebraic system gives

$$(-i\omega)^n \, \widetilde{f}_\ell^\tau = \frac{1}{\Delta t^n} \frac{\widetilde{\mathbf{B}}_n}{\widetilde{\mathbf{A}}_n} \widetilde{f}_\ell^\tau + \varepsilon \tag{4.19}$$

which implies

$$\overline{\omega^n} = \left(\frac{i}{\Delta t}\right)^n \frac{\widetilde{\mathbf{B}}_n}{\widetilde{\mathbf{A}}_n} = \left(\frac{i}{\Delta t}\right)^n \frac{\sum_m b_m^n e^{-i\omega(m\Delta t)}}{\sum_r a_r^n e^{-i\omega(r\Delta t)}} \tag{4.20}$$

The newly introduced variable, $\overline{\omega^n}$, is the effective angular frequency of the compact difference operator, which is a function of the stencil configurations and sampling interval. Note that a subscript under the over-line associates the difference operator with the n^{th} derivative approximation, not the operator raised to a power. In other words, for example, $\overline{\omega^2} \neq \overline{\omega^1}^2$, in the general case. The expression on the right hand side of (4.20) is a generalization to that given by C. Tam and Webb (1993) for an approximation of the first time derivative.

The same methodology holds for the derivation of compact spatial difference operators. Applying the Fourier Derivative theorem (D.3) to (4.11) gives

$$\widetilde{\mathbf{C}}_n (ik)^n \widetilde{f}_\ell^\tau = \frac{1}{\Delta x^n} \widetilde{\mathbf{D}}_n \widetilde{f}_\ell^\tau + \varepsilon \tag{4.21}$$

in which

$$\widetilde{\mathbf{C}}_n = \sum_r c_r^n \widetilde{\mathbf{E}_x^r} \tag{4.22}$$

$$\widetilde{\mathbf{D}}_n = \sum_m d_m^n \widetilde{\mathbf{E}_x^m} \tag{4.23}$$

Solving for the continuous wave number in the algebraic system gives

$$(ik)^n \widetilde{f}_\ell^\tau = \frac{1}{\Delta x^n} \frac{\widetilde{\mathbf{D}}_n}{\widetilde{\mathbf{C}}_n} \widetilde{f}_\ell^\tau + \varepsilon \tag{4.24}$$

which implies

$$\overline{k^n} = \left(\frac{-i}{\Delta x}\right)^n \frac{\widetilde{\mathbf{D}}_n}{\widetilde{\mathbf{C}}_n} = \left(\frac{-i}{\Delta x}\right)^n \frac{\sum_m d_m^n e^{ik(m\Delta x)}}{\sum_r c_r^n e^{ik(r\Delta x)}} \tag{4.25}$$

Like the effective angular frequency, the effective wave number, $\overline{k^n}$, is a function of the stencil configurations and sampling interval. Again, a subscript under the over-line associates the difference operator with the n^{th} derivative approximation, not the operator raised to a power. The expression on the right hand side of (4.25) is a generalization to that given by C. Tam and Webb (1993) for an approximation of the first space derivative. Therefore, definitions (4.20) and (4.25) are consistent with those found in the literature.

The effective angular frequency (4.20) and wave number (4.25) can be expressed in dimensionless form as

$$\overline{\omega^n}\Delta t^n = i^n \frac{\widetilde{\mathbf{B}}_n}{\widetilde{\mathbf{A}}_n} = \frac{i^n \sum_m b_m^n e^{-im(\omega\Delta t)}}{\sum_r a_r^n e^{-ir(\omega\Delta t)}} \tag{4.26}$$

$$\overline{k^n}\Delta x^n = (-i)^n \frac{\widetilde{\mathbf{D}}_n}{\widetilde{\mathbf{C}}_n} = \frac{(-i)^n \sum_m d_m^n e^{im(k\Delta x)}}{\sum_r c_r^n e^{ir(k\Delta x)}} \tag{4.27}$$

Given a set of stencil configurations and coefficients, the dimensionless effective angular frequency and wave number are solely functions of the dimensionless angular frequency, $\omega\Delta t$, and wave number, $k\Delta x$, respectively. The sampling theory states that the smallest resolvable physical scale is twice the sampling interval, which bounds the domain of $\omega\Delta t$ and $k\Delta x$ to $[-\pi, \pi]$ in the difference approximations (e.g., Meijering 2002). Figure 4.3 provides a visual aid to understand the role of (4.26) and (4.27) in spectral space. As shown, take for example an operator element in the continuum, $\omega\Delta t$ or $k\Delta x$, on the positive real axis. The difference approximation maps the domain element on the continuum to a new element representing its approximation over the codomain. The stencil configuration and coefficients ultimately define where the element is mapped to. In general, the polynomial structure of the difference approximation is not one-to-one, in which there multiple root solutions that lead to the same approximation over the codomain. In the schematic on the right of Figure 4.3, the approximation element is mapped back to the continuum, in which one of the roots, referred to as the physical root, recovers the original operator value, with the other roots being so-called parasitic. The root solutions ultimately reflect the linear characteristics of the numerical solution, thus it is paramount to understand their manifestation.

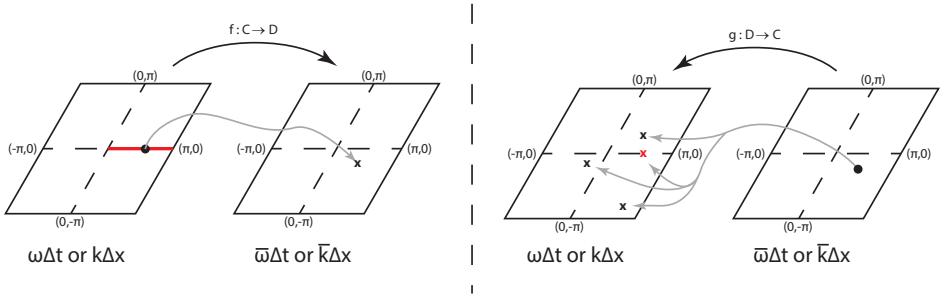

Figure 4.3: Schematic mapping of: (left) an operator in the continuum (C) to its complex difference approximation (D), and (right) the complex difference approximation back to its complex root solutions in the continuum. The red line highlights the positive real axis.

To quantify the spectral performance of the difference approximations, the notion of resolvable bandwidth is introduced to represent the range over which $\overline{\omega^n}\Delta t^n$ and $\overline{k^n}\Delta x^n$ preserves $(\omega\Delta t)^n$ and $(k\Delta x)^n$ within prescribed tolerances. In the next section, stencil configurations and coefficients are presented in order to analyze the resolvable bandwidth of several finite difference schemes found

throughout the literature.

4.3 Operator Schemes

Compact stencils host a liberal framework for constructing diverse finite difference schemes, which are characterized by the stencil configuration and corresponding coefficients. Schemes are essentially algorithms, weighing information as ingredients and combining them in an orchestrated recipe. As implied by the indices (e.g., see (4.8) or (4.11)), compact stencils employ information on a function and its derivatives at neighboring mesh points, leading to an implicit approximation (e.g., Lele 1992). Disregard of the derivative in question at neighboring mesh points reduces degrees of freedom and results in an explicit approximation. The information can manifest from existing mesh points or through successive approximations whose intermediate steps need not obey consistency and stability constraints (e.g., Yanenko and Holt 1971). Nevertheless, as long as consistency and stability are maintained with each application of the algorithm, the scheme is convergent (e.g., Richtmyer and Morton 1967). What dictates implementation of a scheme in practice is the resolvable characteristics weighted against the computational cost, leaving the practitioner to make an informed decision.

The objective of this section is to illuminate linear dispersive and dissipative characteristics for select finite difference schemes commonly found in the literature through (4.26) and (4.27), which are linked to the sampling intervals employed in practical application. Focus is directed on schemes which vary in configuration, including: 1) non dissipative central, and 2) bias schemes which exhibit both dispersive and dissipative errors. Although not explicitly shown herein, coefficients associated with all configurations under consideration are derived by applying the method of undetermined coefficients (e.g., see 4.14) with the objective of achieving the highest formal order of accuracy for a given configuration. For compact schemes, this objective results in Padé approximations (e.g., Kopal 1961; Collatz 1966; Lele 1992). While some of the classic schemes covered herein have been employed in Boussinesq-type applications in the past, little attention has been directed on the fundamental nature of the resolvable characteristics and how they modify the governing PDEs in connection with the sampling intervals invoked by practitioners. Furthermore, implementation of compact difference approximations appear to be new in the practical application of Boussinesq-type equations. The operator analysis carried out in this section lays the foundation for the fully discrete analysis in the subsequent chapter.

4.3.1 Central Schemes

Boussinesq-type equations are inherently non dissipative. Therefore, it is natural to seek out non dissipative difference approximations which adhere to the physics. Schemes which map to the real axis following Fourier-Laplace transforms maintain the dispersive, or dissipative, nature of the operator in question. For schemes which map to the imaginary axis, the approximations are in opposition, meaning dispersive operators are approximated by dissipative processes and dissipative operators are approximated by dispersive processes. In general, schemes which map to complex values in spectral space posses both dispersive and dissipative processes.

On a regular mesh considered herein, the simplest approach to derive real central schemes is to impose symmetrical constraints on the coefficients, as was showcased by example in the method of undetermined coefficients (4.14) above. Depending on the differential operator being approximated, the form of symmetry varies. For odd derivatives, the function coefficients are skew-symmetric about the point of approximation, whereas for even derivatives the function coefficients exhibit bilateral symmetry about the point of approximation. In a compact stencil, coefficients of the derivative in question at neighboring points also exhibit bilateral symmetry about the point of approximation (Lele 1992).

In the application of Boussinesq-type equations, the most common implementation of central schemes is in the context of spatial difference approximations. Below, several schemes are reviewed for approximations to the first, second, and third derivative, with the latter being the highest spatial derivative contained in the governing PDEs herein.

Table 4.1 lists several schemes for central difference approximations to the first derivative, with the first four representing classic explicit schemes. These schemes only employ known information on a function at neighboring mesh points. The last four listed represent compact implicit schemes (e.g., Lele 1992), which contain additional unknown information on the derivative of the function at neighboring mesh points, leading to a narrow banded system of equations. For a given amount of information covered by the stencils, the order of truncation error, which defines how quickly the error decreases with decreasing step size, is the same for both explicit and implicit schemes and grows linearly with additional information.

The table summary is often all that is conveyed to model developers, which in itself is sufficient to build difference approximations. However, it does not tell the whole story. First, for a given amount of information covered by the stencils, comparing the order of truncation error gives the impression that implicit schemes are no better than explicit ones. Second, the order of truncation error is only associated with the leading order error term, whose physical behavior is governed by ∂^{O+1} for the central schemes shown, with O denoting the order listed in the table. Being an odd derivative, the behavior is dispersive. While this knowledge is informative, the corresponding coefficient and

Bilateral Information	$O(\Delta x)$	c_1^1	c_2^1	d_1^1	d_2^1	d_3^1	d_4^1
□ = ● | ●	2			1/2			
□ = ● | ● | ●	4			2/3	-1/12		
□ = ● | ● | ● | ●	6			3/4	-3/20	1/60	
□ = ● | ● | ● | ● | ●	8			4/5	-1/5	$\frac{4}{105}$	$-\frac{1}{280}$
□ | □ = ● | ●	4	1/4		3/4			
□ | □ = ● | ● | ●	6	1/3		7/9	1/36		
□ | □ | □ = ● | ● | ●	8	4/9	1/36	$\frac{20}{27}$	$\frac{25}{216}$		
□ | □ | □ = ● | ● | ● | ●	10	1/2	1/20	$\frac{17}{24}$	$\frac{101}{600}$	$\frac{1}{600}$	

Table 4.1: Stencil configuration and corresponding coefficients for select central difference approximations to the first derivative. Due to symmetry in the configuration, only the right half of the stencils are shown. The circle and square symbols respectively denote the function and its derivative at the mesh points. Symbols colored red denote the point of approximation (i.e. 0-index). Unfilled symbols denote unknown information. The coefficients for the left half of the stencils are given by $c^1_{-j} = c^1_j$ and $d^1_{-j} = -d^1_j$, with the latter being a skew-symmetric relation due to the first derivative approximation. For all configurations shown, $c^1_0 = 1$ and $d^1_0 = 0$.

overall trending behavior beyond the leading order (e.g. phase lead/lag, amplitude growth/decay) are also significant. Characteristics of the leading order truncation error can be bundled into the concept of "accuracy in the small", but one of the best practical ways of understanding the error is to view "accuracy in the large" in spectral space (e.g., Vichnevetsky and De Schutter 1975).

Figure 4.4a plots the resolvable bandwidth (4.27) over the domain $k\Delta x \in [0, \pi]$ for the difference schemes summarized in Table 4.1 above. It is here where the fundamental advantage of implicit schemes becomes clear. While all schemes reveal an increase in resolvable bandwidth with increasing order of approximation, the implicit schemes exhibit a significant increase given the same amount of information covered by the stencil configuration. Calculating the relative error and limiting the ordinate to $\pm 0.1\%$ error, Figure 4.4b reveals the trending behaviour of the leading order truncation error, in which all approximations result in a phase lag with monotonic decay. Comparing the classic $O(\Delta x^4)$ explicit scheme with the compact $O(\Delta x^4)$ implicit scheme, the resolvable bandwidth has increased by nearly 40% and Figure 4.4a shows that it even exceeds the classic $O(\Delta x^6)$ scheme at a higher tolerance for error, becoming comparable to the classic $O(\Delta x^8)$ scheme.

The use of high-order schemes to reduce dispersive errors (i.e. increase resolvable bandwidth) has long been known. In the early works by Kreiss and Oliger (1972), approximate solutions to

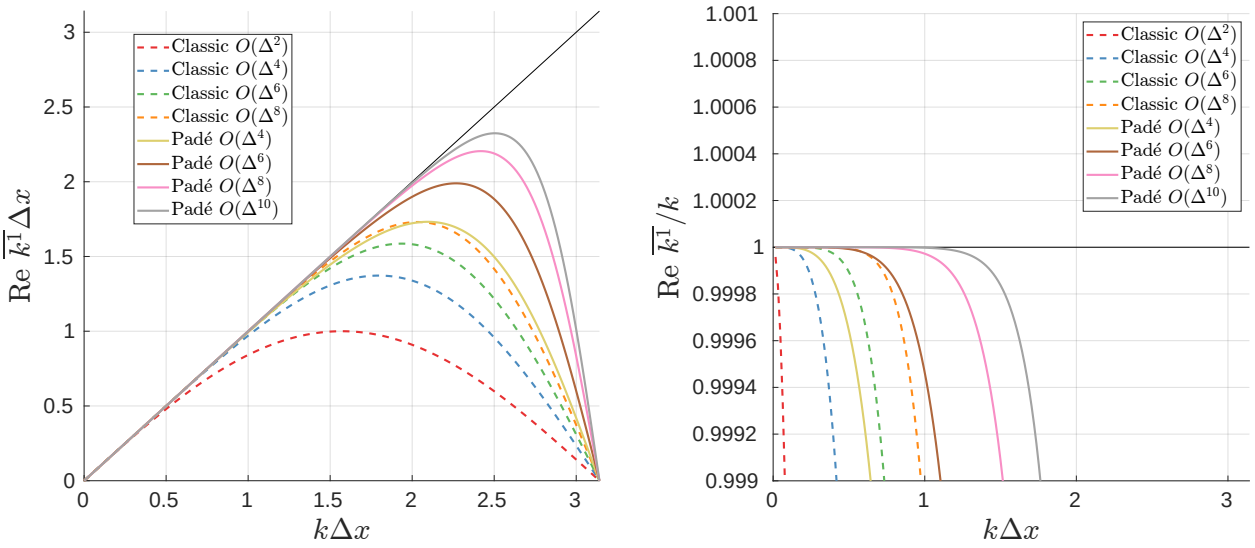

(a) "Accuracy in large"

(b) "Accuracy in small"

Figure 4.4: Resolvable bandwidth of the respective central schemes covered in Table 4.1 over (a) the full domain and (b) to within ±0.1% relative error. Exact solutions are denoted by the solid black line.

linear first order hyperbolic equations were evaluated using classic $O(\Delta x^2)$, $O(\Delta x^4)$, and $O(\Delta x^6)$ central schemes. The relative performance of each scheme was quantified based on an established tolerance for error and number of wave periods to simulate. It was determined that computational complexity increases proportional to the order of accuracy, however the increase in wave number resolution is at a lesser rate. Figure 4.4 clearly supports these observations. Kreiss and Oliger (1972) considered the classic $O(\Delta x^4)$ scheme an optimal compromise between wave number resolution and computation effort. While higher order schemes theoretically apply, the practical advantage in employing classic schemes beyond $O(\Delta x^6)$ to improve wave number resolution was considered futile and it was suggested to seek out alternative methods. The compact schemes presented by Lele (1992) clearly present a viable option. That being said, compact schemes also display the same underlying trend observed by Kreiss and Oliger (1972), in which the order increases at a rate faster than the wave number resolution. By analogy, this would suggest that amongst the compact schemes shown, the $O(\Delta x^6)$ scheme offers an optimal compromise between wave number resolution and computation effort.

Table 4.2 lists several schemes for central difference approximations to the second derivative. Like Table 4.1, the first four schemes represent classic explicit schemes and the last four represent compact implicit schemes. In general, the observations are more or less the same as that for the first derivative, thus omitted for brevity.

Figure 4.5a plots the resolvable bandwidth (4.27) over the domain $k\Delta x \in [0, \pi]$ for the difference

Bilateral Information	$O(\Delta x)$	c_1^2	c_2^2	d_0^2	d_1^2	d_2^2	d_3^2	d_4^2
□ = ● | ●	2			-2	1			
□ = ● | ● | ●	4			-5/2	4/3	-1/12		
□ = ● | ● | ● | ●	6			$-\frac{49}{18}$	3/2	-3/20	1/90	
□ = ● | ● | ● | ● | ●	8			$-\frac{205}{72}$	8/5	-1/5	$\frac{8}{315}$	$-\frac{1}{560}$
□ | □ = ● | ●	4	1/10		-12/5	6/5			
□ | □ = ● | ● | ●	6	2/11		$-\frac{51}{22}$	$\frac{12}{11}$	3/44		
□ | □ | □ = ● | ● | ●	8	$\frac{344}{1179}$	$\frac{23}{2358}$	$-\frac{265}{131}$	$\frac{320}{393}$	$\frac{155}{786}$		
□ | □ | □ = ● | ● | ● | ●	10	$\frac{334}{899}$	$\frac{43}{1798}$	$-\frac{14335}{8091}$	$\frac{1065}{1798}$	$\frac{519}{1798}$	$\frac{79}{16182}$	

Table 4.2: Stencil configuration and corresponding coefficients for select central difference approximations to the second derivative. See Table 4.1 caption for symbolic notation. The coefficients for the left half of the stencils are given by $c_{-j}^2 = c_j^2$ and $d_{-j}^2 = d_j^2$, with the latter being a bilateral symmetric relation due to the second derivative approximation. For all configurations shown, $c_0^2 = 1$.

schemes summarized in Table 4.2 above. As was observed for the first derivative approximation, the compact implicit schemes in general support a higher bandwidth resolution as compared to their explicit counterparts. However, the improvement in bandwidth resolution is noticeably less. Comparing the classic $O(\Delta x^4)$ explicit scheme with the compact $O(\Delta x^4)$ implicit scheme in Figure 4.5b shows the resolvable bandwidth has increased by about 20%, which is still a significant improvement, but about half that for the approximation to the first derivative. All other observations are consistent with those made for the first derivative approximation. It is also observed that the second difference approximations in general have a higher resolvable bandwidth than the first difference approximations. Therefore, for a given dimensionless wave number, $k\Delta x$, the errors in the first difference approximation would be larger than those for the second.

Table 4.3 lists several schemes for central difference approximations to the third derivative. The first three schemes represent classic explicit schemes and the remaining represent compact implicit schemes. Also being odd, the schemes share a lot of same properties as the first difference approximations. However, for a given amount of information covered by the stencils, the third difference approximations are two orders less. In general, this linear trend continues with higher order derivatives requiring more information for a given order of approximation. This is one reason why alternative theoretical (e.g., P. Lynett and P. Liu 2004) and numerical (e.g., Fuhrman and Bingham

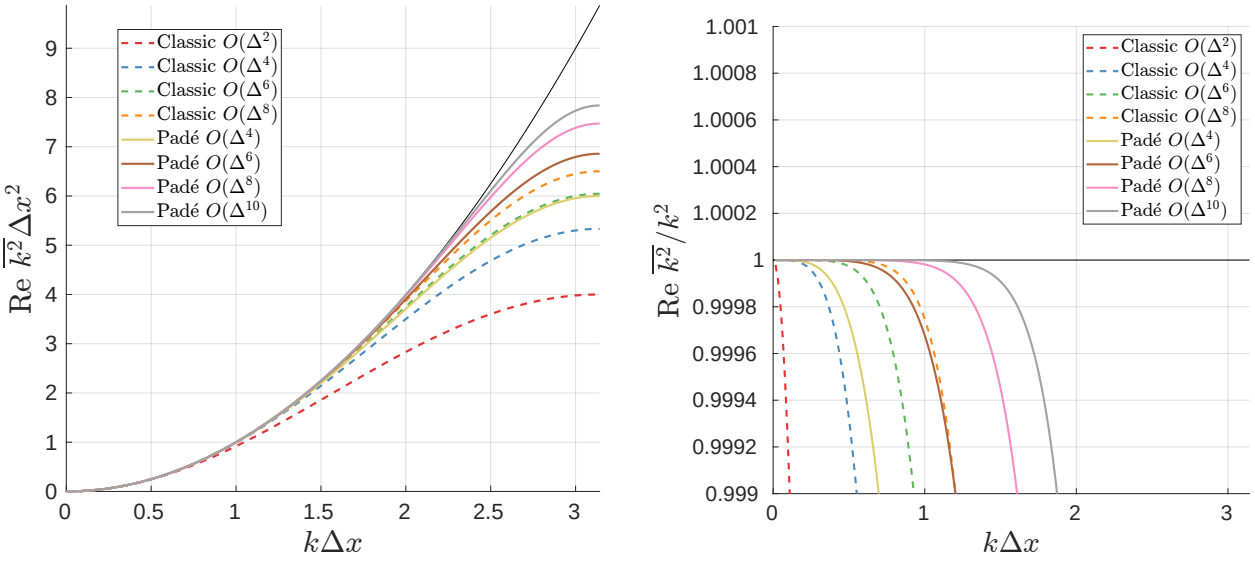

(a) "Accuracy in large"

(b) "Accuracy in small"

Figure 4.5: Resolvable bandwidth of the respective central schemes covered in Table 4.2 over (a) the full domain and (b) to within ±0.1% relative error. Exact solutions are denoted by the solid black line.

2004; Bingham and Agnon 2005) approaches have been proposed for highly dispersive Boussinesq-type equations. It is also what makes the work of Schaffer and P. A. Madsen (1995b) discussed earlier in Chapter 3 attractive. Unlike Gobbi et al. (2000), which employs fifth derivatives, the theory utilizes at most third derivatives to achieve a theoretical frequency dispersion valid beyond the traditional deep water limit. Nevertheless, the method of undetermined coefficients employed herein poses no issues in deriving difference approximations to fifth derivatives for both classic explicit and compact implicit schemes.

Table 4.4 is an extension of Table 4.3, which includes coefficients for the compact penta-diagonal implicit schemes. Comparing the compact $O(\Delta x^6)$ and $O(\Delta x^8)$ configuration stencils, the penta-diagonal schemes carry more information on the derivative and less on the function than their tri-diagonal counter parts. Despite sharing the same order of approximation, this makes them unique, and thus their resolvable bandwidths are also unique.

Figure 4.6a plots the resolvable bandwidth (4.27) over the domain $k\Delta x \in [0, \pi]$ for the difference schemes summarized in Tables 4.3 and 4.4 above. As was observed for the first and second derivative approximations, the compact implicit schemes support a higher bandwidth resolution in comparison to their explicit counter parts of equal order. This trend appears to be an intrinsic property of compact schemes. Contrary to the first and second difference approximations, the compact $O(\Delta x^4)$ implicit scheme not only shows a phase lead, but one which is monotonically increasing over the domain. This illustrates the importance of analyzing the schemes in spectral space, in which

Bilateral Information	$O(\Delta x)$	c_1^3	d_1^3	d_2^3	d_3^3	d_4^3	d_5^3
□ = ● | ● | ●	2		-1	1/2			
□ = ● | ● | ● | ●	4		-13/8	1	-1/8		
□ = ● | ● | ● | ● | ●	6		$-\frac{61}{30}$	$\frac{169}{120}$	-3/10	$\frac{7}{240}$	
□ = ● | ● | ● | ● | ● | ●	8		$-\frac{1669}{720}$	$\frac{4369}{2520}$	$-\frac{541}{1120}$	$\frac{105}{1259}$	$-\frac{41}{6048}$
□ | □ = ● | ● | ●	4	1/2	-2	1			
□ | □ = ● | ● | ● | ●	6	7/16	$-\frac{125}{64}$	1	-1/64		
□ | □ = ● | ● | ● | ● | ●	8	$\frac{205}{472}$	$-\frac{4558}{2333}$	$\frac{2367}{2360}$	$-\frac{167}{9440}$	$\frac{1}{4720}$	
□ | □ | □ = ● | ● | ●	6	See Table 4.4 Below					
□ | □ | □ = ● | ● | ● | ●	8	See Table 4.4 Below					
□ | □ | □ = ● | ● | ● | ● | ●	10	See Table 4.4 Below					

Table 4.3: Stencil configuration and corresponding coefficients for select central difference approximations to the third derivative. See Table 4.1 caption for symbolic notation. The coefficients for the left half of the stencils are given by $c^3_{-j} = c^3_j$ and $d^3_{-j} = -d^3_j$, with the latter being a skew-symmetric relation due to the third derivative approximation. For all configurations shown, $c^3_0 = 1$ and $d^3_0 = 0$.

$O(\Delta x)$	c_1^3	c_2^3	d_1^3	d_2^3	d_3^3	d_4^3
6	$\frac{4}{9}$	$\frac{1}{126}$	$-\frac{40}{21}$	$\frac{20}{21}$		
8	$\frac{147}{332}$	$\frac{1}{166}$	$-\frac{2545}{1328}$	$\frac{80}{83}$	$-\frac{5}{1328}$	
10	$\frac{799}{2739}$	$-\frac{557}{5478}$	$-\frac{1165}{451}$	$\frac{1713}{1030}$	$-\frac{300}{1187}$	$\frac{1}{264}$

Table 4.4: Coefficients for $O(\Delta x^6)$, $O(\Delta x^8)$, and $O(\Delta x^{10})$ penta-diagonal implicit schemes illustrated in Table 4.3 above.

the order of truncation error alone fails to convey this information. For compact implicit schemes whose order is greater than $O(\Delta x^4)$, the behavior changes in which there is a phase lag approaching the Nyquist limit. However, upon closer review, Figure 4.6b reveals that the compact $O(\Delta x^6)$ tri-diagonal implicit scheme is not monotonic, having one inflection point. While it is beyond the scope of this study to give an analytic explanation, the plots indicate the phase error of the tri-diagonal implicit schemes starts out with a lead error then traverses to a lag error. This is clear when

comparing the compact $O(\Delta x^4)$, $O(\Delta x^6)$, and $O(\Delta x^8)$ tri-diagonal implicit schemes. Interestingly, the resolvable bandwidth of the compact $O(\Delta x^6)$ tri-diagonal implicit scheme is greatly improved as a result of the transitioning behavior. As will be discussed in next section, the characteristics mirror those resulting from bandwidth optimization with a single degree of freedom, although all degrees of freedom have been exhausted to maximize the local truncation error. In terms of bandwidth resolution over the range of relative error shown, the compact $O(\Delta x^6)$ tri-diagonal implicit scheme is better than the compact $O(\Delta x^{10})$ penta-diagonal implicit scheme, with the latter being the highest evaluated herein. Judging from the rate of increase in resolvable bandwidth for the compact $O(\Delta x^6)$, $O(\Delta x^8)$, and $O(\Delta x^{10})$ penta-diagonal implicit schemes, it is likely that the resolvable bandwidth of the compact $O(\Delta x^6)$ tri-diagonal implicit scheme exceeds even high order schemes. Nevertheless, this makes the compact $O(\Delta x^6)$ implicit scheme very attractive. Furthermore, the bandwidth resolution of the compact $O(\Delta x^6)$ implicit scheme is more than twice that of the classic $O(\Delta x^6)$ explicit scheme for the same amount of information covered by the stencil.

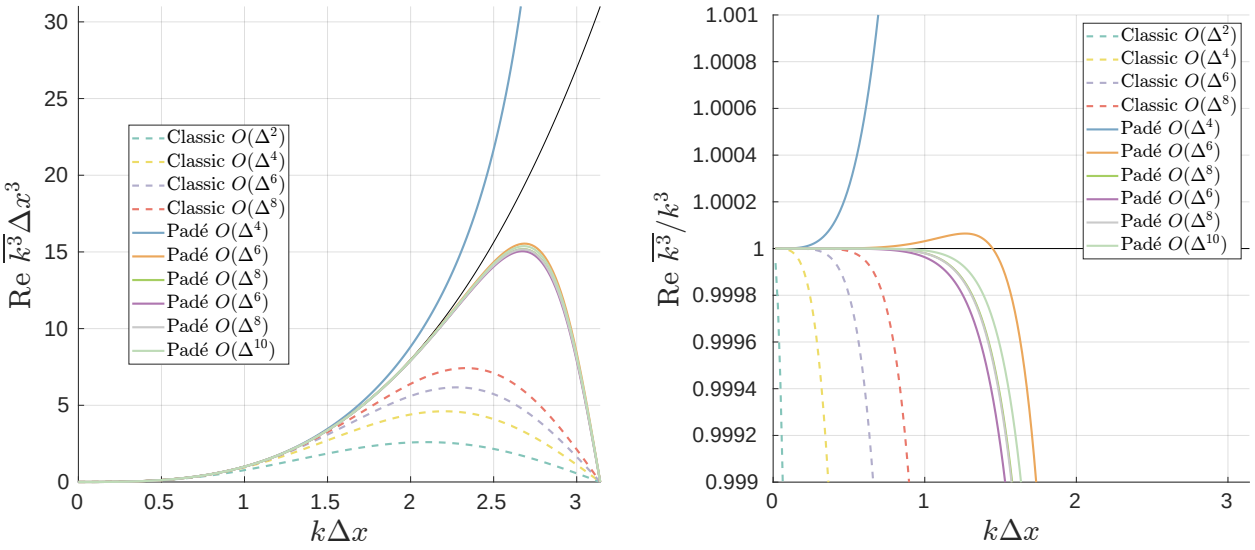

(a) "Accuracy in large" (b) "Accuracy in small"

Figure 4.6: Resolvable bandwidth of the respective central schemes covered in Tables 4.3 and 4.4 over (a) the full domain and (b) to within $\pm 0.1\%$ relative error. Exact solutions are denoted by the solid black line.

It should be emphasized that the central schemes covered herein are presented in the context of spatial difference approximations. This decision was motivated by the routine implementation of central schemes in Boussinesq-type equations. However, the schemes also apply to temporal difference approximations, in which Δt is substituted for Δx without loss. The only modification needed is to identify what is known versus unknown in the configuration, but the coefficients do not change.

4.3.2 Bias Schemes

Implementation of central schemes becomes problematic along non periodic temporal or spatial boundaries. Bias stencils can be employed to address the lack of information along these boundaries by looking back at known information within the domain and utilizing it in the scheme construction. Unlike central schemes, bias schemes often map to complex values in spectral space, leading to both dispersive and dissipative errors. As mentioned prior, Boussinesq-type equations are non dissipative, therefore understanding the potential dissipative properties is of utmost interest. Herein, bias schemes are presented in the context of marching the solution forward in time, with the boundary being defined by unknown information in the future. The known information is assumed smooth and resides on the regular mesh, which facilitates the use of so-called linear multistep schemes.

Consider a linear partial differential equation of the form

$$\frac{\partial f}{\partial t} = G(f) \tag{4.28}$$

where f is an arbitrary function representing the dependent variable to be advanced in time and the function G contains spatial derivatives to be approximated by a spatial difference scheme. To numerically evaluate (4.28), two methods are considered, each of which giving rise to a family of linear multistep schemes. The first involves integrating both sides of the equation, in which the right hand side is approximated by a polynomial and a quadrature formula is applied. The second is to assume the history of f is known and apply a finite difference approximation (4.6) to the left hand side. Combining these two methods gives

$$\sum_r a_r^n G_\ell^{\tau+r} = \frac{1}{\Delta t^n} \sum_m b_m^n f_\ell^{\tau+m} + \varepsilon \tag{4.29}$$

which from an operator perspective, is identical to (4.7) with the only difference being the operator argument resulting from substituting (4.28) into the left hand side. Therefore, the general linear multistep method (4.29) exhibits compact support and forms the basis of linear multistep schemes commonly found in the literature (e.g., LeVeque 2007; Hairer et al. 2009).

Below, several linear multistep schemes are reviewed. Although these schemes are readily found in the literature, it is emphasized that the method of undetermined coefficients has been utilized herein to derive the coefficients for a given configuration. Thus, a unified approach to deriving finite difference schemes for both temporal and spatial difference approximations is verified.

The first family of linear multistep schemes reviewed are those derived by means of numerical integration. The first four schemes listed in Table 4.5 are referred to as explicit Adams-Bashforth schemes, whereas the last four are referred to as implicit Adams-Moulton schemes. Unlike the

Information	$O(\Delta t)$	a^1_{-3}	a^1_{-2}	a^1_{-1}	a^1_0	a^1_1
■ = ● | ○	1				1	
■ | ■ = ● | ○	2			-1/2	3/2	
■ | ■ | ■ = ● | ○	3		5/12	-4/3	$\frac{23}{12}$	
■ | ■ | ■ | ■ = ● | ○	4	-3/8	$\frac{37}{24}$	$-\frac{59}{24}$	$\frac{55}{24}$	
□ = ● | ○	1					1
■ | □ = ● | ○	2				1/2	1/2
■ | ■ | □ = ● | ○	3			-1/12	2/3	5/12
■ | ■ | ■ | □ = ● | ○	4		1/24	-5/24	$\frac{19}{24}$	3/8

Table 4.5: Stencil configuration and corresponding coefficients for select bias difference approximations to the first derivative. See Table 4.1 caption for symbolic notation. For all configurations shown, $b^1_0 = -1$ and $b^1_1 = 1$.

central schemes discussed prior, the symbolic red squares are filled in, indicating that G is known in (4.29) from spatial difference approximations. For a given amount of information covered by the stencils, the order of truncation error is the same for both explicit and implicit schemes and grows linearly with additional information. Contained within this family, the $O(\Delta t)$ schemes correspond to the explicit forward Euler and implicit backward Euler schemes and the $O(\Delta t^2)$ implicit scheme corresponds to the trapezoid scheme.

As mentioned prior, bias schemes often map to complex values in spectral space, leading to both dispersive and dissipative errors. Figures 4.7a and 4.7c plot the real and imaginary resolvable bandwidth (4.26) over the domain $\omega\Delta t \in [0, \pi]$ for the difference schemes summarized in Table 4.5 above. As was the case with the central schemes, the implicit schemes generally exhibit a larger resolvable bandwidth for a given amount of information. For the $(O\Delta t)$ schemes, the real curves overlap, indicating that the schemes share the same dispersive behavior. However, since the imaginary curves are different, the dissipative behavior is different. Thus uniqueness is defined by a complex value, not just the real part. In general, the analysis on the real part is the same as discussed with the central schemes, thus will not be repeated. Instead, focus is directed on Figure 4.8, which plots the complex value of (4.26) over the domain $\omega\Delta t \in [0, \pi]$. For central schemes, the respective curves would lie on the real axis due to the absence of an imaginary component. These curves bound the linear stability of the difference approximation. To identify if an enclosed region is stable, all that is needed is to test if the roots of (4.26) are stable at a point within the region (e.g.

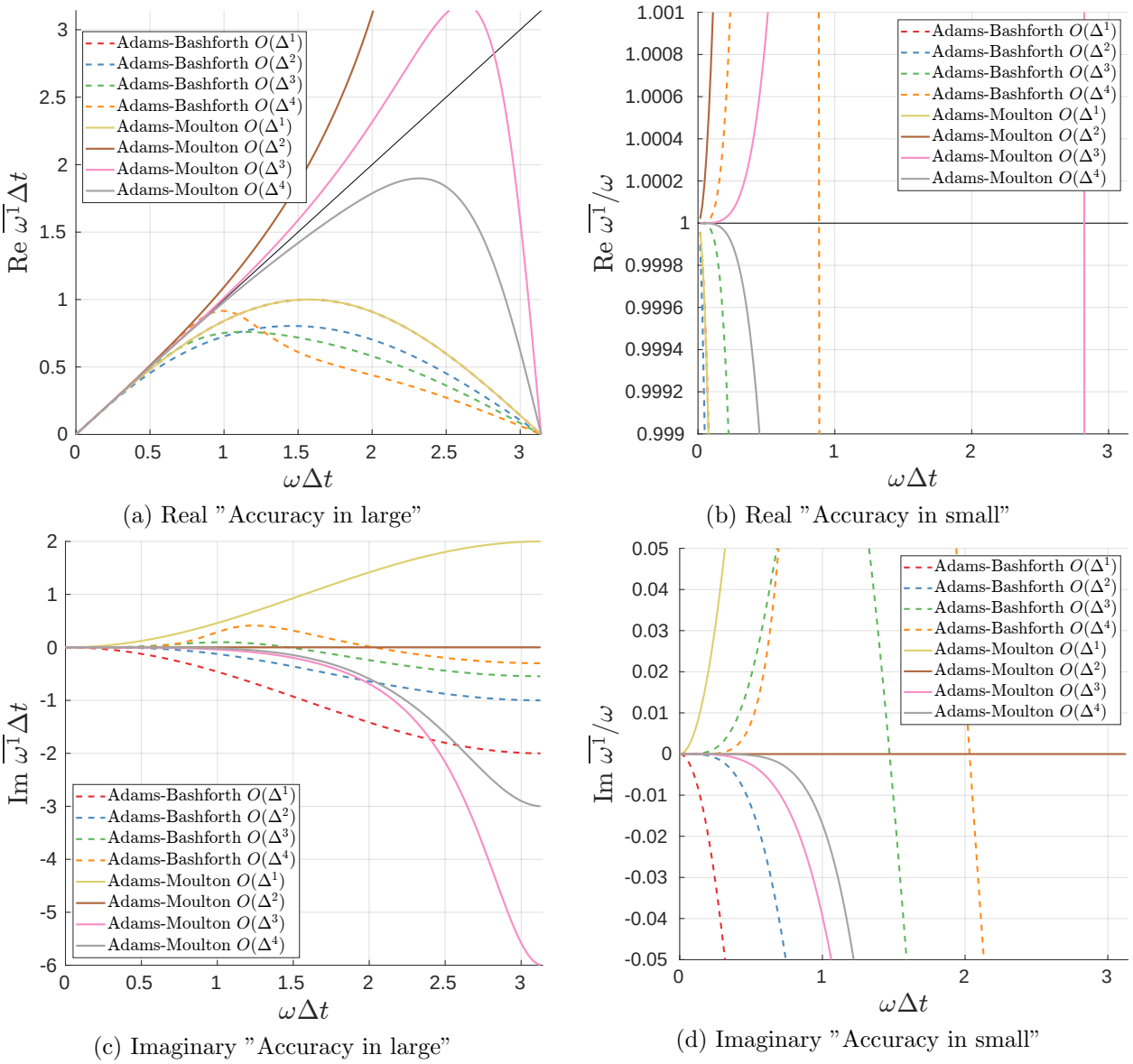

(a) Real "Accuracy in large"

(b) Real "Accuracy in small"

(c) Imaginary "Accuracy in large"

(d) Imaginary "Accuracy in small"

Figure 4.7: Resolvable bandwidth of select Adams schemes covered in Table 4.5 over (a) the full domain and (b) to within ±5% relative error. Exact solutions are denoted by the solid black line.

LeVeque 2007). To elaborate, focus is directed on the Adams-Bashforth $O(\Delta t^4)$ scheme; however the methodology applies to all schemes under consideration herein.

Whether analyzing compact central or bias schemes, it is clear that difference approximations (4.26) and (4.27) are generally represented by a rational function whose numerator and denominator comprise polynomials. As shown in Table 4.5, the polynomials are often of high order, which leads to multiple roots of the rational function. In Figure 4.9, the rational function associated with the Adams-Bashforth $O(\Delta t^4)$ scheme is plotted over the complex plane (Wegert 2012). Although classic

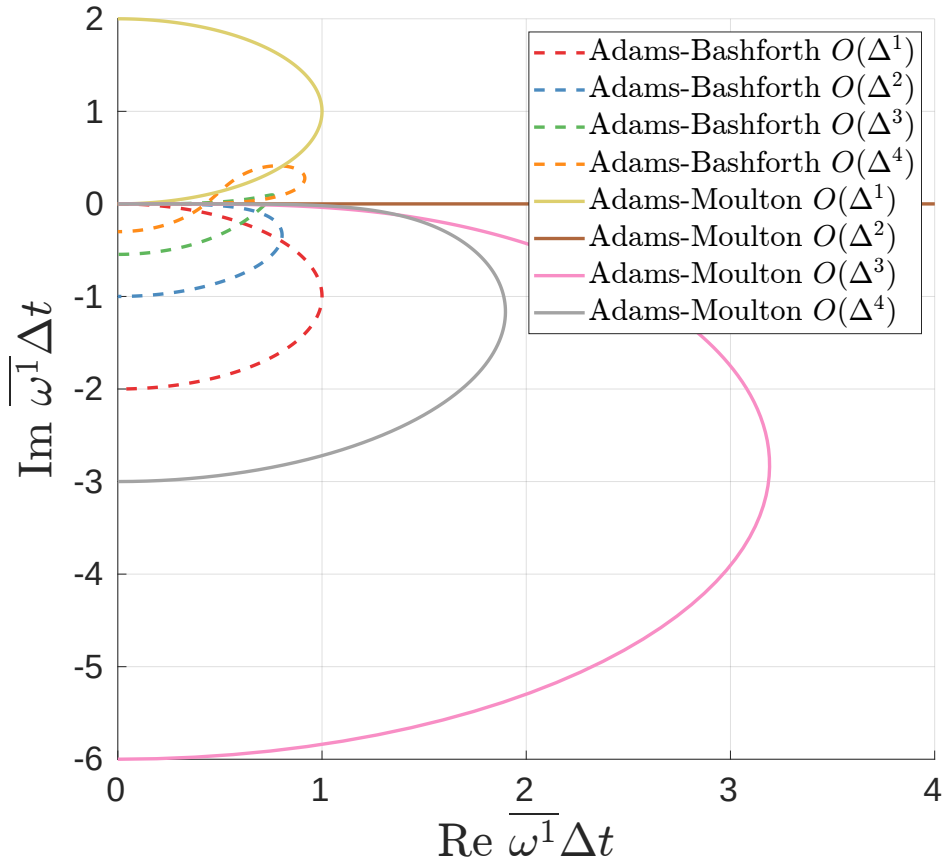

Figure 4.8: Plot of $\overline{\omega^1}\Delta t$ as a function of $\omega\Delta t \in [0, \pi]$ over the complex plane.

interest lies along the real $\omega\Delta t$ axis, in which both ω and Δt are assumed real based on physical grounds, the function domain extends over the complex plane. In this perspective, a zero and three poles are identified, located at 0 and approximately $-0.898i, \pm 1.0182 - 0.45605i$ respectively. Visually, the zeros and poles are easily identified upon acknowledging the phase legend is periodic. Assume a clockwise rotation on the color wheel is defined by traversing down the color bar (green, yellow, red, etc.). If while circumnavigating the zero or pole in question the colors follow the same clockwise ordering, it is a zero, otherwise it is a pole (Wegert 2012). The white x's and o's shown denote the calculated values for verification.

Supplemental to decipher Figure 4.9, Figure 4.10 depicts a component breakdown along the domain $\omega\Delta t \in [0, \pi]$ highlighted by the white solid line. Traversing from the function zero, located at the origin, the function magnitude increases until reaching a maximum near $\omega\Delta t = 1$, which is represented in Figure 4.9 by the potential contours with the dark to light shading in each cell representing an increase in magnitude. Beyond the maximum value, the magnitude decreases with the shading going from light to dark in each cell. The phase starts off at effectively zero, which is represented in Figure 4.9 by the red coloring. The phase slightly increases to a reddish-orange,

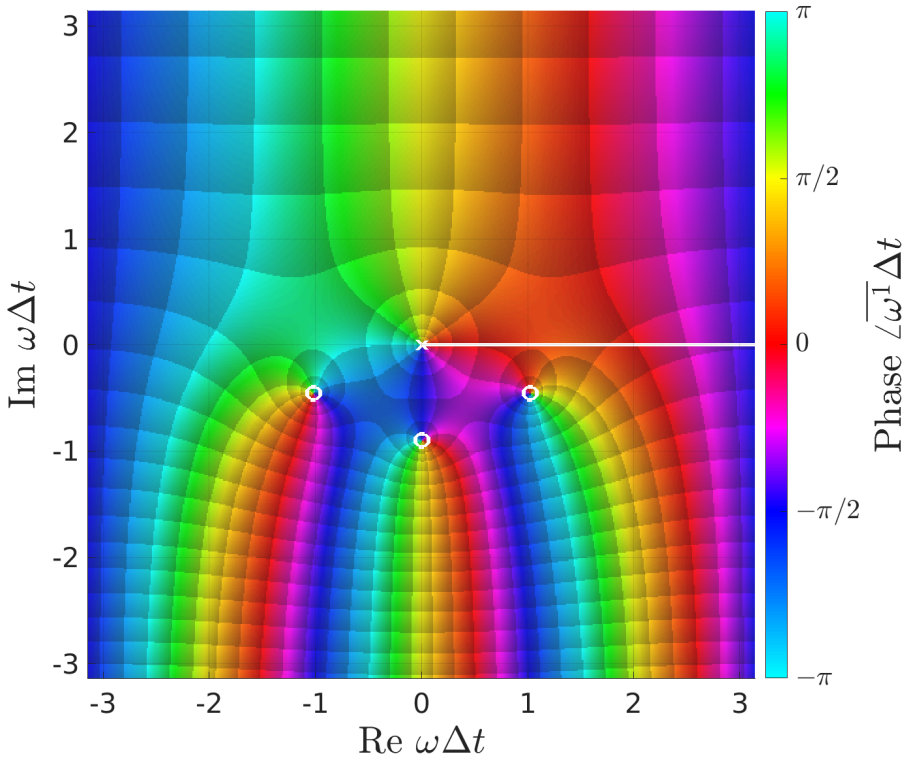

Figure 4.9: Complex plot of $\overline{\omega^1}\Delta t$ for Adams-Bashforth $O(\Delta t^4)$ scheme over the domain $\omega\Delta t \in [-\pi, \pi] \times [-i\pi, i\pi]$. Shading contours and color correspond to magnitude and phase components respectively. Zeros and poles are denoted by x's and o's respectively. The white line highlights the domain $\omega\Delta t \in [0, \pi]$.

then drops continuously after $\omega\Delta t \approx 1.4$, traversing colors red, magenta and blue.

The total number of zeros and poles is equal to the number of roots governing the dispersion and dissipation of the difference approximation. While Figure 4.3 conceptually introduced the significance of the roots, a detailed account is now presented. For the Adams-Bashforth $O(\Delta t^4)$ scheme, there are four roots. Following C. Tam and Webb (1993), a variable substitution $Z = e^{i\omega\Delta t}$ is introduced to give an equation for the roots as

$$-\frac{i}{\overline{\omega^1}\Delta t} + \left(a_0^1 + \frac{i}{\overline{\omega^1}\Delta t}\right) Z + a_{-1}^1 Z^2 + a_{-2}^1 Z^3 + a_{-2}^1 Z^3 + a_{-3}^1 Z^4 = 0 \tag{4.30}$$

The root solutions are numerically derived in complex form $Z_{roots} = a + ib$, converted to polar form $Z_{roots} = re^{i\theta}$, then applying the natural log of both sides gives

$$(\omega\Delta t)_n = \theta_n - i\ln(r_n) \tag{4.31}$$

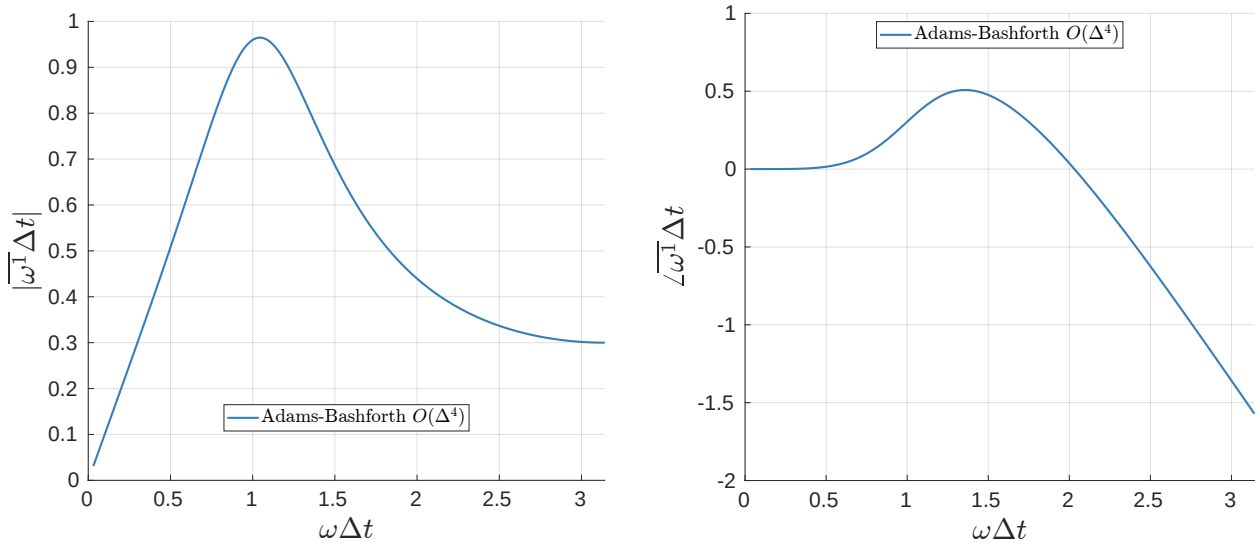

(a) Magnitude (b) Phase

Figure 4.10: Complex components of $\overline{\omega^1}\Delta t$ for Adams-Bashforth $O(\Delta t^4)$ scheme over the domain $\omega\Delta t \in [0, \pi]$ (see white line in Figure 4.9).

where n denotes the root number. Thus, the real and imaginary parts represent the phase and magnitude respectively, in which $\overline{\omega^1}\Delta t$ defines the domain for each function. Clearly for different schemes, the polynomial (4.30) will be different, but the same methodology applies. As mentioned prior, the stability of the regions outlined in Figure 4.8 can be tested by choosing a point within a region of the complex plane, substituting it into (4.31), then determining if the imaginary part for all roots are less than or equal to zero (e.g., LeVeque 2007). While this in itself is very informative, (4.31) gives an explicit account on the dispersive and dissipative nature of the scheme.

In Figure 4.11, the real part of the four root solutions (4.31) over the complex domain encompassing the stability plot are shown for the Adams-Bashforth $O(\Delta t^4)$ scheme. Of the four roots, only one of them is physical and the rest are so-called parasitic. It is emphasized that there is no natural ordering for complex numbers, thus the roots can be interchanged without loss. Specifically, for each point of evaluation over the complex domain, a number of equally valid root solutions is returned, in which the order of solutions can change at the next point of evaluation. Thus, to depict a continuous representation of the individual roots, as presented in Figure 4.11, requires a subjective interpretation. The ordering herein is based on evaluating root solutions along rays emitting from the origin and extrapolating their profiles to compare with successive evaluations along the ray. The ordering which minimizes discontinuity is invoked and the process repeats traversing the ray. In Figure 4.11a, the color scheme shows that the phase follows the scale of the x-axis, thus implying it is the physical root. Furthermore, the phase is fairly uniform in the vertical, which means that the dispersion is less sensitive to the imaginary component of $\overline{\omega^1}\Delta t$ over the analyzed region. The

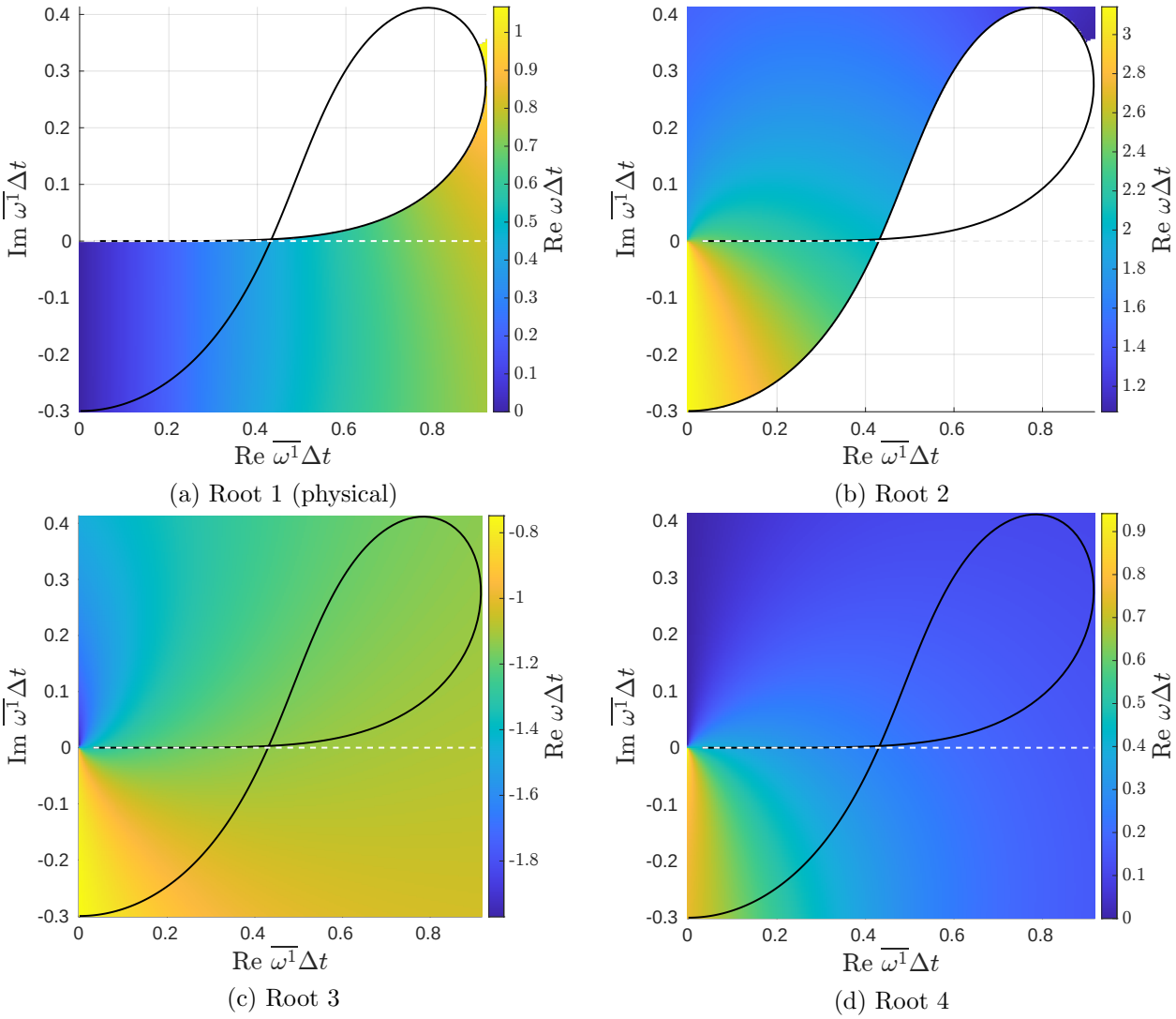

(a) Root 1 (physical)

(b) Root 2

(c) Root 3

(d) Root 4

Figure 4.11: Real components of roots for Adams-Bashforth $O(\Delta t^4)$ scheme over the complex plane (see Figure 4.8). Regions masked out in white are unstable.

parasitic roots do not share the same trend and vary in sign.

The corresponding imaginary part of the four root solutions (4.31) are shown in Figure 4.12, in which the regions masked out in white indicated a positive imaginary value. In these regions, the solutions are amplified and lead to instability if mitigation measures are not imposed. From the four plots, it is easy to see that the only region that is consistently filled in is the one on the lower left. This is the stable region for the Adams-Bashforth $O(\Delta t^4)$ scheme. The physical root shown in Figure 4.12a shows the dissipation is fairly uniform in the horizontal over the stable region. This means that the dissipation is less sensitive to the real component of $\overline{\omega^1}\Delta t$; however, dissipation does occur. Near the origin, the parasitic roots decay significantly, whereas the physical root approaches

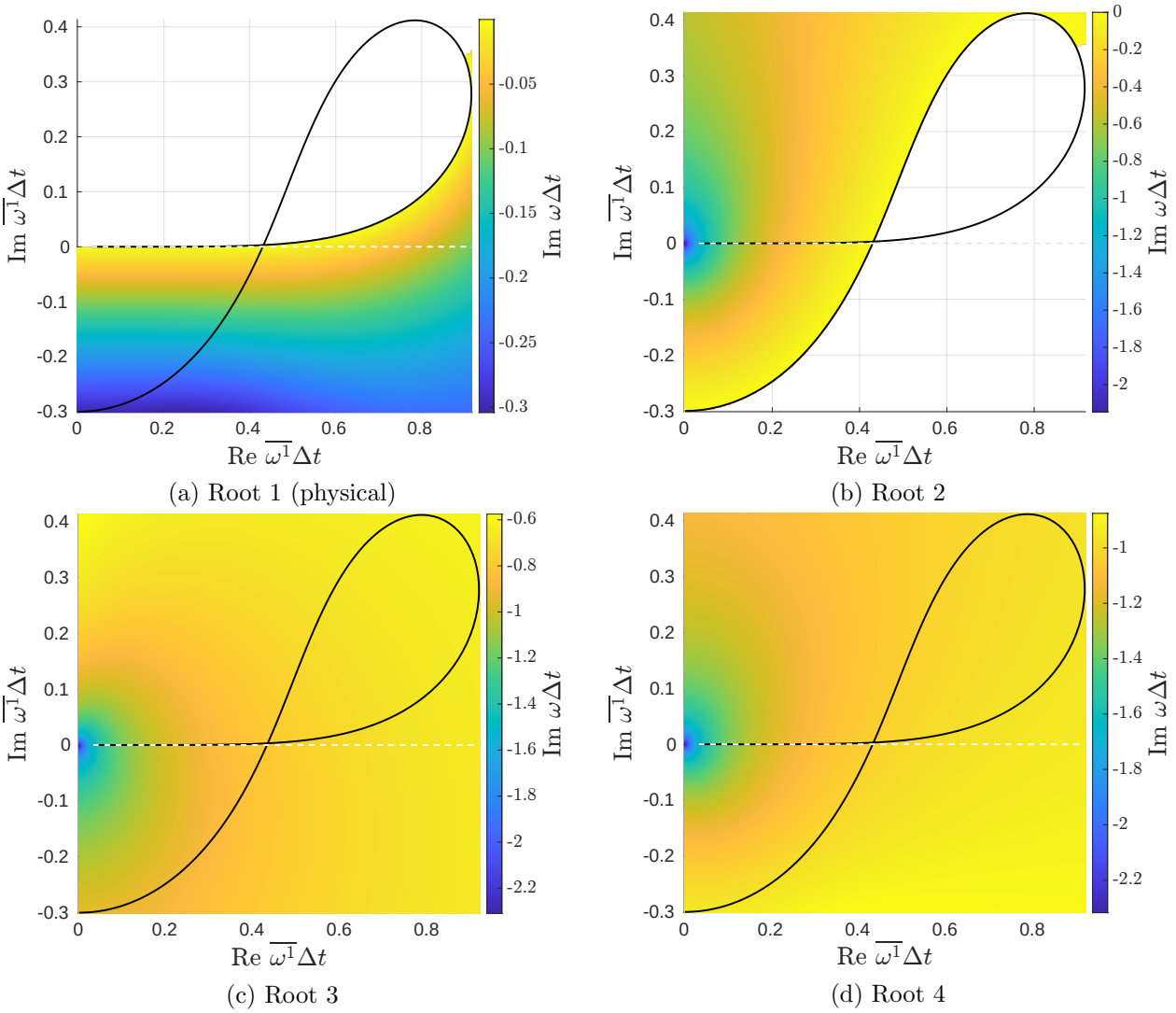

(a) Root 1 (physical)

(b) Root 2

(c) Root 3

(d) Root 4

Figure 4.12: Imaginary components of roots for Adams-Bashforth $O(\Delta t^4)$ scheme over the complex plane (see Figure 4.8). Regions masked out in white are unstable.

zero.

Supplemental to Figures 4.11 and 4.12, Figure 4.13 depicts a component breakdown along the domain $\overline{\omega^1}\Delta t \in [0, \pi]$ highlighted by the white dashed line. The physical root corresponding to figures 4.11a and 4.12a is colored orange. The stability limit of the region is also shown for reference, beyond which one of the parasitic roots in Figure 4.13b becomes positive. Thus, the dashed line is representative of a point on the black stability contour in Figures 4.11 and 4.12 where it crosses the real axis.

In the subsequent chapter, a more detailed analysis is performed to extract the dispersion and

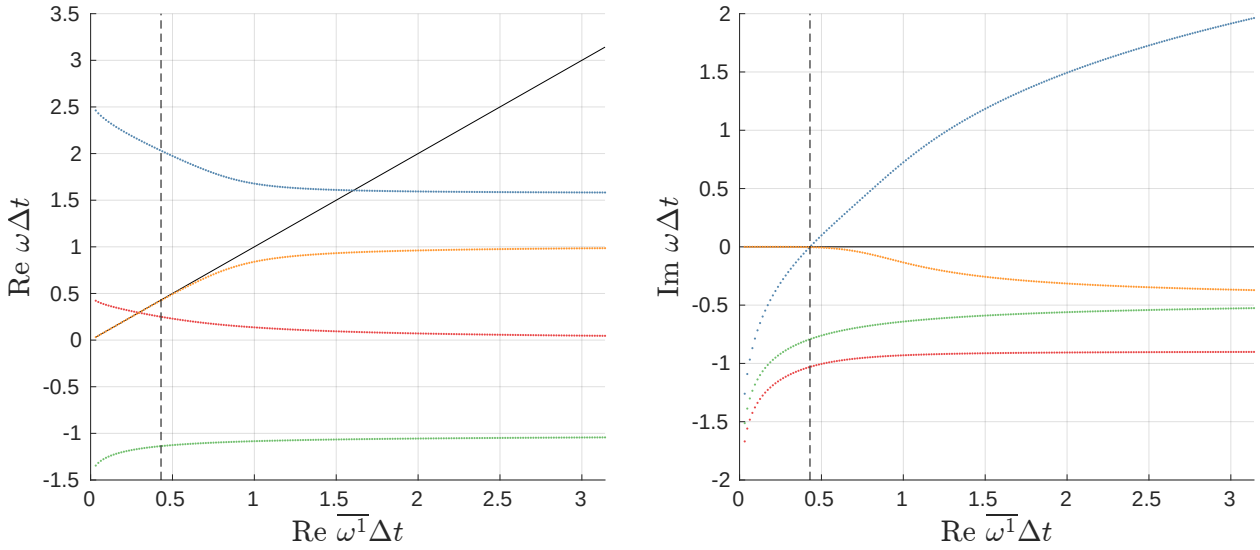

(a) Real Part (b) Imaginary Part

Figure 4.13: Complex components of roots for Adams-Bashforth $O(\Delta t^4)$ scheme over the domain $\overline{\omega^1}\Delta t \in [0, \pi]$ (see white lines in Figure 4.11 and Figure 4.12). The dotted black vertical line denotes the stability limit $\overline{\omega^1}\Delta t \approx 0.4299$, when the imaginary components are no longer all negative.

dissipation coefficients. As mentioned prior, this analysis can be performed on all difference approximations governed by (4.26) and (4.27), either central or bias. The detailed account given herein on the Adams-Bashforth $O(\Delta t^4)$ scheme is twofold. First, being a bias scheme, it contains both real and imaginary parts, thus gives exposure to dispersive and dissipative errors. The central schemes, being only real, do not illuminate all the intricacies. Nevertheless, the methodology applies. Second, Adams-Bashforth schemes were utilized in part by Wei and Kirby (1995) in the practical application of Boussinesq-type equations. Therefore, the analysis is directly relevant to members of the coastal engineering community who followed their lead. Appendix H includes configurations, coefficients, and stability plots for backward difference, Nystrom, and Milne-Simpson schemes (e.g., Hairer et al. 2009). Their inclusion is meant to show that they too are governed by (4.26) and (4.27), thus fall under the umbrella of compact schemes, with the backward difference schemes being the configuration counterpart to the Adams schemes. The Nystrom and Milne-Simpson schemes offer a few of the many examples which leverage the benefits of both the backward difference and Adams schemes. The detailed analysis given above on the Adams-Bashforth $O(\Delta t^4)$ scheme serves as a blue print to analyze other schemes which fall under this umbrella.

4.4 Coefficient Optimization

All schemes discussed to this point have been derived using the method of undetermined coefficients, whose application was showcased by example in (4.14) to derive a compact central scheme. In the example, there were eight unknown coefficients attributed to the configuration. Therefore, it was deemed necessary to provide eight independent equations to solve for a unique set of coefficients. After imposing monic normalization and symmetric constraints on the coefficients, the number of equations needed was reduced to three, which were defined through local series expansions. The choice to employ local series expansions for the remaining equations is actually an optimization objective to maximize the order of the truncation error under the given constraints. Therefore, it is an optimization of "accuracy in the small"; however, it is possible to change the objective to increase the bandwidth resolution, thereby improving "accuracy in the large" (e.g., Lele 1992; C. Tam and Webb 1993; Kim and Lee 1996; Zingg 2000; Bogey and Bailly 2004). Returning to the prior example, one way to achieve this is by replacing the four remaining equations with ones whose objective is to maximize the bandwidth resolution given a tolerance for error. A hybrid approach is also possible, in which the order of the truncation error is constrained.

The optimization objective reflects the underlying goals of the approximation and is therefore subjectively defined by the model developer. Following the work of C. Tam and Webb (1993), a hybrid approach improving the bandwidth resolution of an $O(\Delta x^6)$ explicit central approximation to the first derivative is employed to showcase the methodology. The configuration calls for eight equations, which after imposing monic normalization and symmetric constraints, reduces to three non trivial equations. Herein, the approximation is constrained to $O(\Delta x^2)$, which leaves the need for two non trivial equations. To improve the bandwidth resolution, a measure of error is introduced

$$E(k\Delta x) = \int_0^\Gamma |k\Delta x - \overline{k^1}\Delta x|^2 d(k\Delta x) \tag{4.32}$$

in which Γ is a free parameter defining the bandwidth over which the error is measured. Its significance is appreciated upon review of Figure 4.4a, in which the errors of approximation become excessively large near the Nyquist limit. The free parameter thus allows one to focus on a region of practical interest, bound by some tolerance for error. Note that the measure of error in (4.32) is defined by the square of the L_2-norm; however, some authors also employ a L_1-norm (e.g., Zingg 2000; Bogey and Bailly 2004). In any case, this is a property of how the error function is defined, which varies in the literature. Kim and Lee (1996) introduce a weighting function, which not only allows for the error function to be solved analytically in the application of compact schemes, it also exponentially weights larger errors associated with higher frequencies. It is also worth pointing out that in (4.32), the error is measured for the real component only, which is sufficient for central

schemes, but as shown in Figures 4.11 and 4.12, both real and imaginary errors can occur in the approximation, despite the domain being real (represented by the white dashed line in the figures). In summary, the error function can be defined in many different ways, each leading to a unique solution.

In C. Tam and Webb (1993), the conditions for the error function to be minimal are

$$\frac{\partial E}{\partial d_j} = 0 \tag{4.33}$$

where d_j is the set of unknown coefficients. Continuing with the example introduced above, in which two additional equations were needed, this implies $j = 2$ in (4.33) to close the system. Therefore, given Γ, the solution is obtained and the curves are known. To include Γ as a free parameter, C. Tam and Webb (1993) measure the error in the derivative of the resultant curve and constrain its absolute value to be less than 0.003, which is chosen based on application requirements. The optimization problem is thus to maximize the bandwidth Γ in (4.32) given a tolerance for error.

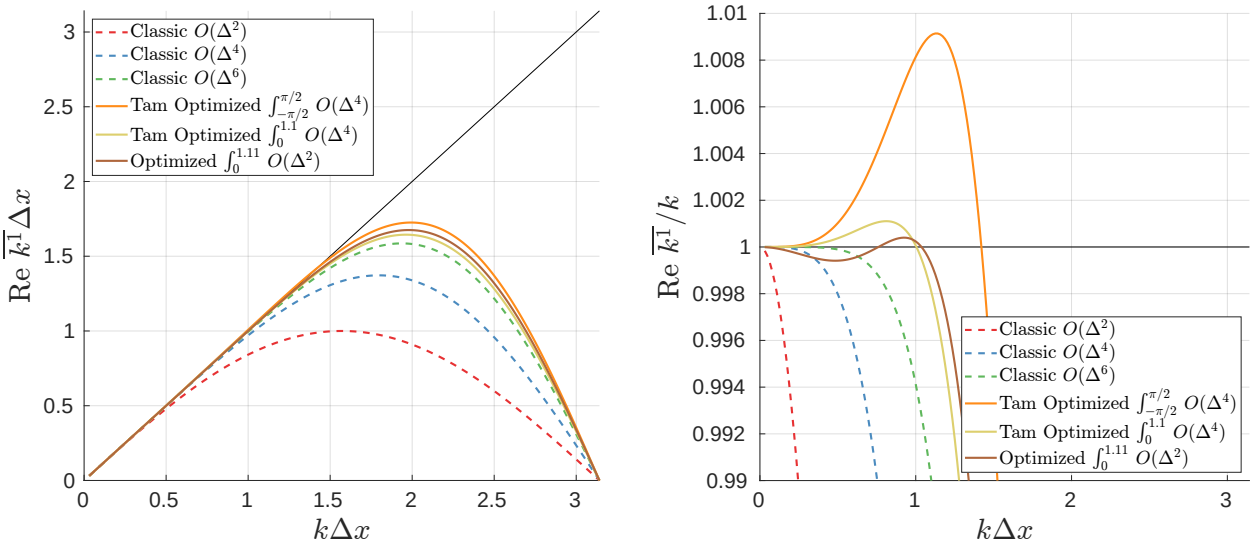

(a) "Accuracy in large"

(b) "Accuracy in small"

Figure 4.14: Resolvable bandwidth of select optimized schemes compared with classic schemes of comparable configuration and order over (a) the full domain and (b) to within ±1% relative error. Exact solutions are denoted by the solid black line.

In Figure 4.14, a comparison between classic and optimal central schemes of similar configuration and order is shown. Included are the $O(\Delta x^4)$ schemes from C. Tam and Webb (1993), with different values of Γ to show its contribution. The optimal $O(\Delta x^2)$ scheme corresponds to $j = 2$ in (4.33), representing a solution with two degrees of freedom. All optimal schemes are built from the classic $O(\Delta x^6)$ configuration, which serves as a baseline comparison in terms of work. As

shown in Figure 4.14b, by sacrificing the formal order of accuracy, the optimal schemes do exhibit a larger bandwidth, but at the expense of oscillation errors. The optimal $O(\Delta x^4)$ schemes, having one degree of freedom, show one inflection point, whereas the $O(\Delta x^2)$ scheme, having two degrees of freedom, shows two inflection points. Comparing the classic and optimal schemes of the same order, it is clear that they all converge in similar fashion. Thus for a bit more work, due to the increased configuration size, a higher bandwidth resolution can be achieved. This is the trade-off between the optimization objectives in the hybrid approach.

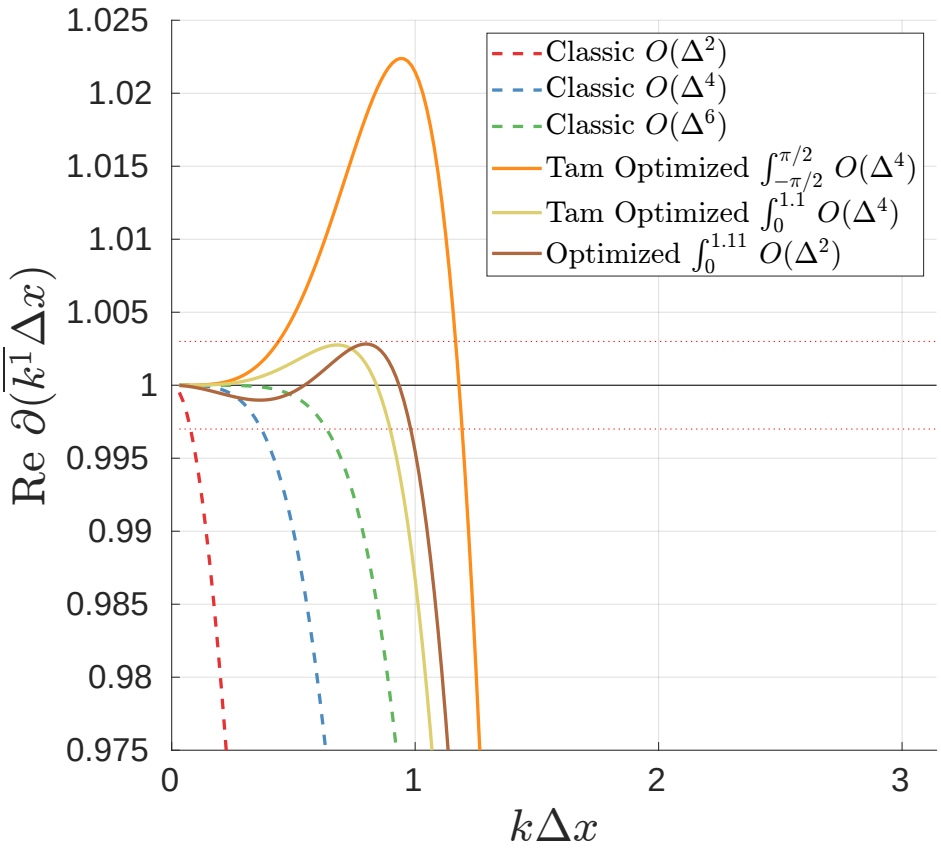

Figure 4.15: Optimization objective constraints on derivative of difference approximation. Red dotted lines denote ± 0.003 tolerance for error.

In Figure 4.15, the constraints imposed by C. Tam and Webb (1993) on the curves in Figure 4.14 are shown with the tolerance for error being denoted by the red dashed lines. Although the optimal $O(\Delta x^4)$ scheme with $\Gamma = \pi/2$ gives a higher bandwidth resolution, it violates the tolerance for error early on. The value of Γ for the optimal $O(\Delta x^2)$ and $O(\Delta x^4)$ schemes clearly obey the constraints, with the former achieving the highest bandwidth resolution due to the extra degree of freedom. In comparison to the classic $O(\Delta x^2)$ scheme, the bandwidth resolution of the optimal $O(\Delta x^2)$ scheme is about five times larger.

The optimization methodology carried out herein applies to compact schemes as well (e.g., Kim and Lee 1996), which based on earlier comparisons with classic schemes, can achieve an even higher bandwidth resolution. For this reason, they are often referred to in the literature as so-called spectral-like schemes, which have only recently been adopted in the free-surface wave modeling community. However, applications mostly focused on spatial discretization schemes with single step Runge-Kutta time integration schemes (e.g., J. Li and Visbal 2006; Cienfuegos et al. 2006; Chiu et al. 2009; Venutelli 2015). By incorporating linear multistep time integration schemes, which have been shown to be bias schemes derived from a compact configuration, the compact finite difference approach herein is consistent across both time and space. While this chapter has not only provided the tools and alternative optimization techniques to derive such schemes, it is only focused on individual operators and not the system of MPDEs as a whole. In the closing chapter, the linear Boussinesq-type equations are discretized and cast into spectral space with the application of (4.26) and (4.27) to evaluate both dispersion and dissipation errors for select schemes.

CHAPTER 5
NUMERICAL MODEL

In the previous chapter, focus was on the introduction of compact finite difference approximations, specifically highlighting linear spectral characteristics of individual operators. In addition to comparing the order of approximation, the notion of resolvable bandwidth was utilized to review "accuracy in the large" over the full spectral domain. Central and bias schemes were shown to result in real and complex spectral transformations respectively. Selecting the Adams-Bashforth $O(\Delta t^4)$ scheme as a proxy for discussion in spectral space, dissipative and dispersive properties were shown to be linked to complex root solutions in the mapping of difference approximations back to the continuum. Central schemes, which result in a real transformation, are purely dispersive due the roots being conjugate pairs, whose imaginary components cancel. Lastly, it was shown that the underlying objective function defining the approximation can be altered to improve the resolvable bandwidth, resulting in a compromise between "accuracy in the small" and "accuracy in the large".

The focus of this chapter is on the novel implementation of compact finite difference operators in application to linear Boussinesq-type equations, which represents a system of equations, and validate the linear dissipative and dispersive characteristics resulting from the difference approximations. The implementation of compact finite difference schemes represents a new approach in the discretization of Boussinesq-type equations. The first section defines a general set of modified PDEs (MPDEs), which include compact schemes. The MPDEs are then mapped into spectral space to derive the integral solution to the difference equations. The second section focuses on the newly derived numerical dispersion relation for Boussinesq-type equations, which links the effective angular frequency of the temporal discretization with effective wave numbers of the spatial discretization. An analytic solution to the difference approximation is then presented for standing waves to be utilized in the verification process, which is covered in the final section.

5.1 Modified PDEs

Introducing a set of new function definitions to isolate partial differential expressions, the linear continuity (3.34) and momentum (3.35) equations are restated as

Continuity

$$P_\eta + Q_u = \psi_\eta \tag{5.1}$$

$$P_\eta = \frac{\partial p_\eta}{\partial t} \tag{5.2}$$

$$Q_u = h\frac{\partial q_u}{\partial x} \tag{5.3}$$

$$p_\eta = \eta - \mu^2\sigma_1 h^2\frac{\partial^2 \eta}{\partial x^2} \tag{5.4}$$

$$q_u = u - \mu^2\sigma_2 h^2\frac{\partial^2 u}{\partial x^2} \tag{5.5}$$

Momentum

$$P_u + Q_\eta = \psi_u \tag{5.6}$$

$$P_u = \frac{\partial p_u}{\partial t} \tag{5.7}$$

$$Q_\eta = \frac{\partial q_\eta}{\partial x} \tag{5.8}$$

$$p_u = u - \mu^2\sigma_3 h^2\frac{\partial^2 u}{\partial x^2} \tag{5.9}$$

$$q_\eta = \eta - \mu^2\sigma_4 h^2\frac{\partial^2 \eta}{\partial x^2} \tag{5.10}$$

The equations contain three partial differential operators; 1) a first derivative with respect to time, 2) a first derivative with respect to space, and 3) a second derivative with respect to space. This is not the only form in which the PDEs can be presented and the choice does have an implication on the numerical solution (e.g., Gray 1980; Vichnevetsky and Bowles 1982). As shown in the previous chapter, the bandwidth resolution of the operators is unique, particularly in the construction of high order schemes. One obvious alternative is to redefine the flux terms by distributing the first derivative with respect to space in (5.3) and (5.8) over (5.5) and (5.10) respectively, resulting in additional operators defined by a third derivatives with respect to space. Nevertheless, the choice to retain the second derivative in the definition of the flux is motivated by the preservation of symmetry presented by the three-parameter family.

Compact difference approximations to the three partial differential operators are given by the substitutions $\partial_t^n = \mathbf{A}_n^{-1}\mathbf{B}_n/\Delta t^n$ and $\partial_x^n = \mathbf{C}_n^{-1}\mathbf{D}_n/\Delta x^n$, in which the inverse operators $\mathbf{A}_n^{-1}$ and

$\mathbf{C}_n^{-1}$ have been applied to (4.8) and (4.11) respectively to facilitate substitution. The functions and their derivatives are assumed to be collocated over a regular mesh for demonstration purposes. Invoking operator substitutions, the compact finite difference approximations are given by

Continuity

$$P_\eta + Q_u = \psi_\eta \tag{5.11}$$

$$\mathbf{A}_1 P_\eta = \frac{\mathbf{B}_1}{\Delta t} p_\eta + \varepsilon \tag{5.12}$$

$$\mathbf{C}_1 Q_u = h \frac{\mathbf{D}_1}{\Delta x} q_u + \varepsilon \tag{5.13}$$

$$\mathbf{C}_2 p_\eta = \mathbf{C}_2 \eta - \mu^2 \sigma_1 h^2 \frac{\mathbf{D}_2}{\Delta x^2} \eta + \varepsilon \tag{5.14}$$

$$\mathbf{C}_2 q_u = \mathbf{C}_2 u - \mu^2 \sigma_2 h^2 \frac{\mathbf{D}_2}{\Delta x^2} u + \varepsilon \tag{5.15}$$

Momentum

$$P_u + Q_\eta = \psi_u \tag{5.16}$$

$$\mathbf{A}_1 P_u = \frac{\mathbf{B}_1}{\Delta t} p_u + \varepsilon \tag{5.17}$$

$$\mathbf{C}_1 Q_\eta = \frac{\mathbf{D}_1}{\Delta x} q_\eta + \varepsilon \tag{5.18}$$

$$\mathbf{C}_2 p_u = \mathbf{C}_2 u - \mu^2 \sigma_3 h^2 \frac{\mathbf{D}_2}{\Delta x^2} u + \varepsilon \tag{5.19}$$

$$\mathbf{C}_2 q_\eta = \mathbf{C}_2 \eta - \mu^2 \sigma_4 h^2 \frac{\mathbf{D}_2}{\Delta x^2} \eta + \varepsilon \tag{5.20}$$

The general formulation gives a conceptual layout for the implementation of compact schemes. Classic spatial schemes are recovered when $\mathbf{C}_2 = \mathbf{I}$, the identity matrix. In the case $\sigma_n = 0$, the operators $\mathbf{C}_2$ in (5.14), (5.15), (5.19), and (5.20) cancel, giving the implementation of compact schemes on the non dispersive linear shallow water equations. To march the solution forward in time, the configurations and their coefficients need to be defined. This will influence how the operations are carried out, with a specific example given later in the chapter.

Although employing compact operators inevitably leads to more computational work, with the added benefit of increased accuracy, theories often utilized in practice, such as that of Nwogu (1993) with $\sigma_{1,4} = 0$, require an inversion of the evolution variable p_u to advance the velocity in time. Therefore, a system of equations needs to be solved regardless. Applying a compact operator results in $\mathbf{C}_2$ having additional bands in the matrix, which presents an incremental effort. The significant difference in computational work is attributed to the additional systems operating on the flux terms in the continuity equation. For high order theories which fully utilize the potential of the three-parameter family, $\sigma_n \neq 0$, such as that of Schaffer and P. A. Madsen (1995b), an

inversion of the evolution variable p_η to advance the free surface elevation in time is also needed. Again, applying a compact operator to this operation presents an incremental effort. In summary, for Boussinesq-type equations requiring solutions to systems of equations (i.e. $\sigma_1 \neq 0$ or $\sigma_3 \neq 0$), the computational overhead of implementing compact schemes is reduced, with the principle effort being attributed to compact operators being applied in the flux terms in either the continuity or momentum equations. The focus herein is on the implementation, in which no attempt has been made to explicitly measure or reduce the computational effort. In this regard, the works of Mahesh (1998) to combine operator solutions or the use of algorithmic structures (e.g., Preissmann 1961; Yanenko and Holt 1971; M. B. Abbott 1979) are of immediate interest. Nevertheless, compact banded systems can be solved very efficiently using direct methods.

Applying Fourier-Laplace transforms, Derivative Theorems (D.3) and (D.7), and substituting in the effective angular frequency (4.20) and wave number (4.25), the system of equations is mapped into spectral space as

Continuity

$$-i\overline{\omega^1}\widetilde{p_\eta} = -\widetilde{Q_u} + \frac{\overline{\omega^1}\widetilde{p_{\eta_o}}}{2\pi\omega} + \widetilde{\psi_\eta} + \varepsilon \tag{5.21}$$

$$\widetilde{Q_u} = ih\overline{k^1}\widetilde{q_u} + \varepsilon \tag{5.22}$$

$$\widetilde{p_\eta} = \widetilde{\eta} + \mu^2\sigma_1 h^2\overline{k^2}\widetilde{\eta} + \varepsilon \tag{5.23}$$

$$\widetilde{q_u} = \widetilde{u} + \mu^2\sigma_2 h^2\overline{k^2}\widetilde{u} + \varepsilon \tag{5.24}$$

$$\tag{5.25}$$

Momentum

$$-i\overline{\omega^1}\widetilde{p_u} = -\widetilde{Q_\eta} + \frac{\overline{\omega^1}\widetilde{p_{u_o}}}{2\pi\omega} + \widetilde{\psi_u} + \varepsilon \tag{5.26}$$

$$\widetilde{Q_\eta} = i\overline{k^1}\widetilde{q_\eta} + \varepsilon \tag{5.27}$$

$$\widetilde{p_u} = \widetilde{u} + \mu^2\sigma_3 h^2\overline{k^2}\widetilde{u} + \varepsilon \tag{5.28}$$

$$\widetilde{q_\eta} = \widetilde{\eta} + \mu^2\sigma_4 h^2\overline{k^2}\widetilde{\eta} + \varepsilon \tag{5.29}$$

in which expressions involving the transform of the initial conditions, $\widetilde{f_{\eta_o}}$ and $\widetilde{f_{u_o}}$, on the right hand side of (5.21) and (5.26) respectively, are due to application of the Laplace Shift Theorem (D.8) in the time integration. Combining the equations above and multiplying through by i gives

the continuity and momentum equations in spectral space as

$$\overline{\omega^1}\left(1+\mu^2\sigma_1 h^2\overline{k^2}\right)\widetilde{\eta}-h\overline{k^1}\left(1+\mu^2\sigma_2 h^2\overline{k^2}\right)\widetilde{u}=\frac{i\overline{\omega^1}}{2\pi\omega}\left(1+\mu^2\sigma_1 h^2\overline{k^2}\right)\widetilde{\eta_o}+i\widetilde{\psi}_\eta+\varepsilon \tag{5.30}$$

$$\overline{\omega^1}\left(1+\mu^2\sigma_3 h^2\overline{k^2}\right)\widetilde{u}-\overline{k^1}\left(1+\mu^2\sigma_4 h^2\overline{k^2}\right)\widetilde{\eta}=\frac{i\overline{\omega^1}}{2\pi\omega}\left(1+\mu^2\sigma_3 h^2\overline{k^2}\right)\widetilde{u_o}+i\widetilde{\psi}_u+\varepsilon \tag{5.31}$$

Importantly, these equations hold independent of operators $\mathbf{A},\mathbf{B},\mathbf{C}$, and $\mathbf{D}$ defining the configurations and coefficients of the difference approximations. Combining the continuity (5.30) and momentum (5.31) equations in matrix form, the system of MPDEs in spectral space is given as

$$\begin{bmatrix}\overline{\omega^1}\left(1+\mu^2\sigma_1 h^2\overline{k^2}\right) & -h\overline{k^1}\left(1+\mu^2\sigma_2 h^2\overline{k^2}\right)\\ -\overline{k^1}\left(1+\mu^2\sigma_4 h^2\overline{k^2}\right) & \overline{\omega^1}\left(1+\mu^2\sigma_3 h^2\overline{k^2}\right)\end{bmatrix}\begin{bmatrix}\widetilde{\eta}\\ \widetilde{u}\end{bmatrix}=\begin{bmatrix}\widetilde{G_1}\\ \widetilde{G_2}\end{bmatrix}+\boldsymbol{\varepsilon} \tag{5.32}$$

in which $\widetilde{\mathbf{G}}$ contains the transform of the respective initial conditions and source terms

$$\widetilde{G_1}=\frac{i}{2\pi}\left(\frac{\overline{\omega^1}}{\omega}\left(1+\mu^2\sigma_1 h^2\overline{k^2}\right)\widetilde{\eta_o}+2\pi\widetilde{\psi}_\eta\right) \tag{5.33}$$

$$\widetilde{G_2}=\frac{i}{2\pi}\left(\frac{\overline{\omega^1}}{\omega}\left(1+\mu^2\sigma_3 h^2\overline{k^2}\right)\widetilde{u_o}+2\pi\widetilde{\psi}_u\right) \tag{5.34}$$

Upon making substitutions $\overline{\omega^1}=\omega$ and $\overline{k^n}=k^n$, the linear system of MPDEs (5.32) is identical to the linear system of PDEs (3.41) introduced prior. Since the compact operators (4.8) and (4.11) are independently composed of polynomials in their own respective shift operators, which give the operator identity for vanishing sampling intervals, the difference approximations, $\lim_{\Delta t\to 0}\overline{\omega^n}=\omega^n$ and $\lim_{\Delta x\to 0}\overline{k^n}=k^n$, are unconditionally consistent (e.g., M. B. Abbott 1979). Furthermore, assuming the approximations employed are stable, the Lax equivalence theorem states the system of MPDEs converges to the system of PDEs at a rate dependent upon the order of approximation (e.g., Richtmyer and Morton 1967). The analysis carried out in chapter 3 readily applies and will not be repeated for brevity. Analogous to (3.53) and (3.54), integral solutions to the homogeneous linear system of equations in terms of the free-surface elevation and velocity are given by

$$\eta=\frac{i\varphi}{2\pi}\int_\Gamma\int_{-\infty}^{\infty}\frac{(1+\sigma_3\overline{k^2}h^2)\left(\overline{\omega^1}(1+\sigma_1\overline{k^2}h^2)\widetilde{\eta_o}+\overline{k^1}h(1+\sigma_2\overline{k^2}h^2)\widetilde{u_o}\right)\frac{\overline{\omega^1}}{\omega}}{\overline{\omega^1}^2(1+\sigma_1\overline{k^2}h^2)(1+\sigma_3\overline{k^2}h^2)-\overline{k^1}^2h(1+\sigma_2\overline{k^2}h^2)(1+\sigma_4\overline{k^2}h^2)}e^{i(kx-\omega t)}dkd\omega \tag{5.35}$$

$$u=\frac{i\varphi}{2\pi}\int_\Gamma\int_{-\infty}^{\infty}\frac{(1+\sigma_1\overline{k^2}h^2)\left(\overline{k^1}(1+\sigma_4\overline{k^2}h^2)\widetilde{\eta_o}+\overline{\omega^1}(1+\sigma_3\overline{k^2}h^2)\widetilde{u_o}\right)\frac{\overline{\omega^1}}{\omega}}{\overline{\omega^1}^2(1+\sigma_1\overline{k^2}h^2)(1+\sigma_3\overline{k^2}h^2)-\overline{k^1}h(1+\sigma_2\overline{k^2}h^2)(1+\sigma_4\overline{k^2}h^2)}e^{i(kx-\omega t)}dkd\omega \tag{5.36}$$

in which Γ is the contour of integration over the ω-plane. It is worth highlighting that the integrals are over the ω and k plane respectively, thus emphasizing the need to map the difference approx-

imations to their root solutions as shown in Figure 4.3, in which the physical root is of principle interest.

5.2 Numerical Dispersion Relation

The denominator expression in (5.35) and (5.36) defines the numerical dispersion function, analogous to (3.55), as

$$\overline{f_D}(\omega, k) = \overline{\omega^1}^2(1 + \sigma_1\overline{k^2}h^2)(1 + \sigma_3\overline{k^2}h^2) - \overline{k^1}^2 h(1 + \sigma_2\overline{k^2}h^2)(1 + \sigma_4\overline{k^2}h^2) \tag{5.37}$$

Setting the numerical dispersion function equal to zero gives the numerical dispersion relation, analogous to (3.56), as

$$\overline{\omega^1}^2 = h\overline{k^1}^2 \frac{(1 + \sigma_2\overline{k^2}h^2)(1 + \sigma_4\overline{k^2}h^2)}{(1 + \sigma_1\overline{k^2}h^2)(1 + \sigma_3\overline{k^2}h^2)} \tag{5.38}$$

in which the function dependencies $\overline{\omega^1}(\omega)$ and $\overline{k^n}(k)$ have been omitted for clarity. The numerical dispersion relation (5.38) is most general and applies to the three-parameter family of dispersive theories discretized by the compact methods discussed herein. Upon selecting a specific theory and specific set of schemes, the numerical dispersion relation is uniquely defined. Figure 5.1 depicts a conceptual flow of information with regard to the numerical dispersion relation. Given a wave number in the continuum, which is often real based on physical basis, (4.27) maps the wave number to the respective effective wave numbers. Employing central schemes, the mapping defines the effective wave numbers to the real line of the complex plane. Substituting the effective wave numbers into (5.38) leads to a real effective angular frequency, $\overline{\omega^1}$, which is then mapped back to the continuum in the form of root solutions, one being physical. Not shown is the mapping of the effective wave numbers back to the continuum, which also results in multiple roots, one being physical. If the spatial discretization includes a dissipative component (e.g., non central scheme or dissipation filter), then the effective angular frequency given by (5.38) is also complex, leading to a different result in the mapping. In summary, the discretization leads to multiple roots, only one of which is physical and the rest are parasitic. The numerical result, being a superposition of the root solutions (e.g., C. Tam and Webb 1993), thus requires mitigation of the parasitic modes to prevent nonphysical results in the numerical simulation.

There are multiple ways to manipulate the numerical dispersion relation (5.38) such that the relation

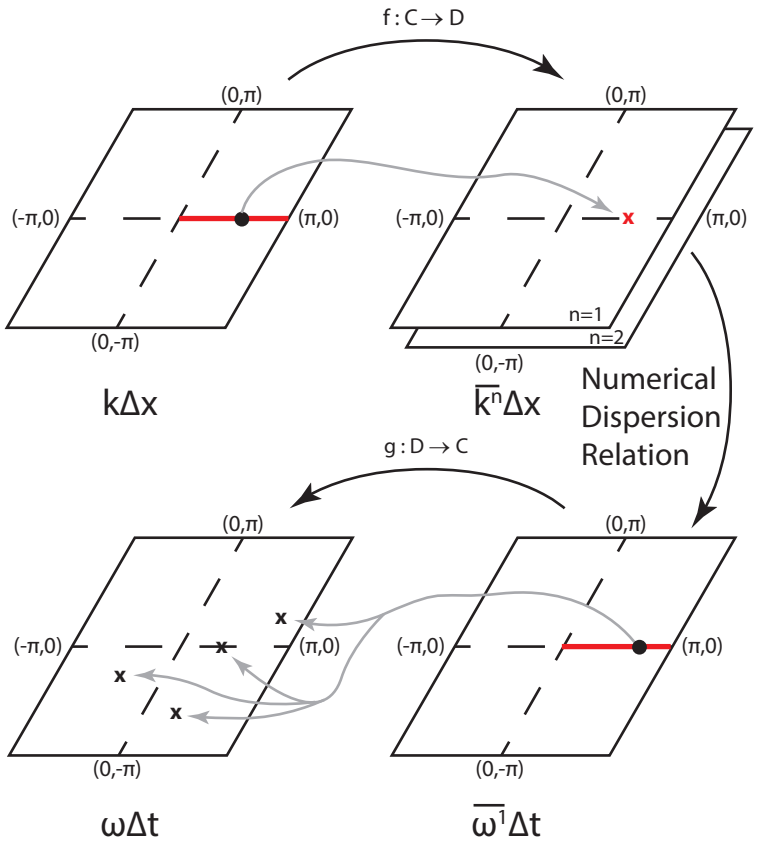

Figure 5.1: Schematic mapping of: (top) the wave number in the continuum (C) to the effective wave numbers (D), and (bottom) the effective angular frequency back to its complex root solutions in the continuum. The red highlights the positive real axis. The link between the effective wave numbers, $\overline{k^n}$, and the effective angular frequency, $\overline{\omega^1}$, is given by the numerical dispersion relation.

is expressed in terms of different dimensionless parameters. Below, a few variants are given

$$\overline{\omega^1}^2 = \frac{1}{h} A_b^2 \left(\overline{k^1}\Delta x\right)^2 \frac{\left(1+\sigma_2 A_b^2\left(\overline{k^2}\Delta x^2\right)\right)\left(1+\sigma_4 A_b^2\left(\overline{k^2}\Delta x^2\right)\right)}{\left(1+\sigma_1 A_b^2\left(\overline{k^2}\Delta x^2\right)\right)\left(1+\sigma_3 A_b^2\left(\overline{k^2}\Delta x^2\right)\right)} \tag{5.39}$$

$$\left(\overline{\omega^1}\Delta t\right)^2 = C_r^2 \left(\overline{k^1}\Delta x\right)^2 \frac{\left(1+\sigma_2 A_b^2\left(\overline{k^2}\Delta x^2\right)\right)\left(1+\sigma_4 A_b^2\left(\overline{k^2}\Delta x^2\right)\right)}{\left(1+\sigma_1 A_b^2\left(\overline{k^2}\Delta x^2\right)\right)\left(1+\sigma_3 A_b^2\left(\overline{k^2}\Delta x^2\right)\right)} \tag{5.40}$$

$$\overline{\omega^1}^2 = \frac{1}{h}\left(\frac{\overline{k^1}}{k}\right)^2 (kh)^2 \frac{\left(1+\sigma_2\frac{\overline{k^2}}{k^2}(kh)^2\right)\left(1+\sigma_4\frac{\overline{k^2}}{k^2}(kh)^2\right)}{\left(1+\sigma_1\frac{\overline{k^2}}{k^2}(kh)^2\right)\left(1+\sigma_3\frac{\overline{k^2}}{k^2}(kh)^2\right)} \tag{5.41}$$

$$\left(\overline{\omega^1}\Delta t\right)^2 = C_r^2 \left(\overline{k^1}\Delta x\right)^2 \frac{\left(1+\sigma_2\frac{\overline{k^2}}{k^2}(kh)^2\right)\left(1+\sigma_4\frac{\overline{k^2}}{k^2}(kh)^2\right)}{\left(1+\sigma_1\frac{\overline{k^2}}{k^2}(kh)^2\right)\left(1+\sigma_3\frac{\overline{k^2}}{k^2}(kh)^2\right)} \tag{5.42}$$

in which $C_r = \sqrt{h}\Delta t/\Delta x$ and $A_b = h/\Delta x$ are the Courant (Courant et al. 1967) and Abbott (M. B. Abbott and Minns 1998) numbers respectively. Although the equations are equivalent, their perspectives are unique. Extracting the dimensionless effective wave numbers, $\overline{k^n}\Delta x^n$, on the right hand side of (5.38) gives rise to the Abbott number, which is a geometric aspect ratio (e.g., Scotti and Mitran 2008) that scales the absolute error of the effective wave numbers (see Figure 4.4a for example). The dimensionless form of (5.39) gives rise to the Courant number through the relation $C_r = A_b/H_e$, where $H_e^2 = h/\Delta t^2$ has the units of acceleration and can be interpreted as a modification to the gravitational constant, which is omitted in the dimensionless form of the governing equations employed throughout herein. Thus, the Courant number can be interpreted as a geometric aspect ratio of the domain over a locally modified gravitational constant. Multiplying the effective wave numbers on the right hand side of (5.38) by k/k gives rise to the relative depth parameter, kh, which scales the relative error of the effective wave numbers $\overline{k^n}/k^n$ (see Figure 4.4b for example). The relation between the Abbott number and relative depth, $kh = k\Delta x A_b$, is thus proportional to the dimensionless wave number. In terms of the relative depth, equations (5.41) and (5.42) give an explicit connection with the physical dispersion relation in dimensional and dimensionless form respectively. As $\lim_{\Delta x \to 0} \overline{k^n} = k^n$, the right hand side of (5.38) equals that of the physical dispersion relation, showing $\overline{\omega^1}(\omega) = \omega$ and $\overline{\omega^1}\Delta t(\omega\Delta t) = \omega\Delta t$ for each of the two equations. However, it is important to remember that the numerical dispersion relation (5.38), or its variants (5.39)-(5.42), simply connect the effective wave numbers with the effective angular frequency. As shown in Figure 5.1, the effects of temporal discretization are introduced in the mapping to the continuum. Therefore, interpreting $\overline{\omega^1}(\omega) = \omega$ as convergence of the full discretization is incomplete.

The various ways in which the numerical dispersion relation can be parameterized has led to different presentations in the literature. The parametrization shown in Figure 5.2 expresses the domain in terms of the dimensionless wave number, relative water depth, and Courant number. Furthermore, visualizing the volume of the three dimensional solution space is difficult in text, therefore authors often take slices through the solution space to expose the interior structure. As an example, L. Li and Cheung (2019) present results using horizontal slices through the volume as a function of the dimensionless wave number and Courant number. Figure 5.2 also provides visual aids on the right to understand how changes, denoted by δ, in $k, h, \Delta t$, and Δx affect the solution. Taking an initial solution, as shown on the left, a volume is defined by a solution vector. A reduction in k (magenta) results in the volume shrinking in height (kh-axis) and width ($k\Delta x$-axis), but no changes occur in the length (C_r-axis). This means that the Courant number is fixed for all wave numbers, which is consistent with its definition. A reduction in h (cyan) results in the volume shrinking in height (kh-axis) and length (C_r-axis), but no changes occur in width ($k\Delta x$-axis). This means that the dimensionless wave number is fixed for all water depths. In summary, changes in k (magenta) and h (cyan) have similar effects, but act along opposing dimensions, which makes sense given that

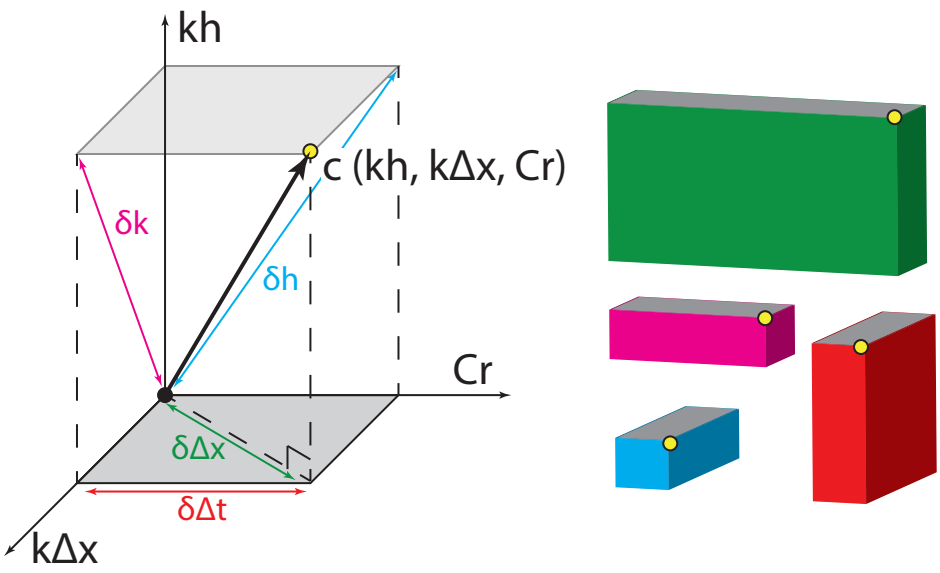

Figure 5.2: Sketch of: (left) numerical domain in terms of dimensionless parameters, and (right) qualitative changes in celerity (yellow dot) and volume due to a decrease in the color-specific parameter defined on the left.

the changes represent opposing diagonals. A reduction in Δt (red) represents the simplest change in volume, in which only the length (C_r-axis) changes. A reduction in Δx (green) results in the volume shrinking in width ($k\Delta x$-axis), but increasing in length (C_r-axis), with no changes in height (kh-axis). As will be discussed in a later section, the solution space is often bound along the C_r-axis by stability constraints, thus a reduction in Δx alone can lead to instabilities. To mitigate the increase in length (C_r-axis), a reduction in either h or Δt is needed, which again, agrees with the definition of the Courant number. To reiterate, Figure 5.2 represents just one of many perspectives, where, for example, a diagonal through the $k\Delta x$-kh plane defines the A_b number and a diagonal through the C_r-A_b plane defines the H_e number, both of which offer valid alternative coordinate axis to interpret the solution space. The choice to work with the C_r-axis herein is mainly due previous instances in the literature.

5.3 Analytic Solution

Analytic solutions to (5.35) and (5.36) are acquired following the same methodology as that presented in chapter 3 to solve (3.53) and (3.54), with the primary difference being that the integrands are in terms of $\overline{\omega}$ and $\overline{k}$, while the integrals are taken over the physical planes. In general, there are N roots over the ω-plane and M roots over the k-plane, which map to the same $\overline{\omega}$ and $\overline{k}$ values respectively. Being linear, the final solution is given by a superposition of the root solutions (C. Tam

and Webb 1993). Focus here will be directed on the physical roots, denoted by ω_p and k_p, in which all other root solutions exhibit the same solution structure, albeit their values are different.

Beginning with the free surface elevation, the Residue Theory is applied to solve the integral over the ω-plane. The numerical dispersion relation gives rise to two poles, $\overline{\omega^1}_1$ and $\overline{\omega^1}_2 = -\overline{\omega^1}_1$, each of which have multiple root solutions corresponding to forward and backward propagating waves. Taking the conjugate of (4.26) and solving for the conjugate roots (e.g., see (4.30)), the follow relation $\omega_p(-\overline{\omega^1}) = -\omega_p^*(\overline{\omega^1})$ is established, where ω_p^* is the conjugate root (e.g., C. Tam and Webb 1993). Therefore, the points of evaluation are defined by the complex expansions, $\omega_p = \mathrm{Re}(\omega_p) + i\mathrm{Im}(\omega_p)$ and $-\omega_p^* = -\mathrm{Re}(\omega_p) + i\mathrm{Im}(\omega_p)$, which accounts for both forward and backward propagating waves. For the physical roots over the ω-plane, the superposition of modes defining the free surface is given by

$$\begin{aligned}\eta = &\int_{-\infty}^{\infty} \frac{1}{2}\left(\widetilde{\eta_o} + \frac{\widetilde{u_o}\overline{k^1}h(1+\sigma_2\overline{k^2}h^2)}{\overline{\omega^1}(1+\sigma_1\overline{k^2}h^2)}\right)\mathcal{A}e^{i(kx-\mathrm{Re}(\omega_p)t)}e^{\mathrm{Im}(\omega_p)t}dk \quad + \\ &\int_{-\infty}^{\infty} \frac{1}{2}\left(\widetilde{\eta_o} - \frac{\widetilde{u_o}\overline{k^1}h(1+\sigma_2\overline{k^2}h^2)}{\overline{\omega^1}(1+\sigma_1\overline{k^2}h^2)}\right)\mathcal{A}^*e^{i(kx+\mathrm{Re}(\omega_p)t)}e^{\mathrm{Im}(\omega_p)t}dk\end{aligned} \tag{5.43}$$

in which

$$\mathcal{A} = \frac{\overline{\omega^1}}{\omega_p\frac{\partial\overline{\omega^1}}{\partial\omega}} \quad , \quad \mathcal{A}^* = \frac{\overline{\omega^1}^*}{\omega_p^*\frac{\partial\overline{\omega^1}^*}{\partial\omega}} \tag{5.44}$$

Collecting like terms gives

$$\begin{aligned}\eta = &\int_{-\infty}^{\infty} \widetilde{\eta_o}\left(\frac{\mathcal{A}^*e^{i\mathrm{Re}(\omega_p)t} + \mathcal{A}e^{-i\mathrm{Re}(\omega_p)t}}{2}\right)e^{\mathrm{Im}(\omega_p)t}e^{ikx}dk \quad - \\ &\int_{-\infty}^{\infty} \frac{i\widetilde{u_o}\overline{k^1}h(1+\sigma_2\overline{k^2}h^2)}{\overline{\omega^1}(1+\sigma_1\overline{k^2}h^2)}\left(\frac{\mathcal{A}^*e^{i\mathrm{Re}(\omega_p)t} - \mathcal{A}e^{-i\mathrm{Re}(\omega_p)t}}{2i}\right)e^{\mathrm{Im}(\omega_p)t}e^{ikx}dk\end{aligned} \tag{5.45}$$

Applying complex identities (G.26) and (G.27) gives

$$\begin{aligned}\eta = &\int_{-\infty}^{\infty} \widetilde{\eta_o}\left(\mathrm{Re}(\mathcal{A})\cos(\mathrm{Re}(\omega_p)t) + \mathrm{Im}(\mathcal{A})\sin(\mathrm{Re}(\omega_p)t)\right)e^{\mathrm{Im}(\omega_p)t}e^{ikx}dk \quad - \\ &\int_{-\infty}^{\infty} \frac{i\widetilde{u_o}\overline{k^1}h(1+\sigma_2\overline{k^2}h^2)}{\overline{\omega^1}(1+\sigma_1\overline{k^2}h^2)}\left(\mathrm{Re}(\mathcal{A})\sin(\mathrm{Re}(\omega_p)t) - \mathrm{Im}(\mathcal{A})\cos(\mathrm{Re}(\omega_p)t)\right)e^{\mathrm{Im}(\omega_p)t}e^{ikx}dk\end{aligned} \tag{5.46}$$

Multiplying the trigonometric identities (G.13) and (G.15) by a gain, $\mathcal{G}$, and introducing a phase

shift, ϕ, the expressions above simplify to

$$\eta = \int_{-\infty}^{\infty} \left(\widetilde{\eta_o} \cos(\mathrm{Re}(\omega_p)t - \phi) - \frac{i\widetilde{u_o}\overline{k^1}h(1+\sigma_2\overline{k^2}h^2)}{\overline{\omega^1}(1+\sigma_1\overline{k^2}h^2)} \sin(\mathrm{Re}(\omega_p)t - \phi) \right) \mathcal{G}e^{\mathrm{Im}(\omega_p)t} e^{ikx} dk \tag{5.47}$$

in which

$$\mathcal{G} = \sqrt{\mathrm{Re}(\mathcal{A})^2 + \mathrm{Im}(\mathcal{A})^2} \tag{5.48}$$

$$\phi = \tan^{-1}\left(\frac{\mathrm{Im}(\mathcal{A})}{\mathrm{Re}(\mathcal{A})} \right) \tag{5.49}$$

In comparison to (3.67), the numerical free surface solution (5.47) includes a phase shift, ϕ, and a gain factor, $\mathcal{G}e^{\mathrm{Im}(\omega_p)t}$, which must be decaying over time for stable solutions. Furthermore, the angular frequency is in terms of the physical root as opposed to the theoretical angular frequency.

The superposition of modes defining the velocity is given by

$$\begin{aligned} u = &\int_{-\infty}^{\infty} \frac{1}{2} \left(\widetilde{u_o} + \frac{\widetilde{\eta_o}\overline{k^1}(1+\sigma_4\overline{k^2}h^2)}{\overline{\omega^1}(1+\sigma_3\overline{k^2}h^2)} \right) \mathcal{A}e^{i(kx - \mathrm{Re}(\omega_p)t)} e^{\mathrm{Im}(\omega_p)t} dk \quad + \\ &\int_{-\infty}^{\infty} \frac{1}{2} \left(\widetilde{u_o} - \frac{\widetilde{\eta_o}k(1+\sigma_4\overline{k^2}h^2)}{\overline{\omega^1}(1+\sigma_3\overline{k^2}h^2)} \right) \mathcal{A}^* e^{i(kx + \mathrm{Re}(\omega_p)t)} e^{\mathrm{Im}(\omega_p)t} dk \end{aligned} \tag{5.50}$$

Applying the same methodology as before, trigonometric form is given as

$$u = \int_{-\infty}^{\infty} \left(\widetilde{u_o} \cos(\mathrm{Re}(\omega_p)t - \phi) - \frac{i\widetilde{\eta_o}k(1+\sigma_4(kh)^2)}{\omega(1+\sigma_3(kh)^2)} \sin(\mathrm{Re}(\omega_p)t - \phi) \right) \mathcal{G}e^{\mathrm{Im}(\omega_p)t} e^{ikx} dk \tag{5.51}$$

In comparison to (3.73) the numerical velocity (5.51) also includes a phase shift, ϕ, and a gain factor, $\mathcal{G}e^{\mathrm{Im}(\omega_p)t}$, which must be decaying over time for stable solutions.

For the spatial schemes considered herein, the physical root over the k-plane is real and identical to the theoretical wave number, $k_p = k$, therefore, standing wave solutions will be of the form

$$\eta = A_s \mathcal{G}e^{\mathrm{Im}(\omega_p)t} \cos(\mathrm{Re}(\omega_p)t - \phi) \cos(\mathrm{Re}(k_p)x) \tag{5.52}$$

$$u = \frac{A_s}{h} \frac{\overline{\omega^1}(1+\sigma_1\overline{k^2}h^2)}{\overline{k^1}(1+\sigma_2\overline{k^2}h^2)} \mathcal{G}e^{\mathrm{Im}(\omega_p)t} \sin(\mathrm{Re}(\omega_p)t - \phi) \sin(\mathrm{Re}(k_p)x) \tag{5.53}$$

in which the equations converge to (3.83) and (3.84) respectively in the case of vanishing sampling intervals. Equations (5.52) and (5.53) will be utilized in numerical experiments carried out in the next section.

In summary, the integrands of the inverse transforms (5.35) and (5.36) are expressed in the form $Fe^{-i(kx-\omega t)}$, where substitutions $t = \tau\Delta t$ and $x = \ell\Delta x$ give the discrete complement. In general, difference approximations produce multiple root solutions, all which contribute in a unique way to the net result. In the perspective of difference approximations, the fundamental question is concerned with what happens over a single sampling interval, thus by setting $\tau = \ell = 1$, focus is directed on the difference schemes. If the roots are assumed complex, the integrands becomes $Ge^{-i(k_R\Delta x-\omega_R\Delta t)}$, where $G = Fe^{-(k_I\Delta x-\omega_I\Delta t)}$ represents the amplitude and $e^{-(k_I\Delta x-\omega_I\Delta t)}$ is often referred to as the amplification factor (e.g., Richtmyer and Morton 1967). Clearly, if $k_I\Delta x-\omega_I\Delta t = 0$, then the amplification factor is equal to unity and there is no growth or decay. An easy way to achieve this is by employing central schemes, which lead to real spectral characteristics. If only central spatial schemes are utilized, $k_I = 0$, then the amplification factor reduces to $e^{\omega_I\Delta t}$, requiring $\omega_I\Delta t \leq 0$ to ensure stability. While the general requirement, $-(k_I\Delta x - \omega_I\Delta t) \leq 0$, does show that an interaction between temporal and spatial schemes is possible, it is important to acknowledge that this further constrains the convergence characteristics. Specifically, the way in which the limits are taken influences the stability.

5.4 Implementation: $O(\Delta t^4)$ Adams-Bashforth, $O(\Delta x^4)$ Tridiagonal Central Compact

In the previous chapter, the $O(\Delta t^4)$ Adams-Bashforth scheme was utilized as proxy for discussion on the complex spectral properties of bias schemes, which include both dispersive and dissipative characteristics. While the characteristics presented are unique to the specific scheme, the lessons learned hold for all bias schemes, be it temporal or spatial discretization. In this section, implementation of the $O(\Delta t^4)$ Adams-Bashforth scheme is presented, in conjunction with a $O(\Delta x^4)$ tridiagonal central compact spatial discretization.

5.4.1 Scheme

The configuration and coefficients for the $O(\Delta t^4)$ Adams-Bashforth temporal scheme can be found in Table 4.5 herein. Likewise, the $O(\Delta x^4)$ tri-diagonal central compact first and second spatial difference schemes can be found in Tables 4.1, and 4.2 respectively. Substituting the coefficient values into (5.11) - (5.20) gives the difference approximations to be employed in practice. Below

the system of equations representing the continuity and momentum equation are given as

Continuity

$$\frac{1}{10}(q_u)_{\ell-1}^{\tau}+(q_u)_{\ell}^{\tau}+\frac{1}{10}(q_u)_{\ell+1}^{\tau}= \tag{5.54}$$
$$\left(\frac{1}{10}-\frac{6\phi_2}{5}\right)(u)_{\ell-1}^{\tau}+\left(1+\frac{12\phi_2}{5}\right)(u)_{\ell}^{\tau}+\left(\frac{1}{10}-\frac{6\phi_2}{5}\right)(u)_{\ell+1}^{\tau}+\varepsilon$$

$$\frac{1}{4}(Q_u)_{\ell-1}^{\tau}+(Q_u)_{\ell}^{\tau}+\frac{1}{4}(Q_u)_{\ell+1}^{\tau}=\frac{h}{\Delta x}\left(-\frac{3}{4}(q_u)_{\ell-1}^{\tau}+\frac{3}{4}(q_u)_{\ell+1}^{\tau}\right)+\varepsilon \tag{5.55}$$

$$(p_\eta)_{\ell}^{\tau+1}=(p_\eta)_{\ell}^{\tau}-\Delta t\left(\frac{55}{24}(Q_u)_{\ell}^{\tau}-\frac{59}{24}(Q_u)_{\ell}^{\tau-1}+\frac{37}{24}(Q_u)_{\ell}^{\tau-2}-\frac{3}{8}(Q_u)_{\ell}^{\tau-3}\right)+\varepsilon \tag{5.56}$$

$$\frac{1}{10}(p_\eta)_{\ell-1}^{\tau+1}+(p_\eta)_{\ell}^{\tau+1}+\frac{1}{10}(p_\eta)_{\ell+1}^{\tau+1}= \tag{5.57}$$
$$\left(\frac{1}{10}-\frac{6\phi_1}{5}\right)(\eta)_{\ell-1}^{\tau+1}+\left(1+\frac{12\phi_1}{5}\right)(\eta)_{\ell}^{\tau+1}+\left(\frac{1}{10}-\frac{6\phi_1}{5}\right)(\eta)_{\ell+1}^{\tau+1}+\varepsilon$$

Momentum

$$\frac{1}{10}(q_\eta)_{\ell-1}^{\tau}+(q_\eta)_{\ell}^{\tau}+\frac{1}{10}(q_\eta)_{\ell+1}^{\tau}= \tag{5.58}$$
$$\left(\frac{1}{10}-\frac{6\phi_4}{5}\right)(\eta)_{\ell-1}^{\tau}+\left(1+\frac{12\phi_4}{5}\right)(\eta)_{\ell}^{\tau}+\left(\frac{1}{10}-\frac{6\phi_4}{5}\right)(\eta)_{\ell+1}^{\tau}+\varepsilon$$

$$\frac{1}{4}(Q_\eta)_{\ell-1}^{\tau}+(Q_\eta)_{\ell}^{\tau}+\frac{1}{4}(Q_\eta)_{\ell+1}^{\tau}=\frac{1}{\Delta x}\left(-\frac{3}{4}(q_\eta)_{\ell-1}^{\tau}+\frac{3}{4}(q_\eta)_{\ell+1}^{\tau}\right)+\varepsilon \tag{5.59}$$

$$(p_u)_{\ell}^{\tau+1}=(p_u)_{\ell}^{\tau}-\Delta t\left(\frac{55}{24}(Q_\eta)_{\ell}^{\tau}-\frac{59}{24}(Q_\eta)_{\ell}^{\tau-1}+\frac{37}{24}(Q_\eta)_{\ell}^{\tau-2}-\frac{3}{8}(Q_\eta)_{\ell}^{\tau-3}\right)+\varepsilon \tag{5.60}$$

$$\frac{1}{10}(p_u)_{\ell-1}^{\tau+1}+(p_u)_{\ell}^{\tau+1}+\frac{1}{10}(p_u)_{\ell+1}^{\tau+1}= \tag{5.61}$$
$$\left(\frac{1}{10}-\frac{6\phi_3}{5}\right)(u)_{\ell-1}^{\tau+1}+\left(1+\frac{12\phi_3}{5}\right)(u)_{\ell}^{\tau+1}+\left(\frac{1}{10}-\frac{6\phi_3}{5}\right)(u)_{\ell+1}^{\tau+1}+\varepsilon$$

in which $\phi_n=\mu^2\sigma_n h^2/\Delta x^2$ has been introduced for clarity. Each of the implicit equations (5.54), (5.55), (5.57), (5.58), (5.59), and (5.61) represents a compact linear system of equations with tridiagonal coefficient matrices, and thus can be solved with high efficiency using direct methods. The order in which the equations are presented corresponds the algorithmic procedure. Given the initial conditions η_o and u_o, equations (5.54) and (5.58) can be solved for $(q_u)_\ell^\tau$ and $(q_\eta)_\ell^\tau$ respectively. Substituting the values into (5.55) and (5.59) gives $(Q_u)_\ell^\tau$ and $(Q_\eta)_\ell^\tau$ respectively, which can then be substituted into (5.56) and (5.60) to march p_η and p_u forward in time from the initial conditions. The updated values are then respectively employed in (5.58) and (5.61) to solve for $\eta_\ell^{\tau+1}$ and $u_\ell^{\tau+1}$ at the new time step, which is where the exchange of information between the

continuity and momentum equation occurs. In the next time step, the process repeats, with (5.54) and (5.58) taking on the updated values.

5.4.2 Linear Stability

Following C. Tam and Webb (1993), a stability analysis is performed to establish a constraint criterion on the maximum numerical time step. Taking the square root of (5.40) gives

$$\overline{\omega^1}\Delta t = \frac{\sqrt{h}\Delta t}{\Delta x}\overline{k^1}\Delta x\sqrt{\frac{\left(1+\sigma_2 A_b^2\left(\overline{k^2}\Delta x^2\right)\right)\left(1+\sigma_4 A_b^2\left(\overline{k^2}\Delta x^2\right)\right)}{\left(1+\sigma_1 A_b^2\left(\overline{k^2}\Delta x^2\right)\right)\left(1+\sigma_3 A_b^2\left(\overline{k^2}\Delta x^2\right)\right)}} \tag{5.62}$$

in which the square root of the rational expression on the right is referred to as the dispersion factor, as it represents a collection of terms involving σ_n associated with various dispersive theories.

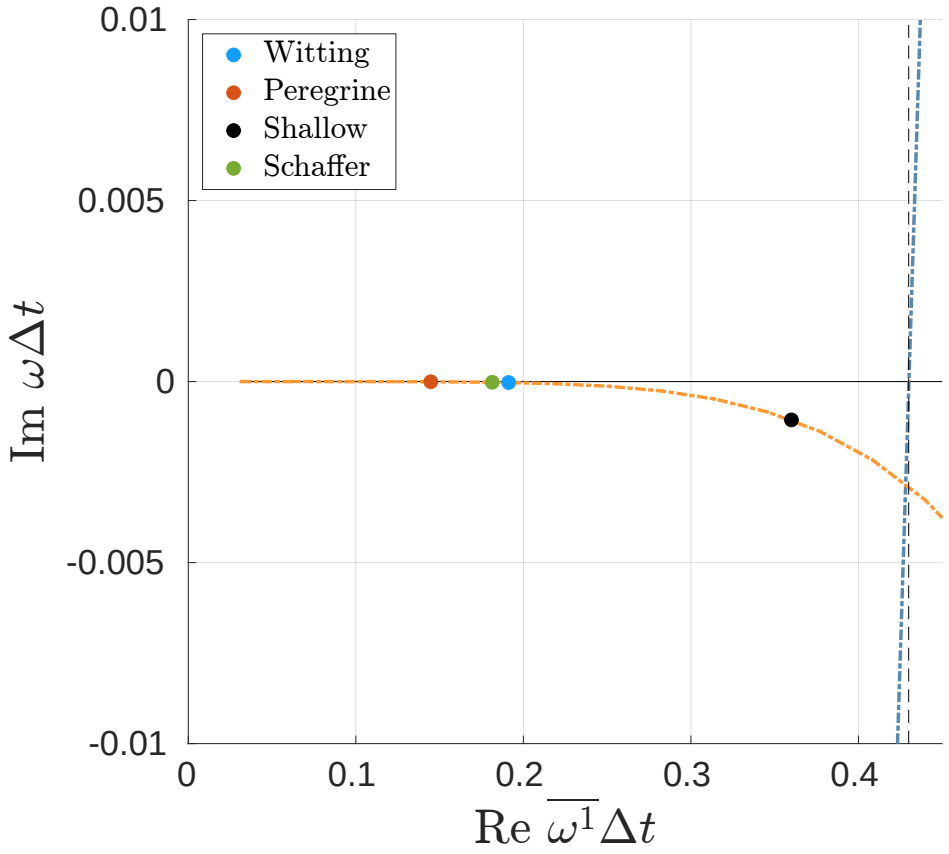

Figure 5.3: Zoom of Figure 4.13b near the stability limit (black dashed line), where one of the parasitic roots (blue dot-dash) becomes positive. As $\overline{\omega^1}\Delta t \to 0$, the physical root (orange dot-dash) approaches zero asymptotically. The ordinate axis represents the decay coefficient. Each of the dots denotes a different theory with the same numerical configuration.

Specific to the $O(\Delta^4)$ Adams-Bashforth scheme, Figure 5.3 shows a zero crossing of the imaginary components at approximately $\overline{\omega^1}\Delta t \approx 0.4299$, which gives an upper bound on the stability. Substituting the value into (5.62) and solving for Δt gives

$$\Delta t \lesssim \frac{0.4299\Delta x}{\left(\overline{k^1}\Delta x\right)\sqrt{h}}\sqrt{\frac{\left(1+\sigma_1 A_b^2\left(\overline{k^2}\Delta x^2\right)\right)\left(1+\sigma_3 A_b^2\left(\overline{k^2}\Delta x^2\right)\right)}{\left(1+\sigma_2 A_b^2\left(\overline{k^2}\Delta x^2\right)\right)\left(1+\sigma_4 A_b^2\left(\overline{k^2}\Delta x^2\right)\right)}} \tag{5.63}$$

To support all effective wave numbers resolved by the spatial difference schemes, the largest values of $\overline{k^1}\Delta x \lesssim 1.7319$ and $\overline{k^2}\Delta x^2 \lesssim 6$, shown in Figures 4.4a and 4.5a respectively, are inserted to give

$$\Delta t \approx \frac{0.2482\Delta x}{\sqrt{h}}\sqrt{\frac{\left(1+6\sigma_1 A_b^2\right)\left(1+6\sigma_3 A_b^2\right)}{\left(1+6\sigma_2 A_b^2\right)\left(1+6\sigma_4 A_b^2\right)}} \tag{5.64}$$

Dividing both sides by $\sqrt{h}$, the left hand side is expressed in terms of H_e^{-1} and the right hand side is a constant times A_b^{-1}, multiplied by the inverse dispersion factor attributed to the theory employed.

Inverse dispersion factors for select theories, which exhibit both dispersive and non dispersive characteristics, are illustrated in Figure 5.4 versus the A_b number. Among the dispersive theories shown, the Padé order of approximation and over/under estimation of the celerity varies to infer trends. The non dispersive shallow water theory is a constant equal to unity, whereas all other dispersive theories have a greater value. For dispersive theories which exhibit a phase lag (see Figure (3.2)), such as that of Peregrine (1967), the inverse dispersion factor is larger than those which exhibit a phase lead and approach a linear relation with the A_b number. For dispersion factors which exhibit a phase lead, such as that of Witting (1984), the dispersion factor approaches a constant as the A_b number increases, with higher order theories approaching a higher constant value. For explicit time integration schemes, the time step should always support the fastest waves governed by the theory (Courant et al. 1967). Therefore, the inverse dispersion factor takes on a value of unity, giving $(H_e^{-1})_{max} \approx 0.2482/A_b$, which by definition gives

$$(C_r)_{max} = 0.2482 \tag{5.65}$$

where as long as $\Delta t \leq 0.2482\Delta x/\sqrt{h}$, the solution will remain stable, regardless of the theory employed. However, the dispersion factor still plays a role in the accuracy and stability. In Figure 5.3, roots corresponding to the theories under investigation are shown for a particular test case. With all else being equal, it is shown that for the theory of Peregrine (1967), which exhibits a phase lag, the root is pushed far to the left. While this does imply less amplitude decay, hence less dispersive error, it also shows that the theory is most penalized by the Courant number constraint.

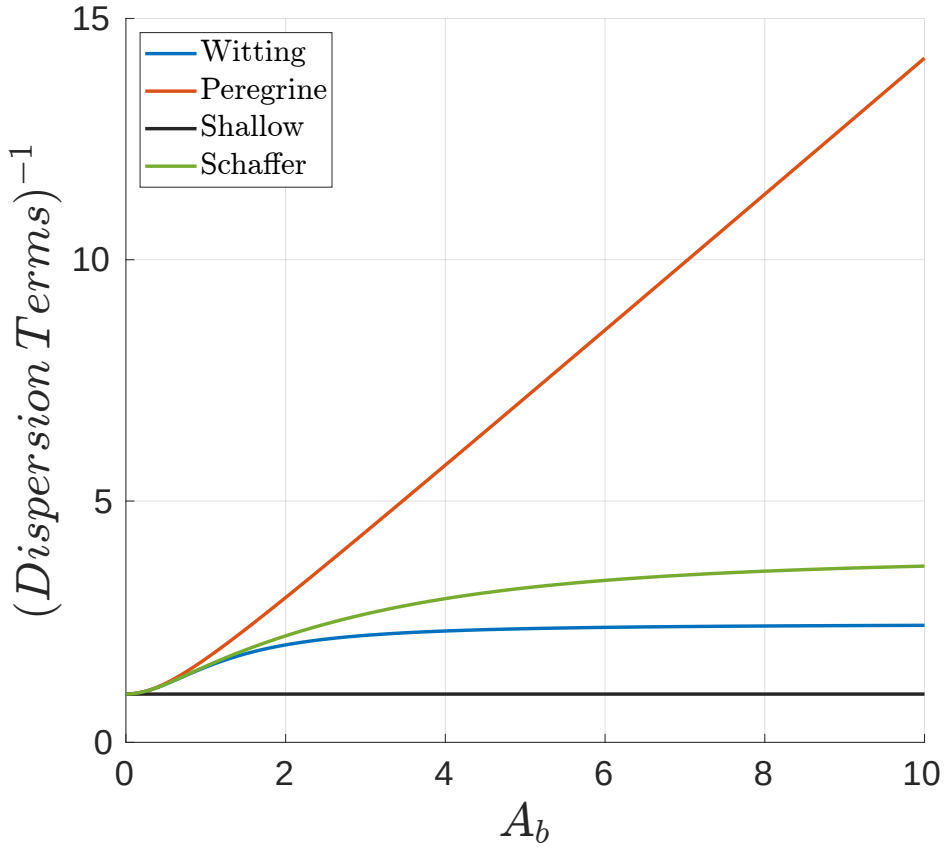

Figure 5.4: Inverse of dispersion factor for select theories.

The shallow water root, located nearest to the stability limit, gives the most amplitude decay, hence the most dispersive error, but remains stable by design. The low Courant constraint is in part due to the implementation of compact schemes, which is a well known trade-off for the improved accuracy at a coarser spatial resolution (e.g., Lele 1992). This is readily understood upon reviewing equation (5.63) in which the maximum effective wave number, $\overline{k^1}$, defines the denominator in the leading fraction. For compact, as well as high order classic schemes, this number increases, hence driving down the C_r constraint. Assuming a fixed water depth, a low C_r number is indicative of high spatial accuracy with a relatively low range of stability, whereas a high C_r number is indicative of low spatial accuracy with a relatively high range of stability. Clearly, $C_r = 1$ if the spatial accuracy and range of stability are the same. Therefore, a high C_r number alone does not indicate one scheme is superior over another.

5.4.3 Linear Celerity

In the previous section, a maximum time-step was determined based on the linear stability constraint of the explicit $O(\Delta t^4)$ Adams-Bashforth scheme, which is a function of the Courant number, derived from the imaginary component of the root solutions. In this section, linear phase errors are evaluated in terms of wave celerity, which is derived from the real component of the root solutions. Boussinesq-type equations themselves serve as an approximation to the linear dispersion relation (see Figure 3.2), thus there are two perspectives on how to interpret phase errors intrinsic to the MPDEs. In the first perspective, the errors are evaluated relative to the PDEs. This perspective is a projection of the collective errors studied in Figures 4.4, 4.5, and 4.11, which, depending on how the errors are interpreted, are then scaled by discrete attributes of the mesh and physical variables of the continuum (see section 5.2 discussion). While informative, the practitioner is ultimately interested in the net error induced by both the theory and the difference approximation. Therefore, a second perspective is defined in which the errors are measured relative to the fully dispersive Airy wave theory. In this perspective, the mesh attributes can be defined such that the net error is minimized over a pertinent range of relative wave numbers by offsetting intrinsic theoretical errors with difference errors (e.g., Imamura and Goto 1988; Cho 1995; L. Li and Cheung 2019). For demonstration purposes, the Padé [2/2] theory of Witting (1984) is employed herein, although the methodology applies to all theories. The selection was made foreseeing the need to carry out numerical experiments, in which the monotonic error characteristics (e.g., see Figure 3.2) make it easier to identify sources of error.

MPDEs vs PDEs

In contrast to the dissipation, which is defined by the imaginary component of the roots, the phase is defined by the real component. For central schemes, there is no imaginary component, thus they only incur phase errors. For these schemes, the physical root shares the same value as the domain of the effective operator, which is the physical wave number. Specific to the $O(\Delta x^4)$ tridiagonal central compact scheme, this means that $k_p = k$, which is true for both first and second difference approximations considered herein. However, it should be emphasized that other roots, which are real, do exist in the mapping to the root solutions, where $k_n \neq k$, for the high order schemes. The wave celerity of the physical root governed by the MPDEs is thus defined by

$$c_p = \frac{\omega_p}{k_p} \tag{5.66}$$

in which the subscript on the celerity is dropped henceforth, with it being understood that the primary focus herein is on the physical root. Since $k_p = k$, all that remains is to define ω_p, which

is a function of the effective angular frequency defined by the numerical dispersion relation (5.38), or any of its variants.

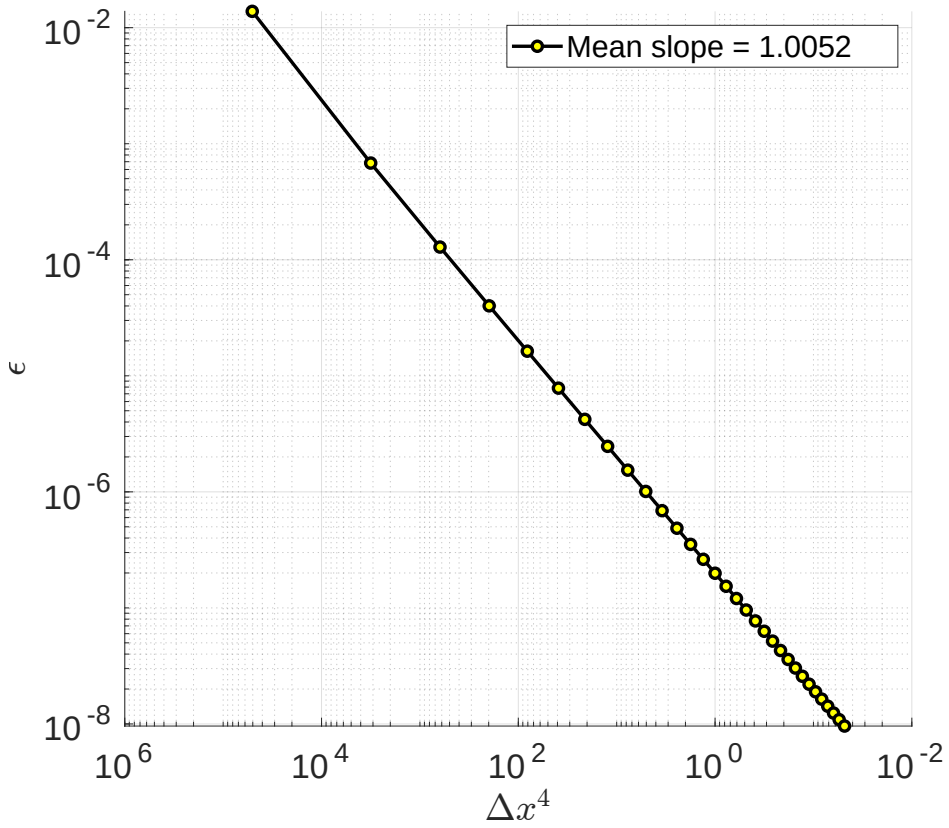

Figure 5.5: Convergence of numerical dispersion relation.

Figure 5.5 expresses the absolute value of the absolute error of the right hand side of (5.38), with respect to the physical dispersion (3.56), as $\Delta x \to 0$, indicating that the aggregate contribution of both first and second difference approximations is indeed $O(\Delta x^4)$ accurate. In addition, this means $\overline{\omega^1}(\omega) \to \omega$ as $\Delta x \to 0$; however, the physical root of $\overline{\omega^1}$ will not coincide with ω due to the complex effective angular frequency approximation. Nevertheless, the effective angular frequency is also $O(\Delta t^4)$ accurate by design, thus the overall scheme is $O(\Delta^4)$ accurate in both time and space.

Upon mapping the effective operators to their root solutions (see equation (4.31) in chapter 4 for general procedure), the celerity of the physical root (5.66) is readily determined. As discussed in section 5.2, the solution domain is multidimensional, thus to visually inspect the effects of the discretization, slices are taken throughout the domain. Oriented in the manner shown in Figure 5.2, Figures 5.6 and 5.7 represent vertical slices along their respective dimension, whereas Figure 5.8 represents horizontal slices over the relative depth.

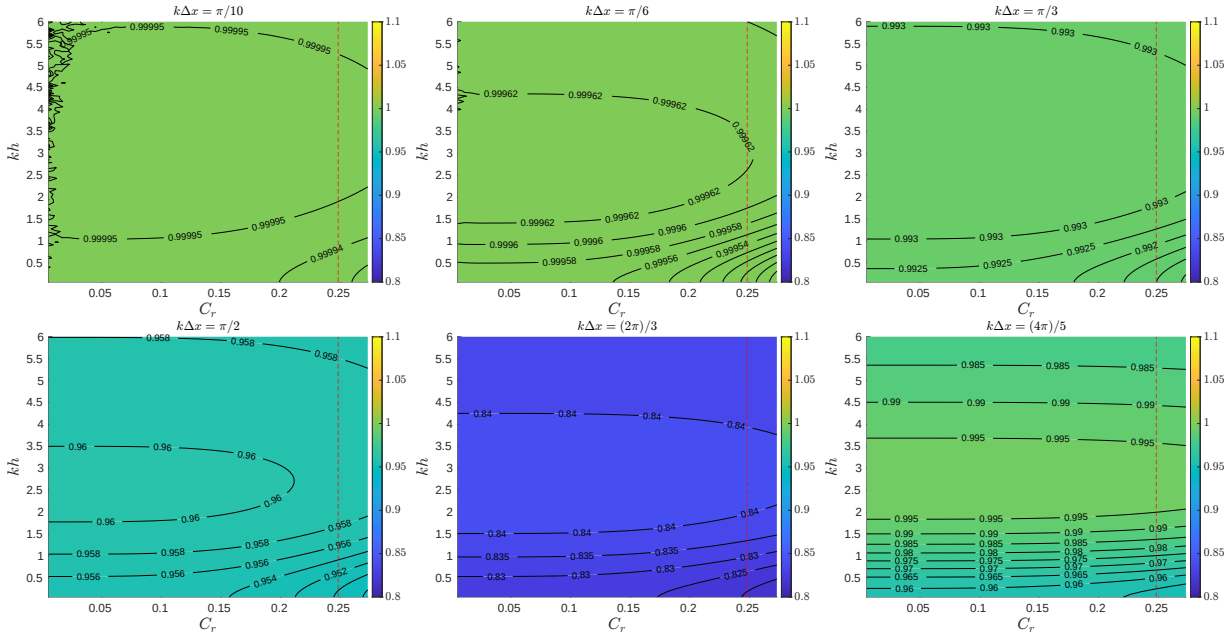

Figure 5.6: Relative celerity, $c/c_{Witting}$, for slices along $k\Delta x$ constant. Red dashed line indicates the stability limit.

Holding $k\Delta x$ constant, Figure 5.6 shows the Courant number has minor impact on the celerity, with the contours being predominately oriented horizontally. This observation is supported by Figure 4.13a, in which the real part of the physical root solution shows little error with respect to the continuum solution over the stability range. Furthermore, since the Courant constraint is bound by the shallow water theory, the dispersion factor acts to increase the accuracy, as discussed in the previous section. Although the horizontal gradients are small, for a given kh, it is observed that as the C_r increases, the celerity generally decreases. Continuing to hold kh fixed, a deeper intuition is sought by holding the wavelength fixed as well. In this particular case, with both kh and k being fixed, h is fixed. Focusing on a single panel implies Δx is fixed, thus the increase in the C_r number can only come from an increase in Δt by definition. In Figure 4.13a, the physical root exhibits a phase lag with respect to the continuum solution as Δt increases, which agrees with the observations above.

The previous analysis on Figure 5.6 accounts for horizontal variations, which are largely monotonic; however, the vertical variations do exhibit more structure. For example, fixing the C_r in Figure 5.6 at the stability limit shown by the red dashed line, focus is directed on the behavior of the error along a vertical path, representing a change in the relative water depth. As the relative water depth increases, the celerity error tends to decrease, then later increase. To better understand this, the wavelength is again held fixed, which implies the depth is increasing as kh increases. Focusing on a single panel, Δx is thus fixed. For a fixed C_r number, this means that Δt must be decreasing

if the water depth is increasing. Collectively, if the wavelength is held fixed in Figure 5.6, Δt is increasing moving left to right along horizontal lines and decreasing moving bottom to top along vertical lines. Comparing the contours across different panels (i.e., different Δx values) shows that the convergent behavior varies. Therefore, the behavior of the celerity error must be explained by convergent interactions associated with the temporal and spatial schemes. Although they are $O(\Delta t^4)$ and $O(\Delta x^4)$ accurate respectively, they are in fact unique. Furthermore, the celerity error reflects interactions governed by the right hand side of (5.38), which emphasizes that the curves shown are dependent upon the theory invoked.

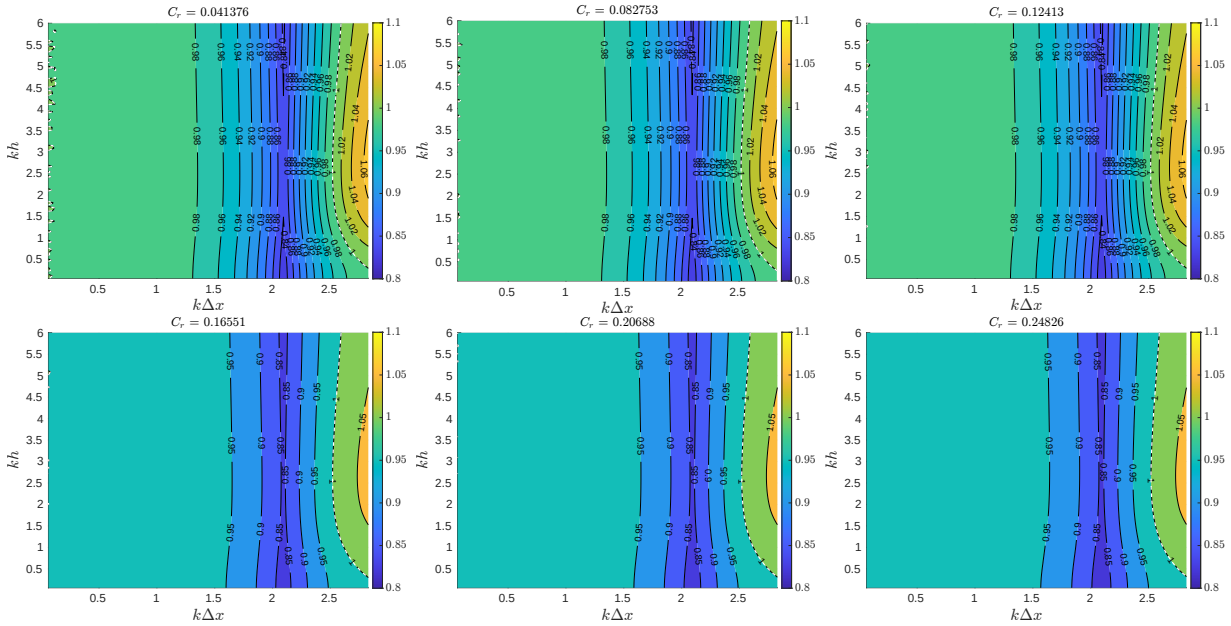

Figure 5.7: Relative celerity, $c/c_{Witting}$, for slices along C_r constant. White dashed lines indicate zero relative error.

In Figure 5.7, the Courant number is fixed. With each slice showing minor change of the contours, which are predominantly oriented vertically, the celerity errors largely reflect those due to the spatial discretization and persist over the relative water depth. Tracing the horizontal gradient along a fixed kh shows that the largest errors occur outside the normal range of operation near the inflection point of the first difference scheme (see Figure 4.4). While the errors do improve beyond the inflection point, the solution space is believed to be dominated by the second spatial root in this region. To reiterate, only the physical root is evaluated herein, as it is of principle interest in practical application. Furthermore, because there is no natural ordering in the complex number system, the "physical root" is subjectively defined. In the closing section of this chapter, the relation between the roots is further addressed in greater detail. Focus is thus directed to the left of the inflection point, which is the normal range of operation. Continuing to hold kh fixed, if the wavelength is fixed, then h is fixed and Δx is increasing moving left to right. Focusing on a fixed

panel, the C_r is fixed, thus Δt must also be increasing when moving left to right. Thus by comparing different panels, differences in the increasing behavior of Δt can be compared. Irrespective of the relative water depth, the celerity error is shown to decrease, which again, agrees with the phase behaviour observed in the discretization schemes.

As before, celerity errors along a vertical path representing changes in the relative water depth are investigated. Take for example $k\Delta x = 1.5$, while the contours do appear vertical, there is a slight decrease in the celerity error as the relative water depth increases. For a fixed wavelength, Δx is fixed, and the water depth increases. Focusing on a single panel, the C_r is fixed, which means Δt must be decreasing moving bottom to top. The minor decrease in celerity error is thus due to a decrease in Δt, which makes sense and further emphasizes that the celerity errors largely reflect those due to the spatial discretization.

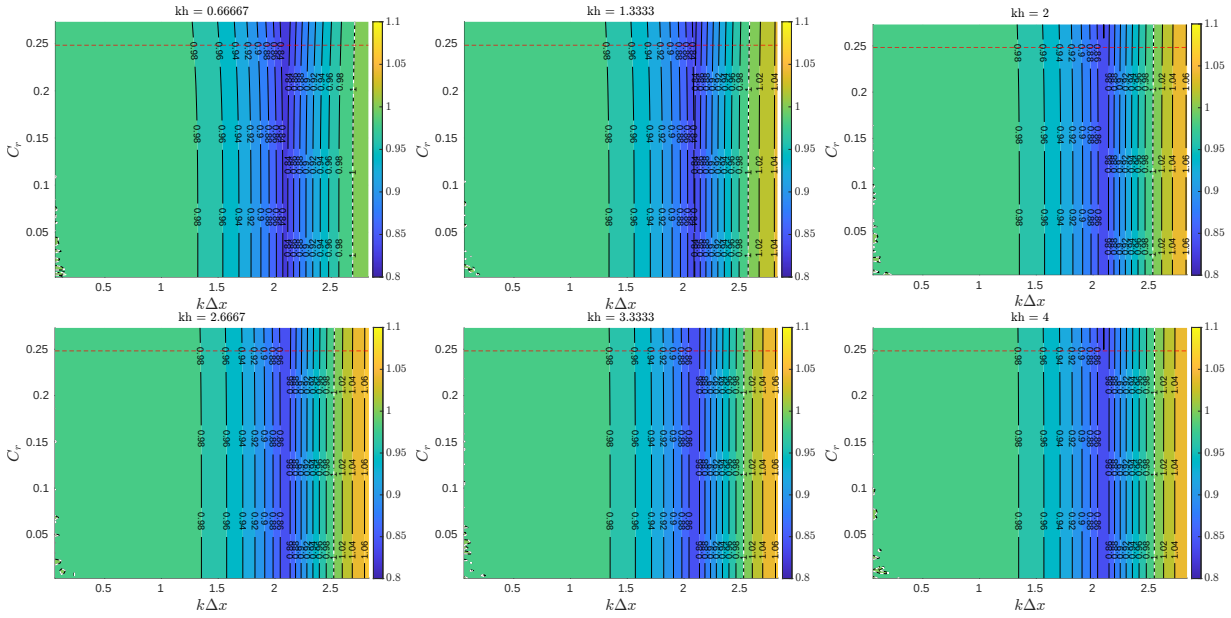

Figure 5.8: Relative celerity, $c/c_{Witting}$, for slices along kh constant. Red and white dashed line indicates the stability limit and zero relative error respectively.

Horizontal slices through the domain at fixed intervals of the relative depth are shown in Figure 5.8, which due to the orientation of the plots, show contours predominantly oriented vertically. The observations are more or less the same as those stated in prior analysis, thus will not be repeated for brevity. Together with Figures 5.6 and 5.7, Figure 5.8 predominantly serves as an aid to help visualize the volume of the solution space.

MPDEs vs Airy

As mentioned prior, quantifying the error relative to Airy wave theory has real practical advantages. Depending on the configuration of the computation, it is quite possible that a large error relative to the PDEs will still offer a valid solution relative to Airy wave theory, which is precisely the reference utilized when judging the quality of a theory in the continuum. Below, the error is measured as c/c_{Airy}, in which the same slices are employed as those utilized to evaluate the error relative to the PDEs. It should be emphasized upfront that the error analysis with respect to the PDEs still holds, thus will not be repeated for brevity. By changing the celerity reference to that of Airy wave theory, the error scale changes and largely masks out the finer details discussed with regard to the PDEs.

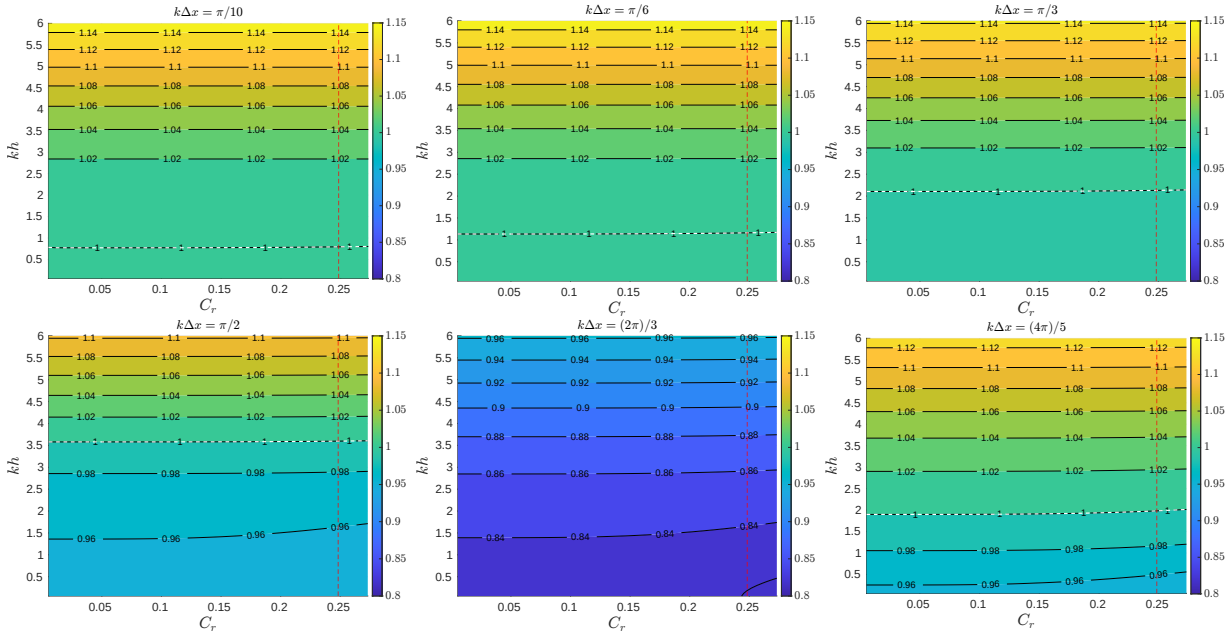

Figure 5.9: Relative celerity, c/c_{Airy}, for slices along $k\Delta x$ constant. Red and white dashed line indicates the stability limit and zero relative error respectively.

Holding $k\Delta x$ constant, Figure 5.9 reveals similar trends to those shown in Figure 5.6, with the contours being predominately oriented horizontally. However, in contrast, the relative celerity errors indicate that some waves travel slower and faster than those defined by Airy wave theory. This is readily explained by reviewing Figure 3.2, in which the theory of Witting (1984) is shown to overestimate the celerity of Airy wave theory. Combined with the underestimation due to the difference approximation, the net result can lead to better agreement with Airy wave theory. For difference approximations which underestimate the celerity of the PDEs, this trend holds true for all theories which overestimate the celerity relative to that of Airy wave theory. For theories which underestimate the celerity of Airy wave theory, such as Peregrine (1967), difference approximations

which overestimate the celerity of the PDEs (e.g., linear finite element) would need to be employed to achieve the same net effect. The nearly horizontal white dashed line, denoting zero relative error, is shown to occur at different levels of kh indicating a $k\Delta x$ dependence. Up to the inflection point (near $k\Delta x = 2\pi/3$), the kh levels increase with increasing $k\Delta x$, then decrease in the last slice shown.

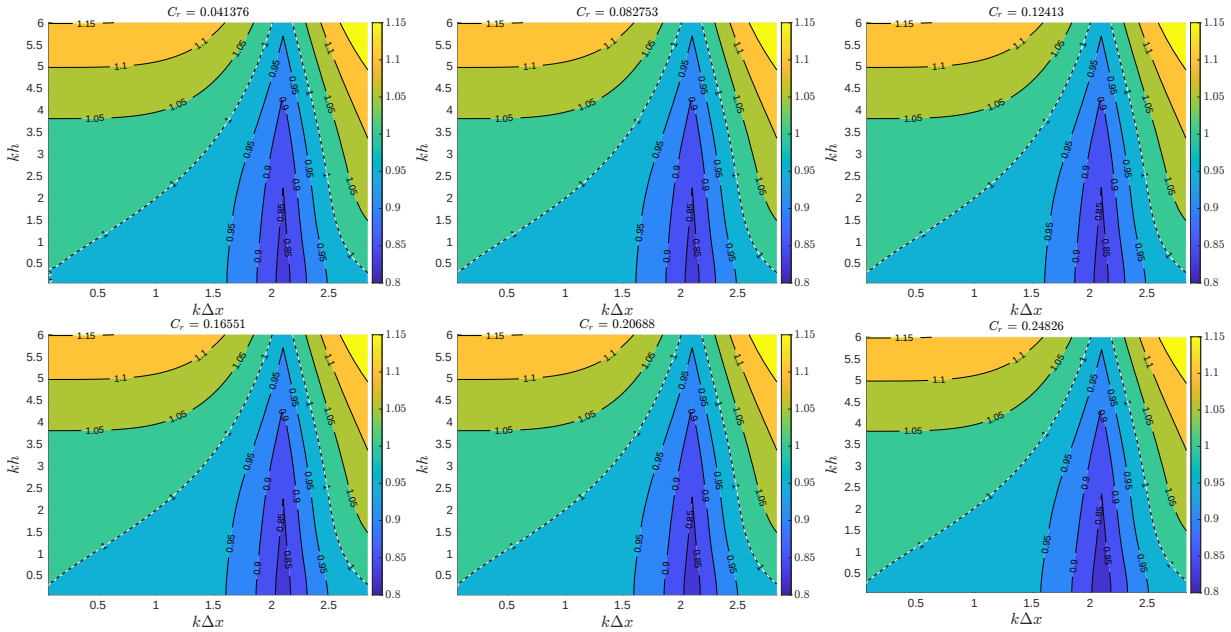

Figure 5.10: Relative celerity, c/c_{Airy}, for slices along C_r constant. White dashed line indicates zero relative error.

As was the case in Figure 5.7, holding the Courant number constant shows little change over each slice in Figure 5.10, indicating that the errors in celerity are dominated by the spatial discretization. However, the contours are dramatically different and reflect errors in the first spatial difference scheme more so than before. The white dashed line, denoting zero relative error, follows the same general trend as the first difference scheme (see Figure 4.4), with the inflection point clearly highlighted by the contour peaks. As indicated before, the solution space is specific to the physical root, where beyond the inflection point, the second root likely plays a more prominent role.

Analogous to Figure 5.8, Figure 5.11 shows horizontal slices through the domain at fixed intervals of the relative depth and serves as an aid to help visualize the volume of the solution space. The white dashed lines, denoting zero relative error, agree with those presented in Figure 5.10 by getting closer together as kh increases.

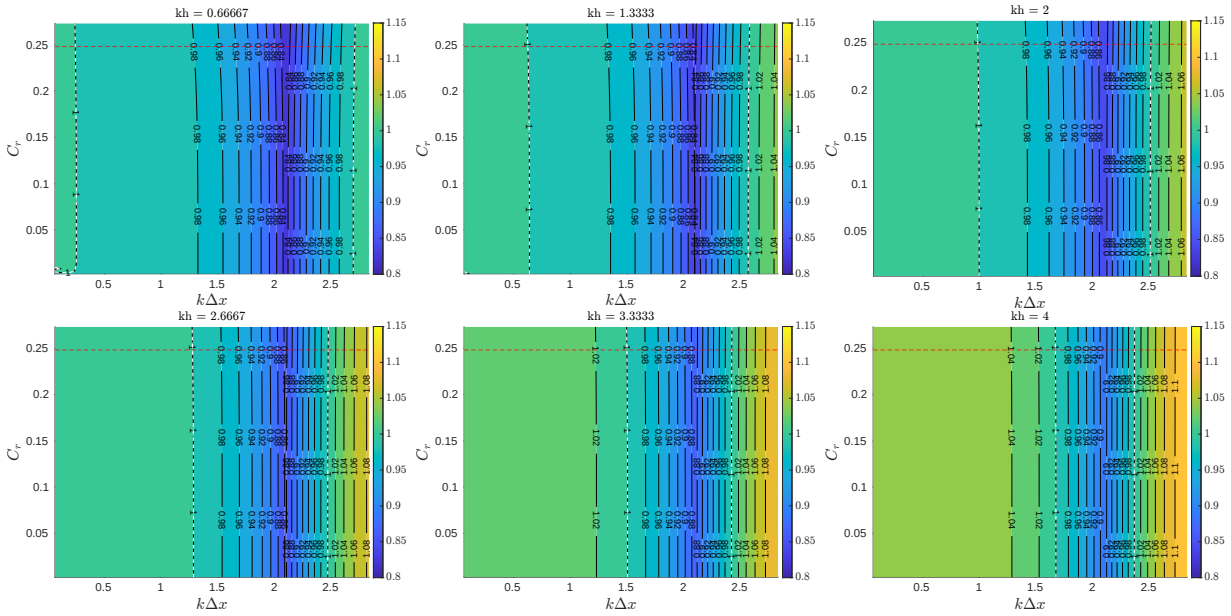

Figure 5.11: Relative celerity, c/c_{Airy}, for slices along kh constant. Red and white dashed line indicates the stability limit and zero relative error respectively.

5.4.4 Computational Experiments

The numerical scheme (5.54)-(5.61) facilitates development of a computational model to verify the linear dissipation and dispersion analysis. A simple, yet effective computational experiment, involves a standing wave in a flume. Herein, the flume length is defined to be one wavelength, with a flat bottom, and periodic boundary conditions. The initial still water conditions correspond to zero velocity and the maximum excursion of the free surface amplitude, $A_s/h = 0.01$, which in theory will oscillate about the still water level with the physical root solution to the free surface and velocity governed by (5.52) and (5.53) respectively. Analytic solutions for the continuum (3.83) and (3.84) are also shown for comparison purposes. Table 5.1 quantifies four test cases, in which parameters $k, h, \Delta x$ vary and the Courant number is fixed to ensure stability. Specific values for the first case were chosen such that numerical errors are inevitable; otherwise the values can be considered random. In the second case, only the wavelength is changed, thus kh and $k\Delta x$ take on a different values. In the third case, both the wavelength and spatial sampling interval are changed, which preserves the value of kh from the second case, but $k\Delta x$ changes. In the final case, only the water depth is changed with respect to the first case, thus preserving $k\Delta x$, but kh changes. By keeping the Courant number fixed, Δt changes in all cases.

Case	k	h	Δx	C_r	kh	$k\Delta x$	A_b	ω	Δt	$\omega\Delta t$
1	$\frac{\pi}{30}$	$\frac{90}{\pi}$	15	0.24	3	$\frac{\pi}{2}$	$\frac{6}{\pi}$	≈ 0.330564	≈ 0.672751	≈ 0.222387
2	$\frac{\pi}{45}$	$\frac{90}{\pi}$	15	0.24	2	$\frac{\pi}{3}$	$\frac{6}{\pi}$	≈ 0.260812	≈ 0.672678	≈ 0.175443
3	$\frac{\pi}{45}$	$\frac{90}{\pi}$	30	0.24	2	$\frac{2\pi}{3}$	$\frac{3}{\pi}$	≈ 0.260812	≈ 1.345355	≈ 0.350885
4	$\frac{\pi}{30}$	$\frac{120}{\pi}$	15	0.24	4	$\frac{\pi}{2}$	$\frac{8}{\pi}$	≈ 0.342030	≈ 0.582568	≈ 0.199255

Table 5.1: Experimental test case parameters: (left) input (right) derived. The Courant number (C_r) is fixed for stability.

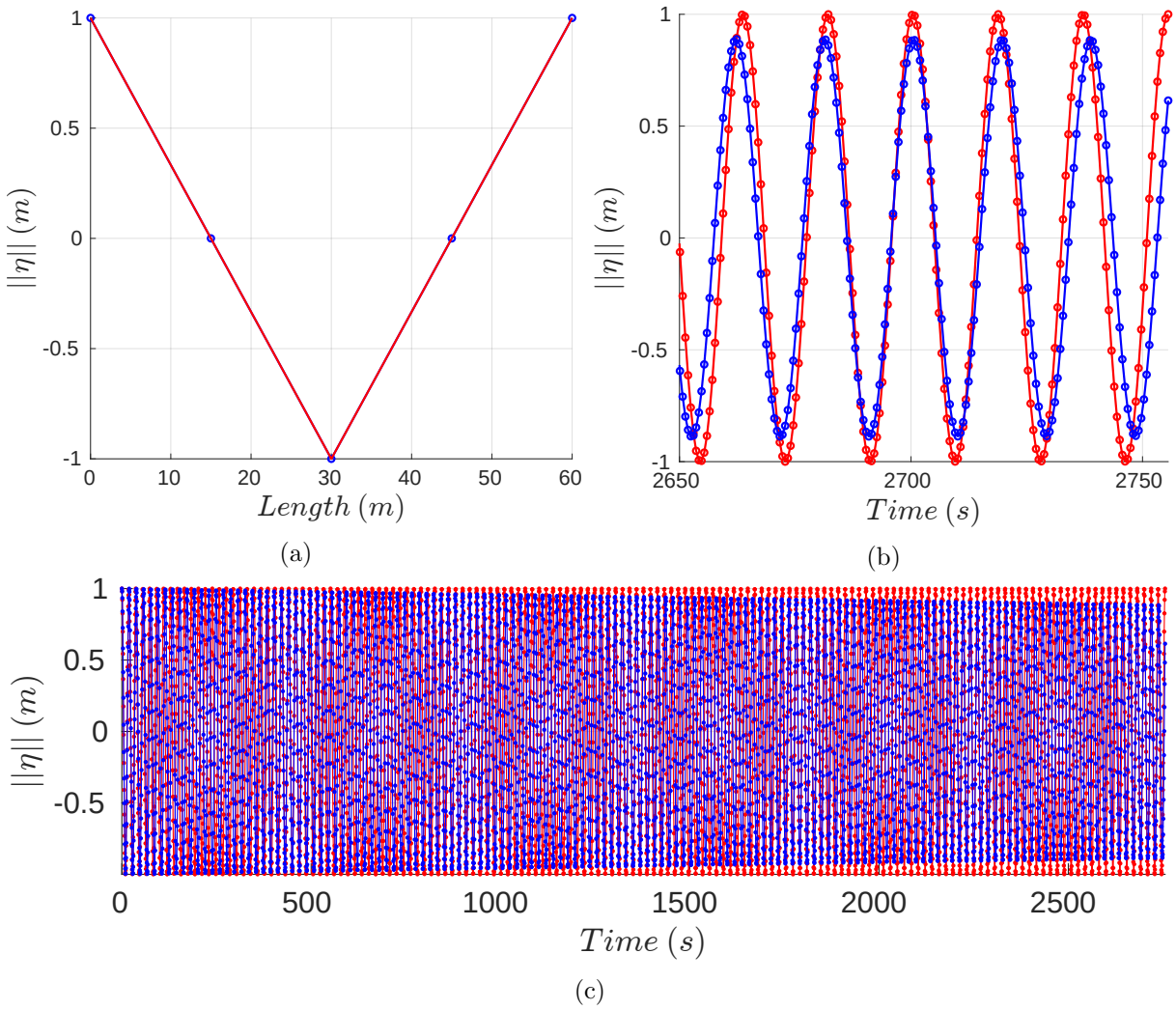

Figure 5.12: Test case 4 (top left) initial profile, (top right) time series snippet, and (bottom) full time series. Blue dotted lines denote the difference solution and red dotted lines denote the continuum solution.

An example of the normalized free surface wave profile is shown in Figure 5.12a for the final test case, which exhibits two nodes and three anti-nodes. For this case, only four cells per wavelength are employed to resolve the wave, hence numerical errors are inevitable (see Figure 4.4 and 4.5 for $k\Delta x = \pi/2$). Each experiment is run for 150 cycles with numerical wave gauges located at the nodes and anti-nodes. Figure 5.12b shows a time series snippet of the free surface elevation at the first anti-node, in which both dissipation and phase errors are clearly shown.

To measure the phase and dissipation errors in the numerical experiment, a Hilbert transform, H_t, analysis is performed over a subset of the time series to give the instantaneous phase and amplitude

$$\phi = tan^{-1}\left(\frac{H_t(\eta)}{\eta}\right) \tag{5.67}$$

$$a = \ln(\sqrt{\eta^2 + H_t(\eta)^2}) \tag{5.68}$$

Figure 5.13 displays the resulting analysis, each with a linear fit whose slope is related to the phase and decay respectively. For verification of the analysis, Figure 5.12b is investigated at $t \approx 2700s$, where the difference and continuum solutions instantaneously align. In Figure 5.13a, the results are presented with respect to wave cycles, which is the elapsed time divided by the wave period. The slope defines the correlation and is unique to the experimental test case. The N^{th} instantaneous alignment is governed by the phase difference and occurs after $N/(1 - slope)$ wave cycles. Multiplying by the period derived from Table 5.1, $\approx 18.37s$, gives the time of occurrence. Solving for N, given $t \approx 2700s$, reveals that Figure 5.12b depicts the 6^{th} occurrence when the signals instantaneously align. For the decay, divide the elapsed time, $t \approx 2700s$, by Δt to get the time index, τ, then calculate $e^{\tau \cdot slope}$ using the slope presented in Figure 5.13a to give an amplification factor of $\approx 0.887m$, which agrees with the normalized amplitude shown in the figure. Supplemental to the decay analysis, Figure 5.12c shows the exponential decay over the full time series.

The previous analysis warrants a digression. Unlike stability, accuracy constraints are application dependent, in which the dissipative and dispersive coefficients can be utilized to quantify the linear propagation characteristics over time and space. Take for example a decay factor, $e^{Im(w)t} = e^{Im(w)\tau\Delta t}$, where $Im(w)\Delta t$ is the decay coefficient. After τ time-steps, the total linear decay can be calculated. If the amount of decay falls outside a tolerance for error, defined by the practitioner, then either the Courant constraint or the spatial sampling interval needs to be reduced. In either case, the result is effectively a reduction in the temporal sampling interval, which reduces the decay and phase error. Nevertheless, these types of predictions can be carried out prior to simulation, thereby mitigating costly convergence tests. The same can be said for the dispersion properties, in which the phase lag can be predicted prior to simulation. In summary, given an application and predefined tolerance for error, the practitioner can establish an adequate sampling interval prior to

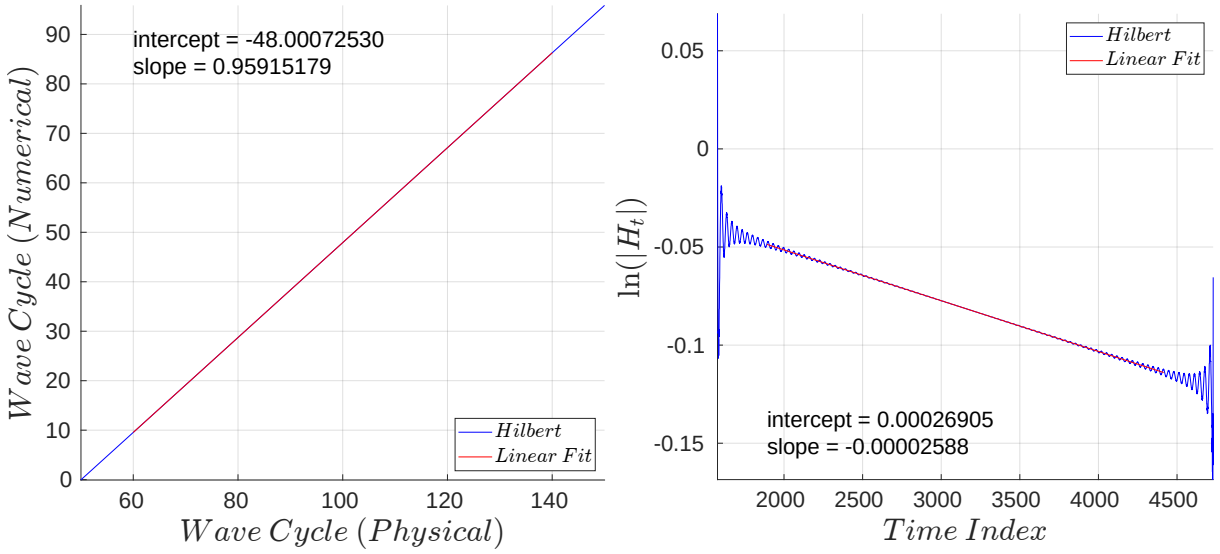

(a) (b)

Figure 5.13: Test case 4 Hilbert transform analysis results on the (left) phase and (right) amplitude calculations.

simulation which maximizes computational efficiency while meeting tolerance constraints.

The four test cases outlined in Table 5.1 serve to verify the linear analysis. Figure 5.14 shows the predicted physical root solutions with an overlay of the experimental results measured by the Hilbert analysis. In all cases, decay and phase results exhibit an absolute error less than 1e-8 between the predicted and measured values. Upon reviewing the errors in calculating the predicted root solutions, a zero error tolerance solution has been determined to be on the order of 1e-12, thus an absolute error of this order represents a perfect solution. In addition to the experimental results, construction lines show predicted solutions for changes in the respective parameter relative to the initial configuration, while keeping all other parameters the same. For example, in test case 2, only the wavelength is changed from case 1, thus kh and $k\Delta x$ take on different values. Comparing Figure 5.14a with Figure 5.14b, it is clear that the construction lines for k are the same, in which the predicted solution traverses along the k-construction line. As discussed in section 5.2, the Courant number is fixed along this construction line. Therefore, if the numerical configuration were applied to a wave spectrum, the predicted solutions for each wave number in the spectrum would follow the k-construction line, hence this line is of principle interest in the numerical modeling of Boussinesq-type waves, not the black curve derived for the continuum solution.

For the h-construction line, the discussion in section 5.2 indicates that the dimensionless wave number, $k\Delta x$, is fixed, however the C_r number and relative water depth, kh, vary. Since all other parameters are fixed along this path, including Δt and Δx, which controls the vertical translation of

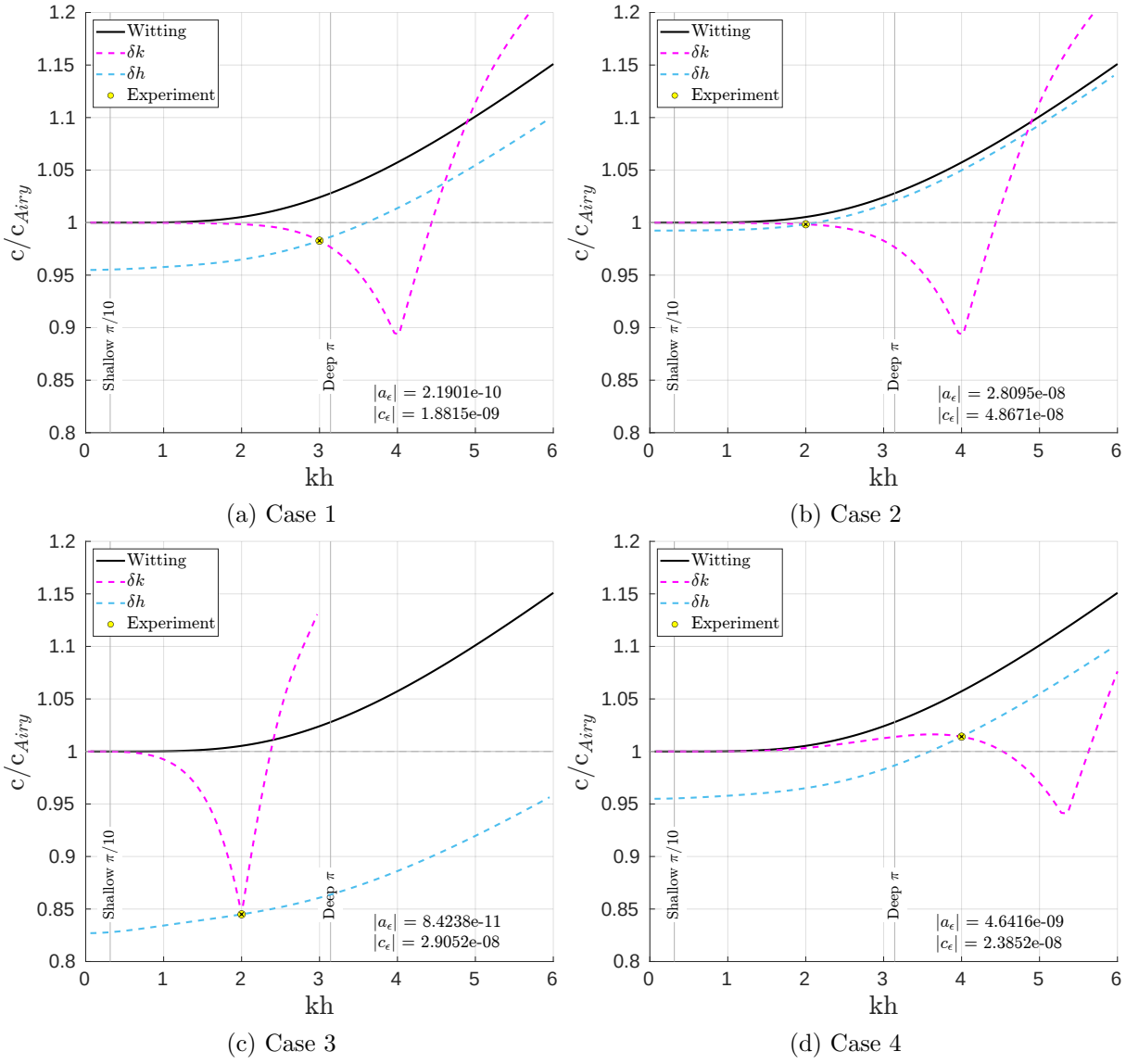

(a) Case 1 (b) Case 2

(c) Case 3 (d) Case 4

Figure 5.14: Test case predictions for the physical root solution (yellow dot) and experimental results (black x). Absolute errors of the decay, a_ϵ, and phase via the celerity, c_ϵ, are shown in text. Dotted construction lines denote how changes in respective parameter modify the predicted solution.

the predicted solution, the curve closely follows that of the PDEs with a vertical translation defined by the initial configuration. While they do appear parallel, Figure 5.6 indicates that they are not. In fact, Figure 5.6 shows that there is a region where the curvature of the difference solution is in closer proximity to the continuum solution. Comparing Figure 5.14a with Figure 5.14d, the h-construction lines are identical. In case 1, $kh = 3$, whereas in case 4, $kh = 4$, thus following the h-construction line in Figure 5.14a out to $kh = 4$, the resulting celerity can be predicted. To

go one step further, the k-construction can then be created, as shown in Figure 5.14d, to predict spectrum solutions. For this k-construction line, if a tolerance for error is $\pm 5\%$, then the resolvable bandwidth is $\approx$ 50% larger, making it a far superior choice for modeling deep water waves or broadband spectra.

Practically speaking, there is not much value in the h-construction line beyond what was just discussed. If the numerical configuration were applied to a variable water depth, then the predicted celerity for a monochromatic wave of fixed wavelength would not necessarily follow this curve. It is well known that the wavelength changes as the depth changes to preserve a constant period. Therefore, k physically cannot remain constant along this curve, despite the mathematical requirement that it does. The h-construction line simply serves as a guide when modifying the initial configuration, whereas stated prior, the k-construction is of principle interest in the numerical modeling of Boussinesq-type waves.

Construction lines for $\delta\Delta t$ and $\delta\Delta x$ are not shown to avoid misinterpretation. Nevertheless, the discussion in section 5.2 indicates that for changes in these parameters the relative depth is fixed, thus they control the vertical translation of the predicted solution. Comparing Figure 5.14b with Figure 5.14c, the predicted solution experienced a vertical translation down, away from the continuum solution. Table 5.1 shows Δx is the only input parameter that changed between these two cases and increases. This asserts consistency, where the solution approaches that of the continuum with vanishing sampling intervals. Also as Δx becomes larger, the k-construction line becomes more compact, thus the bandwidth is reduced. Specifically, the cutoff of the k-construction line is the Nyquest limit, thus for relative depths beyond the cutoff, the waves are aliased.

The inflection point in the k-construction line reflects the inflection point of the $\overline{k^1}$ approximation, where the root solutions intersect. As stated prior, no natural ordering exists for complex numbers, thus the definition of the physical root is subjective. The physical root defined herein was chosen based on that which minimizes the difference between the domain of the effective operator and the physical root solution. In Figure 5.15, the k-construction line for the parasitic root is also shown, which intersects the physical root at the inflection point. Testing which root solution manifests in simulation is difficult for this experimental setup because Δx must remain constant along the k-construction line and only a single wave is being tested. To go beyond the inflection point, two cells are needed, which represents the Nyquest limit. Nevertheless, upon testing, the solution blows up with multiple root solutions present. Tracing each of the spatial root solutions out to $kh = 6$, where the result should lie, the physical root approaches $c/c_{Airy} \approx 1.22$, whereas the parasitic root approaches $c/c_{Airy} \approx 0$, which implies no motion. Thus, the latter should effectively remain stationary, whereas the former should oscillate. With the blowup occurring so rapidly, it is difficult to tell which root is responsible. A more definitive test case, such as one that involves a wave spectrum, is needed for confirmation.

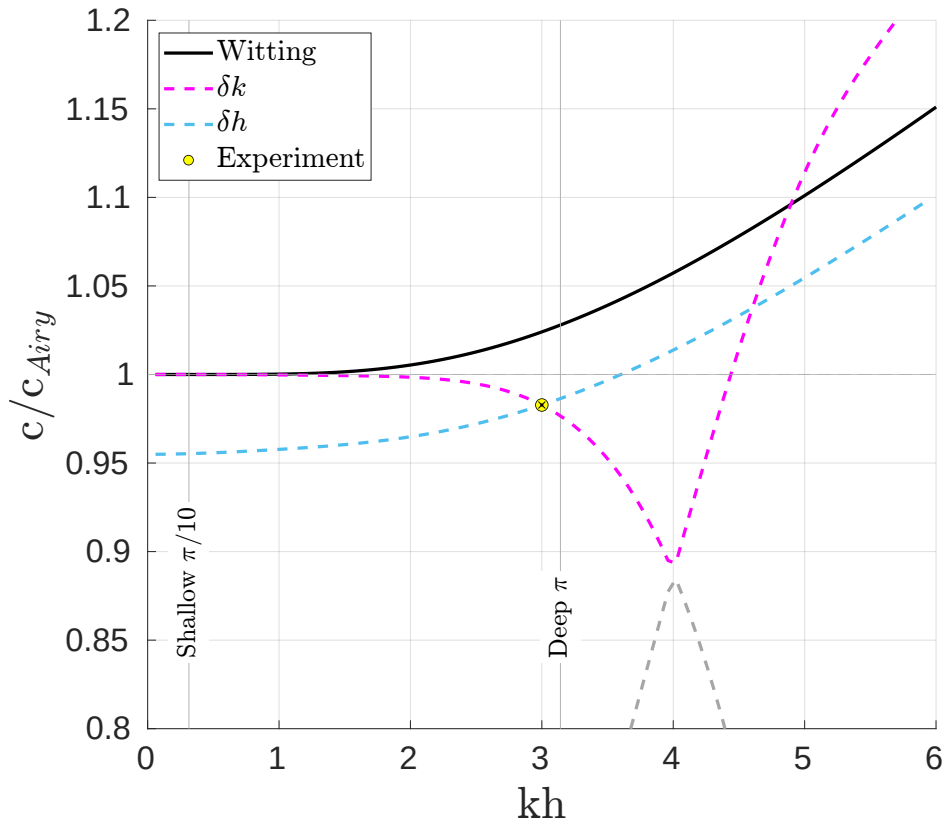

Figure 5.15: Case 1 with both wave number root solutions.

As a final remark, the discrepancy between the predicted and experimental results are addressed. As indicated in prior analysis, the decay and phase results exhibit an absolute error less than 1e-8 between the predicted and measured values for all test cases, with 1e-12 being the order of zero error tolerance. Since the physical root solution to the free surface (5.52) and velocity (5.53) are linear and the computation reflects a linear solution, the absolute error between the predicted and measured values should be on the order of a perfect solution (1e-12). To investigate this further, test case 4 was repeated holding all parameters fixed other than the water depth, which was reduced to a value ten times smaller. Since the C_r number is fixed in the computation, this results in an increase of Δt, which in accordance with Figures 4.13, greatly amplifies the errors. Figure 5.16 shows the time series plots and the error between the analytic and computation solution point by point. This error is different than that measured for the decay and phase, in that an initial amplitude or phase error will lead to an absolute systematic error over the entire time series, whereas the decay and phase are measured relative to the initial conditions. In other words, the decay and phase are properties associated with the propagation. The difference between the predicted and measured values for the decay and phase are actually less than 1e-9 in this test case, but again, that is relative to the initial conditions. Linear multistep schemes rely on previous information to march

the solution forward in time, which poses an issue with the initialization. This is a well known drawback of mutistep schemes, in which either a series of single steps or lower order multisteps are needed to initialize the scheme. Herein, an extrapolation backward in time of the analytic physical root solution was utilized to initialize the scheme. In Figure 5.16b, there is clearly an absolute error on the order of 1e-2 in the initial conditions. This error appears to be a superposition of two waves, one at a frequency associated with the physical root and the other with a parasitic root. Although the error of the latter rapidly decays within a few wave periods, the former persists throughout the computation. The order of error downstream appears to largely make up the 1e-3 discrepancy in both the decay and phase error associated with the propagation. With only the physical root being utilized to initialize the scheme, it appears this could be the source of error. The thought was that by initializing the scheme with the physical root only, the parasitic roots would not be triggered. That being said, the analytic solution is a superposition of all roots, thus it appears that the initial conditions need to take this into consideration. This will be considered in the future to further validate the theory.

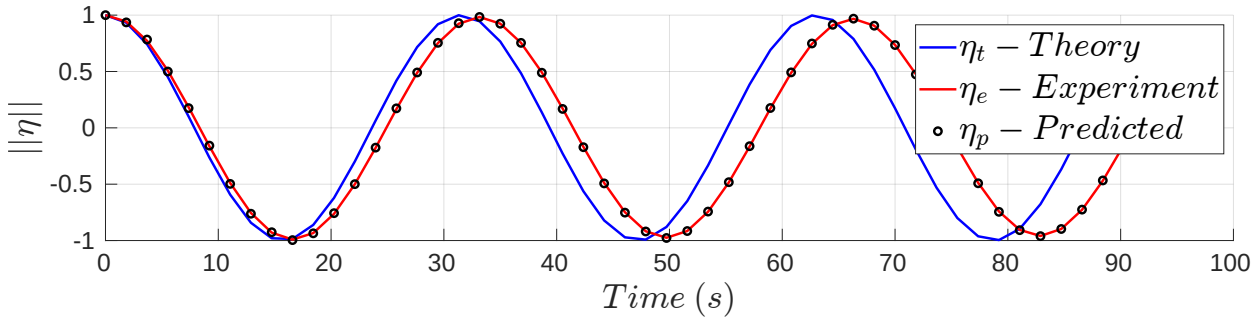

(a) Normalized free surface time series.

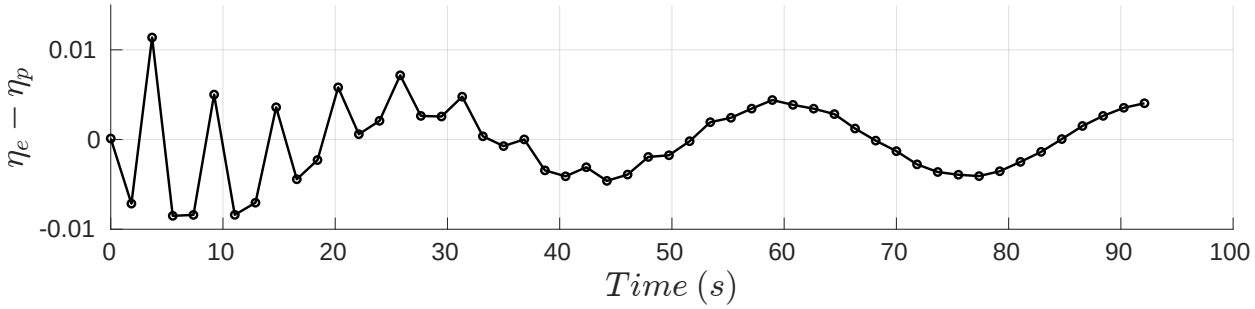

(b) Residual at start of simulation.

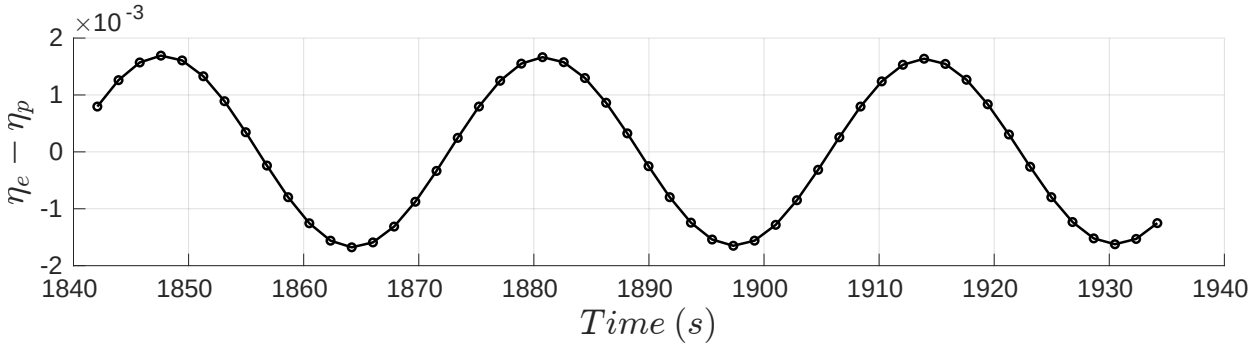

(c) Residual after many wave cycles.

Figure 5.16: Experimental errors for test case 4 at 10x smaller depth.

CHAPTER 6
CONCLUSIONS AND FURTHER STUDIES

This study has synthesized decades of progress made on Boussinesq-type equations, culminating in fundamental insights on mathematical structures that underpin the advancement of both their theoretical and numerical aspects, as well as their applications. The knowledge acquired through an iterative pursuit of abstraction made it easier to recognize and acknowledge the paths being forged by others. An extensive literature review proved essential, where along the way specific research questions were posed to guide advancement in the field of study.

Initial questions focused on the formal equivalence between seemingly distinct equations derived from either a scalar potential or vector velocity approach. An independent derivation of fully nonlinear, weakly dispersive Boussinesq-type equations was carried out by depth integrating the continuity and Euler equations to arrive at a new set of PDEs expressed in conserved variable form. In their final form, the resulting PDEs herein are quite different from the conserved variable form of the state-of-the-art PDEs governing "FUNWAVE-TVD" (Shi et al. 2012). Nevertheless, a proof of formal equivalence demonstrates theoretical consistency. The most striking observation is that the PDEs derived herein mirror those representing the conservation of mass and momentum presented in modulation theory. In this analogy, an expression for the intrinsic radiation stress, which is often imperceptible in other Boussinesq-type formulations, becomes apparent. This feature holds great appeal in practical applications concerning the study of coastal processes, such as wave setup and surf beat. Rather than being constrained to post-processing the effects of radiation stress, the radiation stress itself could be directly queried as a model output. Future studies to explore the connection between the PDEs presented herein and those introduced in modulation theory are needed. Leveraging the well-established nature of the latter, it becomes possible to project clarity onto terms that arise from the asymptotic expansion. Of immediate interest would be the emergence of a wave action equation, which is well known to be more fundamental than an energy equation in modulation theory.

The remaining theoretical question posed addresses the nonlinear enhancement of fully nonlinear, weakly dispersive Boussinesq-type equations. Introducing a new second point of expansion at the free surface and weighting the series expansions at both material surfaces result in an additional nonlinear dispersion term which captures the effects of the free surface curvature. The resulting weight function is independent of that introduced by Kennedy et al. (2001), but found to mirror its nonlinear mathematical structure. Setting the degrees of freedom in each of the weight functions equal results in a single model velocity equation defined at a datum invariant reference with one degree of freedom. Thus, the new equations recover those of Kennedy et al. (2001) upon removal

of the new nonlinear dispersion term. When the PDEs are formulated to include the effects of creeping seabed deformations, the new nonlinear dispersion term at the free surface is balanced by a nonlinear term at the seabed having the same mathematical structure. In the absence of the new nonlinear enhancement and datum invariant reference, the PDEs including creeping seabed deformations appear to recover those of P. Lynett and P. L.-F. Liu (2002). It is hypothesized by deduction that the new nonlinear enhancement will lead to further improvements in the range of kh for nonlinear application. Future studies will include a second order Stokes analysis to verify the hypothesis and quantify the range of kh for nonlinear application due to the new method of nonlinear enhancement presented herein. If the resultant range of kh for nonlinear application shows improvement, then the new methodology will have broad impacts on the community, showing that additional opportunities for nonlinear enhancement do in fact exist following the conventional asymptotic approach.

Switching to numerical facets of this study, the first question addresses a gap in the literature on the implementation of compact finite difference schemes for practical application of Boussinesq-type equations in coastal engineering studies. Following interdisciplinary research in numerical analysis, computational fluid dynamics, and aeroacoustics, an abstraction of the compact methodology is formulated and the implementation is verified by comparing predictions from analytic solutions to the difference equation with results obtained from numerical experiments. The method of undetermined coefficients is universally applicable in the construction of both temporal and spatial schemes employed in practical application. Furthermore, the method of undetermined coefficients can be framed as an optimization problem, in which the order of the local truncation error can be compromised to accommodate additional objective functions. In this context, classic finite difference schemes serve as explicit local approximations of optimal order, which are encompassed within the broader implicit compact framework presented herein. For Boussinesq-type models which require the inversion of evolution variables, the incurred cost of newly implemented compact schemes is partially offset due to the fact that a banded system of equations needs to be solved regardless if the scheme is explicit or implicit. The additional bands introduced in the compact implicit approach result in an additional computational cost that is incidental. Future studies to advance the new implementation of compact finite difference schemes are necessary. Given the implicit nature of the schemes, special attention should be given to the treatment of boundary conditions. To garner broader acceptance within the community, it is imperative to thoroughly address and properly handle the diversity of boundary conditions found in practical application.

The final scientific question emphasizes the necessity of enhancing communication between model developers and stakeholders to effectively convey the implications of numerical discretization on the governing PDEs. Invoking first principles, the linearized three-parameter family of Boussinesq-type equations is discretized in the compact framework and mapped into spectral space using

Fourier-Laplace transforms to evaluate linear dissipation and dispersion properties of both individual operators and the full system of equations. With regard to individual operators, compact schemes exhibit an increase in resolvable bandwidth, which caters to 1) an increase in the sampling interval Δt, or Δx, given ω, or k, and 2) an increase in spectral bandwidth for a given sampling interval. Adhering to lessons learned in the interdisciplinary research, the methodology retains a high level of abstraction by defining dimensionless effective operators $\overline{\omega^n}\Delta t^n$, or $\overline{k^n}\Delta x^n$, which encapsulate the difference approximations in their entirety. The newly derived effective numerical dispersion relation mirrors the intrinsic dispersion relation of the PDEs and serves an equivalent purpose by establishing a connection between the dimensionless wavenumber space and the dimensionless angular frequency space. Furthermore, the linear analytic solution to the MPDEs mirrors that of the PDEs, with the principle difference being that the MPDEs comprise a superposition of multiple root solutions that satisfy the difference approximation. Numerical dissipation and dispersion errors are quantified by comparing the unique root solutions to those of the PDEs over the complex spectral plane. The intrinsic dispersion relation of Boussinesq-type equations is an approximation to that of the fully dispersive Airy wave theory. When the intrinsic celerity is either overestimated or underestimated relative to Airy wave theory, a corresponding underestimation or overestimation of the celerity resulting from the root solutions can lead to improved agreement with Airy wave theory. The key insight lies in the ability to ascertain the linear numerical errors within the compact framework prior to initiating a simulation, representing a crucial takeaway. Given that the errors are dependent on the chosen sampling intervals, which are defined by practitioners themselves, it becomes feasible to circumvent the leading order errors and minimize the need for expensive convergence tests. Focused only on numerical frequency dispersion, this study demonstrates a foundational approach to build upon in future studies on numerical shoaling and nonlinear interactions. These predictive tools are crucial in achieving the overarching goal of improving practitioner awareness.

APPENDIX A
GENERALIZED KINEMATIC BOUNDARY CONDITIONS

Material surface boundaries are defined by the following dimensional kinematic condition

$$\frac{Df'}{Dt'} = \frac{\partial f'}{\partial t'} + (\mathbf{u}' \cdot \nabla) f' = 0 \tag{A.1}$$

where $\mathbf{u}'$ is the vector velocity function, $f'(t', x', y', z')$ is a scalar surface function, and ∇ is the vector calculus gradient operator. Equation (A.1) states that the surface remains a material surface for all time.

Focusing on wave propagation, a vertical boundary surface is defined by the scalar function $f'(t', x', y', z') = s'(t', x', y') - z'$, in which $s'(t', x', y')$ is an arbitrary scalar function measuring vertical displacement relative to the still water level. Substitution into (A.1) and solving for the vertical velocity component gives the general kinematic boundary condition

$$w'|_{s'} = \frac{\partial s'}{\partial t'} + u'|_{s'} \frac{\partial s'}{\partial x'} + v'|_{s'} \frac{\partial s'}{\partial y'} \tag{A.2}$$

where the notation $|_{s'}$ indicates the vertical point of evaluation (e.g., $w'|_{s'} \equiv w'(t', x', y', z' = s'(t', x', y'))$). It is important to note that the function dependency on z' is removed upon evaluation.

The arbitrary scalar displacement function, $s'(t', x', y')$, is scaled vertically by the characteristic water depth, h_c, for consistency. Applying the coordinate (2.6) and vector velocity (2.9) scale arguments, the kinematic condition for the dimensionless vertical boundary surface scalar function, $f(t, x, y, z) = s(t, x, y) - z$, is given by

$$w|_s = \frac{1}{\epsilon} \frac{\partial s}{\partial t} + u|_s \frac{\partial s}{\partial x} + v|_s \frac{\partial s}{\partial y} \tag{A.3}$$

The general scaled kinematic boundary condition can be applied to any material boundary.

APPENDIX B

THE LEIBNIZ INTEGRAL RULE

Depth integrating (i.e. along the z-coordinate) the governing equations of motion (2.10-2.13) results in differentiation under an integral. When applied over the flow depth, boundary dependencies must be considered. For example, integrating the spatial derivative of an arbitrary scalar function, $f(t, x, y, z)$, over the flow depth results in

$$\int_{-h}^{\epsilon\eta} \frac{\partial f}{\partial x} dz = \frac{\partial}{\partial x} \int_{-h}^{\epsilon\eta} f(t, x, y, z) dz - \frac{\partial h}{\partial x} f|_{-h} - \epsilon \frac{\partial \eta}{\partial x} f|_{\epsilon\eta} \tag{B.1}$$

where the notation, $f|_{\epsilon\eta} \equiv f(t, x, y, z = \epsilon\eta(t, x, y))$, indicates function evaluation at the free surface elevation. This theorem is applied extensively throughout the derivation, in which boundary conditions further simplify the expressions.

APPENDIX C
HORIZONTAL SERIES EXPANSION

A local Taylor series expansion of the horizontal velocity function is performed, which follows the same procedure outlined for the vertical velocity in the text. An expansion about an arbitrary point, $z = z_0$, in the water column is given by

$$u(t,x,z) = u|_{z_0} + \frac{\Delta z_0}{1!}\frac{\partial u}{\partial z}|_{z_0} + \frac{(\Delta z_0)^2}{2!}\frac{\partial^2 u}{\partial z^2}|_{z_0} + \frac{(\Delta z_0)^3}{3!}\frac{\partial^3 u}{\partial z^3}|_{z_0} + \dots \tag{C.1}$$

where $\Delta z_0 = z - z_0$ is the vertical displacement between z, the point of evaluation, and z_0, the point of expansion. Applying the continuity equation (2.10) and irrotational condition (2.14) transforms the series (C.1) into an $O(\mu^{2n})$ expansion, in which the even (left) and odd (right) derivatives within the series are tabulated below as

$$\begin{array}{l|l}
\frac{\partial^0 u}{\partial z^0}|_{z_0} = \mu^0 \frac{\partial^0 u}{\partial x^0}|_{z_0} & \frac{\partial u}{\partial z}|_{z_0} = \mu\mu \frac{\partial w}{\partial x}|_{z_0} \\
\frac{\partial^2 u}{\partial z^2}|_{z_0} = -\mu^2 \frac{\partial^2 u}{\partial x^2}|_{z_0} & \frac{\partial^3 u}{\partial z^3}|_{z_0} = -\mu\mu^3 \frac{\partial^3 w}{\partial x^3}|_{z_0} \\
\frac{\partial^4 u}{\partial z^4}|_{z_0} = \mu^4 \frac{\partial^4 u}{\partial x^4}|_{z_0} & \frac{\partial^5 u}{\partial z^5}|_{z_0} = \mu\mu^5 \frac{\partial^5 w}{\partial x^5}|_{z_0} \\
\frac{\partial^6 u}{\partial z^6}|_{z_0} = -\mu^6 \frac{\partial^6 u}{\partial x^6}|_{z_0} & \frac{\partial^7 u}{\partial z^7}|_{z_0} = -\mu\mu^7 \frac{\partial^7 w}{\partial x^7}|_{z_0} \\
\vdots & \vdots \\
\frac{\partial^{2n} u}{\partial z^{2n}}|_{z_0} = (-1)^n \mu^{2n} \frac{\partial^{2n} u}{\partial x^{2n}}|_{z_0} & \frac{\partial^{2n+1} u}{\partial z^{2n+1}}|_{z_0} = (-1)^n \mu\mu^{2n+1} \frac{\partial^{2n+1} w}{\partial x^{2n+1}}|_{z_0}
\end{array} \tag{C.2}$$

in which $n \in \mathbb{N}$, zero inclusive. A general form of the Taylor series expansion is given by

$$u(t,x,z) = \sum_{n=0}^{\infty} (-1)^n \mu^{2n} \frac{\Delta z_0^{2n}}{(2n)!}\frac{\partial^{2n} u}{\partial x^{2n}}|_{z_0} + (-1)^n \mu^{2n+1} \frac{\Delta z_0^{2n+1}}{(2n+1)!}\frac{\partial^{2n+1} \mu w}{\partial x^{2n+1}}|_{z_0} \tag{C.3}$$

If we define the operator $Q^m = \mu^m \Delta z_0^m \frac{\partial^m}{\partial x^m}$, where m is a dummy variable, then the series is given by

$$u(t,x,z) = \sum_{n=0}^{\infty} \left(\frac{(-1)^n}{(2n)!} Q^{2n} u + \frac{(-1)^n}{(2n+1)!} Q^{2n+1} \mu w \right) |_{z_0} \tag{C.4}$$

APPENDIX D
FOURIER-LAPLACE TRANSFORMS

In the sections that follow, f and f_o represent an arbitrary function and its initial conditions respectively. Function transforms are denoted by a tilde, $\widetilde{f}$, or in the event of long expressions, $\mathcal{F}[f]$ for Fourier and $\mathcal{L}[f]$ for Laplace transforms.

D.1 Fourier Transform

The transform and inverse transform pair is

$$\widetilde{f}(k) = \frac{1}{2\pi}\int_{-\infty}^{\infty} f(x)e^{-ikx}dx \tag{D.1}$$

$$f(x) = \int_{-\infty}^{\infty} \widetilde{f}(k)e^{ikx}dk \tag{D.2}$$

The scale factor, $(2\pi)^{-1}$, of the Fourier transform can we weighted between the transform and inverse transform pair. Thus the convention chosen here is only one such option.

Derivative Theorem

The transform of the nth-derivative of f with respect to x is

$$\widetilde{\frac{\partial^n f}{\partial x^n}} = (ik)^n \widetilde{f} \tag{D.3}$$

Shift Theorem

The transform of f evaluated at a shifted location is

$$\mathcal{F}[f(x \pm \Delta x)] = \widetilde{f}e^{\pm ik\Delta x} \tag{D.4}$$

D.2 Laplace Transform

The transform and inverse transform pair is

$$\widetilde{f}(\omega) = \frac{1}{2\pi}\int_0^\infty f(t)e^{i\omega t}dt \tag{D.5}$$

$$f(t) = \int_\Gamma \widetilde{f}(\omega)e^{-i\omega t}d\omega \tag{D.6}$$

Derivative Theorem

The transform of the derivative of f with respect to t is

$$\widetilde{\frac{\partial f}{\partial t}} = -i\omega\widetilde{f} - \frac{f_o}{2\pi} \tag{D.7}$$

Shift Theorem

The transform of f evaluated at a shifted location is

$$\mathcal{L}[f(t \pm \Delta t)] = e^{\mp i\omega\Delta t}\left(\widetilde{f} + \frac{f_o}{2\pi i\omega}\left(1 - e^{\pm i\omega\Delta t}\right)\right) \tag{D.8}$$

APPENDIX E
FOURIER INTEGRAL SOLUTIONS

Dependent variables within the linear system of PDEs take on elementary wave-like solutions of the form

$$\phi(t,x) = Ae^{i(kx-\omega t)} \tag{E.1}$$

in which ϕ represents a dependent variable. The amplitude, A, angular frequency, ω, and wave number, k, are all assumed to be constants. Being linear, the only thing that is needed is a relation between ω and k, which is known as the dispersion relation. In the context of this study, the dispersion relation is presented as a quadratic function governed by two modes, $\omega_1(k)$ and $\omega_2(k)$, over the ω-plane. The odd parity of the relation gives, $\omega_2(k) = \omega_1(-k) = -\omega_1(k)$, where the subscript is dropped to simplify notation. Following Whitham (1974), a formal approach to solving the problem employs Fourier Integrals. In general, a linear dispersion relation containing n modes can be expressed as a superposition of n linear wave-like solutions (E.1), which require n conditions to determine the solution. For the linear system of PDEs herein, the superposition of two wave-like solutions is expressed in terms of Fourier Integrals as

$$\phi(t,x) = \int_{-\infty}^{\infty} \widetilde{f}_1(k) e^{i(kx-\omega(k)t)} dk + \int_{-\infty}^{\infty} \widetilde{f}_2(k) e^{i(kx+\omega(k)t)} dk \tag{E.2}$$

where $\widetilde{f}(k)$ is the transform of an arbitrary function chosen to fit initial or boundary conditions. Two initial conditions, $\phi_1(x) = \phi(0,x)$ and $\phi_2(x) = \phi_t(0,x)$, are prescribed to generate two equations

$$\phi_1(x) = \int_{-\infty}^{\infty} \left(\widetilde{f}_1(k) + \widetilde{f}_2(k) \right) e^{ikx} dk \tag{E.3}$$

$$\phi_2(x) = \int_{-\infty}^{\infty} -i\omega(k) \left(\widetilde{f}_1(k) - \widetilde{f}_2(k) \right) e^{ikx} dk \tag{E.4}$$

By definition of the inverse transform (D.2), it is clear that

$$\widetilde{\phi}_1(k) = \widetilde{f}_1(k) + \widetilde{f}_2(k) \tag{E.5}$$

$$\widetilde{\phi}_2(k) = -i\omega(k) \left(\widetilde{f}_1(k) - \widetilde{f}_2(k) \right) \tag{E.6}$$

in which the two unknown functions can be expresses as

$$\widetilde{f}_1(k) = \widetilde{\phi}_1(k) - \widetilde{f}_2(k)$$
$$\widetilde{f}_2(k) = \widetilde{f}_1(k) + \frac{\widetilde{\phi}_2(k)}{i\omega(k)}$$

Solving the linear system of two equations, the two arbitrary functions have been determined

$$\widetilde{f}_1(k) = \frac{1}{2}\left(\widetilde{\phi}_1(k) + \frac{i\widetilde{\phi}_2(k)}{\omega(k)}\right) \tag{E.7}$$
$$\widetilde{f}_2(k) = \frac{1}{2}\left(\widetilde{\phi}_1(k) - \frac{i\widetilde{\phi}_2(k)}{\omega(k)}\right) \tag{E.8}$$

For negative values of k, the functions make use of the relations for prescribed real initial conditions, $\widetilde{\phi}_1(-k) = \widetilde{\phi}_1^{\,*}(k)$ and $\widetilde{\phi}_2(-k) = \widetilde{\phi}_2^{\,*}(k)$, where the superscript denotes the complex conjugate. Substitution into (E.7) and (E.8) above gives

$$\widetilde{f}_1(-k) = \frac{1}{2}\left(\widetilde{\phi}_1^{\,*}(k) + \frac{\widetilde{\phi}_2^{\,*}(k)}{\omega(-k)}\right) = \frac{1}{2}\left(\widetilde{\phi}_1^{\,*}(k) - \frac{\widetilde{\phi}_2^{\,*}(k)}{\omega(k)}\right) \tag{E.9}$$
$$\widetilde{f}_2(-k) = \frac{1}{2}\left(\widetilde{\phi}_1^{\,*}(k) - \frac{\widetilde{\phi}_2^{\,*}(k)}{\omega(-k)}\right) = \frac{1}{2}\left(\widetilde{\phi}_1^{\,*}(k) + \frac{\widetilde{\phi}_2^{\,*}(k)}{\omega(k)}\right) \tag{E.10}$$

in which the odd parity of the dispersion relation, $\omega(-k) = -\omega(k)$, shows that $\widetilde{f}_1(-k) = \widetilde{f}_1^{*}(k)$ and $\widetilde{f}_2(-k) = \widetilde{f}_2^{*}(k)$. Therefore, real initial conditions must lead to real solutions for real equations.

A formal integral solution can be derived by prescribing a delta function as the initial condition, $\phi_1(x) = \delta(0, x)$, whose time derivative is zero (i.e $\phi_2(x) = 0$). Substituting the initial conditions into equations (E.5) and (E.6) and substituting the Fourier transform of the delta function (G.33) gives the two equations

$$\frac{1}{2\pi} = \widetilde{f}_1(k) + \widetilde{f}_2(k) \tag{E.11}$$
$$0 = -i\omega(k)\left(\widetilde{f}_1(k) - \widetilde{f}_2(k)\right) \tag{E.12}$$

The dispersion relation in (E.12) can not be equal to zero, therefore $\widetilde{f}_1(k) = \widetilde{f}_2(k)$ and the solution to the system of equations is $\widetilde{f}_{1,2}(k) = (4\pi)^{-1}$. Substituting the function solutions into (E.2)

gives

$$\phi(t,x) = \frac{1}{4\pi}\int_{-\infty}^{\infty}\left(e^{-i\omega(k)t} + e^{i\omega(k)t}\right)e^{ikx}dk \tag{E.13}$$

Applying the trigonometric identity (G.1), expanding out the complex exponential, and converting the integral of sums into a sum of integrals gives

$$\phi(t,x) = \frac{1}{2\pi}\left(\int_{-\infty}^{\infty}\cos(kx)\cos(\omega t)dk + i\int_{-\infty}^{\infty}\sin(kx)\cos(\omega t)dk\right) \tag{E.14}$$

in which the Cauchy principle value of the second integral is zero, due to the odd sine function, reducing the solution to

$$\phi(t,x) = \frac{1}{\pi}\int_{0}^{\infty}\cos(kx)\cos(\omega t)dk \tag{E.15}$$

which is a formal integral on which all other solutions are built, given different initial conditions.

APPENDIX F
INITIAL CONDITIONS

Trigonometric initial conditions are of interest in the current study. Their transform and transform integrals are analyzed here for completeness.

Fourier Transform

The Fourier transform an initial condition of the form $\phi_o(0,x) = A\cos(k_o x)$ is obtained by applying (D.1) to give

$$\tilde{\phi}_o(k) = \frac{1}{2\pi}\int_{-\infty}^{\infty} A\cos(k_o x)e^{-ikx}dx$$

The cosine term is expanded using the trigonometric identity (G.1) to give

$$\tilde{\phi}_o(k) = \frac{A}{4\pi}\int_{-\infty}^{\infty}\left(e^{ik_o x} + e^{-ik_o x}\right)e^{-ikx}dx$$

Splitting the integral of a sum into a sum of integrals and combining the exponential expressions gives

$$\tilde{\phi}_o(k) = \frac{A}{4\pi}\left(\int_{-\infty}^{\infty} e^{-i(k-k_o)x}dx + \int_{-\infty}^{\infty} e^{-i(k+k_o)x}dx\right)$$

Using the definition of the δ-function (G.36) to evaluate the integral expression, the transform of the initial condition is

$$\tilde{\phi}_o(k) = \frac{A}{2}\left(\delta(k-k_o) + \delta(k+k_o)\right) \tag{F.1}$$

For an initial condition of the form $\phi_o(x) = A\sin(k_o x)$, the same solution procedure applies to give

$$\tilde{\phi}_o(k) = \frac{A}{2i}\left(\delta(k-k_o) - \delta(k+k_o)\right) \tag{F.2}$$

Transform Integrals

It is also of interest to integrate the transform of the initial conditions while solving for analytic solutions. Specific to (F.1) the constant coefficient, $A/2$, is absorbed into an arbitrary function, $f(k)$, in which equation (G.31) is applied to give

$$\int_{-\infty}^{\infty} f(k)\delta(k-k_o) + f(k)\delta(k+k_o)dk = f(k_o) + f(-k_o) \tag{F.3}$$

It is important to highlight that $f(-k_o) = f^*(k_o)$ for real initial conditions. Substitution of $f(k_o) = A/2$ into the integral solution results in A, which is expected given the even parity of the cosine function in the initial condition. The same analysis applies to (F.2), only in this case $f(k) = -iA/2$ is imaginary. Therefore $f^*(k_o) = iA/2$ and the integral solution is zero, which is expected given the odd parity of the sine function in the initial conditions. While specific solutions have been highlighted, the main point is to show the introduction of the arbitrary function $f(k)$ in formulating (F.3), which is application dependent.

APPENDIX G
FORMULAS AND IDENTITIES

G.1 Euler

Let θ represent an arbitrary function.

$$\cos(\theta) = \frac{e^{i\theta} + e^{-i\theta}}{2}, \qquad \text{parity} = \text{even} \tag{G.1}$$

$$\sin(\theta) = \frac{e^{i\theta} - e^{-i\theta}}{2i}, \qquad \text{parity} = \text{odd} \tag{G.2}$$

$$\tan(\theta) = \frac{e^{i\theta} - e^{-i\theta}}{i\left(e^{i\theta} + e^{-i\theta}\right)}, \qquad \text{parity} = \text{odd} \tag{G.3}$$

Extending identities (G.1) and (G.2) to include coefficients

$$\frac{fe^{i\theta} \pm ge^{-i\theta}}{2} = \frac{f \pm g}{2}\cos(\theta) + i\frac{f \mp g}{2}\sin(\theta) \tag{G.4}$$

$$\frac{fe^{i\theta} \mp ge^{-i\theta}}{2i} = \frac{f \pm g}{2}\sin(\theta) - i\frac{f \mp g}{2}\cos(\theta) \tag{G.5}$$

G.2 Trigonometric

Let θ represent an arbitrary function.

Double-Angle identities are

$$\cos(2\theta) = 2\cos^2(\theta) - 1 \tag{G.6}$$

$$\sin(2\theta) = 2\sin(\theta)\cos(\theta) \tag{G.7}$$

$$\tan(2\theta) = \frac{2\tan(\theta)}{1 - \tan^2(\theta)} \tag{G.8}$$

Half-Angle identities are

$$\cos^2\left(\frac{\theta}{2}\right) = \frac{1+\cos(\theta)}{2} \tag{G.9}$$

$$\sin^2\left(\frac{\theta}{2}\right) = \frac{1-\cos(\theta)}{2} \tag{G.10}$$

$$\tan^2\left(\frac{\theta}{2}\right) = \frac{1-\cos(\theta)}{1+\cos(\theta)} \tag{G.11}$$

Angle sum and differences are

$$\cos(\theta_1+\theta_2) = \cos(\theta_1)\cos(\theta_2) - \sin(\theta_1)\sin(\theta_2) \tag{G.12}$$

$$\cos(\theta_1-\theta_2) = \cos(\theta_1)\cos(\theta_2) + \sin(\theta_1)\sin(\theta_2) \tag{G.13}$$

$$\sin(\theta_1+\theta_2) = \sin(\theta_1)\cos(\theta_2) + \cos(\theta_1)\sin(\theta_2) \tag{G.14}$$

$$\sin(\theta_1-\theta_2) = \sin(\theta_1)\cos(\theta_2) - \cos(\theta_1)\sin(\theta_2) \tag{G.15}$$

Series expansions

$$cos(\theta) = \sum_{n=0}^{\infty} \frac{(-1)^n}{(2n)!}\theta^{2n} = 1 - \frac{\theta^2}{2!} + \frac{\theta^4}{4!} - \frac{\theta^6}{6!} + \dots \tag{G.16}$$

$$sin(\theta) = \sum_{n=0}^{\infty} \frac{(-1)^n}{(2n+1)!}\theta^{2n+1} = \theta - \frac{\theta^3}{3!} + \frac{\theta^5}{5!} - \frac{\theta^7}{7!} + \dots \tag{G.17}$$

G.3 Hyperbolic

Let ϕ represent an arbitrary function.

$$\cos(i\phi) = \cosh(\phi), \qquad \text{parity} = \text{even} \tag{G.18}$$

$$\sin(i\phi) = i\sinh(\phi), \qquad \text{parity} = \text{odd} \tag{G.19}$$

$$\tan(i\phi) = i\tanh(\phi), \qquad \text{parity} = \text{odd} \tag{G.20}$$

To obtain the hyperbolic functions in exponential form, substitute $\theta = i\phi$ into the respective trigonometric functions in the "Euler" section above. In some text, the identities are give with real arguments, thus will not match verbatim. However, the identities above still apply, where the difference is the complex nature of the arbitrary function. Substituting $\phi = -i\gamma$, followed by some algebraic manipulations, different expressions of the identity can be realized.

G.4 Complex

Let $z = a + ib$ be a complex variable whose conjugate is $z^* = a - ib$

$$zz^* = \left|z\right|^2 \tag{G.21}$$

$$\frac{z + z^*}{2} = \mathrm{Re}(z) = a \tag{G.22}$$

$$\frac{z - z^*}{2} = i\,\mathrm{Im}(z) = ib \tag{G.23}$$

$$\frac{ze^{i\theta} + z^*e^{-i\theta}}{2} = a\cos(\theta) - b\sin(\theta) \tag{G.24}$$

$$\frac{ze^{i\theta} - z^*e^{-i\theta}}{2i} = a\sin(\theta) + b\cos(\theta) \tag{G.25}$$

$$\frac{z^*e^{i\theta} + ze^{-i\theta}}{2} = a\cos(\theta) + b\sin(\theta) \tag{G.26}$$

$$\frac{z^*e^{i\theta} - ze^{-i\theta}}{2i} = a\sin(\theta) - b\cos(\theta) \tag{G.27}$$

G.5 Delta function

Definition

The delta function, also known as an impulse function, can be derived from a normalized boxcar function, or unit square pulse, which satisfies the integral identity constraint

$$\int_{-\infty}^{\infty} \delta(x)dx = 1 \tag{G.28}$$

The normalized boxcar function is defined as

$$f_n(x) = \begin{cases} n, & \frac{-1}{2n} \leq x \leq \frac{1}{2n} \\ 0, & \text{otherwise} \end{cases} \tag{G.29}$$

in which the parity of the function is even. Taking the limit as $n \to \infty$, the delta function is defined as $f_\infty(x) = \delta(x) = \infty$ at $x = 0$, otherwise, $\delta(x) = 0$ for all $x \neq 0$. Having an infinite value, the delta function is also sometimes considered as the derivative of a unit step.

The identity integral (G.28) can also be extended to include an arbitrary function

$$\int_{-\infty}^{\infty} f(x)\delta(x)dx = f(0) \tag{G.30}$$

which is said to define the impulse strength. Extending this to the more general case gives the sifting property defined below.

Sifting Property

$$\int_{-\infty}^{\infty} f(x)\delta(x-x_o)dx = f(x_o) \tag{G.31}$$

in which $\delta(x-x_o) = 0, \forall x \neq x_o$.

Fourier Transform

Let $f(x) = \delta(x)$ in (D.1) to obtain

$$\widetilde{\delta}(k) = \frac{1}{2\pi}\int_{-\infty}^{\infty} \delta(x)e^{-ikx}dx \tag{G.32}$$

Applying (G.30) to the integral expression, where $f(x) = e^{-ikx}$, gives the integral solution $f(0) = e^0 = 1$, thus

$$\widetilde{\delta}(k) = \frac{1}{2\pi} \tag{G.33}$$

For the more general case, let $f(x) = \delta(x-x_o)$ and apply the sifting property (G.31) to give the Fourier transform of the shifted delta function

$$\widetilde{\delta}(k) = \frac{1}{2\pi}e^{-ikx_o} \tag{G.34}$$

For the inverse transform, let $\widetilde{f}(k) = \widetilde{\delta}(k)$ in (D.2), then substitute in (G.33) to obtain

$$\delta(x) = \int_{-\infty}^{\infty} \widetilde{\delta}(k)e^{ikx}dk = \frac{1}{2\pi}\int_{-\infty}^{\infty} e^{ikx}dk \tag{G.35}$$

and for the more general case

$$\delta\left(x-x_o\right) = \frac{1}{2\pi}\int_{-\infty}^{\infty} e^{ik(x-x_o)}dk \tag{G.36}$$

APPENDIX H

ADDITIONAL BIAS SCHEMES

H.1 Backward Difference

Information	$O(\Delta t)$	b^1_{-5}	b^1_{-4}	b^1_{-3}	b^1_{-2}	b^1_{-1}	b^1_0	b^1_1
□ = ● | ● | ○	2					1/2	-2	3/2
□ = ● | ● | ● | ○	3				-1/3	3/2	-3	11/6
□ = ● | ● | ● | ● | ○	4			1/4	-4/3	3	-4	$\frac{25}{12}$
□ = ● | ● | ● | ● | ● | ○	5		-1/5	5/4	-10/3	5	-5	$\frac{137}{60}$
□ = ● | ● | ● | ● | ● | ● | ○	6	1/6	-6/5	15/4	-20/3	15/2	-6	$\frac{49}{20}$

Table H.1: Stencil configuration and corresponding coefficients for select bias difference approximations to the first derivative. See Table 4.1 caption for symbolic notation. For all configurations shown, $a^1_1 = 1$.

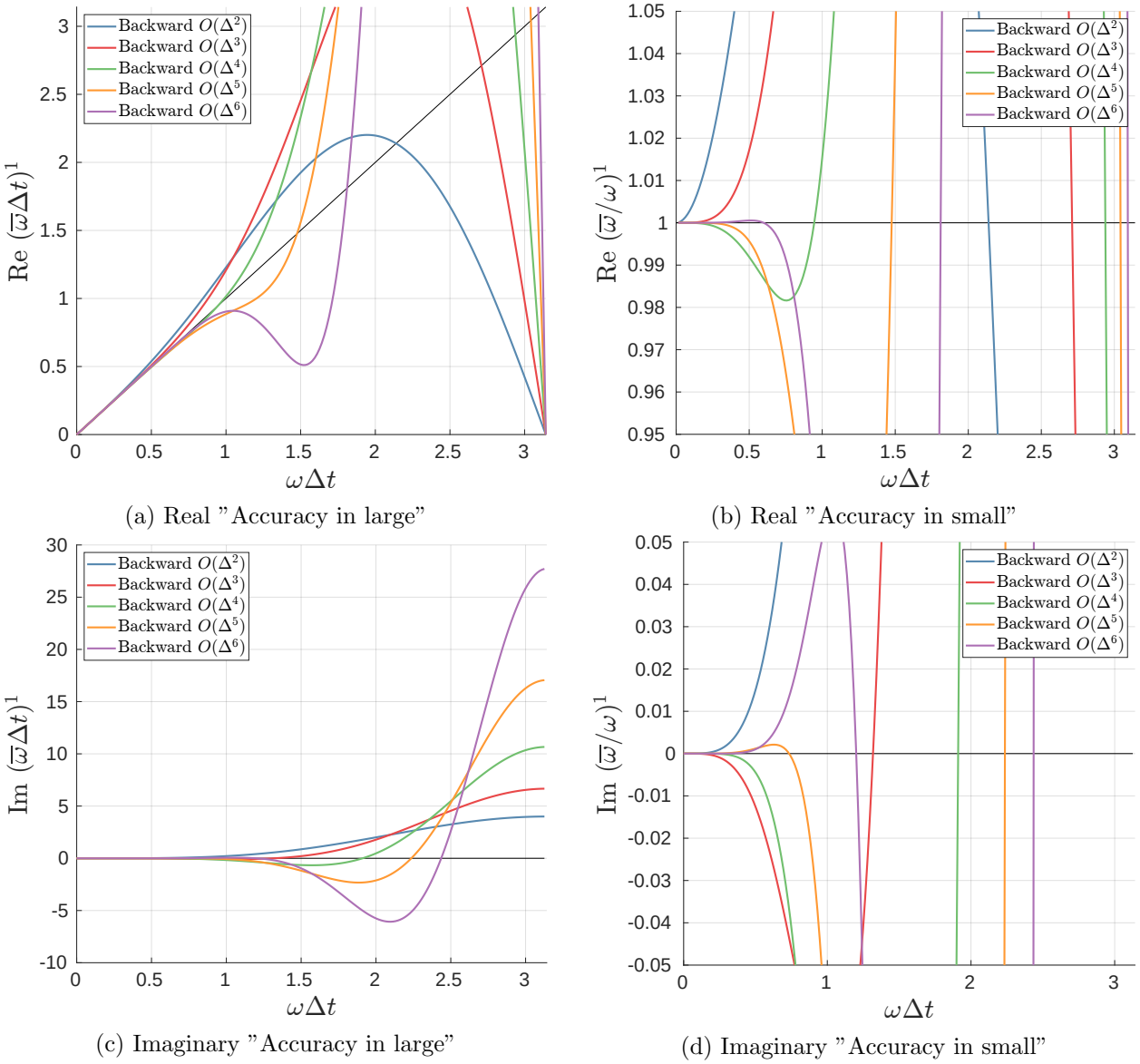

(a) Real "Accuracy in large"

(b) Real "Accuracy in small"

(c) Imaginary "Accuracy in large"

(d) Imaginary "Accuracy in small"

Figure H.1: Resolvable bandwidth of select Backward difference schemes covered in Table H.1 over (a) the full domain and (b) to within ±5% relative error. Exact solutions are denoted by the solid black line.

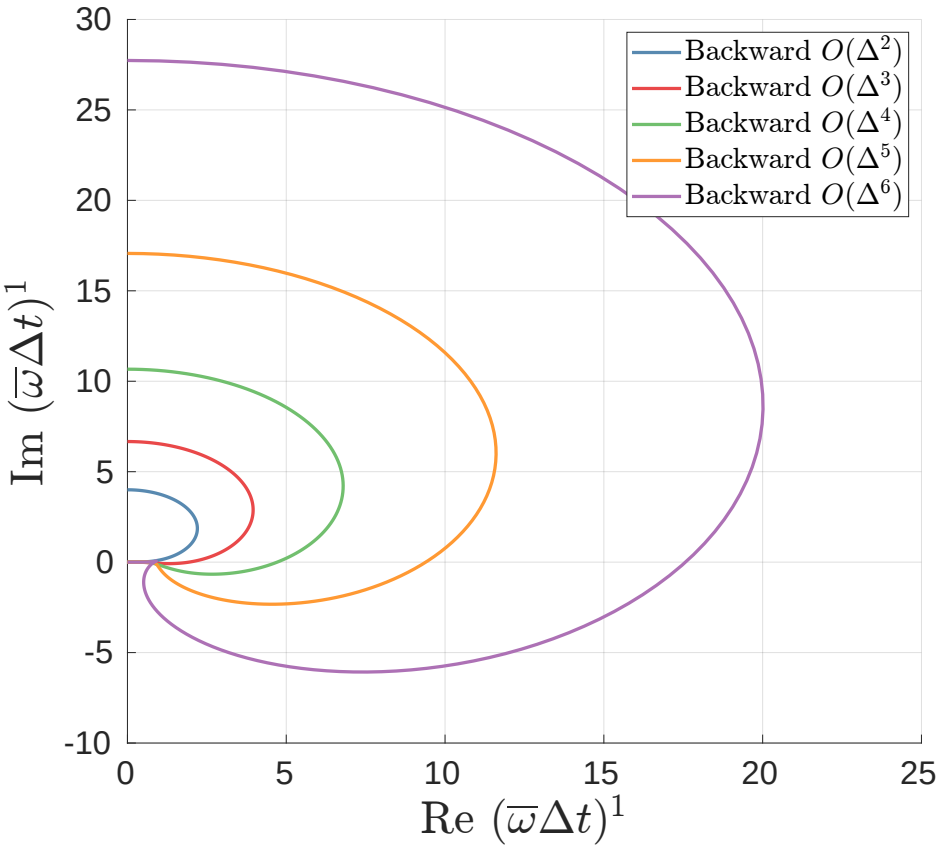

Figure H.2: Plot of $(\overline{\omega}\Delta t)^1$ as a function of $\omega\Delta t$ over the complex plane.

H.2 Nystrom and Milne-Simpson

Information	$O(\Delta t)$	a^1_{-3}	a^1_{-2}	a^1_{-1}	a^1_0	a^1_1
■ = ● | ● | ○	2				2	
■ | ■ | ■ = ● | ● | ○	3		1/3	-2/3	7/3	
□ = ● | ● | ○	1					2
■ | ■ | □ = ● | ● | ○	4			1/3	4/3	1/3
■ | ■ | ■ | ■ | □ = ● | ● | ○	5	-1/90	2/45	4/15	$\frac{62}{45}$	$\frac{29}{90}$

Table H.2: Stencil configuration and corresponding coefficients for select bias difference approximations to the first derivative. See Table 4.1 caption for symbolic notation. For all configurations shown, $b^1_{-1} = -1$, $b^1_0 = 0$, and $b^1_1 = 1$.

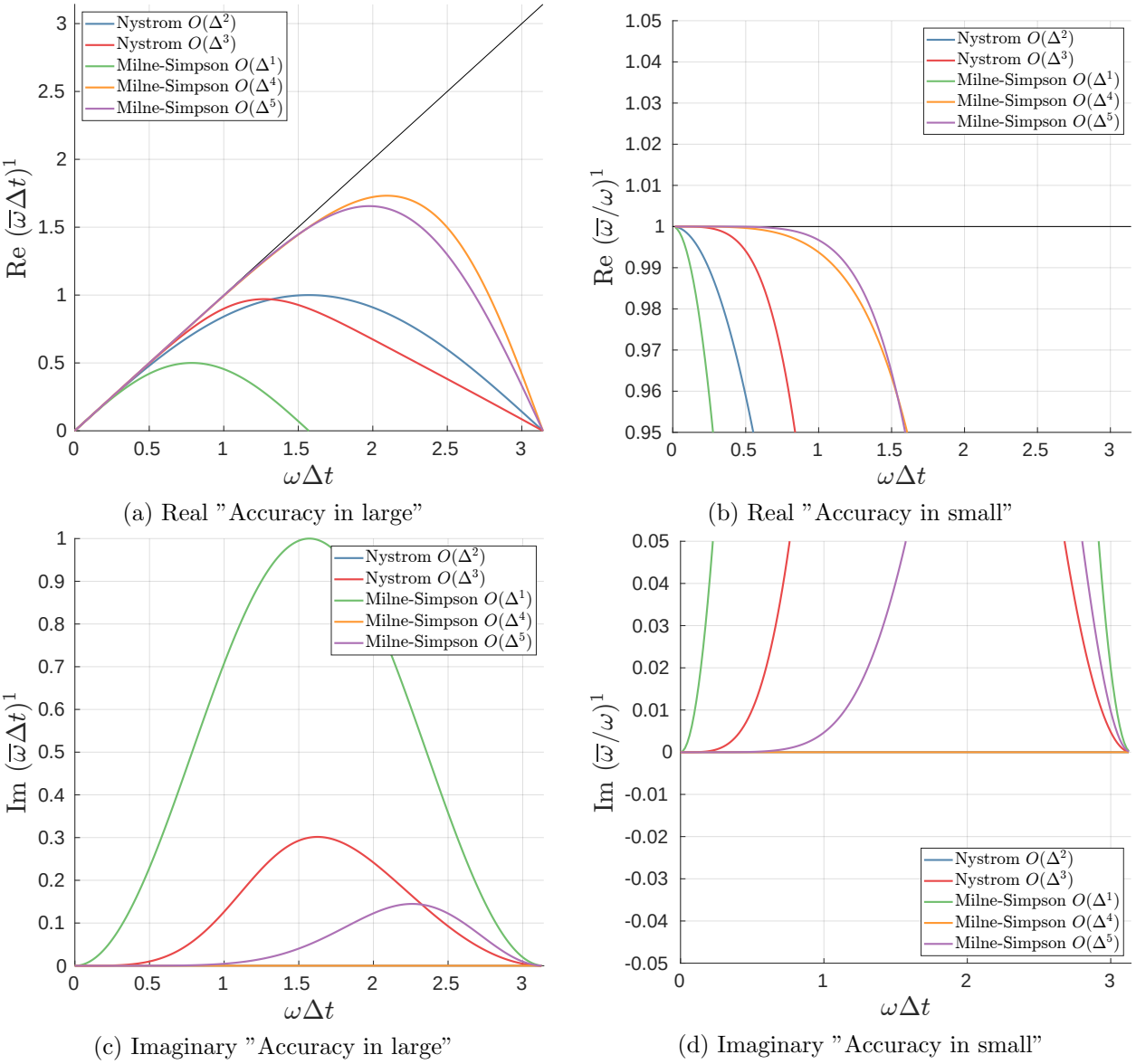

(a) Real "Accuracy in large"

(b) Real "Accuracy in small"

(c) Imaginary "Accuracy in large"

(d) Imaginary "Accuracy in small"

Figure H.3: Resolvable bandwidth of select Backward difference schemes covered in Table H.2 over (a) the full domain and (b) to within ±5% relative error. Exact solutions are denoted by the solid black line.

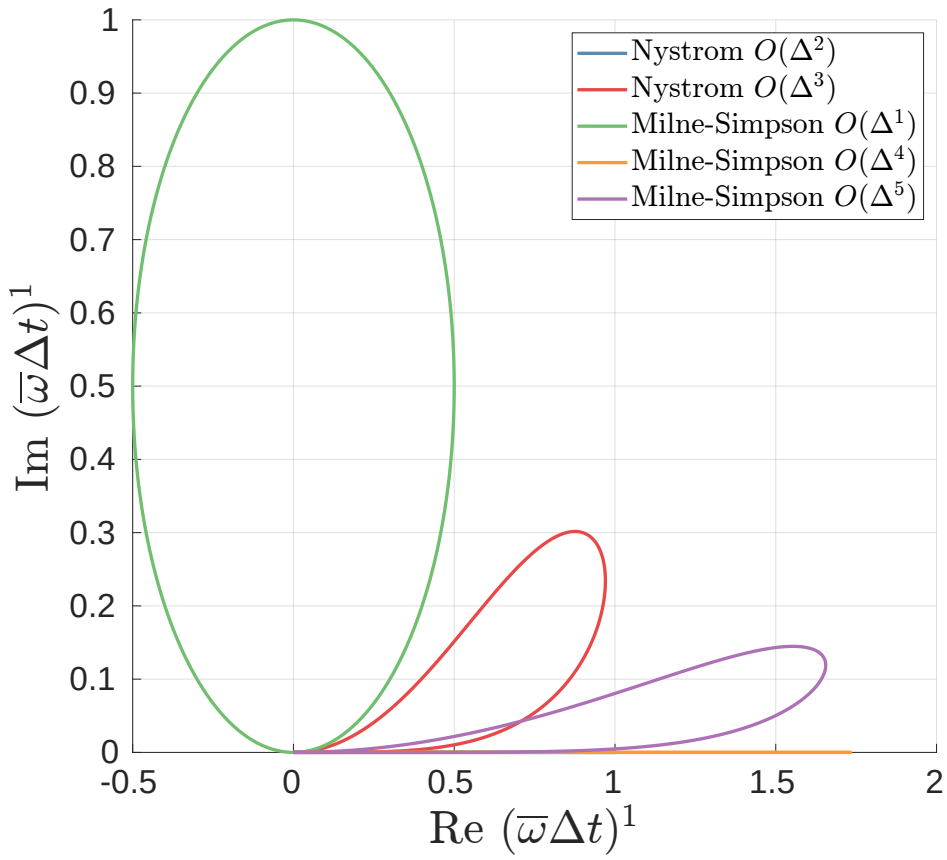

Figure H.4: Plot of $(\overline{\omega}\Delta t)^1$ as a function of $\omega\Delta t$ over the complex plane. Note that the Nystrom $O(\Delta t^2)$ curve lies on the real axis between $[0, 1]$ and is therefore covered by the $O(\Delta t^4)$ Milne-Simpson curve.

BIBLIOGRAPHY

Abbott, M. B. (1976). "Computational Hydraulics: A Short Pathology". In: *Journal of Hydraulic Research* 14.4, pp. 271–285.

Abbott, M. B., A. Damsgaard, and G. S. Rodenhuis (1973). "System 21, "Jupiter" (A Design System for Two-Dimensional Nearly Horizontal Flows)". In: *Journal of Hydraulic Research* 11.1, pp. 1–28.

Abbott, M. B. and F. Ionescu (1967). "On The Numerical Computation Of Nearly Horizontal Flows". In: *Journal of Hydraulic Research* 5.2, pp. 97–117.

Abbott, M. B., H. M. Petersen, and O. Skovgaard (1978). "On the Numerical Modelling of Short Waves in Shallow Water". In: *Journal of Hydraulic Research* 16.3, pp. 173–204.

Abbott, M. B. and G. S. Rodenhuis (1972). "A Numerical Simulation of the Undular Hydraulic Jump". In: *Journal of Hydraulic Research* 10.3, pp. 239–257.

Abbott, M.B., A. McCowan, and I.R. Warren (1981). "Numerical Modeling of Free-Surface Flows That Are Two-Dimensional in Plan". In: *Transport Models/Inland & Coastal Waters*. Elsevier, pp. 222–283.

Abbott, Michael B. (1979). *Computational Hydraulics: Elements of the Theory of Free Surface Flows*. 326 pp.

Abbott, Michael B., Andrew D. McCowan, and Ian R. Warren (1984). "Accuracy of Short-Wave Numerical Models". In: *Journal of Hydraulic Engineering* 110.10, pp. 1287–1301.

Abbott, Michael B. and Anthony W. Minns (1998). *Computational Hydraulics*. 2nd ed. Aldershot ; Brookfield, USA: Ashgate. 557 pp.

Agnon, Y., Per A. Madsen, and Hemming A. Schaffer (1999). "A New Approach to High-Order Boussinesq Models". In: *J. Fluid Mech.* 399, pp. 319–333.

Airy, G.B. (1845). *Tides and Waves: Extracted from the Encyclopaedia Metropolitana, Tom. V P241-396*. William Clowes and Sons.

Arakawa, A (1966). "Computational Design for Long-Term Numerical Integration of the Equations of Fluid Motion: Two-Dimensional Incompressible Flow. Part I". In: *J. Comput. Phys.* 1.1, pp. 119–143.

Baba, Toshitaka et al. (2017). "Accurate Numerical Simulation of the Far-Field Tsunami Caused by the 2011 Tohoku Earthquake, Including the Effects of Boussinesq Dispersion, Seawater Density Stratification, Elastic Loading, and Gravitational Potential Change". In: *Ocean Modelling* 111, pp. 46–54.

Bai, Yefei, Yoshiki Yamazaki, and Kwok Fai Cheung (2018). "Convergence of Multilayer Nonhydrostatic Models in Relation to Boussinesq-Type Equations". In: *J. Waterway, Port, Coastal, Ocean Eng.* 144.2, p. 06018001.

Beji, S and K Nadaoka (1996). "A Formal Derivation and Numerical Modelling of the Improved Boussinesq Equations for Varying Depth". In: *Ocean Engineering* 23.8, pp. 691–704.

Beji, Serdar and Kazuo Nadaoka (1998). "Authors' Reply to Discussion of Schaffer and Madsen on "A Formal Derivation and Numerical Modelling of the Improved Boussinesq Equations for Varying Depth"". In: *Ocean Eng.* 25.7, pp. 615–618.

Benjamin, T. B., J. L. Bona, and J. J. Mahony (1972). "Model Equations for Long Waves in Nonlinear Dispersive Systems". In: *Philosophical Transactions of the Royal Society A: Mathematical, Physical and Engineering Sciences* 272.1220, pp. 47–78.

Bingham, Harry B. and Yehuda Agnon (2005). "A Fourier-Boussinesq Method for Nonlinear Water Waves". In: *European Journal of Mechanics - B/Fluids* 24.2, pp. 255–274.

Bogey, Christophe and Christophe Bailly (2004). "A Family of Low Dispersive and Low Dissipative Explicit Schemes for Flow and Noise Computations". In: *Journal of Computational Physics* 194.1, pp. 194–214.

Bona, Jerry L. and Min Chen (1998). "A Boussinesq System for Two-Way Propagation of Nonlinear Dispersive Waves". In: *Physica D: Nonlinear Phenomena* 116.1-2, pp. 191–224.

Bona, Jerry L. and Ronald Smith (1976). "A Model for the Two-Way Propagation of Water Waves in a Channel". In: *Math. Proc. Camb. Philos. Soc.* 79, p. 167.

Bona, Chen, and Saut (2002). "Boussinesq Equations and Other Systems for Small-Amplitude Long Waves in Nonlinear Dispersive Media. I: Derivation and Linear Theory". In: *J. Nonlinear Sci.* 12.4, pp. 283–318.

Boussinesq, Joseph (1871). "Theorie de l'intumescence Liquide, Applelee Onde Solitaire Ou de Translation, Se Propageant Dans Un Canal Rectangulaire". In: *Comptes Rendus Acad. Sci.* 72, pp. 755–759.

— (1872). "Theorie Des Ondes et Des Remous Qui Se Propagent Le Long d'un Canal Rectangulaire Horizontal, En Communiquant Au Liquide Contenu Dans Ce Canal Des Vitesses Sensiblement Pareilles de La Surface Au Fond". In: *J. Math. Pures Appl.* 17, pp. 55–108.

Brocchini, M. (2013). "A Reasoned Overview on Boussinesq-type Models: The Interplay between Physics, Mathematics and Numerics". In: *Proceedings of the Royal Society A: Mathematical, Physical and Engineering Sciences* 469.2160, pp. 20130496–20130496.

Burwell, David, Elena Tolkova, and Arun Chawla (2007). "Diffusion and Dispersion Characterization of a Numerical Tsunami Model". In: *Ocean Modelling* 19.1-2, pp. 10–30.

Camassa, Roberto and Darryl D. Holm (1993). "An Integrable Shallow Water Equation with Peaked Solitons". In: *Phys. Rev. Lett.* 71.11, pp. 1661–1664.

Chazel, Florent, Michel Benoit, and Alexandre Ern (2011). "Validation of a Double Layer Boussinesq-type Model for Highly Nonlinear and Dispersive Waves". In: *Int. Conf. Coastal. Eng.* 1.32, p. 14.

Chazel, F. et al. (2009). "A Double-Layer Boussinesq-type Model for Highly Nonlinear and Dispersive Waves". In: *Proc. R. Soc. A* 465.2108, pp. 2319–2346.

Chen, M. (2003). "Equations for Bi-Directional Waves over an Uneven Bottom". In: *Mathematics and Computers in Simulation* 62.1-2, pp. 3–9.

Chen, Qin (2003). "Boussinesq Modeling of Longshore Currents". In: *J. Geophys. Res.* 108.C11, p. 3362.

Chen, Qin et al. (1998). "Wave-Current Interaction Based on an Enhanced Boussinesq Approach". In: *Coastal Engineering* 33.1, pp. 11–39.

Chen, Yongze and Philip L.-F. Liu (1995). "Modified Boussinesq Equations and Associated Parabolic Models for Water Wave Propagation". In: *J. Fluid Mech.* 288 (-1), p. 351.

Chiu, P.H., Long Lee, and Tony W.H. Sheu (2009). "A Dispersion-Relation-Preserving Algorithm for a Nonlinear Shallow-Water Wave Equation". In: *Journal of Computational Physics* 228.21, pp. 8034–8052.

Cho, Yong-Sik (1995). "Numerical Simulations of Tsunami Propagation and Run-up". PhD thesis. Cornell.

Cho, Yong-Sik, Dae-Hee Sohn, and Seung Oh Lee (2007). "Practical Modified Scheme of Linear Shallow-Water Equations for Distant Propagation of Tsunamis". In: *Ocean Engineering* 34.11-12, pp. 1769–1777.

Cho, Yong-Sik and Sung Bum Yoon (1998). "A Modified Leap-Frog Scheme for Linear Shallow-Water Equations". In: *Coastal Engineering Journal* 40.2, pp. 191–205.

Cienfuegos, R., E. Barthelemy, and P. Bonneton (2006). "A Fourth-Order Compact Finite Volume Scheme for Fully Nonlinear and Weakly Dispersive Boussinesq-type Equations. Part I: Model Development and Analysis". In: *Int. J. Numer. Meth. Fluids* 51.11, pp. 1217–1253.

Collatz, Lothar (1966). *The Numerical Treatment of Differential Equations*. 3rd ed. Berlin, Heidelberg: Springer Berlin / Heidelberg.

Courant, R, K Friedrichs, and H Lewyt (1967). "On the Partial Difference Equations of Mathematical Physics". In: *IBM J.* P. 20.

Craik, Alex D.D. (2004). "The Origins Of Water Wave Theory". In: *Annual Review of Fluid Mechanics* 36.1, pp. 1–28.

— (2005). "George Gabriel Stokes On Water Wave Theory". In: *Annu. Rev. Fluid Mech.* 37.1, pp. 23–42.

Dean, Robert G. and Robert A. Dalrymple (1991). *Water Wave Mechanics for Engineers and Scientists*. Advanced Series on Ocean Engineering v. 2. Singapore ; Teaneck, NJ: World Scientific. 353 pp.

Dingemans, Maarten W. (1997). *Water Wave Propagation over Uneven Bottoms*. Advanced Series on Ocean Engineering v. 13. River Edge, NJ: World Scientific Pub.

Feynman, Richard P (1970). *Feynman Lectures on Physics*. Boston, MA: Addison Wesley Longman.

Fornberg, Bengt (1998). "Calculation of Weights in Finite Difference Formulas". In: *SIAM Rev.* 40.3, pp. 685–691.

Fuhrman, David R. and Harry B. Bingham (2004). "Numerical Solutions of Fully Non-Linear and Highly Dispersive Boussinesq Equations in Two Horizontal Dimensions". In: *Int. J. Numer. Meth. Fluids* 44.3, pp. 231–255.

George, David L (2006). "Finite Volume Methods and Adaptive Refinement for Tsunami Propagation and Inundation". PhD thesis. University of Washington. 183 pp.

Gobbi, Mauricio F., James T. Kirby, and Ge Wei (2000). "A Fully Nonlinear Boussinesq Model for Surface Waves. Part 2. Extension to O(Kh)4". In: *J. Fluid Mech.* 405, pp. 181–210.

Gray, William G. (1980). "Do Finite Element Models Simulate Surface Flow?" In: *Proc. Third Int. Conf. Finite Elem. Water Resour.* Finite Elements in Water Resources. University of Mississippi, pp. 122–136.

Green, A. E., N. Laws, and P. M. Naghdi (1974). "On the Theory of Water Waves". In: *Proceedings of the Royal Society A: Mathematical, Physical and Engineering Sciences* 338.1612, pp. 43–55.

Ha, Taemin and Yong-Sik Cho (2015). "Tsunami Propagation over Varying Water Depths". In: *Ocean Engineering* 101, pp. 67–77.

Hairer, E., S. P. Norsett, and Gerhard Wanner (2009). *Solving Ordinary Differential Equations I: Nonstiff Problems*. 2nd rev. ed. Springer Series in Computational Mathematics 8. Heidelberg ; London: Springer. 528 pp.

Hansen, Walter (1949). "Die halbtagigen Gezeiten im Nordatlantischen Ozean". In: *Deutsche Hydrographische Zeitschrift* 2.1-3, pp. 44–51.

— (1956). "Theorie zur Errechnung des Wasserstandes und der StrOmungen in Randmeeren nebst Anwendungen". In: *Tellus* 8.3, pp. 287–300.

— (1962). "Hydrodynamical Methods Applied to Oceanographic Problems". In: Symposium on Mathematical Hydrodynamical Methods in Physical Oceanography. Univeristy Hamburg, pp. 25–34.

Heaps, N. S. (1969). "A Two-Dimensional Numerical Sea Model". In: *Philosophical Transactions of the Royal Society A: Mathematical, Physical and Engineering Sciences* 265.1160, pp. 93–137.

Imamura, Fumihiko (1997). "Review of Tsunami Simulation with a Finite Difference Method". In: *Long-Wave Runup Models*. Second International Workshop on Long-Wave Runup Models. Ed. by Harry Yeh, Philip Liu, and Costas Synolakis. Friday Harbor, USA: WORLD SCIENTIFIC, pp. 25–42.

Imamura, Fumihiko and Chiaki Goto (1988). "Truncation Error in Numerical Tsunami Simulation by the Finite Difference Method". In: *Coastal Engineering in Japan* 31.2, pp. 245–263.

Isaacson, E., J.J. Stoker, and A. Troesch (1958). "Numerical Solution of Flow Problems in Rivers". In: *J. Hydraul. Div.* 84.5, pp. 1–18.

Iskandar, Labib and Padam C Jain (1980). "Numerical Solutions of the Improved Boussinesq Equation". In: *Proc. Indian Acad. Sci. (Math. Sci.)* 89.3, pp. 171–181.

Jensen, Robert (1983). "A Consistent Analysis of Boussinesq-Type Water Wave Equations in Continuous and Discrete Form". PhD thesis. Texas A&M.

Jordan, Charles (1979). *Calculus of Finite Differences*. 3. ed., repr. New York: Chelsea Publ. Co. 654 pp.

Kaup, D. J. (1975). "A Higher-Order Water-Wave Equation and the Method for Solving It". In: *Progress of Theoretical Physics* 54.2, pp. 396–408.

Kennedy, Andrew B. et al. (2000). "Boussinesq Modeling of Wave Transformation, Breaking, and Runup. I: 1D". In: *Journal of Waterway, Port, Coastal, and Ocean Engineering* 126.1, pp. 39–47.

Kennedy, Andrew B. et al. (2001). "Boussinesq-Type Equations with Improved Nonlinear Performance". In: *Wave Motion* 33.3, pp. 225–243.

Kim, Jae W. and Duck J. Lee (1996). "Optimized Compact Finite Difference Schemes with Maximum Resolution". In: *AIAA Journal* 34.5, pp. 887–893.

Kobayashi, Marcelo H. (1999). "On a Class of Pade Finite Volume Methods". In: *Journal of Computational Physics* 156.1, pp. 137–180.

Kopal, Zdenek (1961). *Numerical Analysis With Emphasis on the Application of Numerical Techniques to Problems of Infinitesimal Calculus in Single Variable*. 2nd ed. John Wiley. 594 pp.

Korteweg, D. J. and G. de Vries (1895). "XLI. *On the Change of Form of Long Waves Advancing in a Rectangular Canal, and on a New Type of Long Stationary Waves*". In: *The London, Edinburgh, and Dublin Philosophical Magazine and Journal of Science* 39.240, pp. 422–443.

Kreiss, Heinz-Otto and Joseph Oliger (1972). "Comparison of Accurate Methods for the Integration of Hyperbolic Equations". In: *Tellus* 24.3, pp. 199–215.

Lacor, Chris, Sergey Smirnov, and Martine Baelmans (2004). "A Finite Volume Formulation of Compact Central Schemes on Arbitrary Structured Grids". In: *Journal of Computational Physics* 198.2, pp. 535–566.

Lannes, David (2013). *The Water Waves Problem: Mathematical Analysis and Asymptotics*. Mathematical Surveys and Monographs volume 188. Providence, Rhode Island: American Mathematical Society. 321 pp.

Leendertse, J.J. (1967). *Aspects of A Computational Model for Long-Period Water-Wave Propagation*. United States Air Force Project RAND RM-5294-PR, pp. 1–179.

Lele, Sanjiva K. (1992). "Compact Finite Difference Schemes with Spectral-like Resolution". In: *Journal of Computational Physics* 103.1, pp. 16–42.

LeVeque, Randall J. (1992). *Numerical Methods for Conservation Laws*. Second edition. Lectures in Mathematics. Basel: Springer Basel AG. 214 pp.

LeVeque, Randall J. (2007). *Finite Difference Methods for Ordinary and Partial Differential Equations: Steady-State and Time-Dependent Problems*. Philadelphia, PA: Society for Industrial and Applied Mathematics. 341 pp.

Li, Jichun and Miguel R. Visbal (2006). "High-Order Compact Schemes for Nonlinear Dispersive Waves". In: *J Sci Comput* 26.1, pp. 1–23.

Li, Linyan and Kwok Fai Cheung (2019). "Numerical Dispersion in Non-Hydrostatic Modeling of Long-Wave Propagation". In: *Ocean Modelling* 138, pp. 68–87.

Liu, Philip (1994). "Model Equations for Wave Propagations from Deep to Shallow Water". In: *Advances in Coastal and Ocean Engineering*. Vol. 1, pp. 125–157.

Liu, Z. B., K. Z. Fang, and Y. Z. Cheng (2018). "A New Multi-Layer Irrotational Boussinesq-type Model for Highly Nonlinear and Dispersive Surface Waves over a Mildly Sloping Seabed". In: *J. Fluid Mech.* 842, pp. 323–353.

Liu, Zhongbo and Kezhao Fang (2015). "Two-Layer Boussinesq Models for Coastal Water Waves". In: *Wave Motion* 57, pp. 88–111.

— (2016). "A New Two-Layer Boussinesq Model for Coastal Waves from Deep to Shallow Water: Derivation and Analysis". In: *Wave Motion* 67, pp. 1–14.

Long, Robert R. (1964). "The Initial-Value Problem for Long Waves of Finite Amplitude". In: *J. Fluid Mech.* 20.1, pp. 161–170.

Longuet-Higgins, M. S. and R. W. Stewart (1960). "Changes in the Form of Short Gravity Waves on Long Waves and Tidal Currents". In: *J. Fluid Mech.* 8.04, p. 565.

Longuet-Higgins, M S and R W Stewart (1964). "Radiation Stresses in Water Waves; a Physical Discussion, with Applications". In: *Deep-Sea Res.* 11, pp. 529–562.

Lu, Fuqiang (2016). "A Compact Fourth-Order Finite Difference Scheme for the Improved Boussinesq Equation with Damping Terms". In: *JCM* 34.5, pp. 462–478.

Lynch, Daniel R. and William G. Gray (1979). "A Wave Equation Model for Finite Element Tidal Computations". In: *Computers & Fluids* 7.3, pp. 207–228.

Lynett, Patrick J., Tso-Ren Wu, and Philip L.-F. Liu (2002). "Modeling Wave Runup with Depth-Integrated Equations". In: *Coastal Engineering* 46.2, pp. 89–107.

Lynett, Patrick and Philip Liu (2004). "A Two-Layer Approach to Wave Modelling". In: *Proc. Math. Phys. Eng. Sci.* 460.2049, pp. 2637–2669.

Lynett, Patrick and Philip L.-F. Liu (2002). "A Numerical Study of Submarine-Landslide-Generated Waves and Run-Up". In: *Proc. Math. Phys. Eng. Sci.* 458.2028, pp. 2885–2910.

Madsen, O.S. and C. C. Mei (1969). "The Transformation of a Solitary Wave Over an Uneven Bottom". In: *J. Fluid Mech.* 39.4, pp. 781–791.

Madsen, P.A., O.R. Sorensen, and H.A. Schaffer (1997). "Surf Zone Dynamics Simulated by a Boussinesq Type Model. Part II: Surf Beat and Swash Oscillations for Wave Groups and Irregular Waves". In: *Coastal Engineering* 32.4, pp. 289–319.

Madsen, Per A., Harry B. Bingham, and Hua Liu (2002). "A New Boussinesq Method for Fully Nonlinear Waves from Shallow to Deep Water". In: *J. Fluid Mech.* 462, pp. 1–30.

Madsen, Per A., Harry B. Bingham, and Hemming A. Schaffer (2003). "Boussinesq-Type Formulations for Fully Nonlinear and Extremely Dispersive Water Waves: Derivation and Analysis". In: *Proc. Math. Phys. Eng. Sci.* 459.2033, pp. 1075–1104.

Madsen, Per A., David R. Fuhrman, and Benlong Wang (2006). "A Boussinesq-type Method for Fully Nonlinear Waves Interacting with a Rapidly Varying Bathymetry". In: *Coastal Engineering* 53.5-6, pp. 487–504.

Madsen, Per A., Russel Murry, and Ole R. Sorensen (1991). "A New Form of the Boussinesq Equations with Improved Linear Dispersion Characteristics". In: *Coast. Eng.* 15, pp. 371–388.

Madsen, Per A. and Hemming A. Schaffer (1998). "Higher-Order Boussinesq-type Equations for Surface Gravity Waves: Derivation and Analysis". In: *Philosophical Transactions of the Royal Society of London. Series A: Mathematical, Physical and Engineering Sciences* 356.1749, pp. 3123–3181.

Madsen, Per A. and Ole R. Sorensen (1992). "A New Form of the Boussinesq Equations with Improved Linear Dispersion Characteristics: Part 2 A Slowly Varying Bathmetry". In: *Coast. Eng.* 18, pp. 183–204.

Mahesh, Krishnan (1998). "A Family of High Order Finite Difference Schemes with Good Spectral Resolution". In: *Journal of Computational Physics* 145.1, pp. 332–358.

McCowan, A.D. (1978). "Numeical Simulation of Shallow Water Waves". In: *Manag. Coast.* Fourth Australian Conference on Coastal and Ocean Engineering, pp. 133–138.

— (1981). "Developments in Numerical Short Wave Modelling". In: Fifth Australian Conference on Coastal and Ocean Engineering. Perth.

Mei, C. C. and B. Le Mehaute (1966). "Note on the Equations of Long Waves over an Uneven Bottom". In: *J. Geophys. Res.* 71.2, pp. 393–400.

Meijering, E. (2002). "A Chronology of Interpolation: From Ancient Astronomy to Modern Signal and Image Processing". In: *Proc. IEEE* 90.3, pp. 319–342.

Mohsen, A., H. El-Zoheiry, and L. Iskandar (1993). "A Highly Accurate Finite-Difference Scheme for a Boussinesq-Type Equation". In: *Applied Mathematics and Computation* 55.2-3, pp. 201–212.

Nwogu, Okey (1993). "Alternative Form of Boussinesq Equations for Nearshore Wave Propagation". In: *J. Waterway, Port, Coastal, Ocean Eng.* 119.6, pp. 618–638.

Pade, H. (1892). "Sur La Representation Approchee d'une Fonction Par Des Fractions Rationnelles". In: *Ann. Sci. Ecole Norm. Sup.* 9, pp. 3–93.

Peregrine, D. H. (1966). "Calculations of the Development of an Undular Bore". In: *J. Fluid Mech.* 25.2, pp. 321–330.

— (1967). "Long Waves On A Beach". In: *J. Fluid Mech.* 27.4, pp. 815–827.

Peregrine, D. H. (1974). "A Numerical Simulation of the Undular Hydraulic Jump: By M. B. Abbott and G. S. Rodenhuis, Journal of Hydraulic Research, Vol. 10 (1972), No. 3, Pp. 239/257." In: *Journal of Hydraulic Research* 12.1, pp. 141–157.

Pereira, J.M.C., M.H. Kobayashi, and J.C.F. Pereira (2001). "A Fourth-Order-Accurate Finite Volume Compact Method for the Incompressible Navier-Stokes Solutions". In: *Journal of Computational Physics* 167.1, pp. 217–243.

Pereira, Jose M, Marcelo H Kobayashi, and Jose C Pereira (2000). "HIGH ORDER COMPACT SCHEMES IN FINITE VOLUME CONTEXT". In: p. 13.

Phillips, N.A. (1959). "An Example of Nonlinear Computational Instability". In: *The Atmosphere and the Sea in Motion*, pp. 501–504.

Phillips, Owen M. (1966). *The Dynamics of the Upper Ocean*. repr. with corr. Cambridge Monographs on Mechanics and Applied Mathematics. Cambridge: Cambridge Univ. Press. 261 pp.

Platzman, G.W. (1958). "The Lattice Structure of the Finite Difference Primitive and Vorticity Equations". In: *Mon. Weather Rev.* 86, pp. 285–292.

Preissmann, A. (1961). "Propagation Des Intumescences Dans Les Canaux et Rivieres [Propagation of Translatory Waves in Channels and Rivers]". In: *Proc. Ler Congr. Assoc. Francaise Calc.* Grenoble, pp. 433–442.

Reid, R. O. and B. R. Bodine (1968). "Numerical Model for Storm Surges in Galveston Bay". In: *J. Waterw. Harb. Div.* 94.1, pp. 33–57.

Richtmyer, Robert Davis and Keith W. Morton (1967). *Difference Methods for Initial-Value Problems*. 2nd ed. Interscience Tracts in Pure and Applied Mathematics 4. New York, NY: Interscience Publ. 405 pp.

Roeber, Volker and Kwok Fai Cheung (2012). "Boussinesq-Type Model for Energetic Breaking Waves in Fringing Reef Environments". In: *Coastal Engineering* 70, pp. 1–20.

Roeber, Volker, Kwok Fai Cheung, and Marcelo H. Kobayashi (2010). "Shock-Capturing Boussinesq-type Model for Nearshore Wave Processes". In: *Coastal Engineering* 57.4, pp. 407–423.

Saint-Venant, A.J.C. Barre de (1871). "Theorie Du Mouvement Non Permanent Des Eaux, Avec Application Aux Crues Des Rivieres et a l'introduction de Marees Dans Leurs Lits". In: *Comptes Rendus Acad. Sci.* 73, 147–154 and 237–240.

Schaffer, Hemming A. and P. A. Madsen (1995a). "A New Formulation of Higher Order Boussinesq Equations". In: *Proc. Comput. Model. Seas Coast. Reg. II*. Cancun, Mexico, pp. 159–166.

Schaffer, Hemming A. and Per A. Madsen (1995b). "Further Enhancements of Boussinesq-type Equations". In: *Coastal Engineering* 26.1-2, pp. 1–14.

Schaffer, Hemming A and Per A Madsen (1998). "Discussion of "A Formal Derivation and Numerical Modelling of the Improved Boussinesq Equations for Varying Depth"". In: *Ocean Eng.* 25, pp. 497–500.

Schaffer, Hemming A and Per A Madsen (1999). "Further Discussion Related to 'A Formal Derivation and Numerical Modeling of the Improved Boussinesq Equations for Varying Depth' by Beji and Nadaoka". In: *Ocean Eng.* P. 6.

Schaffer, Hemming A., Per A. Madsen, and Rolf Deigaard (1993). "A Boussinesq Model for Waves Breaking in Shallow Water". In: *Coastal Engineering* 20.3-4, pp. 185–202.

Scotti, A. and S. Mitran (2008). "An Approximated Method for the Solution of Elliptic Problems in Thin Domains: Application to Nonlinear Internal Waves". In: *Ocean Modelling* 25.3-4, pp. 144–153.

Serre, Francois (1953). "Contribution to the Study of Permanent and Non-Permanent Flows in Channels". In: *La Houille Blanche* 3, pp. 374–388.

Shannon, C.E. (1949). "Communication in the Presence of Noise". In: *Proc. IRE* 37.1, pp. 10–21.

Shi, Fengyan et al. (2012). "A High-Order Adaptive Time-Stepping TVD Solver for Boussinesq Modeling of Breaking Waves and Coastal Inundation". In: *Ocean Modelling* 43–44, pp. 36–51.

Shi, Fengyan et al. (2018). "Breaking of Ship Bores in a Boussinesq-type Ship-Wake Model". In: *Coastal Engineering* 132, pp. 1–12.

Shuto, N (1991). "Numerical Simulation of Tsunamis - Its Present and Near Future". In: *Nat. Hazards* 4, pp. 171–191.

Shuto, Nobuo and Koji Fujima (2009). "A Short History of Tsunami Research and Countermeasures in Japan". In: *Proc. Jpn. Acad., Ser. B* 85.8, pp. 267–275.

Sobey, R J (1970). *Finite-Difference Schemes Compared for Wave-Deformation Characteristics in Mathematical Modeling of Two-Dimensional Long-Wave Propagation.* U.S. Army, Corps of Engineers Coastal Engineering Research Center 32, p. 51.

Stokes, George Gabriel (1891). "Note on the Theory of the Solitary Wave". In: *Philos. Mag.* 31, pp. 314–316.

Su, C. H. and C. S. Gardner (1969). "Korteweg-de Vries Equation and Generalizations. III. Derivation of the Korteweg-de Vries Equation and Burgers Equation". In: *Journal of Mathematical Physics* 10.3, pp. 536–539.

Svendsen, I.A. (1984). "Wave Heights and Set-up in a Surf Zone". In: *Coastal Engineering* 8.4, pp. 303–329.

Tam, Christopher K W (1995). "Computational Aeroacoustics: Issues and Methods". In: *AIAA J.* 33.10, pp. 1788–1796.

Tam, Christopher and Jay Webb (1993). "Dispersion-Relation-Preserving Finite Difference Schemes for Computational Acoustics". In: *J. Comput. Phys.* 107, pp. 262–281.

Tissier, M. et al. (2012). "A New Approach to Handle Wave Breaking in Fully Non-Linear Boussinesq Models". In: *Coastal Engineering* 67, pp. 54–66.

Titov, Vasily, Utku Kanoglu, and Costas Synolakis (2016). "Development of MOST for Real-Time Tsunami Forecasting". In: *J. Waterway, Port, Coastal, Ocean Eng.* 142.6, p. 03116004.

Titov, Vasily and Costas Emmanuel Synolakis (1995). "Modeling of Breaking and Nonbreaking Long-Wave Evolution and Runup Using VTCS-2". In: *Journal of Waterway, Port, Coastal, and Ocean Engineering* 121.6, pp. 308–316.

Tonelli, Mara and Marco Petti (2009). "Hybrid Finite Volume - Finite Difference Scheme for 2DH Improved Boussinesq Equations". In: *Coast. Eng.* P. 12.

Toro, E. F. (2009). *Riemann Solvers and Numerical Methods for Fluid Dynamics: A Practical Introduction*. 3rd ed. Dordrecht ; New York: Springer. 724 pp.

Ursell, F. (1953). "The Long-Wave Paradox in the Theory of Gravity Waves". In: *Math. Proc. Camb. Phil. Soc.* 49.04, p. 685.

Venutelli, Maurizio (2015). "New Optimized Fourth-Order Compact Finite Difference Schemes for Wave Propagation Phenomena". In: *Applied Numerical Mathematics* 87, pp. 53–73.

Vichnevetsky, R. and F. De Schutter (1975). "A Frequency Analysis of Finite Difference and Finite Element Methods for Initial Value Problems". In: *Mathematics and Computers in Simulation* 17.3, pp. 179–185.

Vichnevetsky, Robert and John B. Bowles (1982). *Fourier Analysis of Numerical Approximations of Hyperbolic Equations*. Society for Industrial and Applied Mathematics.

Wang, Xiaoming and Philip L.-F. Liu (2011). "An Explicit Finite Difference Model for Simulating Weakly Nonlinear and Weakly Dispersive Waves over Slowly Varying Water Depth". In: *Coastal Engineering* 58.2, pp. 173–183.

Warming, R.F and B.J Hyett (1974). "The Modified Equation Approach to the Stability and Accuracy Analysis of Finite-Difference Methods". In: *Journal of Computational Physics* 14.2, pp. 159–179.

Wegert, Elias (2012). *Visual Complex Functions: An Introduction with Phase Portraits*. Basel ; New York: Birkhauser. 360 pp.

Wei, Ge and James T. Kirby (1995). "Time-Dependent Numerical Code for Extended Boussinesq Equations". In: *Journal of Waterway, Port, Coastal, and Ocean Engineering* 121.5, pp. 251–261.

Wei, Ge et al. (1995). "A Fully Nonlinear Boussinesq Model for Surface Waves. Part 1. Highly Nonlinear Unsteady Waves". In: *J. Fluid Mech.* 294, pp. 71–92.

Whitham, G. B. (1974). *Linear and Nonlinear Waves*. Pure and Applied Mathematics. New York: Wiley. 636 pp.

Witting, James M (1984). "A Unified Model for the Evolution of Nonlinear Water Waves". In: *J. Comput. Phys.* 56, pp. 203–236.

Wongsaijai, B., C. Oonariya, and K. Poochinapan (2020). "Compact Structure-Preserving Algorithm with High Accuracy Extended to the Improved Boussinesq Equation". In: *Mathematics and Computers in Simulation* 178, pp. 125–150.

Wu, Theodore Yaotsu (2001). "A Unified Theory for Modeling Water Waves". In: *Advances in Applied Mechanics*. Vol. 37. Elsevier, pp. 1–88.

Yamazaki, Yoshiki, Zygmunt Kowalik, and Kwok Fai Cheung (2009). "Depth-Integrated, Non-Hydrostatic Model for Wave Breaking and Run-Up". In: *Int. J. Numer. Meth. Fluids* 61.5, pp. 473–497.

Yanenko, N. N. and Maurice Holt (1971). *The Method of Fractional Steps: The Solution of Problems of Mathematical Physics in Several Variables*. Berlin, Heidelberg: Springer Berlin Heidelberg.

Yoon, Sung B. (2002). "Propagation of Distant Tsunamis over Slowly Varying Topography". In: *J. Geophys. Res.* 107.C10, p. 3140.

Yoon, Sung B. and Philip L.-F. Liu (1989). "Interactions of Currents and Weakly Nonlinear Water Waves in Shallow Water". In: *J. Fluid Mech.* 205 (-1), p. 397.

Yoon, Sung Bum, Chae Ho Lim, and Junwoo Choi (2007). "Dispersion-Correction Finite Difference Model for Simulation of Transoceanic Tsunamis". In: *Terr. Atmos. Ocean. Sci.* 18.1, p. 031.

Zabusky, N. J. and M. D. Kruskal (1965). "Interaction of "Solitons" in a Collisionless Plasma and the Recurrence of Initial States". In: *Phys. Rev. Lett.* 15.6, pp. 240–243.

Zelt, J.A. (1991). "The Run-up of Nonbreaking and Breaking Solitary Waves". In: *Coastal Engineering* 15.3, pp. 205–246.

Zingg, David W. (2000). "Comparison of High-Accuracy Finite-Difference Methods for Linear Wave Propagation". In: *SIAM J. Sci. Comput.* 22.2, pp. 476–502.

El-Zoheiry, H. (2002). "Numerical Study of the Improved Boussinesq Equation". In: *Chaos, Solitons & Fractals* 14.3, pp. 377–384.